# MODALITÉS DE TOMOGRAPHIE COMPTON: CONCEPT, MODÉLISATION, ET PROBLÈMES INVERSES ASSOCIÉS

# MODALITIES OF COMPTON SCATTERING TOMOGRAPHY: CONCEPT, MODELLING AND ASSOCIATED INVERSE PROBLEMS

❧   ❋   ☙

Thèse de doctorat pour l'obtention du titre de docteur délivré par CY Cergy Paris Université
Ecole doctorale n°405 Économie, Management, Mathématiques, Physique & Sciences
Informatiques (EM2PSI)

Thèse présentée et soutenue à Pontoise, le mardi 7 décembre 2021, par

## Cécilia TARPAU

Devant le jury composé de :

| | | |
|---|---|---|
| Jérôme MARS | Professeur, Institut Polytechnique de Grenoble | Président du jury |
| Kacem CHEHDI | Professeur, Université de Rennes | Rapporteur |
| Voichita MAXIM | Maîtresse de conférences HDR, INSA Lyon | Rapporteure |
| Fabrice MÉRIAUDEAU | Professeur, Université de Bourgogne Franche-Comté | Examinateur |
| Jean-Christophe PESQUET | Professeur, Centrale Supelec | Examinateur |
| Maï K. NGUYEN-VERGER | Professeure, CY Cergy Paris Université | Directrice de thèse |
| Laurent DUMAS | Professeur, Université Versailles Saint-Quentin | Co-directeur de thèse |
| Geneviève ROLLET | Maîtresse de conférences, CY Cergy Paris Université | Encadrante de thèse |
| Jean AVAN | Directeur de recherche, CY Cergy Paris Université | Invité |

*Vous devez être prêt à prendre des risques,*
*et ne pas avoir peur d'échouer.*
*L'échec est la clé du succès.*

Michelle Obama

# Abstract

Since the seminal works of Cormack and Hounsfield, Nobel Prize of Medicine, Computed Tomography (CT) has become one of the privileged imaging techniques to explore internal structures of matter without destroying it. Classical CT uses only transmitted radiation without any deviation from the source to the detector. However, a significant proportion of emitted photons is scattered by Compton effect inside matter. As a consequence, Compton scattering causes serious degradation, in terms of blurring and loss of contrast on reconstructions. This may lead to influence the conclusions of diagnoses. Solving the scattering problem remains an important challenge. Current CT modalities (i.e., configurations) attempt to eliminate these scattered radiations by the use of collimation or filtering allowing to select only the transmitted photons, thanks to their direction or their energy. With such equipment, only few photons arrive at the detector. Compton scattered radiation can also be considered as a useful and significant part of information, which can be used for image reconstruction. This observation is the starting point of the development of imaging systems of Compton Scattering Tomography (CST).

The main objective of this thesis is to introduce a new CST modality, of circular geometry, made of a fixed source and a ring of detectors passing through the source. This CST modality, called Circular CST (CCST), conceptually surpasses the previous proposed systems since no movement of the source and detectors is required to acquire a complete set of data necessary for reconstruction. While CT is modelled by the Radon transform (RT) on lines, the geometry of the scattered radiation leads to consider circle arcs and generalized RT on the convenient family of circle arcs. In the case of CCST, the modelling of its operation leads to a new RT on a specific family of double arcs of circles passing through a fixed point (the point source). The first result of this thesis was the inversion of this RT to solve the reconstruction problem. With collimation at detectors, two approaches for inversion have been proposed. Moreover, the second proposed algorithm has shown promising results for acquisition of both small and large objects with a double scanning configuration. We also studied CCST without collimation. In absence of an analytical inversion formula, we proposed to use a regularization method in order to have simulation results. Otherwise, we studied also the possibility to introduce a movement for detectors. This study results in

the proposition of an inversion formula for the associated RT, in two and three dimensions. The corresponding reconstruction algorithms have proved impossible to use in practice for a CST system.

We also studied two other CST systems. The first one, introduced also during this thesis, consists of a fixed source and a detector rotating around the source. The two-dimensional design of this modality does not use collimation at detectors. Consequently, the modelling of data acquisition leads to a RT on another family of double circle arcs. As a first theoretical result, we established the analytic inversion of the RT. We also investigated its extension in three dimensions and proved the invertibility of the corresponding RT on toric surfaces. The second studied modality, previously introduced by Webber, consists of a pair source detector separated by a fixed distance one from each other. The source and the detector translate simultaneously to perform data acquisition. We suggested a suitable inverse formulation for simulations.

# Résumé

Depuis les travaux précurseurs de Cormack et Hounsfield, Prix Nobel de Médecine, la tomographie (CT) est devenue l'une des techniques d'imagerie privilégiée pour explorer les structures internes de la matière sans la détruire. La CT utilise uniquement le rayonnement transmis sans déviation de la source au détecteur. Cependant, une part importante des photons est diffusée par effet Compton. En conséquence, l'effet Compton cause flou et perte de contraste sur les reconstructions et peut influencer les conclusions d'un diagnostic. La résolution de ce problème de diffusion reste un challenge important. Les modalités (i.e. configurations) actuelles tentent d'éliminer ces rayonnements diffusés avec l'utilisation de collimateurs ou de filtres, permettant de sélectionner uniquement les photons transmis, grâce à leur direction ou leur énergie. Avec un tel équipement, peu de photons arrivent au détecteur. Le rayonnement diffusé par effet Compton peut aussi être considéré comme une part utile de l'information pour la reconstruction d'image. Cette observation marque l'émergence des modalités de tomographie Compton (CST).

L'objectif principal de cette thèse est d'introduire une nouvelle modalité CST. Le système proposé, de géométrie circulaire, est composé d'une source fixe et d'un anneau de détecteurs passant par la source. Cette modalité CST, nommée Tomographie Compton Circulaire (CCST), surpasse conceptuellement les systèmes proposés précédemment car aucun mouvement de la source ni des détecteurs n'est nécessaire pour avoir un ensemble complet de données. Si la tomographie conventionnelle est modélisée par la transformée de Radon (RT) sur les lignes, la géométrie des rayonnements diffusés conduit à considérer des arcs de cercle et ainsi des RT généralisées sur la famille d'arcs de cercle appropriée. Dans le cas de la CCST, la modélisation de l'acquisition d'image conduit à une nouvelle RT sur une famille spécifique d'arcs de cercle passant par un point fixe (le point source). Le premier résultat de cette thèse a consisté en l'inversion de cette RT et résoudre le problème de reconstruction. En considérant des détecteurs collimatés, deux approches pour l'inversion ont été proposées. Le second algorithme proposé a montré des résultats prometteurs pour l'acquisition des objets de petite et de grande taille. Nous avons aussi étudié la CCST sans collimateurs. En l'absence de formule inverse, nous avons proposé une méthode de régularisation afin d'effectuer des simulations. En outre, nous avons étudié la

possibilité d'introduire un mouvement pour les détecteurs. Cette étude a abouti sur la proposition d'une formule inverse analytique pour la RT associée, en deux et en trois dimensions. Cependant, les algorithmes de reconstruction issus de ces formules inverses se sont révélés inutilisables en imagerie.

Nous avons également étudié deux autres systèmes de tomographie Compton. Le premier, introduit dans cette thèse, est composé d'un détecteur non collimaté tournant autour d'une source fixe. La modélisation de l'acquisition des données conduit à une RT sur une famille de double arcs de cercle dont nous avons établi l'inversion. Nous avons également étudié son extension en trois dimensions et prouvé l'inversibilité de la RT correspondante. La seconde modalité étudiée, introduite précédemment par Webber, est composée d'une paire source détecteur séparés par une distance fixe. Cette paire translate pour effectuer l'acquisition des données. Nous avons proposé une formule d'inversion appropriée pour les simulations.

**Mots-clefs :** Systèmes d'imagerie, Tomographie Compton, Transformées de Radon généralisées, Probèmes inverses en imagerie, Reconstruction d'images, Modélisation de l'acquisition des données

# Remerciements

Je souhaite tout d'abord remercier mes directeurs Maï Nguyen, Laurent Dumas et Geneviève Rollet pour leur accompagnement et leur soutien tout au long de ma thèse. Je remercie également Kacem Chehdi et Voichita Maxim d'avoir accepté d'être rapporteurs de mon manuscrit ainsi que Jérôme Mars, Fabrice Mériaudeau, Jean-Christophe Pesquet et Jean Avan pour leur acceptation à la participation au jury de thèse.

J'ai eu l'opportunité lors de cette thèse d'être membre de trois laboratoires me permettant ainsi de découvrir des environnements de travail multiples, différents mais complémentaires dans l'approche de la modélisation de modalités de tomographie Compton. Ces encadrements de thèse pluridisciplinaires m'ont menés avec satisfaction à des travaux mélant théorie, simulations et modélisation.

Je profite pour remercier Mathias Quoy, Jean Avan et Christophe Chalons, respectivement directeurs des laboratoires ÉTIS, LPTM et LMV de m'avoir accueillie et intégrée au sein de leurs équipes. Je remercie aussi Olivier Romain qui a succédé á Mathias Quoy à la direction du laboratoire ÉTIS. Mes remerciements vont également à tous les enseignants, chercheurs et enseignants-chercheurs que j'ai côtoyés dans ces trois laboratoires et qui ont été une source d'inspiration tout au long de ce cursus doctoral. Mes vifs remerciements vont aussi à mes collègues doctorants — docteurs, pour certains maintenant — en particulier Pierre, Amine, Gada, Louis, Ali, Branda, Djenabou, Mohammed, Quentin pour les fructueux et stimulants échanges au cours de ces trois années passées. J'adresse également mes remerciements à Sylvie, Annick et Maryse pour leur précieuse aide dans les démarches administratives ainsi que Cédric et Laurent pour leur accompagnement quotidien sur le volet informatique.

Je remercie tout particulièrement Professeur Tuong Truong pour les échanges et discussions que nous avons eus au long de ma thèse ainsi que pour tout le soutien qu'il m'a toujours témoigné.

J'ai eu la chance aussi de travailler en étroite collaboration avec Javier Cebeiro, post-doctorant à l'Université San Martín en Argentine, que je remercie pour nos fructueuses discussions et pour son partage d'expérience. Je remercie aussi Marcela Morvidone, professeure à l'Université San Martín, pour les échanges que nous avons eus lors de nos publications communes.

J'adresse également de vifs remerciements au Professeur Rudolf Roemer pour son accueil et son accompagnement au quotidien lors de mon séjour de trois mois au sein de son équipe à l'université Warwick à Coventry en Angleterre.

J'exprime aussi ma sympathie et mes encouragements au futur doctorant Ishak et lui souhaite le meilleur pour son parcours de thèse.

Mes remerciements vont également au LabEx MME-DII (Modèles Mathématiques et Économiques de la Dynamique, de l'Incertitude et des Interactions) et au DIM MathInnov (Région Île de France) pour leur accompagnement financier durant ces trois années.

La richesse d'une thèse réside aussi dans les moments de discussions et d'échanges qu'offrent les conférences, les écoles et les workshops. J'y ai notamment rencontré Daniele, Yilbert et Axel avec qui nous avons partagé bien plus que des échanges scientifiques. Je remercie aussi Pierre Weiss, Chargé de recherche CNRS à l'Institut Mathématique de Toulouse, pour nos échanges qui ont contribué à mes travaux de thèse.

J'exprime enfin mon immense gratitude à mes parents, ma sœur ainsi qu'à l'ensemble de ma famille — sans oublier mon auto-proclamée muse qui m'a souvent répété *"trop présé pa ka fè jou ouvè"*[1] afin de modérer ma trop grande impatience — pour leur soutien tout au long de mon parcours scolaire. Je suis extrêmement reconnaissante envers mes parents qui ont toujours tout mis en œuvre afin que l'ensemble des conditions soient réunies pour la réussite de mes études.

---

[1]Proverbe créole, signifiant littéralement: *"être trop pressé ne fait pas le jour se lever plus tôt"*. Équivalent du proverbe français *"tout arrive à point pour qui sait attendre"*.

# Contents

# List of Figures

# List of Tables

# List of Algorithms

# Introduction

## Background

Consider the following imaging tasks: taking pictures of interior parts of the human body, or studying the internal structure of a fossil, or detecting manufacturing defects and anomalies of fabricated parts before they leave the factory, or checking the content of luggage at airport. In other words, *seeing the invisible*. This is the challenge taken up by tomographic imaging. In fact, via the use of X and gamma rays, tomographic imaging is a non-invasive technique able to penetrate matter and to discover its internal structures. Its applications range from medical imaging, to non-destructive inspection, through cultural heritage and security.

Tomography is governed by the Beer-Lambert law, which relates the intensity of the emitted and transmitted photon flux, denoted respectively $I_0$ and $I$, to the attenuation coefficient $\mu$ of the material along the photon path $L$

$$\ln\left(\frac{I_0}{I}\right) = \int_{\ell \in L} \mu(\ell)\, d\ell,$$

where $\ell$ is the elementary length measure on $L$.

The integral on the right-hand side of the above equation is called the Radon transform, in reference to its instigator Radon, who, in 1917, introduced this integral transform [1]. Consequently, data acquisition using conventional tomography is modelled by the Radon transform, which measures the contribution of all points located on a given straight line. From the knowledge of the recovered photon flux, the mathematical challenge raised by tomography consists in inverting the Radon transform to recover the attenuation map of the object. This challenge was taken up by Cormack [2], who won the Nobel Prize of medicine in 1979.

Current computed tomography only exploits primary radiation, that is transmitted radiation recovered by the detector without having undergone any deviation. Thus, tomography considers deviated radiation as damaged since it causes blur, loss of contrast and high noise level on reconstructions. As a consequence, in computed tomography, collimation at detectors eliminate deviated radiation inside matter. In the medium energy range (about hundreds of keV), the proportion of deviated photons is non-negligible. The main interaction for this energy range is the Compton effect [3, 4]. Compton scattering is a well-known photon

interaction, occurring when a photon meets a free electron inside matter. This photon is scattered and looses a part of its energy. The scattering angle $\omega$ is related to the energy $E$ of the scattered photon by a one to one correspondence

$$E(\omega) = \frac{E_0}{1 + \frac{E_0}{mc^2}(1 - \cos\omega)},$$

where $E_0$ is the energy of the emitted radiation and $mc^2$ the energy of an electron at rest.

Instead of attempting the elimination of these scattered photons, we can also take the option of considering them as a significant part of the information of the object under study. This is the challenge proposed by imaging with Compton Scattering Tomography (CST) which rests on the measurement of energy-indexed scattering photons.

Such a type of imaging technique opens the way towards new types of configurations (also called modalities in the literature) [5, 6, 7, 8, 9, 10, 11, 12, 13, 14] towards various applications, for instance in medical imaging [15, 16], earthquake engineering [17], cultural heritage objects imaging [18, 19], landmine detection [20], and agricultural measurements [21]. In fact, the object is no longer necessarily between sources and detectors. In some configurations, sources and detectors can be placed at the same side of the object. The acquisition of one-sided large objects is consequently easier. It is with the latter objective in mind that Norton, in 1994, proposed a modality, made of a source and a line of detectors passing through the source [8]. Note that this modality is completely fixed, making consequently the acquisition easier and faster. Since the main application of tomography remains medical imaging, Nguyen and Truong proposed later in 2010 a configuration suitable for small object scanning [9]. A source and a detector, diametrically opposed, rotate around the object to scan to perform data acquisition. Such CST systems raise also a novel mathematical challenge. In fact, while CT is perfectly modelled by the Radon transform on lines, the geometry of the scattered radiation leads to consider circle arcs and generalized Radon transforms on the convenient family of circle arcs. As a consequence, each CST configuration leads to a different generalized Radon transform on a special family of circle arcs, and image reconstruction requires its inversion.

## Purpose of this thesis

If we compare the two previous mentioned CST proposals, Norton's one has the advantage to be completely fixed, whereas Nguyen and Truong's one is able to scan small objects. The main purpose of this thesis is to introduce a CST modality which gathers both advantages. This modality consists of a source and a set of detectors placed on a ring, the whole remaining completely fixed during acquisition. The circular layout of this modality allows reducing scanning time and time to exposure to radiation. This modality is called Circular Compton Scattering Tomography (CCST). With such a configuration, we meet the requirements of biomedical imaging, since its objective is to scan small objects, as fast as possible.

We will show that the modelling of its operation leads to a new Radon transform on a specific family of double arcs of circles passing through a fixed point, the source point. The next objective is now to propose reconstruction strategies for this system. We chose here to search —as far as possible— for an analytical solution to the studied Radon transform. These analytical reconstruction formulas will lead us to reconstruction algorithms offering fast and exact reconstruction results.

If, at a first sight, CCST has only advantages, this fact has to be counterbalanced with some issues when we want to find the analytic inverse formula of its corresponding Radon transform. We will see that this will imply some constraints for the detectors. We discuss also three-dimensional extensions for CCST.

Then, we present two other CST modalities and provide the analytical inversion formulas for their respective corresponding Radon transforms. The first one, is also introduced during this thesis, consists of a fixed source and an uncollimated detector in rotation around the source. With such a modality, we propose a simpler system, also compact, which does not require collimation at detectors. The second modality, recently introduced in the literature, has a translational geometry. We will propose an inversion formula in association with an efficient reconstruction algorithm.

In the next paragraphs, we present in more details the outline of this thesis.

## Outline of this thesis

This thesis is divided into three parts as follows. While Part I recalls details about current tomographic systems and introduces the functioning of Compton scattering tomography, we expose in Parts II and III the contributions of this thesis.

### Part I: Recall on conventional tomography and motivations for Compton Scattering tomography

Before the introduction of the CCST, we recall some important notions for imaging in the two following chapters.

### Chapter 1: Interactions of ionizing radiation with matter and application in imaging

In the Chapter 1, we discuss the possible photon interactions inside matter. This leads us to consider the Beer Law, which describes macroscopically radiation attenuation. This law is the core of computed tomography. We then explain the limitations of the latter, which led us to consider Compton scattering tomographic imaging systems. We end this chapter by a review of the previous proposed CST modalities and give some details about their corresponding Radon transform and their inversion.

### Chapter 2: Reconstruction methods in classical tomographic imaging

Since one of the main challenges of this thesis is to propose strategies for image reconstruction from CCST measurements, we first review in chapter 2 some existing reconstruction techniques used for classical tomography. We begin with two reconstruction methods based on the analytic inversion formula proposed by Cormack. The first one is the well-known filtered back-projection algorithm. We introduce also a second method, the rho-filtered layergram, where the operations of filtering and back-projection are reversed compared to the filtered back-projection. Then, we introduce regularization techniques that can also be used for reconstruction. We discuss more precisely about two methods for obtaining image reconstruction using Tikhonov regularization method. While the first method consists in applying the well-known matrix formulation of the problem, we discuss also a matrix-free implementation, which allows avoiding the costly computation of the discrete forward operator. We end this chapter providing the obtained reconstruction results and propose a comparison of these methods in terms of computation time, required storage and reconstruction quality.

### Part II: The proposition of the Circular Compton Scattering Tomography

Part II is devoted to the main contribution of this thesis, that is, the proposition and the study of CCST.

### Chapter 3: Presentation of the circular Compton scattering tomography

We present in Chapter 3 the modality and its working principle. We set also its advantages, its potentials and also a comparison with the other proposed CST systems. We then propose a parameterization for the system. We introduce also the generalized Radon transform on double circle arcs modelling data acquisition using CCST, an integral transform that we want to invert for image reconstruction purposes. We end the chapter setting the working assumptions introduced to take up this mathematical challenge.

### Chapter 4: Reconstruction strategies for CCST with collimation at detectors

In chapter 4, we model data acquisition for CCST with collimation at detectors. This implies that the family of scanning double circle arcs can be grouped into a simple family of circle arcs. From this assumption, we propose two reconstruction strategies based on two analytic inverse formulas of the corresponding Radon transform. The first one is deduced from a previous work of Cormack, who established the invertibility of the Radon transform on circles passing through the origin. We show that this Radon transform can be used to model data acquisition of CCST, and propose a filtered back-projection type algorithm suitable for image reconstruction from data on circles. In the second approach, we propose to use geometric inversion to convert the Radon transform on circle arcs which models data into a Radon transform on half-lines, never introduced before. We establish in this work the invertibility of this Radon transform on half-lines and propose a second filtered back-projection type algorithm to obtain reconstructions from data on half-lines. Then, we include this filtered back-projection algorithm into a global algorithm, able to provide image reconstruction from

data of CCST. We illustrate the efficiency of both proposed inversion schemes, performing numerical simulations.

**Chapter 5: CCST without collimation at detectors and three-dimensional extensions**

In the first part of chapter 5, we assume on the other hand that we do not have collimation at detectors of CCST. The objective consists in consequently inverting the Radon transform on double circle arcs. The inversion formula is still an open problem. For reconstructions, we propose an inversion strategy based on Tikhonov regularization. We present, then, in a second time, two three-dimensional extensions of CCST. These configurations suppose, either detectors on a fixed sphere, or detectors on a cylinder, called respectively Spherical CST and Cylindrical CST.

**Chapter 6: Analytical inversion of a Radon transform on a family of cones with pivoting axes**

The work presented in Chapter 6 was born out of the search for an inverse formula for the Radon transform on the double arcs of circles, modelling the acquisition of data for the CCST without collimators. This thinking led us to a Radon transform on a new family of cones with pivoting axes, of which we present here the analytical inversion in two and three dimensions. Simulation results are also carried out.

### Part III: Other CST modalities studied

In this third part, we present the two other modalities studied during this thesis.

**Chapter 7: A CST modality with a fixed source and a rotating detector**

In this chapter 7, we present a new CST configuration made of a fixed source and an uncollimated detector rotating around the source and give the advantages of such a model. The modelling of data acquisition lead to a Radon transform on double circle arcs, whose inversion is established. From this formula, we propose a reconstruction algorithm and carry out simulations to illustrate its efficiency. We also propose a study illustrating the influence of some general parameter choices on simulation results. At the end of the chapter, we discuss also about this CST setup in three dimensions and establish the invertibility of the corresponding Radon transform on toric sections.

**Chapter 8: A CST modality with translational geometry**

In chapter 8, we are working with a modality introduced by Webber and Miller [13]. This modality consists of a source and a detector separated by a fixed distance, which translate simultaneously on a line. In their original study, Webber and Miller proved the invertibility of the corresponding Radon transform, and suggested an inversion formula, using the theory of Volterra integral equations. The numerical realization of such a type of inverse formula may exhibit some difficulties, mainly due to stability issues. Here, we provide a suitable formulation for exact inversion that can be straightforwardly implemented in the Fourier

domain. Simulations are carried out to illustrate the efficiency of the proposed reconstruction algorithm.

This thesis contains also four appendices.

**Appendix A** relates the complete demonstration to obtain the Radon transform modelling data acquisition taking into account realistic parameters. CCST is then simulated using this formula and the result is compared with *ground-truth data* obtained with Monte Carlo simulations.

**Appendix B** deals with the proof of the analytical inversion of the Radon transform on half-lines introduced in Chapter 5.

**Appendix C** gives the technical details in some demonstrations of Chapter 7.

Finally, in **appendix D**, we sum up the advantages and drawbacks of the proposed modalities in this thesis as well as the previously proposed ones in the literature.

## Publications

This thesis has led to several publications, summarized below. Note that [C8] were done during the thesis, but are not presented in details in the manuscript.

**Accepted articles in international scientific journals**

**[J1] Cécilia Tarpau**, Javier Cebeiro, Marcela A. Morvidone and Mai K. Nguyen, "A new concept of Compton scattering tomography and the development of the corresponding circular Radon transform", *IEEE Transactions on Radiation and Plasma Medical Sciences (IEEE-TRPMS)*, vol. 4, no. 4, pp. 433-440, 2020. [doi:10.1109/TRPMS.2019.2943555].

**[J2] Cécilia Tarpau** and Mai K. Nguyen, "Compton scattering imaging system with two scanning configurations", *Journal of Electronic Imaging (JEI)*, vol. 29, no. 1, 2020. [doi: 10.1117/1.JEI.29.1.013005].

**[J3] Cécilia Tarpau**, Javier Cebeiro, Mai K. Nguyen, Geneviève Rollet and Marcela A. Morvidone, "Analytic inversion of a Radon transform on double circular arcs with applications in Compton Scattering Tomography", *IEEE Transactions on Computational Imaging (IEEE-TCI)*, vol. 6, pp. 958-967, 2020. [doi: 10.1109/TCI.2020.2999672].

**[J4]** Javier Cebeiro, **Cécilia Tarpau**, Marcela A. Morvidone, Diana Rubio and Mai K. Nguyen, "On a three-dimensional Compton scattering tomography system with fixed source", *Inverse Problems*, vol. 37, no. 5, 054001, 2021. [doi: 10.1088/1361-6420/abf0f0].

**[J5] Cécilia Tarpau**, Javier Cebeiro, Geneviève Rollet, Mai K. Nguyen and Laurent Dumas, "An analytical reconstruction formula with efficient implementation for a modality

of Compton Scattering Tomography with translational geometry", *accepted for publication in Inverse problems in Imaging*, 2021.

**Paper in preparation**

[PP1] **Cécilia Tarpau**, Javier Cebeiro, Mai K. Nguyen, Geneviève Rollet and Laurent Dumas, "Analytic inversion of a Radon transform of a class of cones with pivoting axes", 2021.

**Preprint**

[P1] **Cécilia Tarpau**, Javier Cebeiro, Mai K. Nguyen, Geneviève Rollet, and Laurent Dumas, "On the design of a CST system and its extension to a bi-imaging modality", *ArXiv preprint arXiv:2007.02750*, 2020.

**Peer-reviewed proceedings of international conferences**

[C1] **Cécilia Tarpau** and Mai K. Nguyen, "A novel modality of Compton Scattering Tomography: Image formation and Reconstruction", 22th *International Conference on Image Processing, Computer Vision and Pattern Recognition (IPCV)*, Las Vegas, United States, 30 July - 2 August 2018.

[C2] Javier Cebeiro, Mai K. Nguyen, Marcela Morvidone and **Cécilia Tarpau**, "An interior Compton Scattering Tomography", *IEEE Nuclear Science Symposium and Medical Imaging Conference (IEEE NSS/MIC)*, Sydney, Australia, 10-17 November 2018.

[C3] Javier Cebeiro, Marcela A. Morvidone, **Cécilia Tarpau** and Mai K. Nguyen, "On the invertibility of a new toric Radon transform with applications in Compton scatter tomography", *VII Congress on industrial, computational and applied mathematics (MACI)*, Comodoro Rivadavia, Argentine, 8-10 May 2019.

[C4] **Cécilia Tarpau** and Mai K. Nguyen, "Scattering imaging system with dual configuration", *14th International conference on Quality Control by Artificial Vision (QCAV)*, Mulhouse, France, 15-17 Mai 2019.

[C5] Javier Cebeiro, Marcela A. Morvidone, Diana Rubio, **Cecilia Tarpau** and Mai K. Nguyen, "A new Transmission Compton Scattering Tomography", *XVIII Workshop on Information Processing and Control (RPIC)*, Bahia Blanca, Argentine, 18-20 September 2019.

[C6] **Cécilia Tarpau**, Javier Cebeiro and Mai K. Nguyen, "A new bi-imaging NDT system for simultaneous recovery of attenuation and electronic density maps", *11th Symposium on NDT in Aerospace*, Paris, France, 13-15 November 2019.

[C7] **Cécilia Tarpau**, Javier Cebeiro, Mai K. Nguyen, Geneviève Rollet and Laurent Dumas, "On 3D imaging systems based on scattered ionizing radiation", *International Conference of*

*SPIE Photonics Europe*, Digital forum, 6-10 April 2020.

**[C8]** Ishak Ayad, **Cécilia Tarpau**, Mai K. Nguyen and Ngoc Son Vu, "Deep Morphological Network-based Artifact Suppression for Limited-angle Tomography", *25th International Conference on Image Processing, Computer Vision and Pattern Recognition (IPCV)*, Las Vegas, United States, 26-29 July 2021.

**Invited presentations at international conferences**

**[I1]** **Cécilia Tarpau**, Javier Cebeiro and Mai K. Nguyen, "Radon transforms on circular arcs and their associated modalities of Compton Scattering Tomography", *10th International Conference on Applied Inverse Problems (AIP)*, Grenoble, France, 8-12 July 2019.

**[I2]** Javier Cebeiro, **Cécilia Tarpau**, Marcela A. Morvidone, Diana Rubio and Mai K. Nguyen, "A new toric Radon transform and its connection with other Radon type transforms", *10th International Conference on Applied Inverse Problems (AIP)*, Grenoble, France, 8-12 July 2019.

# Part I

# Recall on conventional tomography and motivations for Compton scattering tomography

We present in Chapter 1 the main physical interactions photon/matter and introduce the functionning principle of conventional tomography. We underline the limits of classical tomography and then the interest of taking into account photons scattered by the Compton effect in the imaging process. We review also the modalities of Compton scattering tomography previously proposed in the literature.

In chapter 2, we review some classical methods of reconstruction in classical tomographic imaging.

# 1

# Interactions of ionizing radiation with matter and applications in imaging

**Synopsis**  We review in this chapter the main interactions a photon can undergo inside matter. This leads us to introduce the Beer's law, which is the basis of computed tomography. We also introduce the functioning principle of Compton scattering tomography and present the previously proposed systems.

## 1.1  Individual photon interactions inside matter

When a photon goes through matter, the latter may be subject to several kinds of interactions with consequences on its energy. Depending on the experienced interaction, it can either lose all or a part of its energy, or keep its initial energy, which corresponds respectively to an absorption, an elastic or an inelastic scattering. Individual photon interactions are expressed in terms of cross-sections. The cross-section $\sigma$ is a surface quantity related to the probability of interaction between a particle and a photon. When the interaction refers to a photon scattering, the angular distribution is defined by a differential cross-section $(d\sigma/d\Omega)$ where $d\Omega$ stands for the solid angle. The corresponding total cross-section is obtained by integration of the differential cross-section over the scattering angular domain

$$\sigma = 2\pi \int \left( \frac{d\sigma}{d\Omega} \right)_\theta \sin\theta \, d\theta. \tag{1.1}$$

We describe in this section the four fundamental X-ray interactions as well as their corresponding cross-sections (and/or differential cross-sections if relevant).

### 1.1.1  Elastic scattering

Elastic scattering refers to Thomson and Rayleigh scattering. Thomson scattering stands for the interaction between a photon and a free charged particle. The particle, generally an electron, absorbs the photon and a new one is emitted. The emitted photon has the same energy as the absorbed one, but may have a different direction. Given a scattering angle $\theta$,

Thomson showed that the differential cross-section is given by

$$\frac{d\sigma_{\text{th}}}{d\Omega} = \frac{r_0^2}{2}(1 + \cos^2 \theta),$$ (1.2)

where $r_0$ is the classical radius of the electron, $r_0 = 2.818 \times 10^{-15}$m. By integration, one can obtain

$$\sigma_{\text{th}} = \frac{8\pi r_0^2}{3}.$$ (1.3)

Rayleigh scattering refers to a similar phenomenon with the same consequences when the photon interacts, this time, with individual atoms or molecules.

### 1.1.2 Inelastic scattering

Inelastic scattering refers to Compton scattering. When a photon of energy $E_0$ interacts with a charged particle, usually an electron, this photon is scattered with an angle $\omega$ and transfers a part of its energy to the charged particle. The energy of the scattered photon $E$ is related by a one to one correspondence to $\omega$ according to the relation

$$E(\omega) = \frac{E_0}{1 + \frac{E_0}{mc^2}(1 - \cos \omega)},$$ (1.4)

where $mc^2 = 0.511$ MeV is the energy of an electron at rest.
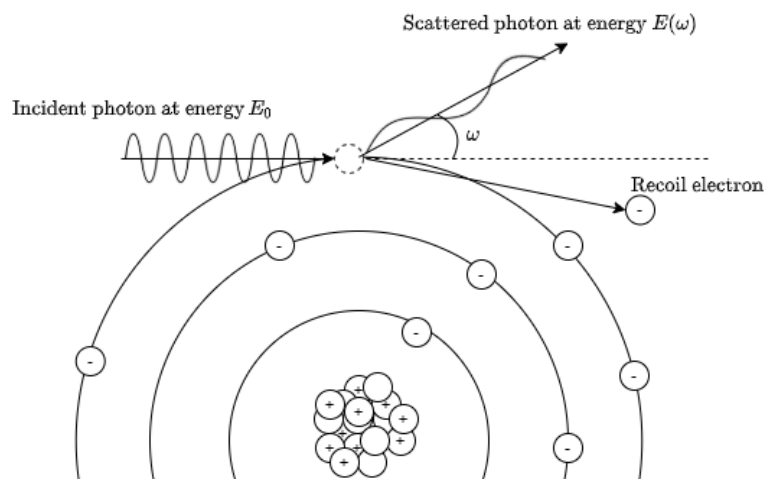


**Figure 1.1** – Compton effect - The interaction of the incident photon and an electron results in a scattered photon whose energy $E(\omega)$ is related to scattering angle $\omega$ according to Compton formula (1.4).

The probability for a photon of being scattered in the solid angle $d\Omega$ with a scattering angle

$\omega$ is given by [22]

$$P(\omega) = \frac{1}{2} \left( 1 + \frac{\epsilon^2 (1 - \cos\omega)^2}{(1 + \cos^\omega)(1 + \epsilon(1 - \cos\omega))} \right) \frac{1 + \cos^2\omega}{(1 + \epsilon(1 - \cos\omega))^2}, \tag{1.5}$$

where $\epsilon = E_0/mc^2$, $m$ is the electron mass and $c$ is the speed of light. The differential cross-section is proportional to $P(\omega)$

$$\left( \frac{d\sigma_c}{d\Omega} \right)_\omega = r_0^2 P(\omega) \tag{1.6}$$

and it was also proven in [22] that

$$\sigma_c = \frac{3\sigma_{th}}{4} \left( \frac{2(1+\epsilon)^2}{\epsilon^2(1+2\epsilon)} + \frac{\ln(1+2\epsilon)}{\epsilon} \left( \frac{1}{2} - \frac{1+\epsilon}{\epsilon^2} \right) - \frac{1+3\epsilon}{(1+2\epsilon)^2} \right). \tag{1.7}$$

### 1.1.3  Photoelectric effect

The photoelectric effect occurs when the energy of the incident photon is greater than or equal to the binding energy. The photon then gives up all its energy to an internal electron and is absorbed.

An electron from a higher layer then fills the vacant space and leads either to the emission of a photon or to the emission of an Auger electron.



(a)        (b)
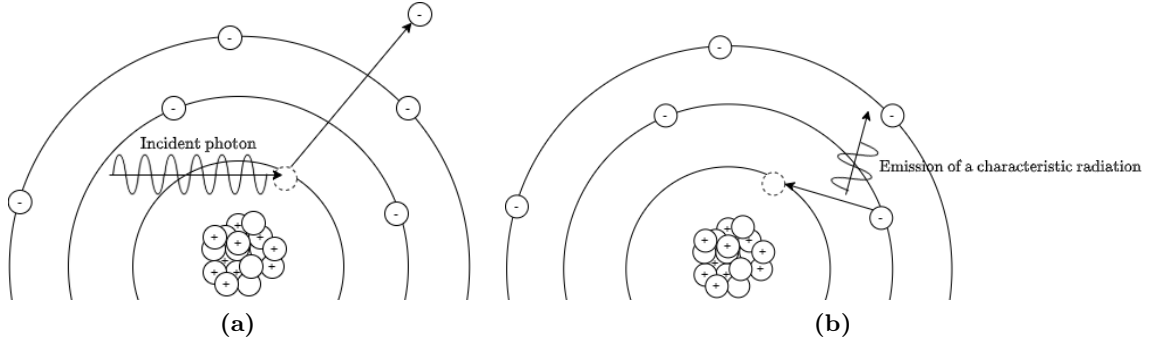
**Figure 1.2** − Photoelectric effect with photon emission - (a) The energy of the incident photon is given entirely to an electron, which is ejected. (b) Another electron from a higher layer takes the vacant place, which results in the emission of a characteristic radiation.

The photoelectric cross-section is experimentally given by

$$\sigma_f = k \frac{Z^n}{(h\nu)^m}, \tag{1.8}$$

where $k$ is a constant, $Z$ is the atomic number and $n$ and $m$ are exponents respectively in the range $3.6 - 5.3$ and $2.5 - 3.5$ and are largest for low atomic numbers.

### 1.1.4   Pair production

Pair production refers to the creation of an electron-positron pair. This phenomenon occurs when the photon, with an energy greater or equal to 1022 keV, interacts with a nucleus. The electron is quickly absorbed, and the positron combines with an electron and two photons of energy 511 keV are created by annihilation. These photons travel in matter in opposite directions.
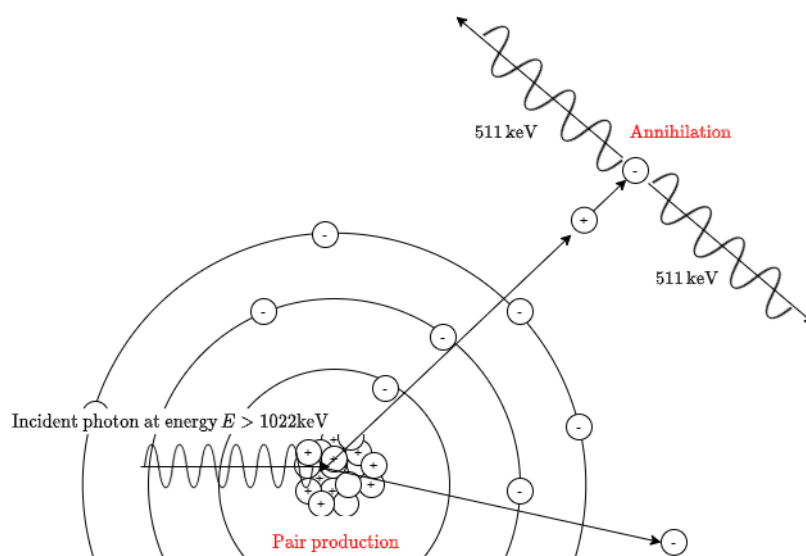


**Figure 1.3** – Pair production: A pair electron positron is produced after the interaction of a photon with the nucleus of an atom. Annihilation: Two photons of energy 511 keV emerges from the combination of the positron and another electron.

## 1.2   Macroscopic point of view of photon interactions

In the latter section, we described the possible interactions a photon can undergo individually. When we consider a beam of photons, the attenuation inside matter sums up all these interactions. Denoting $I_0$ the intensity of the incident photon flux, the intensity $I$ of the transmitted beam of photons after passing through a medium of width $x$ is given by Beer-Lambert law

$$I = I_0 \exp\left(-\mu x\right), \tag{1.9}$$

where $\mu$ is the linear attenuation coefficient of the medium.

According to the area of dominance of the different photon interactions (see Figure 1.4), when we consider incident photons of energy about a few hundred of keV, the attenuation is caused by photoelectric absorption and Compton scattering. The attenuation coefficient values for each chemical element $\mu$ are available in terms of mass attenuation coefficients in databases provided by the National Institute of Standards and Technology (NIST) [23].
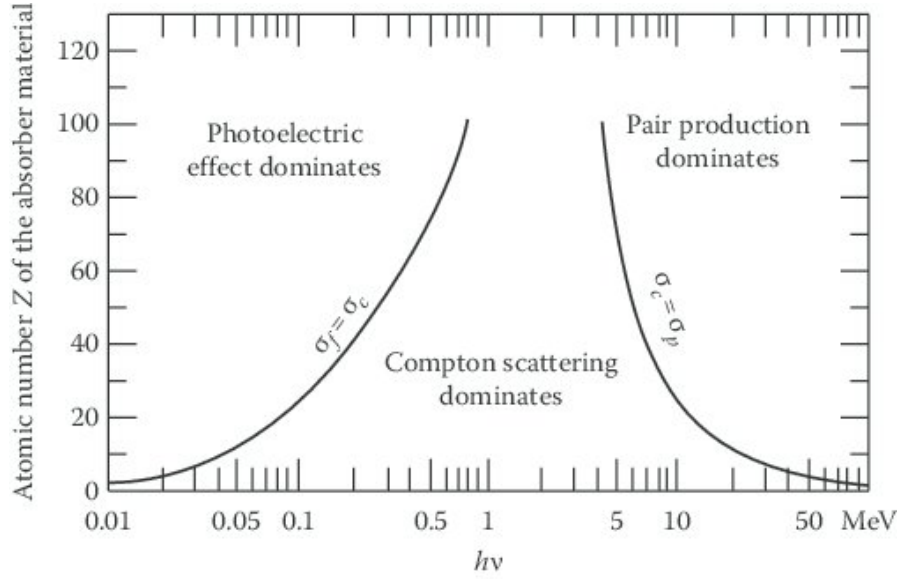
**Figure 1.4** – Area of dominance of photoelectric absorption, Compton effect and pair production (source [3]) according to energy $h\nu$ and atomic number $Z$ of the considered material. Their respective cross-sections are denoted $\sigma_f$, $\sigma_c$ and $\sigma_p$. Thompson scattering, less predominant than the others interactions, is not represented.

## 1.3  Applications in imaging

### 1.3.1  Conventional Computed tomography (CT)

Computed tomography is an imaging technique exploiting radiation attenuation through matter along linear paths. A source $S$ emits rays of intensity $I_0$ travelling along lines inside matter, and these photons are recovered with an intensity $I < I_0$ by a detector $D$. The simplest CT system, pictured in figure 1.5, is composed of a line of sources and a line of detectors, which requires a rotation to reconstruct the attenuation map of the object.

Image reconstruction consists in the recovery of the attenuation map $\mu$ of the object from the known values of $I$ and $I_0$. According to the Beer Law, the equation to solve is

$$\ln\left(\frac{I_0}{I(L)}\right) = \int_{(x,y)\in L} \mu(x,y)d\ell, \tag{1.10}$$

where $d\ell$ stands for the elementary length measure on the considered line $L$. The above right-hand side integral, which models image formation, is the classical Radon transform on the line $L$ [1]. As a consequence, image reconstruction, i.e. recovering the attenuation map $\mu$, supposes the inversion of this integral. Cormack, who established the analytical inversion formula of this Radon transform, was awarded the Nobel Prize of Medicine in 1979 for his work contributing to the invention of the CT scan. The first part of Chapter 2 is devoted to the presentation of some reconstruction methods from the proposed inversion formula.
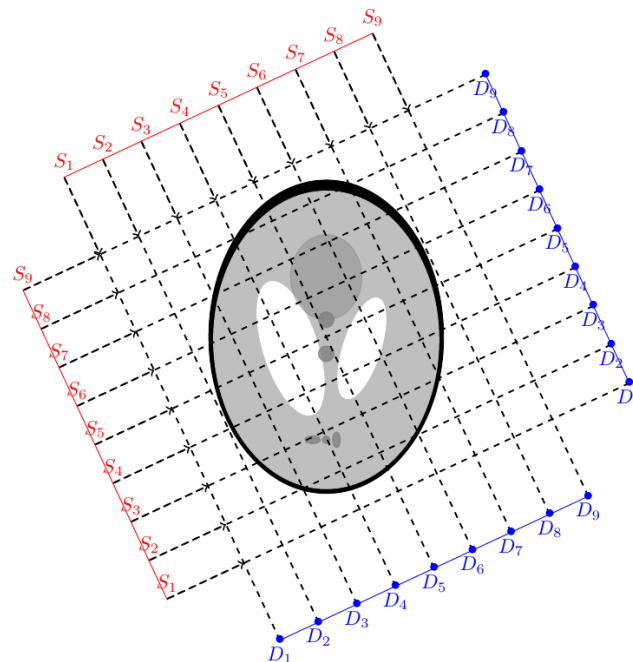
**Figure 1.5** – Functioning principle of computed tomography. The arrays of sources and detectors are respectively represented in red and blue at two different times during acquisition. In fact, the system needs to rotate to perform a full data acquisition. The dashed lines represent the corresponding X-ray paths.

### 1.3.2 Limitations of computed tomography

In the middle energy range and particularly for low atomic number materials, Compton effect is the predominant phenomenon responsible for radiation attenuation. In addition, detected Compton scattered radiation may also induce blur, high noise level and a loss of contrast on reconstructions. Small details of reconstructions, extremely important for biomedical imaging applications or non-destructive evaluation, may be lost and consequently lead to incorrect diagnoses. CT modalities attempt to eliminate these scattered radiation by the use of collimation or filtering. With such equipment, only one photon over ten thousand arrives at the detector [24].

On the other hand, Compton scattered radiation can also be considered as a useful and significant part of information, which can also be used for tomographic reconstruction. This statement notes the emergence of Compton Scattering Tomography (CST) modalities.

### 1.3.3 Compton scattering tomography

The working principle of CST systems rests on the collection of the intensity of Compton scattered photons according to their energy $E(\omega)$ by a detector $D$. If we consider only

first-ordered scattered radiation[1] and according to the one to one correspondence between $E(\omega)$ and $\omega$ (1.4), simple geometric considerations show that, photons recovered with a given energy $E(\omega)$ are scattered at different sites $M_i$ located on a circle arc passing through the source $S$ and $D$ (see Fig. 1.6). This circle arc subtends the angle $(\pi - \omega)$. This explains why the acquisition process for CST modalities can be modelled by Radon transforms on families of circle arcs, depending on the considered modality. Denoting $f$ an unknown function, the general formulation for such a Radon transform is

$$\mathcal{R}^{\mathrm{CST}} f(S, D, \omega) = \int_{\mathcal{C}(S,D,\omega)} f(M) w(S, D, \omega, M) d\ell(M), \tag{1.11}$$

where $\mathcal{C}(S, D, \omega)$ is the considered family of circle arcs, $w(S, D, M)$ is a weighting function and $dl$ the elementary arc length measure on the considered arcs. In a physical meaning, the function $f$ is a map of the electronic density of the object. The flux of photons of energy $E(\omega)$ registered at the detector site $D$ is proportional to the integral of $f$ and $w$ on the circle arcs $\mathcal{C}$. The weighting function allows incorporating in the model some physical effects such as attenuation and realistic aspects of the source and the detector.
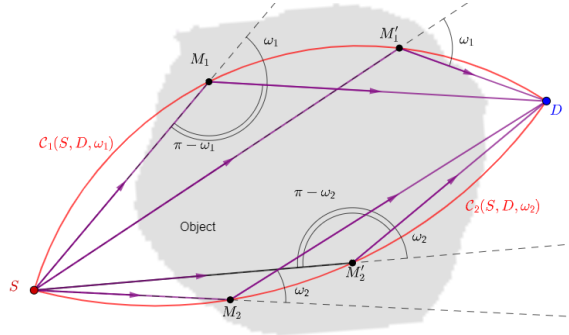


**Figure 1.6** $-$ General functioning principle of a CST system. Photons are emitted by source $S$ (in red), interact at sites $M$, and are recorded at site $D$ (in blue). When a photon is detected carrying an energy $E(\omega_1)$ (resp. $E(\omega_2)$), the possible interaction sites lie on the upper (resp. lower) circle arc which subtends the angle $(\pi - \omega_1)$ (resp. $(\pi - \omega_2)$).

Imaging using CST systems offers several advantages, such as

- the possibility to have source and detector on the same side of the sample. This feature is particularly interesting for scanning large objects [25].

- the higher contrast of scattering based images compared to CT images. This is helpful for tracking tumours [15, 16], without additional radiation dose.

Compton scattering tomography has been early studied by Lale [5], Clarke [6] and Farmer [7]. However, CST presents a double challenge, both mathematical and technological, which

---

[1]This assumption is motivated by the fact that first order scattering is predominant in front of higher orders.

has hindered its development. First, we saw that image formation differs completely from that of classical tomography, with scanning manifolds on circle arcs instead of lines. As a consequence, the modelling of data acquisition leads to generalizations of Radon transforms on families of circle arcs, according to the geometry of the CST system under study. The new objective is to propose an inversion for these integral transforms. Second, the proposition of a prototype requires multi-energy detectors with a sufficient energy resolution.

We concentrate here on the mathematical challenge raised by Compton scattering tomography. This work is in line with the previous works of Norton [8], Nguyen and Truong [9, 10]. In the next paragraph, we present briefly their works, as well as other more recent propositions. For a complete review about CST systems, the reader can refer to [24].

### 1.3.4  Previous proposed two-dimensional CST modalities

We present, first, the previous proposed two-dimensional systems. These modalities suppose plate collimation to restrict emitted photons to a plane. For each modality, we present the setup, give the Radon transform modelling data acquisition and present the used procedures for inversion.

In the following, $(r, \theta)$ are the polar coordinates of a running point $M$ on the considered family of scanning circle arcs.

**Norton's modality (1994)**

**Setup**  The first modality whose data measurement has been modelled by a Radon transform was proposed in 1994 by Norton [8]. The system is made of a fixed source $S$ and a detector $D$ moving on a line in intersecting the source site[2]. See Figure 1.7.

We note $x_D$ the distance between $S$ and $D$. The upper part of the space is considered using a system of collimation on the source and the detector. With $S$ at the origin of the polar coordinates and $D$ on the $x$-axis, the scattering sites are on circle arcs of the polar equation

$$r = \rho(x_D, \omega) \cos(\theta - \phi(x_D, \omega)), \theta \in [0, \pi], \tag{1.12}$$

where $\rho$ is the diameter of the circle arc and $\phi$ its angle relative to $x$-axis. This relation originates from the polar equation on the family of circles passing through the origin, with a restriction on the domain of $\theta$.

The parameters $\rho$ and $\phi$ of the circle arcs are related to the position of detector $x_D$ and scattering angle $\omega$,

$$\rho(x_D, \omega) = \frac{x_D}{\cos\left(\omega - \frac{\pi}{2}\right)} \text{ and } \phi(x_D, \omega) = \omega - \frac{\pi}{2}. \tag{1.13}$$

---

[2]Equivalently, a fixed array of detectors $D_k$ can be used.
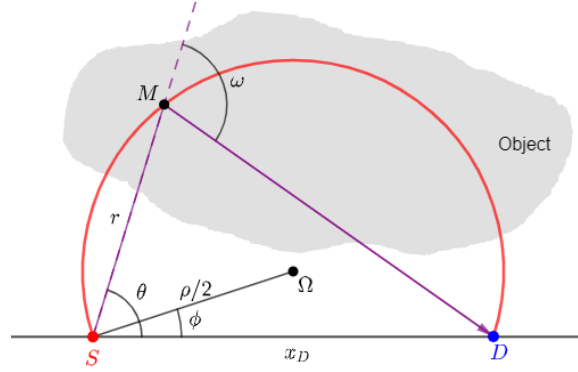
**Figure 1.7** – Norton's modality - 1994. The source $S$ is represented by a red point. The detector, localized at the distance $x_D$ of the source, is represented by a blue point. $M(r, \theta)$ is a running point, in black, and an example of scattering site. An example of trajectory for a photon whose scattering site is $M$ is shown in purple. The corresponding scattering angle is denoted $\omega$. The object to scan is represented in grey. The red continuous curve in an example of scanning circle arc. $\Omega$ is the centre of the supporting circle, $\rho$ its diameter and $\phi$ its angle relative to the $x$-axis.

**Radon transform modelling data acquisition** Assuming first-ordered Compton scattering is the predominant interaction inside matter and neglecting attenuation, the data measurement with Norton's modality is mathematically modelled by equation [8]

$$\mathcal{R}^{\text{Nor}} f(\rho, \phi) = \int_{\phi - \pi/2}^{\phi + \pi/2} \int_{-\infty}^{\infty} \rho f(r, \theta) w(r, \theta; \rho, \phi) \delta(r - \rho \cos(\theta - \phi)) dr \, d\theta, \qquad (1.14)$$

where $\delta$ stands for the Dirac delta distribution. The weighting function $w$ is defined by

$$w(r, \theta, \rho, \phi) = \frac{ars(\theta) r_0^2 P(\phi + \pi/2)}{4\pi \rho^4 \sin^2 \theta}, \qquad (1.15)$$

where $a$ is the area of a detector, $s(\theta)$ is the measure of the angular dependence of an anisotropic source and $r_0^2 P(\omega)$ is the Klein Nishina cross-section (1.6) for the scattering angle $\omega$. The interested reader by the derivation of the weighted function can refer to the original reference [8]. As a result, equation (1.14) is a weighted Radon transform of the function $f$ along the scanning circle arcs (1.12).

**Proposed procedure for inversion** The proposed inversion formula by Norton [8] rests on the property of factorization of the function $w$. In fact, one can write $w$ as the product of two functions $w_1(r, \theta)$ and $w_2(\rho, \phi)$. As a result, (1.14) becomes

$$\mathcal{R}^{\text{Nor}} f(\rho, \phi) = w_2(\rho, \phi) \int_{\phi - \pi/2}^{\phi + \pi/2} \int_{-\infty}^{\infty} \rho f(r, \theta) w_1(r, \theta) \delta(r - \rho \cos(\theta - \phi)) dr \, d\theta. \qquad (1.16)$$

Then, let $\tilde{f}(\xi, \theta)$ be the Fourier transform with respect to $r$ of $f(r, \theta)w_1(r, \theta)$

$$\tilde{f}(\xi, \theta) = \int_0^\infty f(r, \theta)w_1(r, \theta) \exp\left(-i\xi r\right)dr. \tag{1.17}$$

The corresponding inverse Fourier transform is

$$f(r, \theta)w_1(r, \theta) = \frac{1}{2\pi} \int_{-\infty}^\infty \tilde{f}(\xi, \theta) \exp\left(i\xi r\right)d\xi. \tag{1.18}$$

Substituting $f(r, \theta)w_1(r, \theta)$ by its expression (1.18) in (1.16), and changing the order of integration, one gets

$$\mathcal{R}^{\text{Nor}} f(\rho, \phi) = \frac{w_2(\rho, \phi)}{2\pi} \int_0^\pi \int_{-\infty}^\infty \tilde{f}(\xi, \theta) \exp\left(i\xi\rho\cos\left(\theta - \phi\right)\right)d\xi d\theta. \tag{1.19}$$

Let

$$\mathcal{R}_1^{\text{Nor}} f(\rho, \phi) = \frac{2\mathcal{R}^{\text{Nor}} f(\rho, \phi)}{\pi w_2(\rho, \phi)} \tag{1.20}$$

and

$$\tilde{f}_1(\xi, \theta) = \tilde{f}(\xi, \theta)/|\xi|. \tag{1.21}$$

From (1.19), one has

$$\mathcal{R}_1^{\text{Nor}} f(\rho, \phi) = \frac{1}{\pi^2} \int_0^\pi \int_{-\infty}^\infty |\xi|\tilde{f}_1(\xi, \theta) \exp\left(i\xi\rho\cos\left(\theta - \phi\right)\right)d\xi d\theta. \tag{1.22}$$

The left-hand side of the equation (1.22) is the two-dimensional Fourier transform of $\tilde{f}_1$ in polar coordinates. Applying the inverse Fourier transform yields the above equation

$$\tilde{f}_1(\xi, \theta) = \int_0^{2\pi} \int_0^\infty \rho\, \mathcal{R}_1^{\text{Nor}} f(\rho, \phi) \exp\left(i\xi\rho\cos\left(\theta - \phi\right)\right)d\rho d\phi. \tag{1.23}$$

Furthermore, using (1.9) in (1.18), one gets the following relation

$$f(r, \theta)w_1(r, \theta) = \frac{1}{2\pi} \int_{-\infty}^\infty |\xi|\tilde{f}_1(\xi, \theta) \exp(i\xi r)d\xi. \tag{1.24}$$

Finally, substituting (1.23) into (1.24), changing the order of integration, weighting both sides by $1/w_1(r, \theta)$ and going back to the original function $\mathcal{R}^{\text{Nor}} f$ and $w$, the function $f$ can be recovered from the following equation

$$f(r, \theta) = \frac{1}{2\pi^2} \int_0^{2\pi} \frac{\mathcal{R}^{\text{Nor}} f(\rho, \phi)}{w(r, \theta, \rho, \phi)} h(r - \rho\cos\left(\theta - \phi\right)d\phi, \tag{1.25}$$

with

$$h(x) = \int_{-\infty}^\infty \exp(-i\xi x)|\xi|d\xi.$$

Data acquisition for Norton's modality can also be modelled by the Radon transform on circles passing through the origin, assuming that the lower part (below the $x$-axis) gives no contribution. This family of circles is a special case of curves studied by Cormack [26, 27], who gave also an inverse formula for the corresponding Radon transform[3]. In [24], Truong and Nguyen gave details about this approach applied to Norton's modality. In [28], following the Chapman and Cary approach [29], Rigaud proposed a numerical reconstruction algorithm for the regularized inverse formulation in circular harmonic decomposition. Note also that the closed inversion formula given by Cormack in [27] can be also used to model Norton's modality. As a result, a similar derivation as proposed by us in Chapter 4 for CCST can be carried out.

**Nguyen and Truong's modality (2010)**

**Setup**   The model proposed by Nguyen and Truong [9] supposes a source $S$, placed at a distance $2p$ from a detector $D$. The pair source-detector is in rotation around the middle of the segment $SD$, according to variable $\varphi$. A system of collimation is also used, in order to consider uniquely the upper part of the system. See figure 1.8.
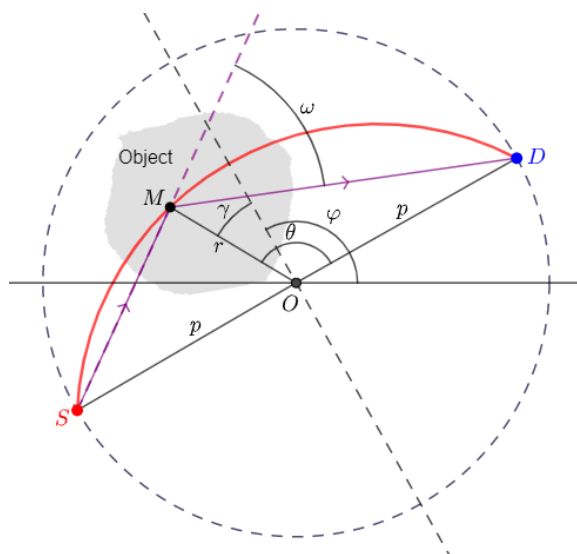


**Figure 1.8** − Nguyen and Truong's modality - 2010. The colour code is the same as in figure 1.7. The dashed circle represents the circular path on which moves the pair source-detector.

Note that an external scanning for this modality was discussed in [24], by the authors. This external scanning allows placing the object outside the circular path of the source and the detector. Since the mathematical development is similar, we will only discuss the internal scanning here.

---

[3]In his work, Cormack established inversion formulas for the Radon transform on his family of curves in a mathematical point of view. His work is not referred to any imaging system and consequently, no realistic effect was considered.

The family of circle arcs of interest here admits a radius of $p/\sin\omega$ and subtends an angle $(\pi - \omega)$. The angle between the mediator line $SD$ and $OM$ is denoted $\gamma$. We define also variable $\tau$ as $\tau = \cot\omega$. In that case, scanning circle arcs are defined by equation

$$r = r(\cos\gamma) = p\left(\sqrt{1 + \tau^2\cos^2\gamma} - \tau\cos\gamma\right), \tag{1.26}$$

where $\gamma \in ]\pi/2, \pi/2[$. Similarly, the parametric equation of the circle arc can be also written as

$$\cos\gamma = \frac{1}{2\tau}\left(\frac{p}{r} + \frac{r}{p}\right). \tag{1.27}$$

**Radon transform modelling data acquisition** The authors proposed a theoretical study of the Radon transform modelling data acquisition, without weighting function. Making explicit the circle-arc integration element $ds$ as

$$ds = r\sqrt{\frac{1 + \tau^2}{1 + \tau^2\cos^2\gamma}}d\gamma. \tag{1.28}$$

one gets:

$$\mathcal{R}^{\mathrm{Ngu}}f(\tau, \varphi) = \int_{-\frac{\pi}{2}}^{\frac{\pi}{2}} r(\cos\gamma)\, f\left(r(\cos\gamma), \varphi - \gamma\right)\frac{\sqrt{\tau^2 + 1}}{\sqrt{\tau^2\cos^2\gamma + 1}}d\gamma. \tag{1.29}$$

**Proposed procedure for inversion** The first step for inverting this Radon transform consists in using the circular harmonic expansion to establish a relation between the components of a function $f$ and $\mathcal{R}^{\mathrm{Ngu}}f$. The procedure was previously introduced by Cormack [26]. In what follows, the circular harmonic expansions of $f$ and $\mathcal{R}^{\mathrm{Ngu}}f$ are respectively denoted $f_l$ and $(\mathcal{R}^{\mathrm{Ngu}}f)_l$

$$f(r, \theta) = \sum_{l=-\infty}^{\infty} f_l(r)e^{il\theta} \tag{1.30}$$

$$\mathcal{R}^{\mathrm{Ngu}}f(\tau, \varphi) = \sum_{l=-\infty}^{\infty} (\mathcal{R}^{\mathrm{Ngu}}f)_l(\tau)e^{il\varphi} \tag{1.31}$$

where

$$f_l(r) = \frac{1}{2\pi}\int_0^{2\pi} f(r, \theta)e^{-il\theta}d\theta \tag{1.32}$$

$$(\mathcal{R}^{\mathrm{Ngu}}f)_l(\tau) = \frac{1}{2\pi}\int_0^{2\pi} \mathcal{R}^{\mathrm{Ngu}}f(\tau, \varphi)e^{-il\varphi}d\varphi \tag{1.33}$$

for $l \in \mathbb{Z}$.

Using the parity of the integrand of (1.29), one gets

$$(\mathcal{R}^{\mathrm{Ngu}}f)_l(\tau) = 2\int_0^{\frac{\pi}{2}} r(\cos\gamma)\sqrt{\frac{1+\tau^2}{1+\tau^2\cos^2\gamma}}\, f_l(r(\cos\gamma))\cos(l\gamma)d\gamma. \tag{1.34}$$

With the change of variable $r$ in the above integral and

$$\frac{r(\cos\gamma)}{\sqrt{1+\tau^2\cos^2\gamma}}d\gamma = \frac{dr}{\sqrt{\tau^2 - \frac{1}{4}\left(\frac{p}{r}-\frac{r}{p}\right)^2}}, \tag{1.35}$$

(1.34) becomes

$$\frac{\tau}{\sqrt{1+\tau^2}}(\mathcal{R}^{\mathrm{Ngu}}f)_l(\tau) = 2\int_{p(\sqrt{1+\tau^2}-\tau)}^p \frac{\cos\left(l\cos^{-1}\left(\frac{1}{2\tau}\left(\frac{p}{r}-\frac{r}{p}\right)\right)\right)}{\sqrt{\tau^2-\frac{1}{4}\left(\frac{p}{r}-\frac{r}{p}\right)^2}}f_l(r)dr. \tag{1.36}$$

Let now

$$q = \frac{1}{\tau} = \tan\omega \ \text{ and } \ \frac{1}{s} = \frac{1}{2}\left(\frac{p}{r}-\frac{r}{p}\right).$$

Straightforward computations show that $r = p(\sqrt{1+s^{-2}}-s^{-1})$, $\tau(1+\tau^2)^{-1/2} = (1+q^2)^{-1/2}$ and $r^{-1}dr = s^{-1}(1+s^2)^{-1/2}ds$. Let also $h_l(r) = rf_l(r)$. From (1.36), one gets

$$\frac{(\mathcal{R}^{\mathrm{Ngu}}f)_n(1/q)}{\sqrt{1+q^2}} = 2\int_q^\infty \frac{1}{s\sqrt{1+s^2}}\,h_l\left(p\left(\sqrt{1+s^{-2}}-s^{-1}\right)\right)\frac{\cos\left(l\cos^{-1}(q/s)\right)}{\sqrt{1-(q/s)^2}}ds. \tag{1.37}$$

Multiplying both sides of equation (1.37) by

$$\frac{\cosh\left(l\cosh^{-1}(q/t)\right)}{q\sqrt{(q/t)^2-1}},$$

and integrating over $q$ from $t$ to infinity, one gets, after rearranging the two-dimensional integration of the right-hand side

$$\int_t^\infty \frac{\cosh\left(l\cosh^{-1}(q/t)\right)}{q\sqrt{(q/t)^2-1}}\frac{(\mathcal{R}^{\mathrm{Ngu}}f)_l(1/q)}{\sqrt{1+q^2}}dq =$$
$$2\int_t^\infty \frac{1}{s\sqrt{1+s^2}}h_l\left(p\left(\sqrt{1+s^{-2}}-s^{-1}\right)\right)\int_t^s \frac{\cosh\left(l\cosh^{-1}(q/t)\right)}{q\sqrt{(q/t)^2-1}}\frac{\cos\left(l\cos^{-1}(q/s)\right)}{\sqrt{1-(q/s)^2}}dq\,ds. \tag{1.38}$$

According to [26], the $q$-integral is $\pi/2$. This relation leads us to,

$$\int_t^\infty \frac{1}{s\sqrt{1+s^2}} h_l\left(p\left(\sqrt{1+s^{-2}-s^{-1}}\right)\right) ds = \frac{1}{\pi}\int_t^\infty \frac{\cosh(l\cosh^{-1}(q/t))}{q\sqrt{(q/t)^2-1}} \frac{(\mathcal{R}^{\mathrm{Ngu}}f)_l(1/q)}{\sqrt{1+q^2}} dq. \tag{1.39}$$

Then, we go back to coefficients $f_l$ with a differentiation with respect to the variable $t$

$$\frac{-\pi}{t\sqrt{1+t^2}} p\left(\sqrt{1+t^{-2}}-t^{-1}\right) f_l\left(p\left(\sqrt{1+t^{-2}}-t^{-1}\right)\right) = \left[\frac{d}{dt}\int_t^\infty \frac{\cosh(l\cosh^{-1}(q/t))}{q\sqrt{(q/t)^2-1}} \frac{(\mathcal{R}^{\mathrm{Ngu}}f)_l(1/q)}{\sqrt{1+q^2}} dq\right]_{t=\frac{2pr}{p^2-r^2}}. \tag{1.40}$$

Substituting $p\left(\sqrt{1+t^{-2}}-t^{-1}\right)$ by $r$, one gets

$$t = \frac{2pr}{p^2-r^2} \quad \text{and} \quad \frac{1}{t\sqrt{1+t^2}} = \frac{2pr}{p^2+r^2}.$$

These expressions allow having the following relation

$$f_l(r) = (-)\frac{(p^2+r^2)}{2\pi pr^2}\left[\frac{d}{dt}\int_t^\infty \frac{\cosh\left(l\cosh^{-1}(q/t)\right)}{q\sqrt{(q/t)^2-1}} \frac{(\mathcal{R}^{\mathrm{Ngu}}f)_l(1/q)}{\sqrt{1+q^2}} dq\right]_{t=\frac{2pr}{p^2-r^2}}. \tag{1.41}$$

A change of variable in the integration gives finally the last relation

$$f_l(r) = (-)\frac{(p^2+r^2)}{2\pi pr^2}\left[\int_t^\infty \frac{\cosh\left(l\cosh^{-1}(q/t)\right)}{\sqrt{q^2-t^2}} \frac{d}{dq}\left(\frac{(\mathcal{R}^{\mathrm{Ngu}}f)_l(1/q)}{\sqrt{1+q^2}}\right) dq\right]_{t=\frac{2pr}{p^2-r^2}}. \tag{1.42}$$

Equation (1.42) ensures that the function $f$ can be completely recovered via its circular harmonic expansion $f_l$ from the circular harmonic expansion of data measurement $(\mathcal{R}^{\mathrm{Ngu}}f)_l$. This relation was numerically implemented in [28] following the method proposed by Chapman and Cary [29].

**Truong and Nguyen's modality (2011)**

**Setup**  This second modality was proposed by Truong and Nguyen in [10]. As their first proposed modality, this system is made also of a source $S$ and a detector $D$ moving on a fixed circle of centre $O$ and radius $p$. This circle is called $\Gamma_p$. However, $S$ and $D$ are no longer diametrically opposed. Instead, $S$ and $D$ are separated by an angular distance $(2\gamma_0)$, which depends on the scattering angle $\omega$, such that $\omega = \gamma_0 + \pi/2$. As a consequence, the circles supporting the scanning arcs intersect the circular path at points $S$ and $D$ orthogonally. The photons, emitted by the source, are scattered by an object, placed outside the circular path

of the source and the detector[4]. Thus, the detector $D$ registers scattered photons of energy $E(\omega)$ from the exterior part of a circle of centre, $\Omega$ which subtends the angle $(\pi - \omega)$. The radius of this circle is equal to $p\sqrt{\tau^2 - 1}$, where $\tau = 1/\cos\gamma_0$. See Figure 1.9.



**Figure 1.9** − Truong and Nguyen's modality - 2011. The colour code is the same as in figure 1.7. The dashed circle represents the circular path on which moves the pair source-detector.

Moreover, these scanning circle arcs admit as polar equation

$$r = r(\cos\gamma) = p(\tau\cos(\gamma) + \sqrt{\tau^2\cos^2(\gamma) - 1}), \gamma \in ]-\gamma_0, \gamma_0[. \qquad (1.43)$$

**Radon transform modelling data acquisition** The authors proposed a theoretical study of the corresponding Radon transform modelling data measurement without weighting function. Denoting $\varphi$ the angle between the $Ox$-axis and the segment $O\Omega$, this Radon transform has the following expression

$$\mathcal{R}^{\mathrm{Tru}}f(\tau, \varphi) = \int_{-\gamma_0}^{\gamma_0} r(\cos\gamma)\sqrt{\frac{\tau^2 - 1}{\tau^2\cos^2\gamma - 1}} f(r(\cos\gamma, \gamma + \varphi)d\gamma. \qquad (1.44)$$

As for their first modality, the authors established a relation between circular harmonic expansions of object $f$ and data $\mathcal{R}^{\mathrm{Tru}}f$, denoted respectively $f_l$ and $(\mathcal{R}^{\mathrm{Tru}}f)_l$:

$$\frac{(\mathcal{R}^{\mathrm{Tru}}f)_l(\tau)}{\sqrt{\tau^2 - 1}} = 2\int_1^\tau \frac{\cos\left(l\cos^{-1}(s/\tau)\right)}{\sqrt{1 - (s/\tau)^2}} \frac{p\left(s + \sqrt{s^2 - 1}\right)}{\sqrt{s^2 - 1}} f_l\left(p\left(s + \sqrt{s^2 - 1}\right)\right) dr. \qquad (1.45)$$

---

[4]A internal scanning for this modality was also discussed one year after in [24]

**Proposed procedure for inversion**  For inversion purposes, they followed the same procedure, resulting in an inversion formula for the circular harmonic components

$$f_l(r) = \frac{1}{2\pi r} \left(\frac{r}{p} - \frac{p}{r}\right) \left[\frac{d}{dt} \int_1^t \frac{\cosh\left(l\cosh^{-1}(t/\tau)\right)}{\sqrt{(t^2 - \tau^2)(\tau^2 - 1)}} (\mathcal{R}^{\mathrm{Tru}}f)_l(\tau)d\tau\right]_{t=\frac{1}{2}\left(\frac{r}{p} - \frac{p}{r}\right)}. \qquad (1.46)$$

As for their first modality, this inversion formula can be numerically implemented following the Chapman and Cary approach. Nevertheless, the authors proposed also to go one step further for this modality, deriving a closed form for the inversion formula. This closed inversion formula allows recovering the function $f$ directly from data $\mathcal{R}^{\mathrm{Tru}}f$ without the calculation of their respective circular harmonic expansion. The final inversion is

$$f(r, \theta) = \frac{1}{4\pi^2 r} \left(\frac{r}{p} - \frac{p}{r}\right)$$
$$\mathrm{p.v.} \int_0^{2\pi} \frac{1}{\cos(\theta - \varphi)} \left\{\mathrm{p.v.} \int_1^\infty d\tau \left(\frac{d}{d\tau} \frac{\mathcal{R}^{\mathrm{Tru}}f(\tau, \varphi)}{\sqrt{\tau^2 - 1}}\right) \frac{1}{\frac{1}{2}\left(\frac{p}{r} + \frac{r}{p}\right) - r\cos(\theta - \varphi)}\right\} d\varphi.$$
$$(1.47)$$

This inversion formula is obtained introducing the consistency conditions in terms of Cormack sense [27]. For the details of computation, the reader can refer to the original article [10]. We will follow also this scheme to obtain the inversion formula for the second proposed modality in this thesis. As a result, even no simulation results were carried out by the authors, one can also deduce from the closed formulation a reconstruction formula more suitable for numerical computations. Compared to the Chapman and Cary approach, adopting such technique will require less computational resources.

**Webber and Miller's modality (2020)**

**Setup**  A CST system was also proposed by Webber and Miller in [13]. This system is made of a source and a detector separated by a fixed distance $d = 2$ from each other. The source and the detector move respectively on a horizontal line, and their position is marked by their common abscissa $x_0$. This system may also be sketched with fixed lines of sources and detectors which will be used in pair. No collimation is used at the detector to split up photons coming from different circle arcs. As a consequence, the acquisition is performed on a family of double circle arcs[5]. See figure 1.10.

This modality is able to acquire data of one-sided large objects, and its geometry makes this modality suitable for baggage screening applications. Given a scattering angle $\omega$, scattering

---

[5]In the original publication[13], the scanning manifold is described as a family of toric sections. The qualification of *family of double circle arcs* seems to be more appropriated, since only a part of the supporting toric section, denoted $S_{1,2,3,4}$, was considered for calculations.
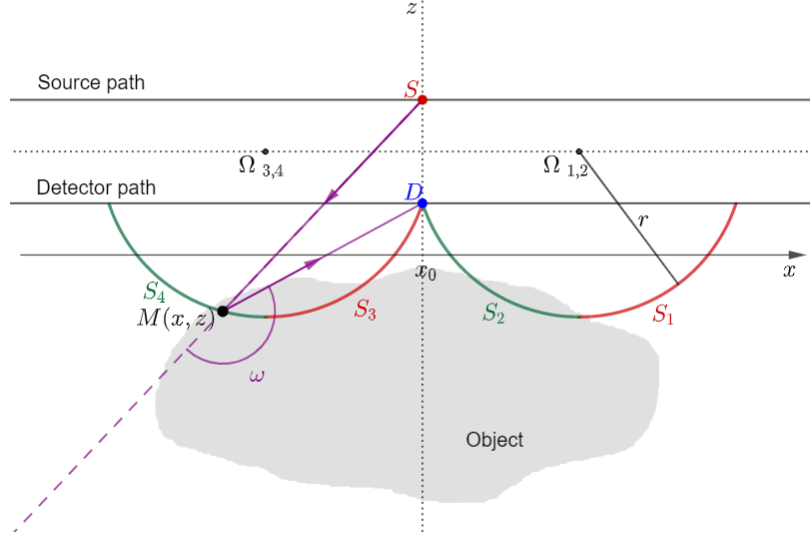
**Figure 1.10** − Webber and Miller's modality - 2020. The colour code is the same as in figure 1.7. The dotted lines represent the linear paths on which moves the pair source-detector.

sites are located on two circle arcs of radius $r = 1/\sin(\pi - \omega)$. These two circle arcs are parametrized into four circle arcs $S_j(x_0, r)$, $j \in \{1, 2, 3, 4\}$ of respective equation

$$x_1 = x_0 + \sqrt{r^2 - 1} + \sqrt{r^2 - (z-2)^2}, \quad x_2 = x_0 + \sqrt{r^2 - 1} - \sqrt{r^2 - (z-2)^2},$$
$$x_3 = x_0 - \sqrt{r^2 - 1} + \sqrt{r^2 - (z-2)^2}, \quad x_4 = x_0 - \sqrt{r^2 - 1} - \sqrt{r^2 - (z-2)^2}$$

and $z \in ]2 - r, 1[$.

**Radon transform modelling data acquisition**   The corresponding modality is defined as follows,

$$\mathcal{R}^{\text{Web}} f(x_0, r) = \sum_{j=1}^{4} \int_{S_j(x_0, r)} f(x, z) ds_j, \tag{1.48}$$

where $ds_j$ is the arc length measure on $S_j$. Since

$$ds_j = \frac{r}{\sqrt{r^2 - (z-2)^2}},$$

the image formation is modelled by the following Radon transform,

$$\mathcal{R}^{\text{Web}} f(x_0, r) = \int_{1}^{r} \frac{r}{\sqrt{r^2 - (z-2)^2}} \left( \sum_{j=1}^{2} f_1 \left( \sqrt{r^2 - 1} + (-1)^j \sqrt{r^2 - z^2} + x_0, z \right) + \right.$$
$$\left. f_1 \left( -\sqrt{r^2 - 1} + (-1)^j r \sqrt{r^2 - z^2} + x_0, z \right) \right) dz. \tag{1.49}$$

where $f_1(x, z) = f(x, 2 - z)$.

**Proposed procedure for inversion**   In the original article [13], the invertibility of this Radon transform (1.49) as well as an analytical inversion formula were established. The invertibility was proven using the theory of integral equations. In what follows, we denote $R = \sqrt{r^2 - 1}$. Let also $r_m > 1$.

The proof starts by expressing the Fourier transform of the Radon transform according to the first variable,

$$\widehat{\mathcal{R}^{\text{Web}}}f(\xi, r) = \int_{\mathbb{R}} \mathcal{R}^{\text{Web}}f(x_0, r)e^{-ix_0\xi}dx_0 \tag{1.50}$$

$$= \int_1^r \frac{rK(r, z)}{\sqrt{r^2 - z^2}}\widehat{f}(\xi, z)dz, \tag{1.51}$$

where $K(r, z) = 4\cos(\xi R)\cos(\xi\sqrt{r^2 - z^2})$. Substituting $z$ by $z^2$ and letting $f_2(\xi, z) = \frac{f_1(\xi, \sqrt{z})}{2\sqrt{z}}$, one gets

$$\widehat{\mathcal{R}_1^{\text{Web}}}f(\xi, r) = \frac{\widehat{\mathcal{R}^{\text{Web}}}f(\xi, \sqrt{r})}{4\sqrt{r}} = \cos\left(\xi\sqrt{r - 1}\right)\int_1^r \frac{\cos(\xi\sqrt{r - z})}{\sqrt{r - z}}\widehat{f}_2(\xi, z)\,dz. \tag{1.52}$$

Suppose that $|\xi| < \frac{\pi}{2\sqrt{r_m^2 - 1}}$ and $1 < r < r_m^2$. Then, $\cos\left(\xi\sqrt{r - 1}\right) > 0$. One has

$$\widehat{g}(\xi, r) = \frac{\widehat{\mathcal{R}_1^{\text{Web}}}f(\xi, r)}{\cos\left(\xi\sqrt{r - 1}\right)} \tag{1.53}$$

$$= \int_1^r \frac{\cos\left(\xi\sqrt{r - z}\right)}{\sqrt{r - z}}\widehat{f}_2(\xi, z)dz. \tag{1.54}$$

The latter integral is a Volterra integral equation of the first kind with a weakly singular kernel [30]. Then, applying the Abel transform to both sides allows removing the singularity:

$$\int_1^s \frac{\widehat{g}(\xi, r)}{\sqrt{s - r}}dr = \int_1^s \int_1^r \frac{\cos\left(\xi\sqrt{r - z}\right)}{\sqrt{r - z}\sqrt{s - r}}\widehat{f}_2(\xi, z)dzdr$$

$$= \int_1^s \left[\int_z^s \frac{\cos\left(\xi\sqrt{r - z}\right)}{\sqrt{r - z}\sqrt{s - r}}dr\right]\widehat{f}_2(\xi, z)dz \tag{1.55}$$

The latter expression is of the form

$$\int_1^s \frac{\widehat{g}(\xi, r)}{\sqrt{s - r}}dr = \int_1^s K_1(s, z)\widehat{f}_2(\xi, z)dz, \tag{1.56}$$

where

$$K_1(s, z) = \int_z^s \frac{\cos\left(\xi\sqrt{r - z}\right)}{\sqrt{r - z}\sqrt{s - r}}dr = \int_0^1 \frac{\cos\left(\xi\sqrt{u}\sqrt{s - z}\right)}{\sqrt{u}\sqrt{1 - u}}du \tag{1.57}$$

if we make the change of variable $r \longrightarrow z + (s - z)u$.

Then, one has $K_1(s, s) = \pi$. The first derivative of $K_1$ with respect to $s$ is

$$\frac{d}{ds}K_1(s, z) = -\xi^2 \int_0^1 \frac{u}{\sqrt{u}\sqrt{1-u}} \frac{\sin(\xi\sqrt{u}\sqrt{s-z})}{\xi\sqrt{u}\sqrt{s-z}} du$$

$$= -\xi^2 \int_0^1 \frac{\sqrt{u}}{\sqrt{1-u}} \operatorname{sinc}(\xi\sqrt{u}\sqrt{s-z}) du. \tag{1.58}$$

Finally,

$$\widehat{g}_1(\xi, s) = \frac{1}{\pi}\frac{d}{ds}\int_1^s \frac{\widehat{g}(\xi, r)}{\sqrt{s-r}} dr \tag{1.59}$$

$$= -\frac{\xi^2}{\pi}\int_1^s \left[\int_0^1 \frac{\sqrt{u}}{\sqrt{1-u}}\operatorname{sinc}\xi\sqrt{u}\sqrt{s-z}du\right]\widehat{f}_2(\xi, z)dz + \widehat{f}_2(\xi, s) \tag{1.60}$$

$$= -\frac{\xi^2}{\pi}\int_1^s K_2(s, z)\widehat{f}_2(\xi, z)dz + \widehat{f}_2(\xi, s). \tag{1.61}$$

One can show that $K_2$ is a bounded kernel, since $|K_2| < \pi/2$. This Volterra equation of the second kind is thus invertible, and its solution is given by the theory about integral equations [30, 13]:

$$\widehat{f}_2(\xi, s) = -\frac{\xi^2}{\pi}\int_1^s H(s, z)\widehat{g}_1(\xi, z)dz + \widehat{g}_1(\xi, s) \tag{1.62}$$

where

$$H(s, z) = \sum_{\nu=0}^{\infty}\left(\frac{-\xi^2}{\pi}\right)^{\nu} K_{2,\nu+1}(s, z) \tag{1.63}$$

and the kernels $K_{2,\nu}$ are computed iteratively

$$K_{2,1}(s, z) = K_2(s, z) \text{ and } K_{2,\nu+1}(s, z) = \int_0^s K_2(s, u)K_{2,\nu}(u, z)du \text{ when } \nu \geq 1. \tag{1.64}$$

The numerical computation of such equation require high computational time and/or memory. Furthermore, as mentioned in the paper, this approach is severely ill-posed in terms of stability. In Chapter 8, we propose an alternative formulation for inverting (1.49), and demonstrate its efficiency for simulation purposes.

### 1.3.5 Previous proposed three-dimensional CST modalities

The direct reconstruction of volumes is also of interest with the proposition of three-dimensional CST systems. These modalities use uncollimated sources and detectors. Consequently, data acquisition is performed on toric surfaces, resulting in the $2\pi$-rotation of a scanning circle arc on the source-detector axis. The proposed three-dimensional systems result often in extensions of two-dimensional CST systems.

As an example, in [12], an extension of the first system proposed by Nguyen and Truong was studied. A source and a detector, diametrically opposed on a sphere, rotate synchronously. The invertibility of the corresponding Radon transform is established in this work. In absence of inversion formula, the authors used Tikhonov regularization to provide reconstruction results.

The 3D extension of the translational geometric system proposed by Webber and Miller is also discussed in [13]. As for its two-dimensional version, the authors established the invertibility of the corresponding Radon transform on toric surfaces.

In [31], several potential configurations considering fixed, or rotating sensors were proposed. The author studied then the class of Radon transforms modelling data and provide a reconstruction algorithms to recover contours of the object under study.

## 1.4 Concluding remarks

In the energy range commonly used for scanning objects, the Compton effect is non-negligible. Instead of considering these scattered photons as noise, Compton scattering tomography aims at exploiting these photons to reconstruct the object under study.

Several configurations have been proposed previously, with each its advantages and drawbacks. One of the major advantage of Compton tomography compared to conventional tomography is that the source and detector(s) can be placed at the same side of the object. We find this advantage in Norton's, Truong and Nguyen's and Webber and Miller's modalities. As a consequence, this possibility widens the fields of applications for tomography to the imaging of one-sided large objects. However, to be able to scan large objects, some configurations, like Truong and Nguyen's and Webber and Miller's modality, register only backscattered photons (that is, photons scattered with an angle $\omega > \pi/2$), which are less probable than forward scattered photons (photons scattered with an angle $\omega < \pi/2$). On the contrary, since the object is placed inside the source-detector circle path for Nguyen and Truong's modality, this object should be small, which is an advantage if the target application is biomedical.

A second advantage of Compton imaging system is their ability to provide a completed set of information while being completely fixed. We find this advantage in the modalities of Norton and Webber and Miller, if the latter is sketched with multiple sources and detectors. Nevertheless, in the case of an implementation of Webber and Miller's modality with linear arrays of sources and detectors, note that a small offset is required to prevent the detector array from blocking photons. In other terms, while the array of sources is on the plane $(x, 0, z)$, the array of detectors is on the plane $(x, \epsilon, z)$, with $\epsilon$ small. The consequences of such offset in a practical scenario remains to be explored.

Furthermore, the modelling of data acquisition for such novel type of imaging leads to the introduction of generalized Radon transforms on families of circles arcs, depending on the

considered placement for the source and the detector(s). We introduced, in this chapter, the corresponding Radon transform for each previously proposed modality. We discussed also the proposed schemes of inversion. Norton proposed an inversion formula able to take into account practical physical factors if these terms are factorizable in two different functions, one according to the parameters of data, and the other relatively to the position of the scattering site. He mentioned in his article some issues concerning streak artefacts and contrasts issues at reconstruction, due to the finite size of the detector array. Nguyen and Truong privileged the resolution of the theoretical Radon transform without weighting function, and followed a scheme provided by Cormack earlier. Their demonstration led to an inversion formula linking Fourier series of object to those of data. Later, Rigaud carried out simulation results for this modality following the Chapman and Cary approach. With their second modality, Truong and Nguyen went a step further with also an inversion formula linking directly the object and to the data. Note that this scheme can be also applied in Norton's case. Webber and Miller used instead the theory of integral equation to establish their inversion formula.

Even all these methods lead to an inverse formula, and by the way, allow answering the mathematical challenge of object reconstruction with Compton tomography modalities, the formulation of the inverse formula has a huge impact on the possibility of performing simulation results. As an example, Webber and Miller proposed an inversion formula with a kernel, which has to be computed iteratively. Using Chapman and Cary approach involves the recursive computation of integrals. Consequently, implementing such methods will require time and memory. Choosing a closed formulation seems to be the best choice, since it will be less demanding in memory and time of calculation, while being also an exact reconstruction algorithm. In our contributions, we will therefore focus on proposing inverse formulas that can be implemented straightforwardly in the Fourier domain.

<p style="text-align: right;">2</p>

# Reconstruction methods in classical tomographic imaging

**Synopsis** As mentioned in the previous chapter, reconstruction in X-ray tomography consists in finding the object studied from the ratio of rays received by detectors. These projection data are the classical Radon transform on lines. After, a short presentation of this Radon transform, we review the main reconstruction approaches for recovering the object under study.

## 2.1 The classical Radon transform

In polar coordinates, the parametrization of an arbitrary line $L$ in the space can be written as

$$L(\rho, \phi) : \rho = r \cos(\theta - \phi), \qquad (2.1)$$

where $\rho \in \mathbb{R}$ is the distance of $L$ to the origin and $\phi \in [0, \pi[$ the angle of the normal vector to $L$ with respect to the $x$-axis (see Figure 2.1). We give now the definition of the classical Radon transform on lines.
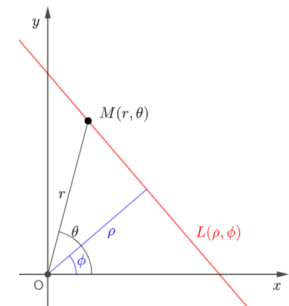


**Figure 2.1** − Chosen parameterization for the lines in the plane. An arbitrary line $L$ is represented in red.

**Definition 2.1.1** (Classical Radon transform). *Denoting $f$ an unknown, non-negative, continuous and compactly supported function in $\mathbb{R} \times [0, \pi[ \longrightarrow \mathbb{R}$, the classical Radon transform $\mathcal{R}$ maps $f$ into lines as*

$$\mathcal{R}f(\rho, \phi) = \int \int_{(r,\theta) \in \mathbb{R} \times [0,\pi[} f(r, \theta) \delta(\rho - r \cos(\theta - \phi)) dr d\theta, \qquad (2.2)$$

*where $\delta$ is the delta Dirac distribution.*

We define also some alternative expressions for the Radon transform of a function $f : \mathbb{R}^2 \longrightarrow \mathbb{R}$

<p style="text-align: right;">**33**</p>

defined in Cartesian coordinates :

$$\mathcal{R}f(\rho, \phi) = \int\int_{(x,y)\in\mathbb{R}^2} f(x,y)\delta(\rho - x\cos\phi - y\sin\phi)dxdy \tag{2.3}$$

$$= \int_{v\in\mathbb{R}} f(\rho\cos\phi - v\sin\phi, \rho\sin\phi + v\cos\phi)dv. \tag{2.4}$$

## 2.2 Analytic reconstruction methods

The analytic inverse formula for (2.2) is given by Cormack in [2, 27]

$$f(r, \theta) = \frac{-1}{2\pi^2} \int_0^\pi d\phi \text{ p.v.} \left\{ \int_{-\infty}^\infty \frac{d\rho}{\rho - r\cos(\theta - \phi)} \frac{\partial}{\partial\rho} \mathcal{R}f(\rho, \phi) \right\} \tag{2.5}$$

and p.v. is the Cauchy principal value. For simulation purposes, many approaches have been proposed, see [32, 33]. In what follows, we present the well-known filtered back-projection method and the rho-filtered layergram reconstruction formula.

### 2.2.1 The filtered back-projection reconstruction formula

From (2.5), using the definition of the Hilbert transform

$$\mathcal{H}\{u\}(t) = \frac{1}{\pi} \text{ p.v.} \left\{ \int_{-\infty}^\infty \frac{u(\tau)}{t - \tau} \right\} d\tau, \tag{2.6}$$

one gets

$$f(r, \theta) = \frac{1}{2\pi} \int_0^{2\pi} d\phi \, \mathcal{H}\left(\frac{\partial\mathcal{R}f(\rho, \phi)}{\partial\rho}\right)(r\cos(\theta - \phi)). \tag{2.7}$$

Then, changing to Cartesian coordinates,

$$f(x, y) = \frac{1}{2\pi} \int_0^\pi d\phi \, \mathcal{H}\left(\frac{\partial\mathcal{R}f(\rho, \phi)}{\partial\rho}\right)(x\cos\phi + y\sin\phi). \tag{2.8}$$

The Hilbert transform is then easily computed using a one-dimensional Fourier transform, denoted $\mathcal{F}$

$$\mathcal{H}\{u\}(t) = \mathcal{F}^{-1}(-i \cdot \text{sign}(\nu) \cdot \mathcal{F}(u)(\nu))(t). \tag{2.9}$$

Furthermore, the Hilbert transform of the derivative of a signal is equivalent to a ramp filter in the Fourier domain :

$$\mathcal{H}\left\{\frac{\partial u}{\partial t}\right\}(t) = \mathcal{F}^{-1}(|\nu| \cdot \mathcal{F}(u)(\nu))(t). \tag{2.10}$$

With (2.10), one obtains the final reconstruction formula

$$f(x,y) = \frac{1}{2\pi} \int_0^\pi d\phi \, \mathcal{F}^{-1} \left( |\nu| \mathcal{F} \left( \mathcal{R}f(\rho, \phi) \right) (\nu) \right) (x \cos \phi + y \sin \phi). \tag{2.11}$$

The above relation (2.11) is the filtered back-projection reconstruction formula, which consists in (i) filtering data and (ii) back-projecting it on the lines. Given $g \in \mathbb{R} \times [0, \pi[$, the back-projection operator $\mathcal{R}^\dagger$ acts on $g$ as follows,

$$\mathcal{R}^\dagger g(x,y) = \frac{1}{2\pi} \int_0^\pi g(x \cos(\phi) + y \sin(\phi), \phi) d\phi. \tag{2.12}$$

The algorithm 2.1 sums up the different steps of the associated reconstruction algorithm.

---

**Algorithm 2.1:** Filtered back-projection. Reconstruction of object $f$ from projection data on lines $\mathcal{R}f$

---

    **Data:** $\mathcal{R}f(\rho, \varphi)$, projections on lines of function $f$
    **Result:** $f(x,y)$

**1**    Perform a one-dimensional Fourier transform of the projections according to the first variable and weight the result by the ramp filter.

**2**    For each $\phi$, interpolate the data on the considered lines.

**3**    Sum the weighted interpolations on all directions $\phi$.

**4**    Normalize by $1/2\pi$.

---

### 2.2.2    The rho-filtered layergram reconstruction formula

In the rho-filtered reconstruction algorithm, data is back-projected before the filtering operation. Let us derive the reconstruction formula. From the definitions of the Radon transform in Cartesian coordinates (2.4) and the back-projection operator for variable $\phi_c$, one gets

$$
\begin{aligned}
\mathcal{R}^\dagger \mathcal{R}f(x,y) &= \frac{1}{2\pi} \int_0^\pi \mathcal{R}f(x \cos \phi + y \sin \phi, \phi) d\phi \\
&= \frac{1}{2\pi} \int_0^\pi \int_{-\infty}^\infty f((x \cos \phi + y \sin \phi) \cos \phi - v \sin \phi, \\
&\qquad\qquad\qquad\qquad (x \cos \phi + y \sin \phi) \sin \phi + v \cos \phi) d\phi \\
&= \frac{1}{2\pi} \int_0^\pi \int_{-\infty}^\infty f(x + \sin \phi(-x \sin \phi + y \cos \phi - v), \\
&\qquad\qquad\qquad\qquad y + \cos \phi(x \sin \phi - y \cos \phi + v)) d\phi.
\end{aligned}
$$

With the substitution $(x \sin \phi - y \cos \phi + v) \longrightarrow r$, $\phi \longrightarrow \phi - \pi/2$ and using the periodicity

of trigonometric functions, the above relation is equivalent to

$$\mathcal{R}^\dagger \mathcal{R} f(x,y) = \frac{1}{2\pi} \int_0^{2\pi} \int_0^\infty f(x - r\cos\phi, y - r\sin\phi) \, dr d\phi, \tag{2.13}$$

and, as a result, equal to the 2D-convolution of $f$ with the function $\gamma : (x,y) \longrightarrow (x^2 + y^2)^{-1/2}$:

$$\mathcal{R}^\dagger \mathcal{R} f(x,y) = \frac{1}{2\pi} (f \star \gamma)(x,y). \tag{2.14}$$

Taking the two-dimensional Fourier transform on both sides of (2.14), one has,

$$\mathcal{F}_2(\mathcal{R}^\dagger \mathcal{R} f)(k_x, k_y) = \frac{1}{2\pi} \mathcal{F}_2(f)(k_x, k_y) \cdot \mathcal{F}_2(\gamma)(k_x, k_y). \tag{2.15}$$

It was shown that $\mathcal{F}_2(\gamma)(k_x, k_y) = \gamma(k_x, k_y)$ (see [34, 35]). We obtain finally the rho-filtered layergram inversion formula

$$f(x,y) = \frac{1}{2\pi} \mathcal{F}_2^{-1} \left( \sqrt{k_x^2 + k_y^2} \cdot \mathcal{F}_2(\mathcal{R}^\dagger \mathcal{R} f(\rho, \phi))(k_x, k_y) \right)(x,y). \tag{2.16}$$

---

**Algorithm 2.2:** Rho filtered layergram algorithm. Reconstruction of object $f$ from projection data on lines $\mathcal{R}f$

---

   **Data:** $\mathcal{R}f(\rho, \varphi)$, projections on lines of function $f$

   **Result:** $f(x,y)$

**1**   Back-projection of data on the entire domain of $\phi$.

**2**   Perform a two-dimensional Fourier transform of the back-projected data, and weight the result by $\sqrt{k_x^2 + k_y^2}$, where $k_x$ and $k_y$ are the duals of $x$ and $y$.

**3**   Perform the two-dimensional inverse Fourier transform and normalize the result by $1/2\pi$.

---

Note that $\gamma$ has a Fourier transform, even if this function is not $L_2(\mathbb{R}^2)$. For more details about this reconstruction algorithm, the reader can refer to [34].

The filtered back-projection is the privileged analytical reconstruction method. Actually, we introduced the rho-filtered layergram algorithm because we will find elements of the demonstration of this formula in one of the works presented in the framework of this thesis.

However, the filtered back-projection algorithm may have drawbacks in the case of missing data. The numerical simulation of such method requires important constraints on the data acquisition process, such as having a sufficient number of data, evenly distributed over the entire angular domain. However, in many realistic imaging situations, these conditions cannot be ensured. For instance, some imaging conditions require a low dose of radiations, or only a

region of interest exposure. If we perform reconstruction with the filtered back-projection algorithm, this results in artefacts. On the other way, one can use alternatively optimization techniques, where it is easier to incorporate prior knowledge. We present in the next section a classical method, Tikhonov regularization.

## 2.3   Regularization reconstruction techniques

We introduce first some useful notations for the presentation of these methods.

### 2.3.1   Computed tomography: a subset of the inverse problems

Tomography is a subset of the inverse problems, which consists in *finding* parameters (or the input) $f$ from a set of data (or measurements) $g$. Both are related by a forward operator, $A$ which models data acquisition (as accurately as possible). Symbolically, given $X$ and $Y$ two Hilbert spaces, the forward model is

$$g = A(f). \tag{2.17}$$

where $A : D(A) \longrightarrow Y$ the forward map $A$ is bounded in $D(A)$, a subset of $X$. However, as stated previously, only a noised version $g^\varepsilon$ of the measurement $m$ is often available, hence the forward model becomes

$$g^\varepsilon = A(f) + \varepsilon, \tag{2.18}$$

where $\varepsilon$ represents the amount of noise.

With this representation, we can easily make the link between the continuous and the discrete formulations. If A is a linear operator, the matrix form for (2.17) is

$$\mathbf{g} = \boldsymbol{A}\mathbf{f}, \tag{2.19}$$

where $\mathbf{g} \in \mathbb{R}^M$ is the vector form containing $M$ values for data, $\mathbf{f} \in \mathbb{R}^{N^2}$ the vector representing the $N^2$ pixels of the object and $\boldsymbol{A} \in \mathbb{R}^M \times \mathbb{R}^{N^2}$ is the matrix form of the operator A.

For tomographic reconstruction, the matrix $\boldsymbol{A} = (a_{mn})_{m\in\{1,M\},n\in\{1,N^2\}}$ is a (large) sparse matrix containing the contribution of the position of each pixel in the sinogram. Several methods exist to fill this matrix. The simplest way is probably to assign 1 to coefficient $a_{mn}$ where the line $L_m$ travels in the $n$th pixel and 0 otherwise. Another method, finer, consists in assigning to the $(a_{mn})$ the distance of the line $L_m$ which traverses the $n$th pixel. In Section 2.4, we will use instead a kernel-based method.

Then, each value $\mathbf{g}_{m \in \{1,M\}}$ of the vector $\mathbf{g}$ is calculated with

$$\mathbf{g}_m = \sum_{i=1}^{N^2} a_{mi} \mathbf{f}_i. \tag{2.20}$$

A naive method of reconstruction would be to consider the least square solution. However, unless you use exactly the same matrix $\boldsymbol{A}$ — and be guilty of inverse crime —, the inversion is not stable. Small degradation in measurement will lead to an unsatisfactory reconstruction. The analysis of the singular values of $\boldsymbol{A}$ may also give intuition about ill-posedness of the considered inverse problem. In particular, a large condition number (i.e., the ratio between the larger and the lower non-zero singular value) means that the inverse of $\boldsymbol{A}$ is numerically unstable. This illustrates the ill-posedness of the tomographic reconstruction problem and explains also why we need optimization methods for reconstruction.

### 2.3.2   Variational regularization methods

A regularized solution for (2.19) is obtained by minimizing the following functional,

$$\mathcal{T}_{\alpha,g^{\varepsilon}}(f) := ||A(f) - g^{\varepsilon}||_V^2 + \alpha \mathcal{F}(f), \tag{2.21}$$

where $\mathcal{F}$ is a convex functional and $\alpha > 0$ is the regularization parameter. The minimization of such expression (2.21) means that we want to make as small as possible at the same time the error between $A(f)$ and $g^{\varepsilon}$ and the convex functional $\mathcal{F}(f)$. Among the existing variational methods, the most well-known are probably Tikhonov and TV-regularization [36], described each by a particular choice for $\mathcal{F}$:

- Tikhonov regularization[1] : $\mathcal{F}(f) = ||f||_{L^2}^2$,

- TV-regularization : $\mathcal{F}(f) = ||Df||_{L^1}$,

where $D$ is the gradient operator. Important questions concern now the existence, stability and convergence of a solution of (2.21). These results are now well established, see for instance [37, 38], assuming a condition on the operator $A$. This theoretical condition uses results on topology, but however, in practice, the proof of the boundedness of the operator $A$ seems to be sufficient [39], and this condition is always verified when we handle discrete operators.

---

[1]If one has a-priori information about the tackled problem, he/she has the possibility to use also a generalized version of Tikhonov regularization, where the convex functional may be $||D(f)||_{L^2}$, where $D$ is a differential operator, $||f - f_\Delta||_{L^2}$ with $f_\Delta$ a vector close to the expected solution, or a functional combination of the two above.

**Tikhonov regularization**

We give in this paragraph two formulations for Tikhonov regularization, one using matrix calculation and the other an iterative scheme. The two following paragraphs are based on [40] and the interested reader may refer to this reference for a deeper insight.

**Matrix formulation**    Tikhonov functional admits a unique minimum for any $\alpha > 0$ which satisfies

$$\mathbf{f}_\alpha^{\text{Tikhonov}} = (\boldsymbol{A}^T\boldsymbol{A} + \alpha\boldsymbol{I})^{-1}\boldsymbol{A}^T\mathbf{g}, \tag{2.22}$$

where $^T$ refers to the transposition operator and $\boldsymbol{I}$ to the identity matrix. The later equation can be used directly to reconstruct $\mathbf{f}$. This equation exists also in a stacked form, which allows reducing computation time, for medium-scale inverse problem (the dimensions of $M$ and $N^2$ are about $10^3$).

**Iterative formulation**    For a large-scale implementation, one can opt for a matrix-free implementation, namely a technique where we do not need to compute explicitly the matrix $\boldsymbol{A}$. Instead, we need two routines which compute the forward and adjoint transform of vectors. These routines will replace respectively the matrix products $\boldsymbol{A}\mathbf{u}$ and $\boldsymbol{A}^T\mathbf{v}$ where $\mathbf{u}$ and $\mathbf{v}$ are respectively vectors of $\mathbb{R}^{N^2}$ and $\mathbb{R}^M$. With such operators, the Tikhonov problem can be solved using iterative optimization methods, for instance, the conjugate gradient method. See Algorithm 2.3, where the operator $\boldsymbol{Q}$ refers to the operation $(\boldsymbol{A}^T\boldsymbol{A} + \alpha\boldsymbol{I})$ [2].

---

[2] We continued here to use a matrix formulation in reference to the forward and adjoint operator, for the sake of readability of the algorithm. However, in practice, it should be replaced by the forward and adjoint routines discussed previously.

---

**Algorithm 2.3:** Conjugate gradient algorithm, adapted for Tikhonov regularization

---

**Data:** $\mathbf{g}^\varepsilon$, projection on lines

**Result:** $\mathbf{f}_\alpha^{\text{Tikhonov}}$, Tikhonov solution

1    Choose a regularization parameter $\alpha$ and a number of iterations $K$

2    Initialize $\mathbf{f}_0 \in \mathbb{R}^{N^2}$

3    $\mathbf{d}_0 \leftarrow \boldsymbol{A}^T \mathbf{g}^\varepsilon - \boldsymbol{Q}\mathbf{f}_0$

4    $\mathbf{b}_0 \leftarrow -\mathbf{d}_0$

5    **for** $k \leftarrow 0$ **to** $K - 1$ **do**

6        $\alpha_k \leftarrow -\dfrac{\mathbf{b}_k^T \mathbf{d}_k}{\mathbf{d}_k^T \boldsymbol{Q} \mathbf{d}_k}$

7        $\mathbf{f}_{k+1} \leftarrow \mathbf{f}_k + \alpha_k \mathbf{d}_k$

8        $\mathbf{b}_{k+1} \leftarrow \boldsymbol{Q}\mathbf{f}_{k+1} - \mathbf{g}^\varepsilon$

9        $\beta_k \leftarrow -\dfrac{\mathbf{b}_{k+1}^T \boldsymbol{Q} \mathbf{d}_k}{\mathbf{d}_k^T \boldsymbol{Q} \mathbf{d}_k}$

10      $\mathbf{d}_{k+1} \leftarrow \mathbf{b}_{k+1} + \beta_k \mathbf{d}_k$

11   **end**

12   $\mathbf{f}_\alpha^{\text{Tikhonov}} \leftarrow \mathbf{f}_K$

---

Several methods exist in order to choose an *optimal* regularization parameter $\alpha$. For instance, there is Morozov's discrepancy principle [37], the L-curve method [41] or cross-validation [42]. However, there are counter examples, where such procedures converge toward a non-optimal choice for $\alpha$. See for instance the references [40, 43] for some illustrations where the L-curve method fails. Furthermore, the choice of $K$, the number of iterations, is also of interest. Its choice seems to be an open question for a numerical approximation purpose according to [40]. In some references referring to similar iterative reconstruction algorithms, its choice seems to be completely arbitrary, just to make sure that the algorithm has already converged. In the proposed simulations with this method, we also adopt this point of view.

## 2.4   Implementation of these analytical and regularization methods

We now illustrate this presentation with image reconstructions for current tomography using back-projection, filtered back-projection algorithm, the rho-filtered layergram method and the two formulations of Tikhonov regularization.

### 2.4.1   General parameter choices

The object to scan was the Shepp-Logan phantom (see figure 2.4a) of size $N \times N = 100 \times 100$ pixels. For calculations, the object was centered at the origin of the coordinate system.

Data acquisition was performed on the full angular projection view ($[0, 180[$ degrees) with an angular step of one degree. We chose a detector array of length 101 pixels.

Note that the chosen parameters for data acquisition are ideal, and in this case filtered back-projection is the preferred method. Nevertheless, we will propose reconstructions from the four methods presented above (filtered back-projection, rho-filtered layergram, Tikhonov with matrix computation, Tikhonov matrix-free implementation) to compare the computation time and memory required for each one.

### 2.4.2   Some details about the computation of the forward operator

**Discretization of the integral formulation**

For simulation, we compute a discrete version of (2.4) approximating the integral by a sum

$$\mathcal{R}f(\rho_i, \phi_j) = \sum_{k=-v_m}^{v_m} f(\rho_i \cos\phi_j - k\sin\phi_j, \rho_i \sin\phi_j + k\cos\phi_j). \tag{2.23}$$

The position of the object and the scanning lines are made coincident by linear interpolation.

**Construction of the matrix operator**   From (2.2), we calculate the Point Spread Function (PSF), that is the response of the classical Radon transform to a Dirac delta distribution is non-zero at an arbitrary point of the plane. This gives us the kernel $\mathcal{K}$ of the classical Radon transform:

$$\mathcal{K}(\rho, \phi; r, \theta) = \frac{1}{r}\delta(\rho - \cos(\theta - \phi)). \tag{2.24}$$

For numerical calculation purposes, we choose to approximate the Dirac delta distribution of the kernel by an exponential, denoted $\eta_b$ where

$$\eta_b(x) = \frac{1}{b}\eta\left(\frac{x}{b}\right) \text{ where } \eta(x) = \frac{1}{\sqrt{\pi}}\exp\left(-x^2\right), \tag{2.25}$$

and $b > 0$. In the case of the classical Radon transform, for each couple $(\rho_m, \phi_m)$ and $(r_n, \theta_n)$ the coefficients $(a_{mn})$ of the operator $\boldsymbol{A}$ are therefore calculated according to the relation

$$a_{mn} = \frac{1}{b\sqrt{\pi}}\exp\left(-\frac{(\rho_m - r_n\cos(\theta_n - \phi_m))^2}{b^2}\right). \tag{2.26}$$

### 2.4.3   Simulation results

**Data acquistion**

In figure 2.2, we show data acquired from the straightforward discretization of the Radon transform (Fig. 2.2a) and from the computation of a matrix operator (Fig. 2.2b).

(a)



(b)
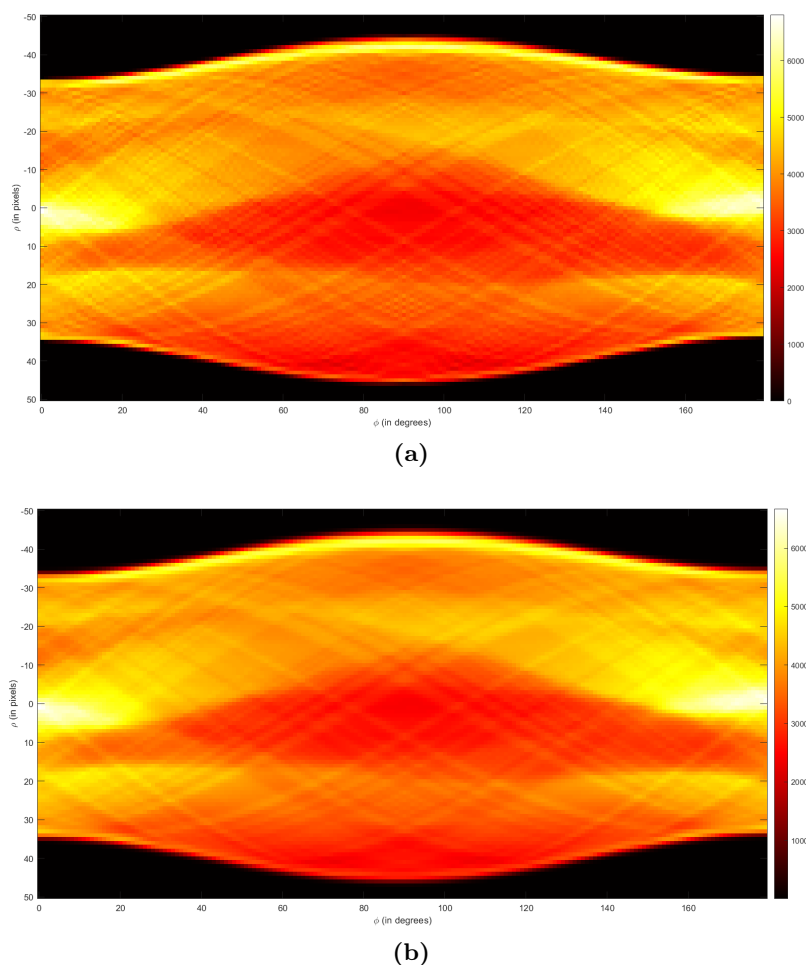
**Figure 2.2** – Data acquisition on lines using (a) the discretization of the forward operator ((2.23)) and (b) a matrix operator ((2.26) with $b = 1$).

Moreover, we study the ill-posedness of our problem by computing the singular value of the matrix operator $\boldsymbol{A}$. See Figure 2.3.

### Image reconstruction

Reconstruction results from the back-projection operator, the filtered back-projection and rho-filtered layergram algorithms and Tikhonov regularization are presented in figure 2.4. Note that, to avoid inverse crime, we used a different model to generate data. For the method where we had to make explicit the matrix operator, we performed data acquisition with a slight different $b$. In the matrix-free implementation case, we changed the discretization.

We give comparison of computation time and required storage according to the used reconstruction method in table 2.1.
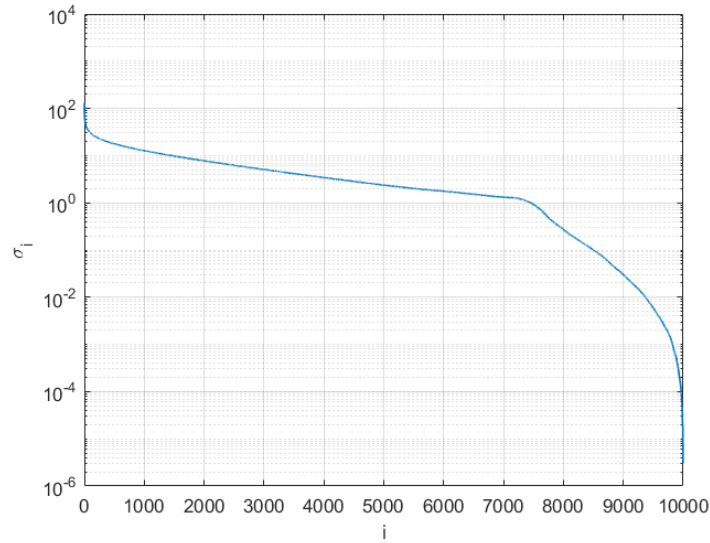
**Figure 2.3** – Singular values $\sigma_i$ of the Radon operator $\boldsymbol{A}$. Condition number : $4.3 \times 10^7$

**Table 2.1** – Comparison of computation time, required storage for data acquisition and image reconstruction and error reconstruction with NMSE according to the used method. (n/a stands for non-applicable.)

| Method | Computation time | | Required storage | | NMSE |
|---|---|---|---|---|---|
| | Data acquisition | Recons. | Data acquisition | Recons. | |
| Filtered back-projection | 0.26 s | 0.026 s | n/a | n/a | 0.0026 |
| Rho-filtered layergram | 0.26 s | 0.0746 s | n/a | n/a | 0.0202 |
| Tikhonov (with matrix) | $2.5 \times 10^3$ s | $1.6 \times 10^3$ s | 786 Ko | n/a | 0.0076 |
| Tikhonov (matrix-free, 100 it.) | 0.26 s | 0.44 s | n/a | 240 Ko between two iterations | 0.0115 |

## 2.5 Discussions

In this chapter, we reviewed some reconstruction techniques used in conventional tomography. From Cormack's inversion formula, we made explicit the well known filtered back-projection
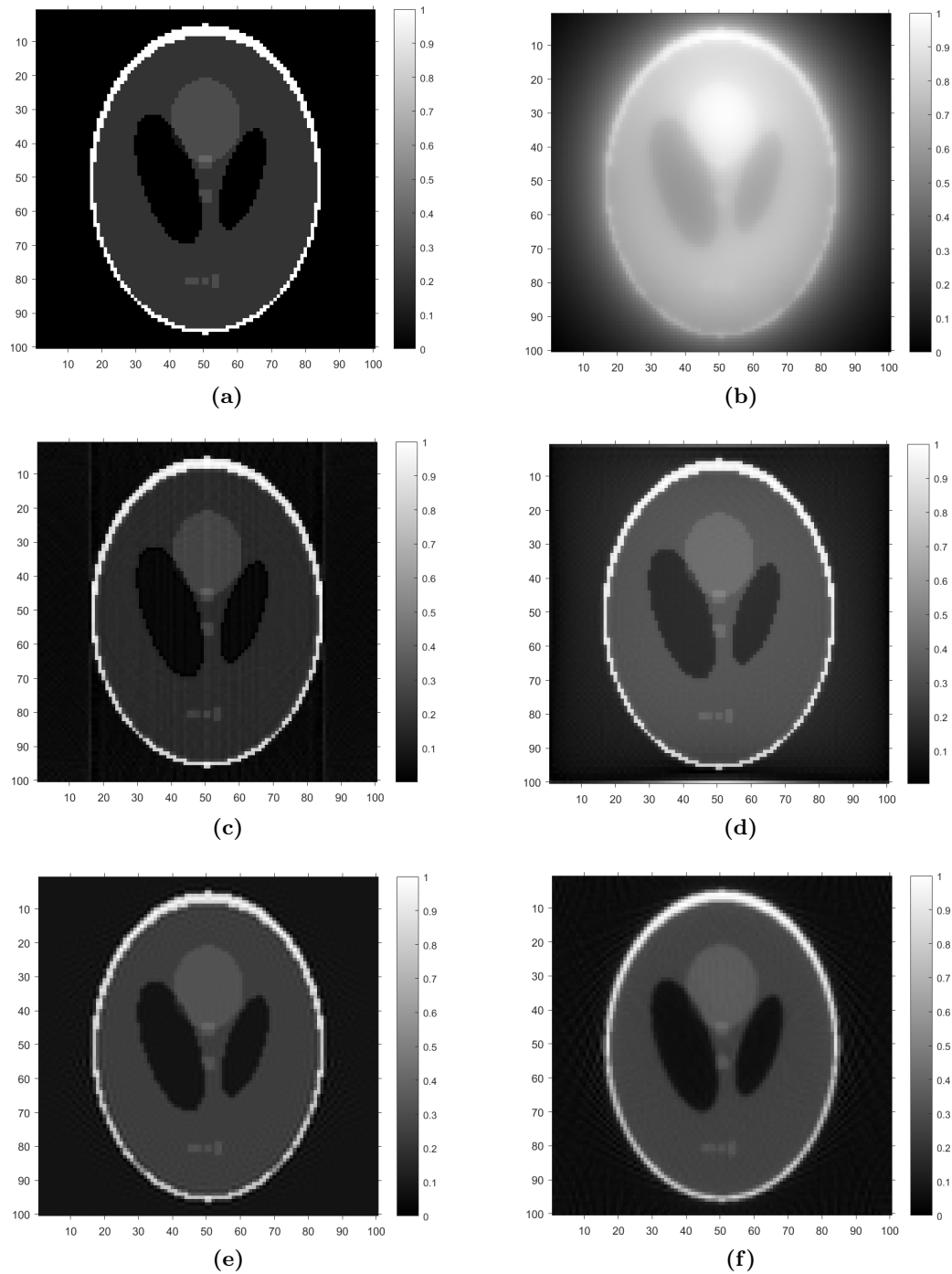
**Figure 2.4** – Reconstruction results of (a) Shepp-Logan phantom using (b) back-projection, (c) filtered-back projection, (d) rho-filtered layergram, (e) Tikhonov regularization with a matrix operator and (f) Tikhonov regularization with a matrix-free implementation.

algorithm, which consists in, first, filtering data in the Fourier domain, and second, back-projecting these filtered data on the appropriated lines. A second reconstruction algorithm,

issued from an analytical derivation, is presented. This method is the rho-filtered layergram algorithm. Effectively, the latter differs from the filtered back projection algorithm by the reverse order of the filtering and back-projection operation. This results in a computation time in the same order of magnitude. The reconstruction from the rho-filtered layergram exhibits a slight loss of contrast. The origin of these differences has been discussed in the literature, the interested reader can refer to [34].

Then, we also introduced a classical regularization method used in inverse problems. This method is Tikhonov regularization. Such a type of method is interesting to introduce a more complete model of a given system, since, in that case, we do not need an analytical inversion to perform reconstruction. These methods are also of interest in case of missing data. The classical way to deal with such a method is no construct a matrix operator which models data acquisition. This matrix operator replaces then the computation of the forward Radon transform in the case of computed tomography. The computation of such matrix operator requires both computation time and memory. For our simulation, the computation time of the matrix was $10^4$ more important than the one needed for computing the discretization of the integral form. Moreover, it limits also the possibility of having large objects and data, since the resulting matrix is equal to the product of their sizes. We can also notice that the resulting data seems to be less precise than the one obtained by discretization of the integral (see Figure 2.2). If we compare now the simulation results, the difference between the two images is mainly in the contrast obtained. The result obtained from Tikhonov regularization provides also some smoothing. This can be solved by choosing an *optimal* value for $\alpha$ [37, 41, 42], or by considering a generalized Tikhonov regularization with the introduction of a-priori information about the solution.

Aware of the disadvantages of the Tikhonov regularization with a matrix formulation in terms of computation time for the forward operator, we also implemented another procedure where an iterative process replaces the calculation of the matrix. Such a method uses the discrete formulation of the integral transform, and as a consequence requires the same computational time for data acquisition as the one needed before using the filtered back-projection algorithm and the rho-filtered layergram. It requires also less storage than the matrix form (about three times less in our simulations). Thus, this matrix free implementation is suitable for large-scale problems. However, this raises a question about the required number of iterations. As far as the author's knowledge, this question is again an open question, and the choice of a sufficient (but large) amount is often privileged. If we analyse now reconstruction quality, the obtained result seems to be smoother than the one obtained with the matrix operator. This may be due to the successive iterations resulting in larger numerical approximations. The introduction of a-priori information about the solution may also reduce this problem.

We introduced these classical examples since, in what follows, we will refer to them. In fact, during some of our contributions, we will propose new filtered back-projection type algorithms on different manifolds for image reconstruction from different CST configurations

(see Chapters 4 and 7). Moreover, in another result of this thesis, we will find elements of the demonstration of the rho-filtered layergram reconstruction formula. See Chapter 6. Finally, when we will be in situations where we do not have an exact inversion formula (Chapter 5 and 7), we will propose reconstruction results obtained from Tikhonov regularization. We opted for Tikhonov regularization, since it is a well-known technique able to give good reconstruction results from ill-posed inverse problems, when we have a set of complete data, as shown here for computed tomography. However, other regularization techniques can be used to solve this imaging inverse problem. The second most well-known method is undoubtedly the total variation regularization [36, 44] which allows preserving better edges than Tikhonov regularization [40]. Iterative algorithms for tomographic reconstruction, such as the algebraic reconstruction technique [32], have been also introduced. We can also mention statistical-based approaches [45, 46, 47, 48], which provides better noisy models close to the reality. More recently, iterative reconstruction techniques combined with deep learning have been also proposed, see for instance in [49, 50, 51].

# Part II

# The proposition of the Circular Compton Scattering Tomography

This part is devoted to the proposition of a CST modality, called Circular Compton Scattering Tomography (CCST).

In chapter 3, we present the modality as well as its advantages in front of the previous proposed systems. We derive also a general formulation of the corresponding Radon transform and precise the working assumptions that will be used in the next chapters.

In chapters 5 and 4, we model CCST with and without collimation at detectors, and propose reconstruction techniques for both situations.

Finally, in Chapter 6, we investigate further the search for an inverse analytical formula for the Radon transform modeling the data acquisition for the CCST without collimators.

$$3$$

# Presentation of the circular Compton scattering tomography

**Synopsis** This chapter introduces the proposed modality called Circular Compton Scattering Tomography. We state also the advantages and potentials of such a system and make a comparison with existing CST configurations. The parameterization of the proposed system is given, as well as the modelling of data measurement with such a system.

## 3.1 Working principle

The Circular Compton Scattered Tomography (CCST) system is made of a source $S$ and $K$ fixed detectors $D_k$, $k \in \{1, ..., K\}$ placed on a ring passing through the source (see Figure 3.1). The object is placed inside the detector ring[1].
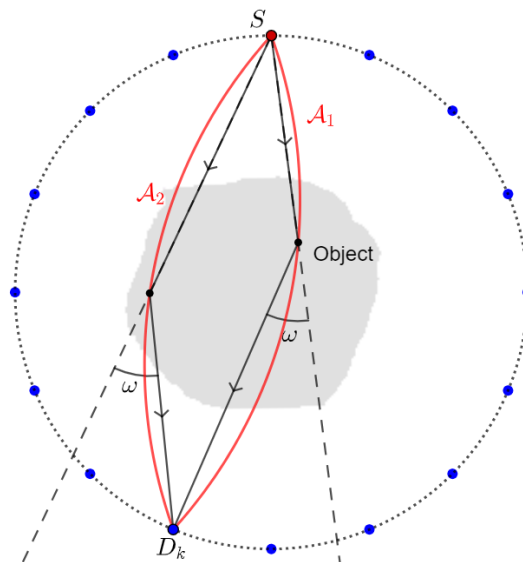


**Figure 3.1** – Presentation of CCST. The dotted line represents the ring containing point-like detectors in blue. We find also the source, in red, on the ring. For an arbitrary detector $D_k$ and a scattering angle $\omega$, the corresponding double scanning arc $\mathcal{A}_1 \cup \mathcal{A}_2$ is showed in red.

---

[1]This is the main scanning mode. We will see then that a second acquisition mode is also possible, with an object placed outside the ring.
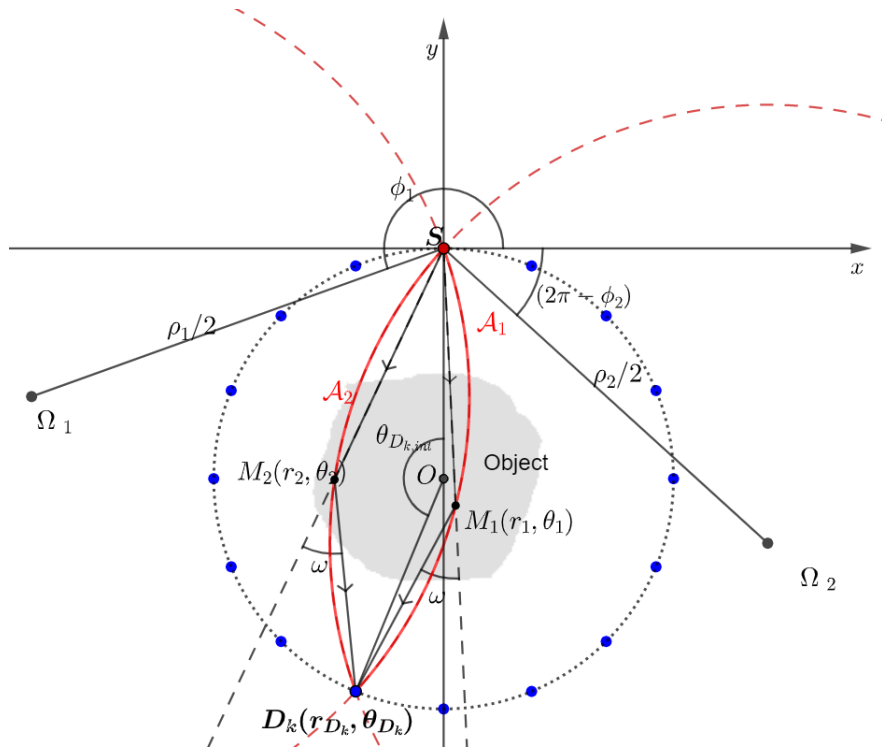
**Figure 3.2** – Parameterization of CCST. The color code is the same as that used in the figure 3.1.

Note that this modality was studied independently at the same time by another team [52]. Even if the starting system is identical, the solution of the inverse problem is completely different from what will be presented in the following. In the publication [52], it is proposed to reconstruct only the singular support of the object under study.

## 3.2 Advantages, potentials of CCST and comparison with existing systems

CCST presents interesting advantages in terms of geometry. First, the source and the detectors do not require any rotation or movement during acquisition. The use of such a system, as compared to the first Nguyen and Truong's modality for instance, leads to a diminution of duration for acquisition and consequently time to exposure to radiation. Second, the compact and circular layout of CCST reduces also the size of the system in comparison with Norton's or Webber - Miller's linear ones. Third, its geometry is identical to that of the conventional Fan-beam computed tomography. There is the possibility to combine both imaging techniques in the same system. If detectors of such a bi-imaging system are set to recover primary transmitted photons at energy $E_0$, then the systems works as Fan-beam CT. Otherwise, when detectors register the energies lower than $E_0$, the system

operates as CCST. Then, this bi-imaging system provides both the attenuation map (by fan-beam CT) and the distribution of electrons (by CCST), which are two physical properties of the object under study.

In addition, CCST can also scan one-sided large objects or objects which cannot be placed inside the ring. This feature comes from the fact that CCST is a generalization of Norton's modality, where the diameter of the ring tends towards infinity.

Consequently, this CST proposal groups the main advantages of existing models in terms of geometry. CCST is thus convenient for imaging in various domains, from biomedical imaging to non-destructive evaluation and cultural heritage.

## 3.3   Setup of the system

The fixed source is placed at the origin of the coordinate system. The ring of $K$ detectors $D_k$ with $k \in \{1, 2, ..., K\}$ passing through the source is modelled a circle of polar equation,

$$r = P \cdot \cos\left(\theta + \frac{\pi}{2}\right), \theta \in [\pi, 2\pi[, \tag{3.1}$$

where $P$ is the diameter of the ring and $O$ denotes its center. In order to have a constant distance between adjacent detectors, we define first $\theta_{D_{k,int}}$ the angle subtending the $y$-axis and the radius $OD_k$ of the fixed ring (see Figure 3.2):

$$\theta_{D_{k,int}} = 2\pi \frac{k}{K+1}. \tag{3.2}$$

Angle $\theta_{D_{k,int}}$ is related to polar angular coordinate $\theta_{D_k}$ of detector $D_k$ according to the relation

$$\theta_{D_k} = \pi + \frac{\theta_{D_{k,int}}}{2}. \tag{3.3}$$

With (3.2) and (3.3), one can make explicit polar coordinates $(r_{D_k}, \theta_{D_k})$ of each detector $D_k$:

$$D_k(r_{D_k}, \theta_{D_k}) \text{ with } \begin{cases} r_{D_k} &= P\cos\left(\theta_{D_k} + \frac{\pi}{2}\right) \\ \theta_{D_k} &= \pi\left(1 + \frac{k}{K+1}\right). \end{cases} \tag{3.4}$$

Elementary geometry allows to verify that the distance $d$ between adjacent detectors is constant:

$$d = ||D_{k+1}D_k|| = P\sin\left(\frac{\pi}{K+1}\right) = \text{constant}. \tag{3.5}$$

In the case of a practical setting, finite-sized source and sensors have to be considered. Given the geometry of the system, we consider realistic source and detectors having a circular shape of a certain arc length $L$. This is achieved considering a angular domain of angle $2\Delta D$

around the value of each $\theta_{D_{k,int}}$: we have in that case $\theta_{D_{k,int},r} \in [\theta_{D_{k,int}} - \Delta D, \theta_{D_{k,int}} + \Delta D]$. There is obviously a maximum value for $\Delta D$ to avoid *superposition* of detectors: here, $\Delta D \leq \Delta D_{\max} = \pi/(N_D + 1)$, which corresponds to the condition on the arc length $L \leq L_{\max} = 2P\Delta D_{\max}$.

## 3.4 Data measurement model

We denote $I$ the intensity of the flux of photons with energy $E_\omega$ collected by a detector $D_k$. This quantity can be expanded according to the scattering order of the photons, $I = I_0 + I_1 + I_2 + \ldots$ where $I_0$ accounts for the quantity of transmitted photons and $I_i$ is the intensity of photons scattered $i$ times. In this work, we will exploit only first-order scattering. The other scattering orders, less predominant than first order are considered as noise. With CCST system, first-order scattered recovered photons by a detector $D_k$ at same energy arise from scattering sites lying on two circle arcs with $S$ and $D_k$ as end-points subtending the angle $(\pi - \omega)$. These scanning circle arcs $\mathcal{A}_1$ and $\mathcal{A}_2$ admit for equation

$$\mathcal{A}_i(\rho_i(\omega, \theta_{D_k}), \phi_i(\omega, \theta_{D_k})) : r_i = \rho_i(\omega, \theta_{D_k}) \cos(\theta_i - \phi_i(\omega, \theta_{D_k})), \quad i \in \{1, 2\}, \qquad (3.6)$$

where

$$\rho_1(\omega, \theta_{D_k}) = P \cos(\theta_{D_k} + \pi/2) / \sin(\omega) = \rho_2(-\omega, \theta_{D_k}), \qquad (3.7)$$

$$\phi_1(\omega, \theta_{D_k}) = \theta_{D_k} - \omega - \pi/2 = \phi_2(-\omega, \theta_{D_k}), \qquad (3.8)$$

$\rho_i$ is the diameter of the circle arc $\mathcal{A}_i$, $\phi_i$ its angle relative to $x$-axis, $\theta_1 \in [\theta_{D_k}, \theta_{D_k} + \omega]$ and $\theta_2 \in [\theta_{D_k} - \omega, \theta_{D_k}]$. See Figure 3.2. The next definition gives the measurement model of first-scattered photons with CCST.

**Definition 3.4.1.** *The flux $I_1$ corresponding to the interaction of first-scattered photons with electrons in the cross-section of the object along one of the circle arcs $\mathcal{A}_1$ and $\mathcal{A}_2$ has for general expression*

$$I_1(D_k, E(\omega)) = \int_{M_1 \in \mathcal{A}_1} a_{11}(SM_1, E_0) \, f(M_1) \, q(M_1, D_k, \omega) \, a_{21}(M_1 D_k, E(\omega)) \, dl(M_1) +$$
$$\int_{M_2 \in \mathcal{A}_2} a_{12}(SM_2, E_0) \, f(M_2) \, q(M_2, D_k, \omega) \, a_{22}(M_2 D_k, E(\omega)) \, dl(M_2). \quad (3.9)$$

*where $a_{1i}$ and $a_{2i}$ are the attenuation factors of emitted and transmitted rays along linear paths $SM_i$ and $M_i D$. $q$ is the weighting function which groups other physical quantities. $f$ denotes the electron density of the considered cross-section of the object. This integral is a weighted Radon transform on the family of circle arcs $\mathcal{A}_1 \cup \mathcal{A}_2$.*

The complete derivation of this expression is given in Appendix A. We performed also simulations of this formula and compared them with Monte Carlo simulations.

## 3.5 General working assumptions used in the next chapters

In the next chapters 4 and 5, we are interested in the associated Radon transform (3.9) modelling data acquisition with CCST in a more mathematical point of view in order to be able to derive an exact analytic inversion for the Radon transform. We adopt consequently some necessary assumptions, common in the literature about the study of the Radon transforms in association to a CST system [8, 11, 9, 53, 54]. The next paragraphs present and justify these conditions. The consequences of these assumptions on data acquisition is also evaluated in Appendix A.

**About attenuation inside matter** First, it is assumed that attenuation is absent, and we suppose idealized point-like source and detectors, with perfect energy resolution[2]. Consequently, the product of the above-mentioned coefficients $a_1$ and $a_2$ and the weighting function $q$ are drastically set to one. Equation (3.9) is rewritten as

$$\mathcal{R}_{\mathcal{A}_1 \cup \mathcal{A}_2} f(D_k, E(\omega)) = \int_{M \in (\mathcal{A}_1 \cup \mathcal{A}_2)} f(M) \, dl(M). \tag{3.10}$$

Working on the Radon transform modelling data acquisition in an idealistic situation has however an important role for reconstruction strategy in the attenuated case. In fact, some studies [55, 56] show the possibility to correct *a posteriori* either the reconstruction or data using respectively adapted forms of generalized Chang correction [57] or iterative pre-correction [58] algorithms.

**About finite-sized source and detectors** Moreover, source and detectors have to be considered as point-like elements. Although no study explore the consequences in CST cases, similarly to that it was observed in photo-acoustic tomography, blur can be expected at reconstruction and deblurring algorithms such as the ones proposed in [59] may be a solution. Non-ideal energy resolution of detectors has also an impact, as showed in an unpublished work [60] and in [61], where an abrupt cut-off on projections has been observed. Smoothing filters are a possibility to decrease the influence of this parameter.

**About collimation** First, for our works in two-dimensions, a plate collimator in the source is used to restrict emitted photons to the plane $(x, y)$. Furthermore, the intrinsic geometry of CCST introduces furthermore an ambiguity on the localization of the scattering sites, which can be either on $\mathcal{A}_1$ or $\mathcal{A}_2$. In previous proposed CST systems, this type of ambiguity is removed by the use of collimation (or filtering) at detectors, and such technique can also be used for this system. In the work [52], collimation at detectors is also supposed in the proposed modelling. This means that we are able to dissociate photons incoming from

---

[2]By *perfect energy resolution*, we mean a convenient energy resolution for the use of the proposed algorithms.

one arc to the other. We propose in this work to study both cases, first in next chapter 4, CCST with collimation at detectors and second, in chapter 5, CCST without collimation.

# Reconstruction strategies for CCST with collimation at detectors

**Synopsis**  With collimation on detectors, scanning arcs $\mathcal{A}_1 \cup \mathcal{A}_2$ can be combined into one, denoted $\mathcal{A}$. Consequently, the Radon transform $\mathcal{R}_{\mathcal{A}_1 \cup \mathcal{A}_2}$ is denoted in this chapter $\mathcal{R}_{\mathcal{A}}$. This chapter presents two strategies for reconstruction in this situation.

## 4.1  Inversion of $\mathcal{R}_{\mathcal{A}}$ considering the circles supporting the family of circle arcs

In this first strategy, we consider the circles which are supporting the considered circle arcs, with the understanding that the exterior part (outside the detector ring) of the circles gives no contribution in data acquisition. This family of circles $\mathcal{C}$ admits the same polar equation than the scanning circle arcs $\mathcal{A}$ with no restriction of the angular domain

$$\mathcal{C}(\rho(\omega, \theta_{D_k}), \phi(\omega, \theta_{D_k})) : r = \rho(\omega, \theta_{D_k}) \cdot \cos(\theta - \phi(\omega, \theta_{D_k})), \theta \in [0, \pi[, \qquad (4.1)$$

and $\rho(\theta_{D_k}, \omega) = P \cos\left(\theta_{D_k} + \frac{\pi}{2}\right) / \sin(\omega)$ and $\phi(\theta_{D_k}, \omega) = \theta_{D_k} + \omega - \pi/2$.

### 4.1.1  Corresponding Radon transform and its analytic inversion formula

The Radon transform $\mathcal{R}_{\mathcal{A}}$ becomes a Radon transform on circles passing through the origin denoted in the following $\mathcal{R}_{\mathcal{C}}$ :

$$\mathcal{R}_{\mathcal{A}} f(\rho, \phi) = \mathcal{R}_{\mathcal{C}} f(\rho, \phi) = \int_0^\infty \int_0^\pi \rho\, f(r, \theta)\, \delta(r - \rho \cos(\theta - \phi))\, dr\, d\theta. \qquad (4.2)$$

This family of circles is a special case of Cormack's beta-curves [26, 27]. Defining consistency conditions [27], he proposed a stable solution for the inverse transform for its family of curves. For the special case of circles passing through the origin, the Cormack reconstruction equation is

$$f(r, \theta) = \frac{1}{2\pi^2 r} \int_0^{2\pi} d\phi \text{ p.v. } \left\{ \int_0^\infty d\rho \frac{\partial \mathcal{R}_{\mathcal{C}} f(\rho, \phi)}{\partial \rho} \frac{\rho}{r - \rho \cos(\theta - \phi)} \right\}, \qquad (4.3)$$

where p.v. denotes Cauchy principal value. From above equations, numerical formulations of (4.2) and (4.3) are proposed in the following.

### 4.1.2 Numerical formulation for implementation

**Step 1: Image formation** A parameterization in Cartesian coordinates (instead of equations in polar coordinates) is preferable to perform numerical simulations. This allows us having the same distance between adjacent running points on the considered scanning circle. With the use of collimated detectors with *perfect* energy resolution, it is equivalent to characterize scanning arcs according to $(\theta_{D_k}, \phi)$ instead of $(\omega, \theta_{D_k})$. We denote $\Omega$ the center of the corresponding circle $\mathcal{C}$. Cartesian coordinates of $\Omega$ are

$$(x_\Omega, y_\Omega) = \frac{\rho(\theta_{D_k}, \phi)}{2} (\cos\phi, \sin\phi). \tag{4.4}$$

Then, a point $M$ with the Cartesian coordinates $(x, y)$ belongs to the circle $\mathcal{C}$, centered at $\Omega$ if

$$(x(\gamma), y(\gamma)) = (x_\Omega, y_\Omega) + \frac{\rho(\theta_{D_k}, \phi)}{2}(\cos\gamma, \sin\gamma), \gamma \in [0, 2\pi[. \tag{4.5}$$

We finally obtain the forward transform formula for implementation

$$\mathcal{R}_\mathcal{C} f(\theta_{D_k}, \phi) = \frac{\rho}{2} \int_0^{2\pi} f(x(\gamma), y(\gamma)) \, d\gamma. \tag{4.6}$$

**Step 2: Image reconstruction** In order to numerically implement (4.3), we use the Hilbert transform (2.6) to reformulate the Cauchy principal value:

$$f(r, \theta) = \frac{1}{2\pi r} \int_0^{2\pi} d\phi \, \frac{1}{\cos(\theta - \phi)} \mathcal{H} \left\{ \frac{\partial \mathcal{R}_\mathcal{C} f(\rho, \phi)}{\partial \rho} \cdot \rho \right\} \left( \frac{r}{\cos(\theta - \phi)} \right). \tag{4.7}$$

From (2.9) and switching from polar to Cartesian coordinates

$$r = \sqrt{x^2 + y^2} \text{ and } r\cos(\theta - \phi) = x\cos\phi + y\sin\phi, \tag{4.8}$$

ones gets finally the equation for image reconstruction

$$f(x, y) = \frac{1}{2\pi} \int_0^{2\pi} d\phi \, \frac{1}{x\cos\phi + y\sin\phi} \cdot$$
$$\mathcal{F}^{-1} \left( -i \cdot \text{sign}(\nu) \mathcal{F} \left( \frac{\partial \mathcal{R}_{Cir} f(\rho, \phi)}{\partial \rho} \rho \right) (\nu) \right) \left( \frac{x^2 + y^2}{x\cos\phi + y\sin\phi} \right). \tag{4.9}$$

which is converted in the algorithm 4.1 for the purposes of simulation.

---

**Algorithm 4.1:** Reconstruction algorithm of the object $f$ from projections on circles $\mathcal{R}_\mathcal{C}$

---

**Data:** $\mathcal{R}_\mathcal{C} f(\rho, \varphi)$, projections on circles of function $f$

**Result:** $f(x, y)$

**1** Compute the discrete derivation of the projections and multiply the result by $\rho$.

**2** Apply the filter associated to Hilbert transform (2.9) in Fourier domain.

**3** For each $\phi$, interpolate the data on the considered circles.

**4** Weight the result with factor $1/(x \cos \phi + y \sin \phi)$.

**5** Sum the weighted interpolations on all directions $\phi$.

**6** Normalize by $1/2\pi$.

---

## 4.2 Inversion of $\mathcal{R}_\mathcal{A}$ using an intermediate Radon transform

In this method, we only take into account the useful part of the scanning arc $\mathcal{A}$. We go back to this family of circle arcs with a restriction for the angular domain according to variable $\phi$

$$\mathcal{A}(\rho(\omega, \theta_{D_k}), \phi(\omega, \theta_{D_k})) : r = \rho(\omega, \theta_{D_k}) \cdot \cos(\theta - \phi(\omega, \theta_{D_k})), \ \theta \in [\theta_1(\omega, \theta_{D_k}), \theta_2(\omega, \theta_{D_k})], \tag{4.10}$$

where

$$\theta \in [\theta_1, \theta_2] = \begin{cases} [\theta_{D_k}, \theta_{D_k} + \omega] & \text{if } \phi \in \left[0, \frac{3\pi}{2}\right[ \\ [\theta_{D_k} + \omega, \theta_{D_k} + \pi] & \text{if } \phi \in \left[\frac{3\pi}{2}, 2\pi\right[. \end{cases} \tag{4.11}$$

### 4.2.1 Corresponding Radon transform

The corresponding Radon transform is

$$\mathcal{R}_\mathcal{A} f(\rho, \phi) = \int_0^\infty \int_{\theta_1}^{\theta_2} \rho \, f(r, \theta) \, \delta(r - \rho \cos(\theta - \phi)) \, dr \, d\theta, \tag{4.12}$$

where $[\theta_1, \theta_2]$ is the considered domain for $\theta$ according to (4.11).

### 4.2.2 Proposed procedure for inversion

We use geometric inversion, a planar transformation which converts circular arcs passing through the origin on a family of half lines, denoted in the rest of paper $\mathcal{H}$. Consequently, this transformation converts our circular arc Radon transform $\mathcal{A}$ in a Radon transform on half-lines, never made explicit before, and the inversion of this new Radon transform is established in this section.

**Equivalent family of half-lines**  Geometric inversion is characterized in polar coordinates by the change of variables

$$r' = q^2/r, \tag{4.13}$$

where $q$ is the module of inversion. Geometric inversion allows converting the CCST modality into an apparent imaging system. Regarding the scanning manifold, the family of circle arcs has the origin of the coordinate system as their common extremity point. This point is rejected to infinity after geometric inversion. The other extremity point, located before GI on a circle, are now on a straight line. Considering these two points, the family of circle arcs $\mathcal{A}$ is converted in a family of half-lines with extremity into a horizontal line. This family of half-lines, denoted $\mathcal{H}$ in the following, is located below this horizontal line and admits for equation

$$\mathcal{H}(\rho'(\omega, \theta_{D_k}), \phi(\omega, \theta_{D_k})) : \rho'(\omega, \theta_{D_k}) = r' \cos(\theta - \phi(\omega, \theta_{D_k})), \tag{4.14}$$

where $\rho'(\omega, \theta_{D_k}) = q^2/\rho(\omega, \theta_{D_k})$ and $\theta \in [\theta_1, \theta_2]$. Furthermore, this horizontal line is the location of the apparent detectors, since it is the geometric inversion of the ring of detectors. Finally, the object under study $f$ is by geometric inversion converted into an apparent object $f_{\text{app}}$ of equation

$$f_{\text{app}}(r, \theta) = \frac{q^2}{r^2} f\left(\frac{q^2}{r}, \theta\right). \tag{4.15}$$

Figure 4.1 illustrates the principle of geometric inversion schematically. The operation is characterized geometrically by an inversion circle denoted $\Gamma$ of center $S$ (the origin of Cartesian coordinates) and radius $|q|$, with $q \in \mathbb{R}^*$.

The fixed detector ring is represented by the fixed circle in black. This ring is converted into a fixed horizontal line of the plane, of equation $y = -q^2/P$. The apparent detectors are located on this horizontal line. As an example, in Fig. 4.1, the apparent detector $D'$ corresponds to the geometric inversion of the detector $D$. For an arbitrary position for the detector $D$ (in light blue), an example of arc is shown in red. Then, by geometric inversion, the interior arc is converted into the red half-line located above the apparent line of detectors. In the rest, for the sake of readability of next equations, the ordinate of apparent detectors is noted $a$ instead of $-q^2/P$.

Note that, an exterior scanning can be also considered, using the exterior part of the circles as scanning arcs. Parametric equation of these exterior arcs are simply obtained taking the complementary domain for $\theta$. Consequently, considering internal or external mode does not change anything for the equation of the associated Radon transform (4.12) except the considered angular domain.

This external scanning is the second scanning mode introduced in section 3.2. An example of these exterior arcs is presented in Fig. 4.1. By geometric inversion, this arc is converted into the blue half-line, located above the line of detectors. Similarly, we can conclude that the family of exterior arcs becomes by geometric inversion the family of half-lines located
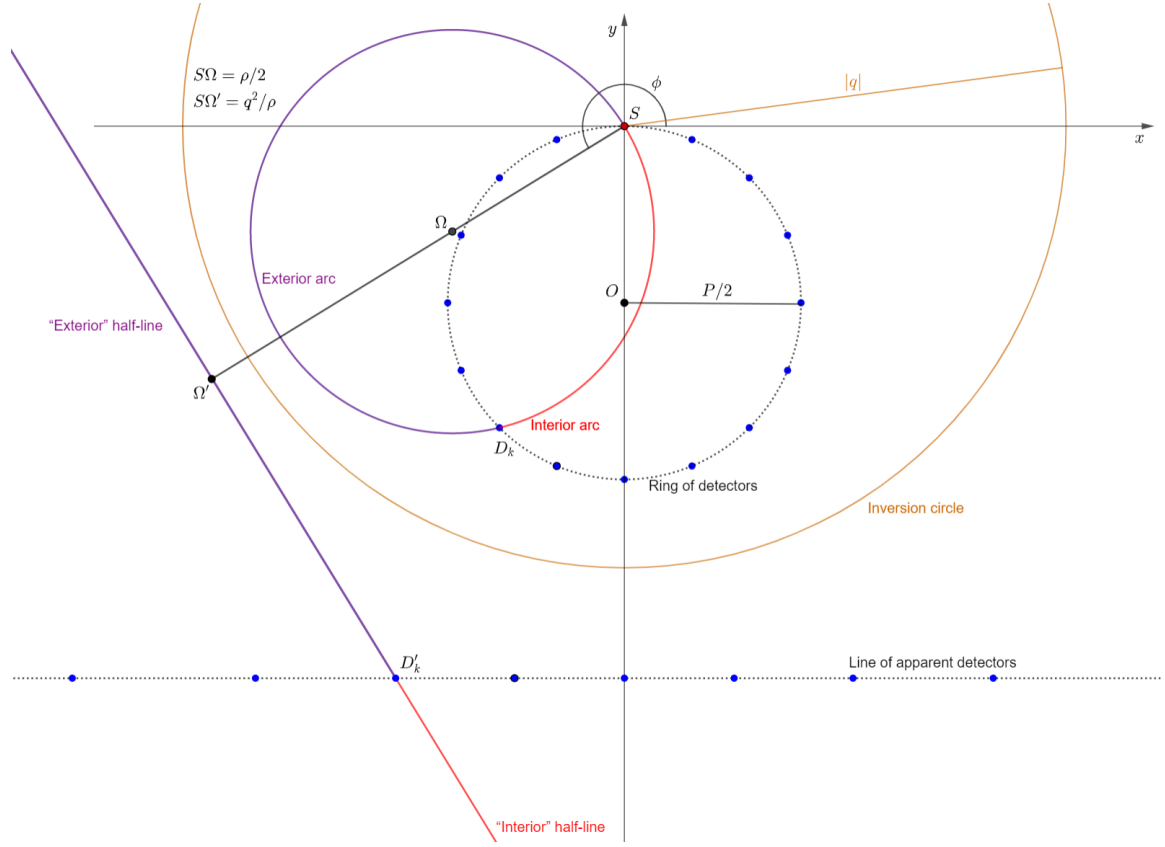
**Figure 4.1** – Geometric inversion of the interior and exterior circular arcs. The color code used for the CCST setup is the same as that used in the figure 3.1. The orange circle is the inversion circle. The line of apparent detectors is the dotted line. The red continuous curve is an example of interior arc. The half-line obtained by geometric inversion is the red half-line. An exterior arc is represented by the purple curve, and its geometric inversion is the purple half-line.

above the line of apparent detectors.

**The Radon transform on half-lines and its relation with $\mathcal{R}_\mathcal{A}$** The following proposition gives us the correspondence between $\mathcal{R}_\mathcal{A}$ and $\mathcal{R}_\mathcal{H}$.

**Proposition 4.2.1.** *Let $f$ be an unknown function.*

$$\mathcal{R}_\mathcal{A} f(\rho, \phi) = \int_{\mathbf{R}^+ \times [\theta_1, \theta_2]} r' \frac{q^2}{r'^2} f\left(\frac{q^2}{r'}, \theta\right) \cdot \delta(\rho' - r' \cos(\theta - \phi)) \, dr' \, d\theta. \tag{4.16}$$

*Then, projection measurements along the circle arcs of $f$ and those on half-lines are related*
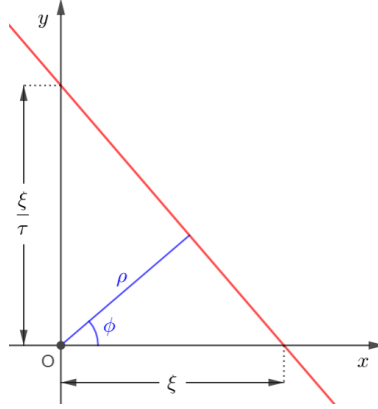
**Figure 4.2** − Chosen parameters for a straight line in Cartesian coordinates

*by the following expression*

$$\mathcal{R}_{\mathcal{A}} f(\rho, \phi) = \mathcal{R}_{\mathcal{H}} f_{app}\left(\frac{q^2}{\rho}, \phi\right),\tag{4.17}$$

Applying the change of variables $r' = q^2/r$ to (4.12), one gets

Consequently, by geometric inversion, the integral transform on circle arcs $\mathcal{R}_{\mathcal{A}}$ of a function $f$ leads to a the Radon transform on half-lines $\mathcal{R}_{\mathcal{H}}$ of the *apparent* function $f_{app}$

Furthermore, since the considered family of half-lines is delimited by a horizontal line, it might be convenient considering the situation in Cartesian coordinates. According to Fig. 4.2 this is achieved with the change of variables $(\rho, \phi) \longrightarrow (\xi, \tau)$

$$\tau = \tan\phi, \; \xi = \frac{\rho}{\cos\phi}, \; d\xi\, d\tau = \frac{1}{\cos\phi}d\rho\, d\phi,\tag{4.18}$$

and the Radon transform on half lines admits for equation

$$\mathcal{R}_{\mathcal{H}}^{a\pm} f_{app}(\xi, \tau) = H_a^{\pm}(y) \int_{\mathbb{R}} dy \; \sqrt{1 + \tau^2} f_{app}(\xi - y\tau, y).\tag{4.19}$$

$\mathcal{R}_{\mathcal{H}}^{a^-} f_{app}$ maps the object on half-lines located below the line of equation $y = a$ whereas $\mathcal{R}_{\mathcal{H}}^{a^+} f_{app}$ refers to measurements on half-lines located above the horizontal line. For image reconstruction, we need the analytical inversion of $\mathcal{R}_{\mathcal{H}}^{a\pm}$.

### 4.2.3   Analytical inversion of $\mathcal{R}_{\mathcal{H}}^{a\pm}$

A previous work of Truong and Nguyen [62] proposed the inversion of the Radon transform in half space. This corresponds to our family of half-lines with the $x$-axis as the fixed dividing line. Here we generalize this work in order to invert the Radon transform on half-lines, called

HlineRT, considering any arbitrary fixed horizontal line separating the plane. This horizontal line will contain the extremities of half-lines. After calculations (summed up in the appendix B), *apparent* function $f_{app}$ can be entirely recovered from projections of respectively $\mathcal{R}_a^- f_{app}$ and $\mathcal{R}_a^+ f_{app}$ using formula

$$f_{app}(x,y) = \frac{1}{2\pi^2} H_a^{\pm}(y) \text{ p.v.} \int_{\mathbf{R^2}} \frac{d\tau\, d\xi}{\sqrt{1+\tau^2}} \frac{1}{(\xi - \tau y - x)} \frac{\partial}{\partial \xi} \mathcal{R}_{\mathcal{H}}^{a\pm} f_{app}(\xi, \tau). \qquad (4.20)$$

Then, going back to parameter $(\rho, \phi)$ with the substitution

$$\phi = \tan^{-1} \tau, \ s = \frac{\xi}{\sqrt{1+\tau^2}} \text{ and } ds\, d\phi = \frac{1}{(1+\tau^2)^{\frac{3}{2}}} d\xi\, d\tau, \qquad (4.21)$$

the analytic inversion formulas of $\mathcal{R}_a^{\pm} f_{app}$ is in polar coordinates

$$f_{app}(x,y) = \frac{1}{2\pi^2} H_a^{\pm}(y) \int_0^{2\pi} d\phi \text{ p.v.} \left\{ \int_0^{\infty} \frac{d\rho}{\rho - x\cos\phi - y\sin\phi} \frac{\partial}{\partial \rho} \mathcal{R}_a^{\pm} f_{app}(\rho, \phi) \right\}, \quad (4.22)$$

Finally, the function $f$ is recovered from $f_{app}$ with the equation

$$f(x,y) = \frac{q^2}{x^2+y^2} f_{app}\left(\frac{q^2\, x}{x^2+y^2}, \frac{q^2\, y}{x^2+y^2}\right) \qquad (4.23)$$

in Cartesian coordinates.

### 4.2.4 Numerical formulation for implementation

This sections gives details about practical simulations of internal and external scanning modes for CCST.

**Step 1: Image formation** First step is similar as the one described for the first strategy in section 4.1.2. Scanning arcs are parametrized in Cartesian coordinates as follows:

$$\mathcal{A} : \begin{cases} x(\gamma) & = \frac{\rho(\theta_{D_k}, \phi)}{2} \left(\cos(\gamma) + \cos(\phi)\right) \\ y(\gamma) & = \frac{\rho(\theta_{D_k}, \phi)}{2} \left(\sin(\gamma) + \sin(\phi)\right), \end{cases} \qquad (4.24)$$

where the respective domain of $\gamma \in [\gamma_1, \gamma_2]$ is

- for the internal scanning case

$$\gamma \in [\gamma_1, \gamma_2] = \begin{cases} [\phi - 2\omega - \pi, \phi - \pi] & \text{if } \phi \in \left[0, \frac{3\pi}{2}\right[ \\ [\phi - \pi, \phi - 2\omega + \pi] & \text{if } \phi \in \left[\frac{3\pi}{2}, 2\pi\right[, \end{cases} \qquad (4.25)$$

- for the external scanning case

$$\gamma \in [\gamma_1, \gamma_2] = \begin{cases} [\phi + \pi, \phi - 2\omega + \pi] & \text{if } \phi \in \left[0, \frac{3\pi}{2}\right[ \\ [\phi - 2\omega - \pi, \phi - \pi] & \text{if } \phi \in \left[\frac{3\pi}{2}, 2\pi\right[. \end{cases} \tag{4.26}$$

Image acquisition is performed in Cartesian coordinates with

$$\mathcal{R}_{\mathcal{A}}^{a\pm} f(\theta_{D_k}, \phi) = \frac{\rho(\theta_{D_k}, \phi)}{2} \int_{\gamma_1}^{\gamma_2} f\left(x(\gamma), y(\gamma)\right) \, d\gamma. \tag{4.27}$$

**Step 3: Geometric inversion of acquired data**  After the interpolation of $\mathcal{R}_{\mathcal{C}}(\theta_{D_k}, \phi)$ on parameters $(\rho, \phi)$, acquired data is transposed to a projection on half-lines via geometric inversion with (4.17).

**Step 4: Reconstruction of the apparent object**  The apparent object is recovered with relation (4.20). Again, this equation is reformulated with the Hilbert transform to obtain the final expression

$$f_{app}(x, y) = \frac{1}{2\pi} \int_0^{2\pi} d\phi \, \mathcal{F}^{-1} \left( |\nu| \mathcal{F} \left( \mathcal{R}_{\mathcal{H}}^{a\pm} f_{app}(\rho, \phi) \right) (\nu) \right) (x \cos \phi + y \sin \phi). \tag{4.28}$$

Algorithm 2 summarizes the different steps for reconstructing the apparent object.

---

**Algorithm 4.2:** Reconstruction of apparent object $f_{app}$ from projections on half-lines $\mathcal{R}_{\mathcal{H}}^{a\pm}$

---

**Data:** $\mathcal{R}_{\mathcal{H}}^{a\pm} f_{app}(\rho, \phi)$, projections on half-lines of *apparent* function $f_{app}$

**Result:** $f_{app}(x, y)$

1  Weight $\mathcal{R}_{\mathcal{H}}^{a\pm} f_{app}(\rho, \phi)$ in the Fourier domain with the ramp filter.

2  **for** *each* $\phi_l$ **do**

3  $\quad$ Interpolate filtered data on the considered circle of coordinates $X \cos \phi_l + Y \sin \phi_l$, where $[X, Y]$ are the matrices of Cartesian coordinates of $f_{app}$.

4  **end**

5  Sum the weighted interpolations.

6  Normalize by $1/2\pi$.

---

**Step 6: Reconstruction of the original object**  The original object $f(x, y)$ is recovered via geometric inversion of $f_{app}(x, y)$ according relation (4.23).

## 4.3   Numerical experiments

This section presents the performed simulations for internal and external cases.

### 4.3.1   General parameter choices

**Chosen objects**   We used for internal scanning the phantom Shepp-Logan (Fig. 4.3a) of
size $512 \times 512$ pixels and for external scanning a cracked bar (Fig. 4.3b) of size $1200 \times 360$
pixels. These phantoms allow the visual evaluation of different criteria such as spatial
resolution, contrast and the ability of the proposed algorithms to reconstruction singularities
tangent to lines with arbitrary slopes.

**Parameter choices for the fixed setup**   The CCST system used for these simulations
is the same for both internal and external configurations, in order to show the ability of
CCST modality to reconstruct both small and large objects.

Consequently, the diameter $P$ of the fixed ring, $N_D$ and $N_\phi$ the respective number of
detectors and scanning circles (or circle arcs) per detector are chosen only once for all
simulations. $N_D = 3217$ detectors are equally placed on a ring of diameter $P = 1024$, that is
two times larger than the Shepp-Logan phantom. The number of projections $N_\phi$ is set to
3000. Note that these numbers have been chosen to largely satisfy the well known condition
[63] reformulate in our case as

$$N_D \times N_\phi > N_1 \times N_2, \tag{4.29}$$



**(a)** Sheep-Logan phantom                    **(b)** Cracked bar
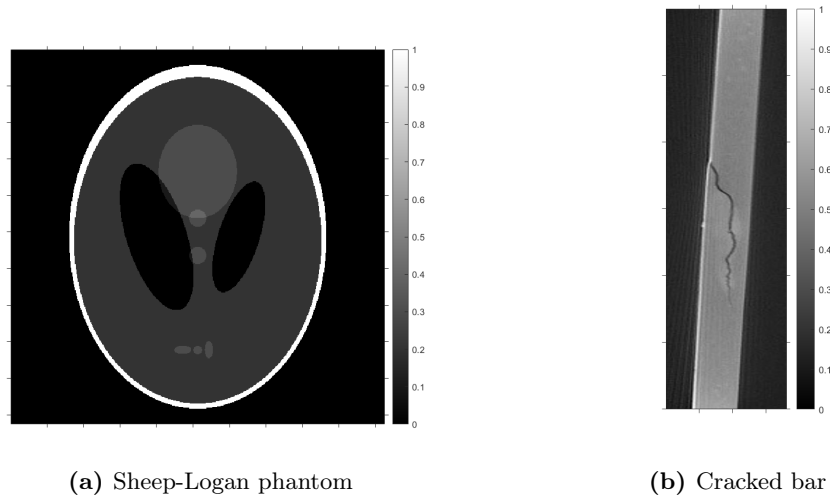
**Figure 4.3** − Original objects $f$ for (a) internal scanning and (b) external scanning. Size of
the objects: (a) $512 \times 512$ pixels, (b) $1200 \times 360$ pixels.

where $(N_1, N_2)$ represents the size of the scanned object. A careful study on the choice of
these parameters for a second proposed system is presented next in chapter 7. Similar results
are expected in the present case.

### 4.3.2    Simulation results

**Internal scanning**    Figures 4.4a and 4.5a show the respective acquired projections using the first and the second proposed methods. Then data are rearranged under parameters $(\rho, \phi)$, see figures 4.4b and 4.5b.
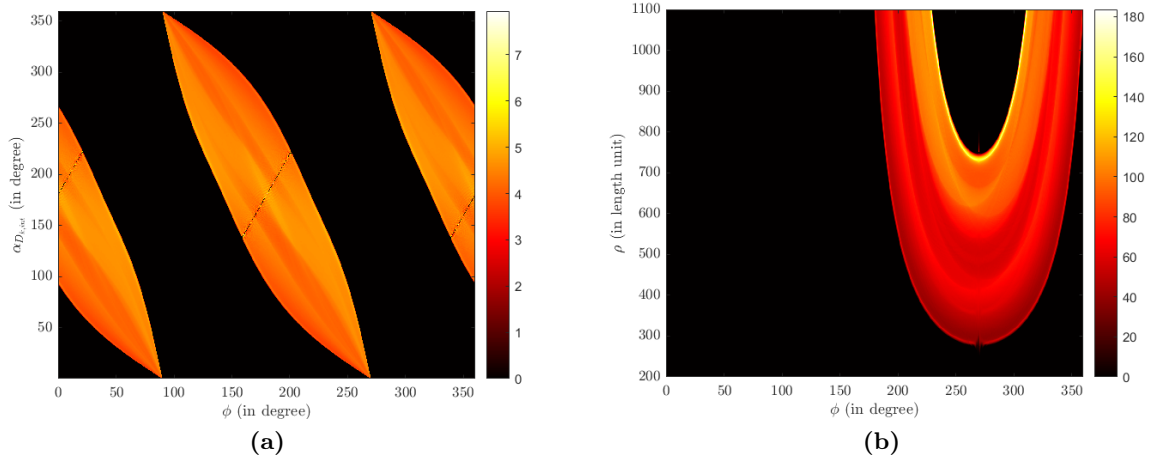


**Figure 4.4** – Data acquisition process using the first method. (a) Image formation $\mathcal{R}_{\mathcal{C}}f(\theta_{D_{k,int}}, \phi)$ on circles of $f$. (b) Rearranged data $\mathcal{R}_{\mathcal{C}}f(\rho, \phi)$.

As expected, acquired projection and rearranged data are strictly equivalent for both methods. Moreover, we observe slight holes in the middle of figures 4.4a and 4.5a. These holes are due to the missing detectors near to the source. These holes are equivalently present on the basis of the U-shape of rearranged data, and are filled with spline interpolation in figures 4.4b and 4.5b.

The second procedure necessitates an intermediate step to convert data on circle arc to data on half-lines (see figure 4.5c) before reconstruction.

The obtained reconstruction results for both methods are presented in figure 4.6.

**External scanning**    Figure 4.7a and 4.7b show respectively acquired and rearranged data on circle arcs. Then, data are rearranged by geometric inversion on half-lines, see figure 4.7c, before reconstruction in figure 4.8a.

## 4.4    Discussions and concluding remarks

We introduced in this chapter two reconstruction methods based on the analytic inversion of the Radon transform on circle arcs modelling data acquisition using CCST with collimation at detector. The first method rests on the inversion formula proposed by Cormack for the Radon transform on circles passing through the origin. As in conventional tomography

(a)



(b)



(c)
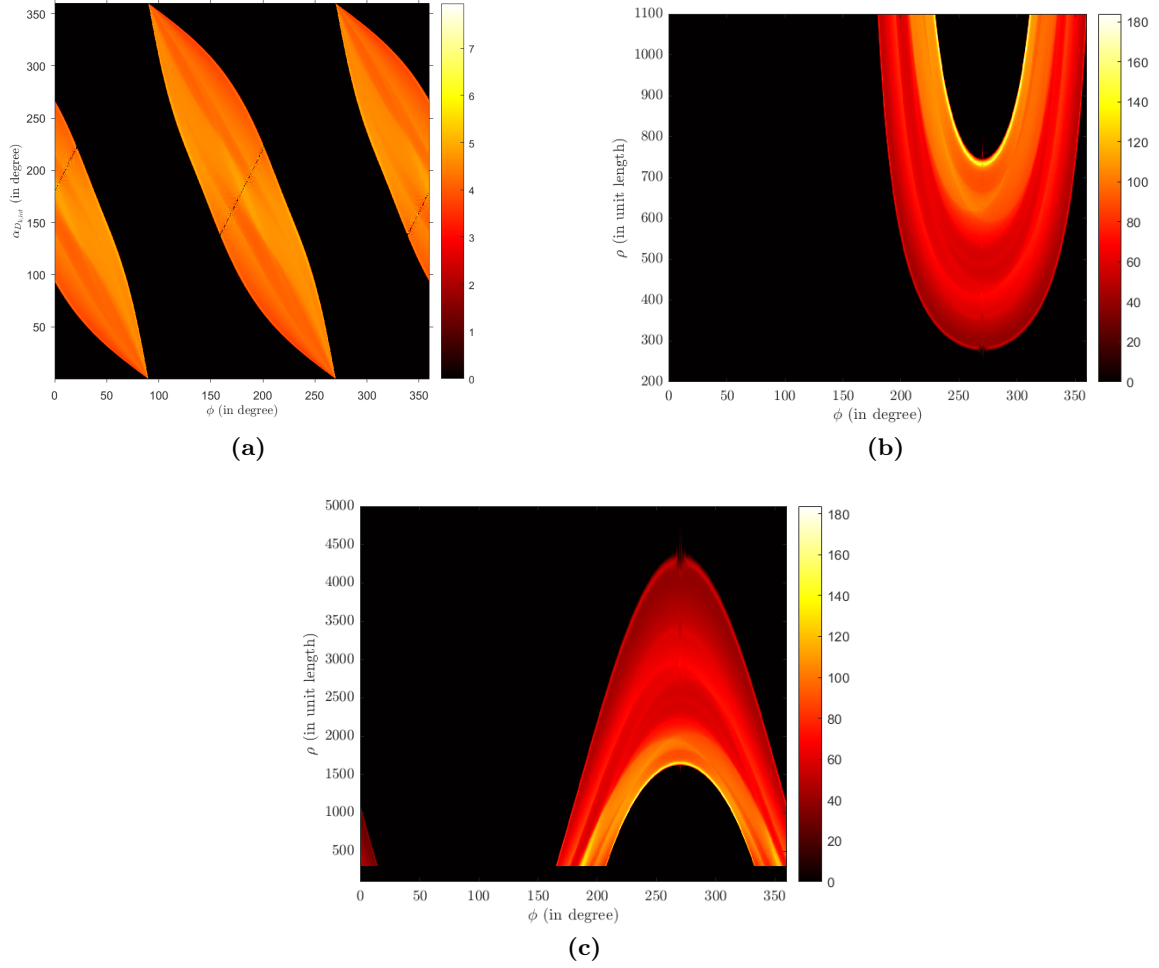
**Figure 4.5** – Data acquisition process with the second method. (a) Image formation $\mathcal{R}_{\mathcal{A}}f(\theta_{D_{k,int}}, \phi)$ on circles arc of $f$. (b) Rearranged data $\mathcal{R}_{\mathcal{A}}f(\rho, \phi)$. (c) Rearranged data on half-lines $\mathcal{R}_{\mathcal{H}}f(\rho, \phi)$

with the classical Radon transform on lines, we provide, from this inversion formula, a fast reconstruction algorithm, having also a first step of filtering data and a second step which consists in back-projecting on the appropriated circles. With the second approach, we proceed by geometric inversion, to convert a Radon transform on circle arcs to a Radon transform on half-lines, never introduced before. In fact, this family of half-lines is a generalization of one previously considered by Truong and Nguyen. We established in this work the inversion formula for this Radon transform on half-lines. As a result, we derived also a filtered-back projection type algorithm to reconstruct the apparent object on half-lines. The two proposed filtered back-projection algorithms ensures us having fast and exact simulation results.

Both obtained reconstruction results (for internal scanning) are similar in terms of quality,
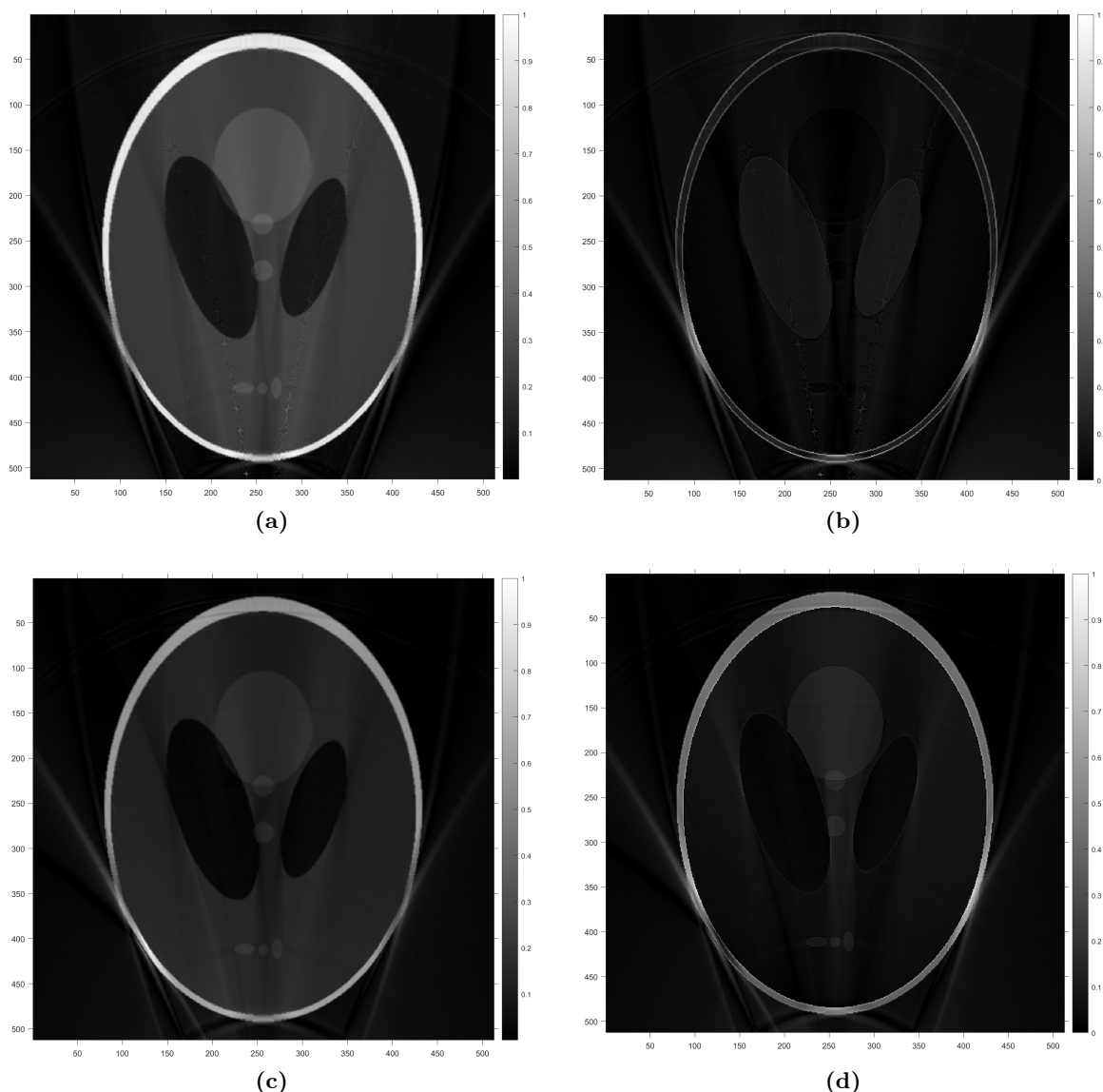
**Figure 4.6** – Reconstruction results for internal scanning from (a) projection on circles $\mathcal{R}_{\mathcal{C}} f(\theta_{D_{k,int}}, \phi)$ (NMSE = 0.0063) and (c) projection on circle arcs $\mathcal{R}_{\mathcal{A}} f(\theta_{D_{k,int}}, \phi)$ via the projection on half-lines $\mathcal{R}_{\mathcal{H}} f(\rho, \phi)$ (NMSE = 0.014). (b) and (d): Differences (in absolute value) between the respective obtained reconstruction (a) and (c) and the original image (Fig. 4.3a).

with a good reconstruction of little nodules, even if we can note a slight loss of contrast on the reconstruction result obtained with the second method. This may be due to the supplementary steps of geometric inversion, since it necessarily introduces more numerical approximations.

In addition to this, the reconstruction results exhibit some artefacts on the left and right sides of the object. Note also the presence of a slight deformation of the outer contours at

**(a)**



**(b)**



**(c)**
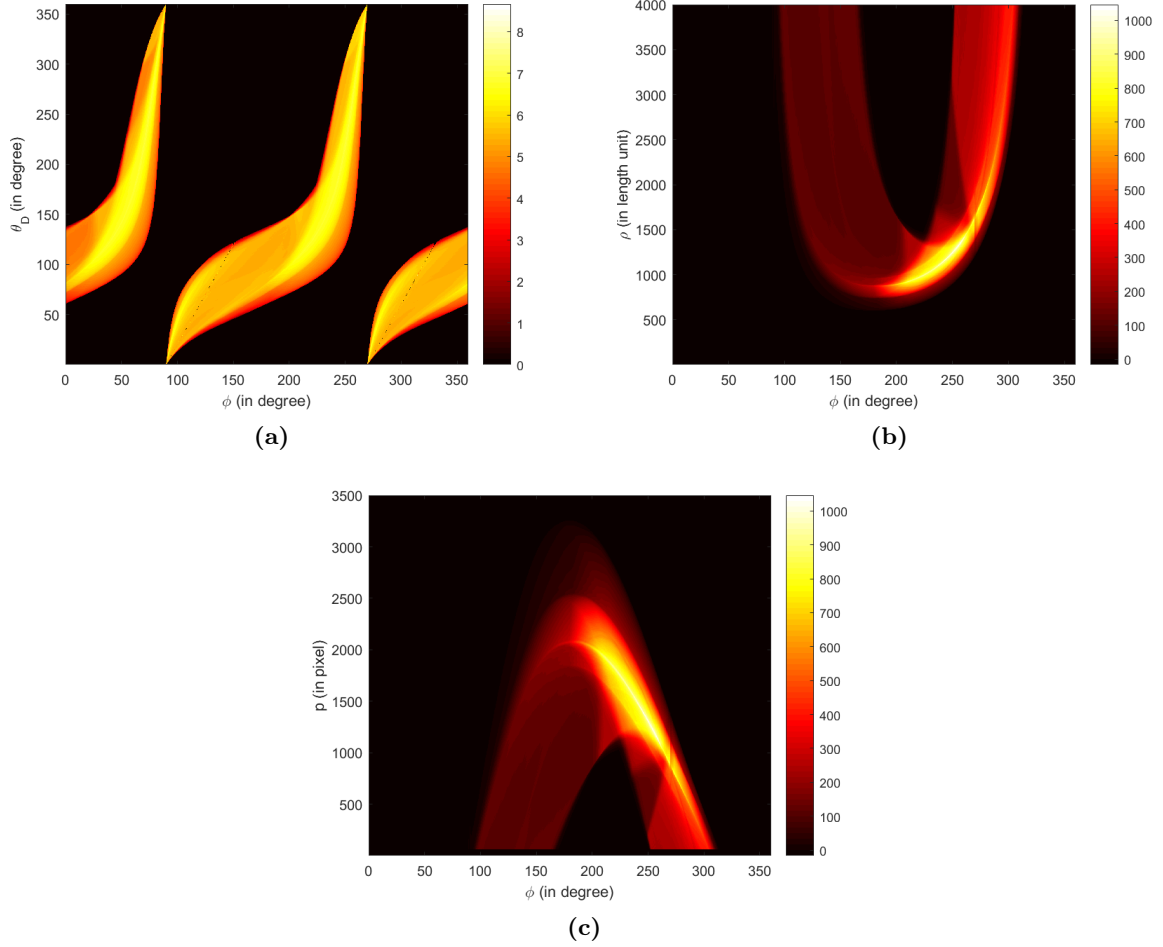
**Figure 4.7** – Data acquisition process and reconstruction result for external scanning. (a) Image formation $\mathcal{R}_{\mathcal{A}}f(\theta_{D_{k,int}}, \varphi)$ on circles arc of $f$. (b) Rearranged data $\mathcal{R}_{\mathcal{A}}f(\rho, \phi)$. (c) Rearranged data on half-lines $\mathcal{R}_{\mathcal{H}}f(\rho, \phi)$.

these locations. This type of artefacts is an intrinsic problem due to missing data, since projections are limited to circles with a finite diameter, i.e. diameter $\rho$ labelling data is constrained to a range $[0, \rho_{max}]$. In fact, they can be explained via microlocal analysis. In the case of the Radon transform on straight lines studied by Nosmas [64], Quinto, Frikel and Krishnan [65, 66, 67] microlocal analysis allowed artefact characterization and image enhancement. These articles considered cases where missing data was deliberately chosen to mimic a real limitation in the scanning. Some properties established by Frikel and Quinto can be extrapolated to our generalized Radon transform. In fact, it can be proven that this Radon transform on circle arcs is an Integral Fourier Operator (IFO), like the classical Radon transform. Considering the integral definition of Dirac distribution,

$$\delta(s) = \frac{1}{2\pi} \int_{-\infty}^{+\infty} e^{i\xi s} d\xi, \tag{4.30}$$
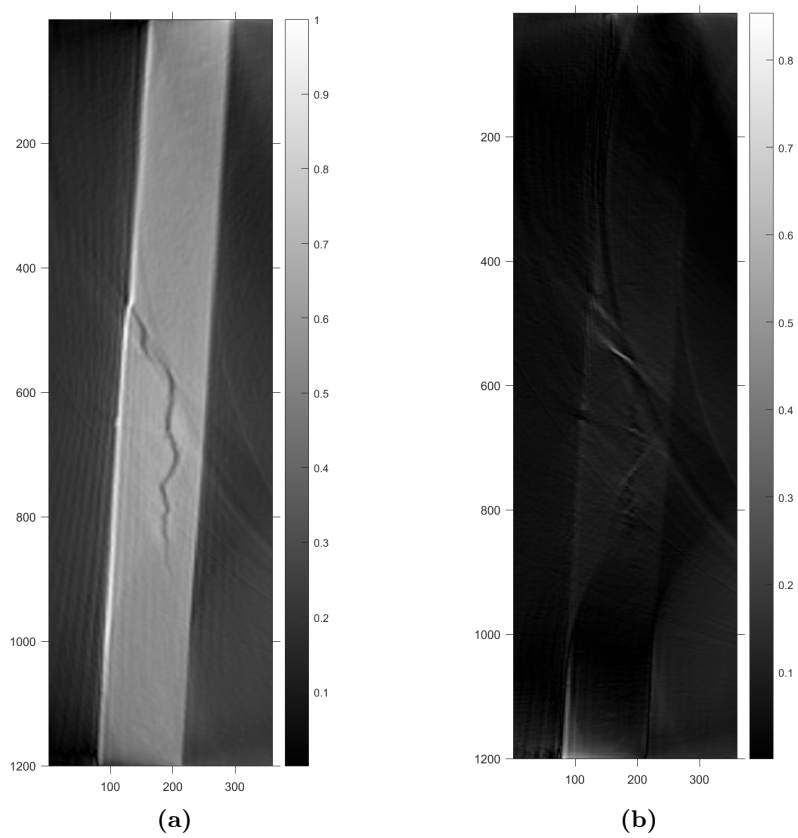
**Figure 4.8** − (a) Reconstruction result for external scanning (NMSE = 0.055). (b) Difference (in absolute value) between the obtained reconstruction (a) and the original image (Fig. 4.3b).

the Radon transform can be rewritten as

$$\mathcal{R}_{\mathcal{A}}f(\rho,\phi) = \int_{R^2 \times [\theta_1,\theta_2]} \frac{\rho}{2\pi r} f(r,\theta) e^{i\xi(\rho - r\cos(\theta-\phi))} r \, d\xi \, dr \, d\theta. \tag{4.31}$$

Thus, this formulation shows that the Radon transform on circle arcs under study is an IFO with phase function $\Phi(\xi) = \xi(r - \rho\cos(\theta - \phi))$ and amplitude $\rho/(2\pi r)$. Then, provided that $\mathcal{R}_{\mathcal{C}}$ in an IFO, we can extend the results established for IFO's in the literature in the form of a principle predicting reconstruction quality:

**Proposition 4.4.1.** *The boundary of an object is visible if there exists a scanning circle with is locally tangent to this boundary. If any scanning curve is not tangent to a local part of the boundary, this local part of the boundary is considered as invisible, and will not be well reconstructed.*

According to the previous proposition, the lower reconstruction quality in the upper right and lower left edges of the object is a consequence of the lack of scanning circle arcs locally tangent to these parts. The circle arcs responsible for the reconstruction of these parts are those with a larger diameter than the chosen $\rho_{max}$. The higher $\rho$ is, the better will be the reconstruction result, but the computation time will be higher.

Note also that, this problem of artefacts is caused by the necessary rearranging step before reconstruction. One way to have a reconstruction without this type of artefact would consist in avoiding this change of variables. Thus, instead of rearranging data, one solution is to make the substitution $(\rho,\phi) \longrightarrow (\omega, \theta_{D_k})$ from equation (4.9), for instance. However, this change of variable may involve extra difficulties for implementation.

The second approach for inverting the considered Radon transform on circle arcs led us to investigate the possibility of an external scanning. In that situation, the object is placed outside the ring of detectors. Thus, the object may be larger than the ring of detectors. For our simulations, we considered an object more than two time larger than the radius of the system. The object is well reconstructed, and in particular, the failure is well reconstructed. We find again some artefacts in the reconstruction, which can also be explained as previously.

# 5

# CCST without collimation at detectors and three-dimensional extensions

**Synopsis**  In this chapter, we consider the CCST without collimation. In the absence of analytical inversion for the corresponding Radon transform, we propose reconstruction results via Tikhonov regularization. The CCST without collimation leads us naturally towards three-dimensional extensions, where the plate collimators of the source and the detectors are removed. We can now reconstruct directly volumes. We discuss at the end of this chapter two possible 3D extensions for CCST.

## 5.1 Corresponding Radon transform of CCST without collimation

We consider CCST without collimation. Consequently, given a scattering angle $\omega$, we cannot know if the scattering site is located on either the circle arc $\mathcal{A}_1$ or $\mathcal{A}_2$. Going back to (3.10), we first make explicit the Radon transform modelling data for CCST without collimation and then give its adjoint. We follow the same notations as in Chapter 3.

### 5.1.1 Definition

**Definition 5.1.1.** *Let $f$ be an unknown function, non-negative, continuous and compactly supported inside the disc of diameter $P$ and centered at $O = (0, -P/2)$. Let $\epsilon_{1,2} > 0$. The Radon transform on double circular arcs of the function $f$ $\mathcal{R}_{\mathcal{A}_1 \cup \mathcal{A}_2} f$ maps $f$ into the set of its integrals over the family of double circular arcs $\mathcal{A}_1 \cup \mathcal{A}_2$ as*

$$\mathcal{R}_{\mathcal{A}_1 \cup \mathcal{A}_2} f(\omega, \theta_{D_k}) = \int_{-\infty}^{\infty} \left[ \int_{\theta_{D_k}}^{\theta_{D_k}+\omega} f(r,\theta) \rho(\omega, \theta_{D_k}) \delta(r - \rho(\omega, \theta_{D_k}) \cos(\theta - \phi(\omega, \theta_{D_k}))) d\theta \right.$$

$$\left. + \int_{\theta_{D_k}-\omega}^{\theta_{D_k}} f(r,\theta) \rho(-\omega, \theta_{D_k}) \delta(r - \rho(-\omega, \theta_{D_k}) \cos(\theta - \phi(-\omega, \theta_{D_k}))) d\theta \right] dr. \quad (5.1)$$

*Recall that $\rho(\theta_{D_k}, \omega) = P \cos\left(\theta_{D_k} + \frac{\pi}{2}\right) / \sin(\omega)$ and $\phi(\theta_{D_k}, \omega) = \theta_{D_k} + \omega - \pi/2$.*

### 5.1.2    Is $\mathcal{R}_{\mathcal{A}_1 \cup \mathcal{A}_2}$ invertible ?

This question remains still open. The difficulty with this transform lies in the fact that the family of double circle arcs has no invariance neither by rotation nor by translation, which can be exploited to demonstrate invertibility. In fact, in many references dealing with the invertibility of generalized Radon transform, if the considered manifold admits a rotational invariance, one of the key steps in the proof is to use circular (respectively spherical) harmonic expansion in two (resp. three) dimensions in order to dissociate the *radial* component[1] to those which define the rotational invariance [10, 9, 26, 27, 70, 12, 71, 69, 68]. By the way, in [72], a general result about the invertibility of the rotational invariant Radon transform has been established. Similarly, one can also find an equivalent result when the considered manifold admits this time a translational invariance [13, 62, 73, 74, 75]. Of course, this remark does not mean that this Radon transform is not invertible. Nevertheless, it must be difficult to use these common techniques to conclude about the invertibility of the Radon transform we are interested in. Since we cannot conclude about this question, we apply in next paragraph Tikhonov regularization for reconstruction.

### 5.1.3    Numerical simulations

For simulations, we chose here to apply the iterative formulation of Tikhonov regularization (see Algorithm 2.3). Before computing the adjoint transform, we propose an alternative formulation suitable for the rest of our calculations.

**Reformulation of the forward Radon transform and derivation of the adjoint**

We have the following proposition:

**Proposition 5.1.1.** *Going back to variable $\theta_{D_{k,int}}$ with relation (3.3) and denoting*

$$\mathcal{R}_1 f(\omega, \theta_{D_{k,int}}) = \int_0^\infty \int_0^{2\pi} f(r,\theta)\rho(\omega, \theta_{D_{k,int}})\delta(r - \rho(\omega, \theta_{D_{k,int}})\cos(\theta - \phi(\omega, \theta_{D_{k,int}})))d\theta dr, \tag{5.2}$$

*equation 5.1 reads now,*

$$\mathcal{R}_{\mathcal{A}_1 \cup \mathcal{A}_2} f(\omega, \theta_{D_{k,int}}) = \mathcal{R}_1 f(\omega, \theta_{D_{k,int}}) + \mathcal{R}_1 f(-\omega, \theta_{D_{k,int}}). \tag{5.3}$$

*Proof.* Since the object $f$ is compactly supported inside the ring of detectors, we can consider

---

[1]According the chosen parameterization, this *radial* component is not necessarily a length, but it may directly be related to a length (without the need of extra variables, except constants). See for instance [68, 69].

the toric section supporting the double circle arcs. From equation (5.1), one gets

$$\mathcal{R}_{\mathcal{A}_1 \cup \mathcal{A}_2} f(\omega, \theta_{D_k}) = \int_{-\infty}^{\infty} \int_{\pi}^{2\pi} f(r, \theta) \rho(\omega, \theta_{D_k}) \left[ \delta\big(r - \rho(\omega, \theta_{D_k}) \cos(\theta - \phi(\omega, \theta_{D_k}))\big) + \right.$$
$$\left. \rho(-\omega, \theta_{D_k}) \delta\big(r - \rho(-\omega, \theta_{D_k}) \cos(\theta - \phi(-\omega, \theta_{D_k}))\big) \right] d\theta dr, \quad (5.4)$$

and denoting

$$\mathcal{R}_1^{\pm} f(\omega, \theta_{D_k}) = \int_{-\infty}^{\infty} \int_{\pi}^{2\pi} f(r, \theta) \rho(\pm\omega, \theta_{D_k}) \delta\big(r - \rho(\pm\omega, \theta_{D_k}) \cos(\theta - \phi(\pm\omega, \theta_{D_k}))\big) d\theta dr, \quad (5.5)$$

we have

$$\mathcal{R}_{\mathcal{A}_1 \cup \mathcal{A}_2} f(\omega, \theta_{D_k}) = \mathcal{R}_1^{+} f(\omega, \theta_{D_k}) + \mathcal{R}_1^{-} f(\omega, \theta_{D_k}). \quad (5.6)$$

Furthermore,

$$\mathcal{R}_1^{\pm} f(\omega, \theta_{D_k}) = \int_{-\infty}^{0} \int_{\pi}^{2\pi} f(r, \theta) \rho(\pm\omega, \theta_{D_k}) \delta\big(r - \rho(\pm\omega, \theta_{D_k}) \cos(\theta - \phi(\pm\omega, \theta_{D_k}))\big) d\theta dr$$
$$+ \int_{0}^{\infty} \int_{\pi}^{2\pi} f(r, \theta) \rho(\pm\omega, \theta_{D_k}) \delta\big(r - \rho(\pm\omega, \theta_{D_k}) \cos(\theta - \phi(\pm\omega, \theta_{D_k}))\big) d\theta dr$$
$$= \int_{0}^{\infty} \int_{\pi}^{2\pi} \left[ f(r, \theta) \rho(\pm\omega, \theta_{D_k}) \delta\big(r - \rho(\pm\omega, \theta_{D_k}) \cos(\theta - \phi(\pm\omega, \theta_{D_k}))\big) \right.$$
$$\left. + f(r, \theta + \pi) \rho(\pm\omega, \theta_{D_k}) \delta\big(r + \rho(\pm\omega, \theta_{D_k}) \cos(\theta - \phi(\pm\omega, \theta_{D_k}))\big) \right] d\theta dr$$
$$= \int_{0}^{\infty} \int_{\pi}^{2\pi} f(r, \theta) \rho(\pm\omega, \theta_{D_k}) \delta\big(r - \rho(\pm\omega, \theta_{D_k}) \cos(\theta - \phi(\pm\omega, \theta_{D_k}))\big) d\theta dr$$
$$+ \int_{0}^{\infty} \int_{2\pi}^{3\pi} f(r, \theta) \rho(\pm\omega, \theta_{D_k}) \delta\big(r - \rho(\pm\omega, \theta_{D_k}) \cos(\theta - \phi(\pm\omega, \theta_{D_k}))\big) d\theta dr$$
$$= \int_{0}^{\infty} \int_{0}^{2\pi} f(r, \theta) \rho(\pm\omega, \theta_{D_k}) \delta\big(r - \rho(\pm\omega, \theta_{D_k}) \cos(\theta - \phi(\pm\omega, \theta_{D_k}))\big) d\theta dr$$
$$(5.7)$$

Relation 5.3 is then obtained by expressing the angular position of detectors according to $\theta_{D_{k,int}}$. $\qquad \square$

We are now able to derive the expression of the adjoint transform of $\mathcal{R}_{\mathcal{A}_1 \cup \mathcal{A}_2}$.

**Proposition 5.1.2.** *Let $g$ be a function of $]0, \pi[ \times ]0, 2\pi[$. The operator $\hat{\mathcal{R}}_1^{\pm}$, of expression,*

$$\hat{\mathcal{R}}_1^{\pm} g(r, \theta) =$$
$$\int_{0}^{\pi} -sign(\sin(\pm\omega)) \sin(\theta'/2) g(\pm\omega, \theta') d(\pm\omega)_{|\theta' = \arccos\left( \frac{-2\sin(\pm\omega)}{P} r + \cos(\theta - (\pm\omega)) \right) + \theta - (\pm\omega)} \quad (5.8)$$

*is the adjoint of $\mathcal{R}_1^{\pm}$. Then, by linearity of the inner product, the adjoint of $\mathcal{R}_{\mathcal{A}_1 \cup \mathcal{A}_2}$ is the*

operator $\hat{\mathcal{R}}_{\mathcal{A}_1 \cup \mathcal{A}_2}$:

$$\hat{\mathcal{R}}_{\mathcal{A}_1 \cup \mathcal{A}_2}^{\pm} g(r,\theta) = \hat{\mathcal{R}}_1^+ g(r,\theta) + \hat{\mathcal{R}}_1^- g(r,\theta). \tag{5.9}$$

*Proof.*

$$\langle \mathcal{R}_1^{\pm} f, g \rangle = \pm \int_0^{\pi} \int_0^{2\pi} \mathcal{R}_1^{\pm} f(\omega, \theta_{D_{k,int}}) g(\pm\omega, \theta_{D_{k,int}}) d\theta_{D_{k,int}} d\omega$$

$$= \int_0^{2\pi} \int_0^{\infty} f(r,\theta) \hat{\mathcal{R}}_1^{\pm} f(r,\theta) dr d\theta = \langle f, \hat{\mathcal{R}}_1^{\pm} g \rangle. \tag{5.10}$$

where

$$\hat{\mathcal{R}}_1^{\pm} g(r,\theta) = \pm \int_0^{\pi} \int_0^{2\pi} g(\pm\omega, \theta_{D_{k,int}}) \rho(\theta_{D_{k,int}}, \pm\omega)$$

$$\delta(r - \rho(\theta_{D_{k,int}}, \pm\omega) \cos(\theta - \phi(\theta_{D_{k,int}}, \pm\omega))) d\theta_{D_{k,int}} d\omega. \tag{5.11}$$

We make explicit the Dirac delta distribution

$$\delta(r - \rho(\theta_{D_{k,int}}, \pm\omega) \cos(\theta - \phi(\theta_{D_{k,int}}, \pm\omega)))$$

$$= \delta\left( r \pm \frac{P \sin(\theta_{D_{k,int}}/2)}{\sin(\omega)} \cos\left( \theta - \left( \frac{\theta_{D_{k,int}}}{2} \pm \omega + \frac{\pi}{2} \right) \right) \right)$$

$$= \frac{2|\sin\omega|}{P} \delta\left( \pm \frac{2\sin(\omega)}{P} r + \left( \cos(\theta_{D_{k,int}} - \theta \pm \omega) - \cos(\theta \mp \omega) \right) \right). \tag{5.12}$$

In addition, noting that the relation $\pm \frac{2\sin(\omega)}{P} r + \left( \cos(\theta_{D_{k,int}} - \theta \pm \omega) - \cos(\theta \mp \omega) \right) = 0$ is equivalent to $\theta_{D_{k,int}} = \arccos\left( \frac{\mp 2\sin\omega}{P} r + \cos(\theta \mp \omega) \right) + \theta \mp \omega$, one gets finally (5.9).   $\square$

### Parameter choices

We carried out simulations for the Shepp-Logan phantom of size $N \times N = 128 \times 128$. This object is placed inside a ring of detectors of diameter $P = 256$ with $N_D = 805$ detectors, which is one detector per unit length.

### Simulation results

Figure 5.1 shows the obtained data acquisition and image reconstruction results. For the proposed simulations, we performed $K = 100$ iterations and chose a regularization parameter $\alpha = 0.01$.

### 5.1.4   Discussions

We studied, in this first part, the CCST without collimators. In absence of inverse formula, we proposed a reconstruction with Tikhonov regularization. We opted for the matrix free

(a)

(b)

(c)
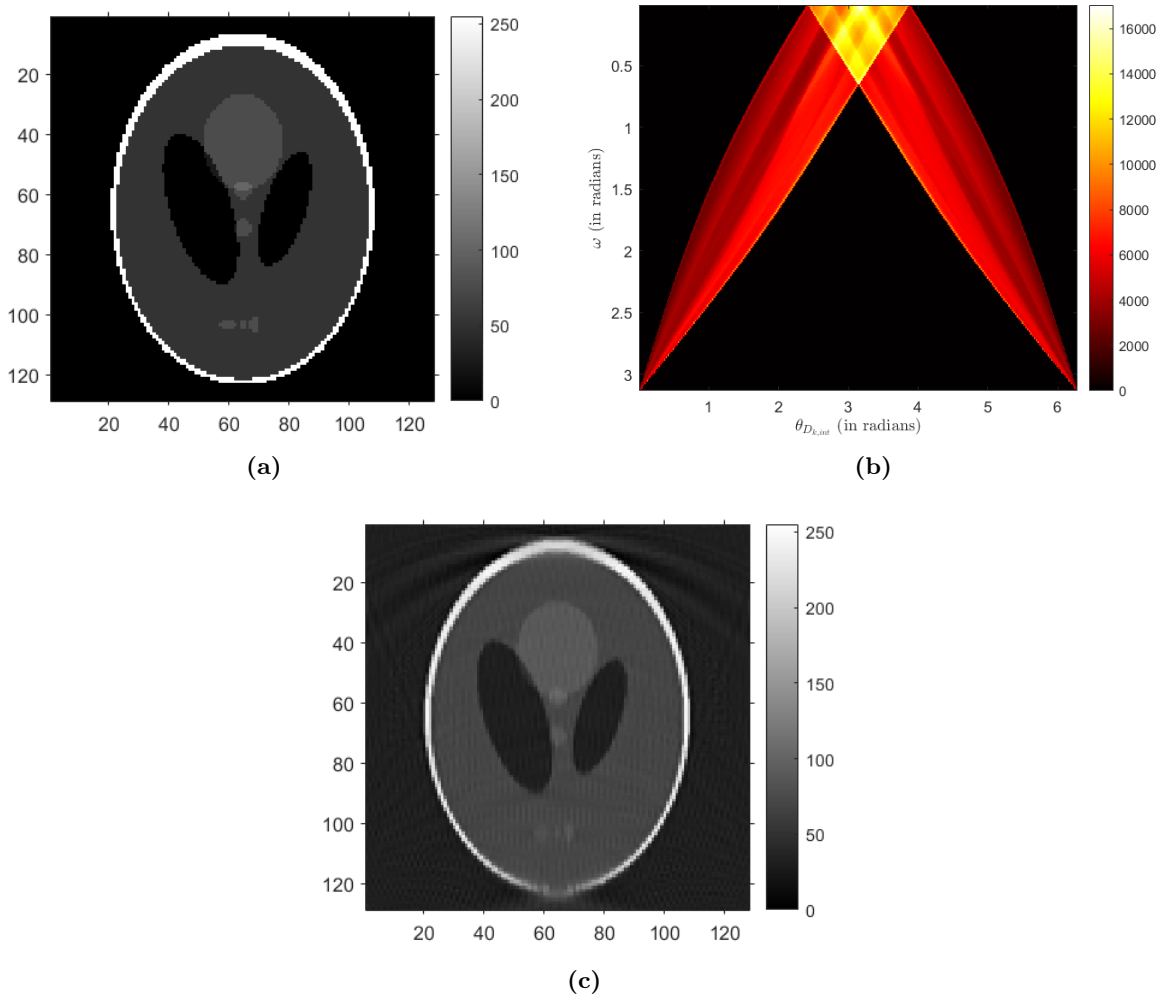
**Figure 5.1** − Simulation results obtained by Tikhonov regularization using CCST without collimation. (a) Original object. (b) Data acquisition on double circle arcs. (c) Reconstruction.

implementation to avoid limitations in terms of memory.

The obtained quality of reconstruction is similar to that obtained in computational tomography, in particular in terms of contrast. The reconstruction of the little nodules is quite good. Moreover, note that, the reconstruction exhibits artefacts completely different from those observed with the proposed algorithms during the modelling of CCST with collimators. In fact, as explained before, these streak artefacts were due to the loss of a part of data during the rearrangement step. With regularization methods, as proposed here in the absence of an inverse formula, this constraint is removed. This shows that acquisition using CCST allows us to really have a complete set of data for image reconstruction.

Instead, we observe here two slightly blurred areas on the top and the bottom of the object,

with a streak artefact on the top of the object. This corresponds to the areas of the object furthest and closest to the source. The blurred area on the bottom of the object may be explained by the fact that, due to the shape of the double scanning arcs, only few of them contain information about this part of this object. This remains to be confirmed by comparing this result with those of other regularization methods [36, 44, 76].

## 5.2    Two possible extensions for CCST in three dimensions: Spherical CST and Cylindrical CST

We now discuss two possible extensions for CCST in three dimensions. The idea is to remove the plate collimator for the source of CCST. We can now recover information directly about the volume of the object. To preserve the assets of CCST, that is having a system completely fixed and compact, detectors can now be placed either on a sphere or on a cylinder containing the source. These modalities are called respectively in the following Spherical CST (SCST) and Cylindrical CST (CylCST). See Figure 5.2.



|         (a)          |         (b)          |
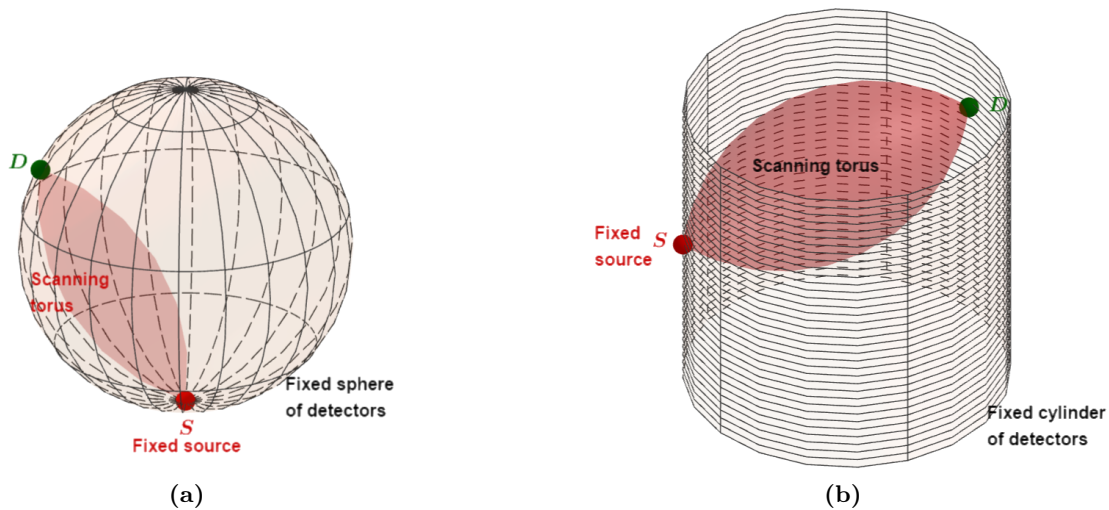
**Figure 5.2** – Possible extensions of CCST in three dimensions. (a) SCST with detectors on a sphere and (b) CylCST with detectors on a cylinder.

Possible applications for CylCST are in the biomedical field or non-destructive testing, whereas SCST is more convenient for industrial applications, due to the closed geometry of the system.

Similarly as for CCST, assuming that first order scattering is dominant compared to multiple scattering and attenuation is absent inside matter, data acquisition using SCST and CylCST is modelled by a Radon transform on toric surfaces passing through the source and the considered detector, either on the sphere or the cylinder. These toric surfaces originate from a rotation around the source-detector axis of the family of double scanning circle arcs

previously described.

These systems were introduced in the international conference SPIE Photonics Europe [77] with a numerical approach for image reconstruction. In fact, the invertibility of the corresponding Radon transforms is not established yet. In the same period, another team studied also these two three-dimensional modalities in reference [78] and their results overpass the preliminary results presented during this conference. In particular, this study introduces incomplete data issues arising with these modalities, which can be due to energetic and/or due to the problem of limited angle. Consequently, it was more interesting to our mind to continue our research on the subject of the invertibility of these Radon transforms on toric surfaces.

We mentioned earlier that the fact of not having any invariance to exploit could be the reason for not being able to find an inverse formula. What happens if we *add* this invariance?

We propose in the next chapter to study a Radon transform on V-lines (and respectively on cones in three dimensions) obtained by geometric inversion of the family of double circle arcs (respectively toric surfaces), to which we add a degree of liberty to introduce the missing invariance. We establish in this chapter the invertibility of this Radon transform. We discuss then the consequences of this additional degree of liberty on the imaging system.

# Analytical inversion of a Radon transform on a family of cones with pivoting axes

**Synopsis** From this first study of CCST without collimation and its extensions in three dimensions, we want to go a step further in the study of the invertibility of the associated Radon transform. Recall that, what blocked us before, is the absence of invariance by rotation or translation of our family of double arcs of circle. We propose here to add a degree of freedom to our problem. In order to see which degree of freedom can be added, we will work with the equivalent problem obtained by geometric inversion. This leads us to a Radon transform of a family of V-lines in two dimensions (and a family of cones in three-dimensions) whose axes are passing through the origin of the coordinate system. In this chapter, we establish the analytic inversion of this Radon transform in two and three dimensions and discuss the obtained results.

## 6.1 Study of a Radon transform on a family of V-lines

In this section, we introduce a new family of V-lines and study its Radon transform.

### 6.1.1 How do we select this V-line manifold ?

The choice of this family of V-lines originates from our previous study on CCST without collimation. We obtained it after adding a degree of freedom to the geometric inversion of the family of its scanning double circle arcs.

Rather than long calculations to establish the relation between the family of double circle arcs and its analogue by geometric inversion, we propose to proceed geometrically. From paragraph 4.2.2, we already know that the ring of detectors $D_k, k \in \{1, K\}$ is converted to an apparent horizontal line of detectors $D'_k, k \in \{1, K\}$. Moreover, each arc $\mathcal{A}_i$ of a given double circle arc is converted into a half-line $\mathcal{H}_i$ having a common end-point, the considered apparent detector $D'_k$. The union of both $\mathcal{H}_1$ and $\mathcal{H}_2$ gives a V-line, denoted $\mathcal{V}$. More generally, the family of double circle arcs under study is converted into a set of pivoting V-lines of axes the line passing through $S$, the considered detector $D_k$ and its apparent position $D'_k$ after geometric inversion and of half-opening angle $\omega$. See figure 6.1.
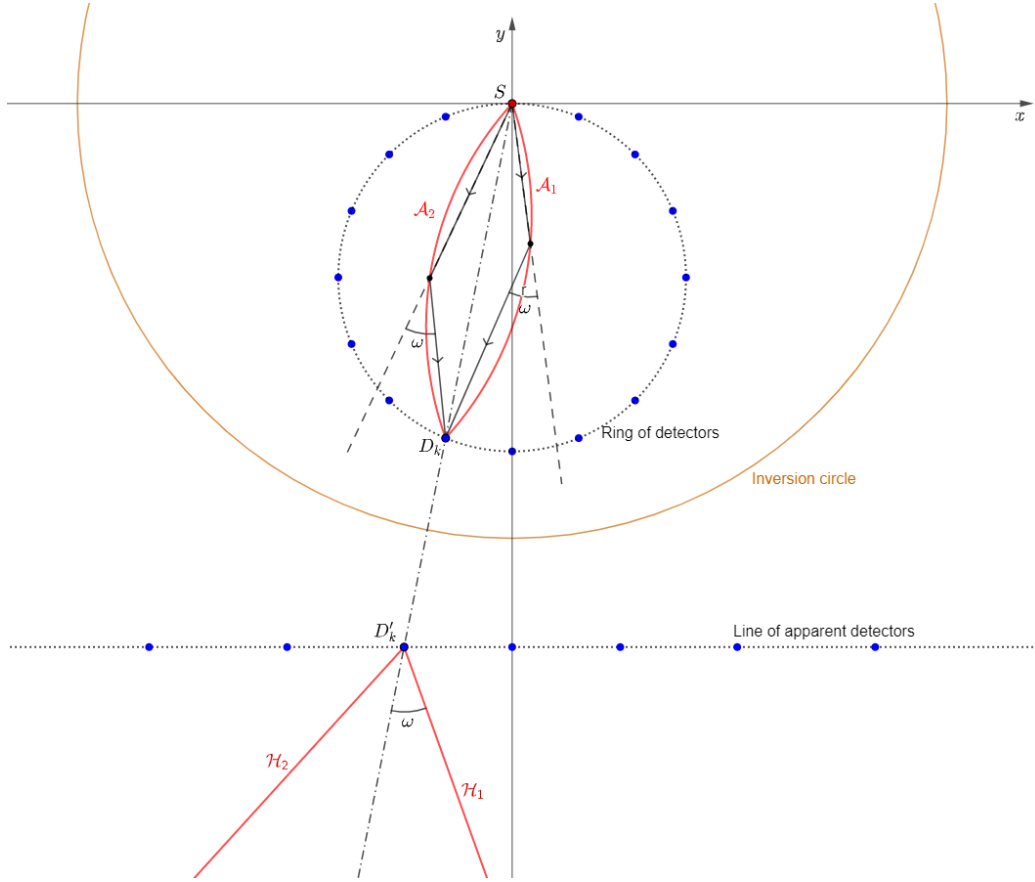
**Figure 6.1** − Example of obtained V-lines by geometric inversion of an arbitrary set of double circle arc. The colour code is the same as that used in the figure 4.1.

### 6.1.2 Introduction of a degree of freedom for this family of V-lines and the corresponding Radon transform

We assume now that the family of V-line where the line containing the vertices is no longer fixed and study the corresponding Radon transform. This line can translate in the space.

For the purposes of the following calculations, the equation of the family of V-lines is given in Cartesian coordinates:

$$
\begin{aligned}
\mathcal{V}(\omega, \theta_{D_k}, a) = (&\mathcal{H}_1(a, \theta_{D_k}, \omega) \cup \mathcal{H}_2(a, \theta_{D_k}, \omega)) \\
= &\left\{ \left( \frac{a}{\tan \theta_{D_k}} + r \cos(\varphi + \omega), a + r \sin(\theta_{D_k} + \omega) \right), \right. \\
&\left. \left( \frac{a}{\tan \theta_{D_k}} + r \cos(\theta_{D_k} - \omega), a + r \sin(\theta_{D_k} - \omega) \right), r \in \mathbb{R}^+ \right\}, \quad (6.1)
\end{aligned}
$$

where, as a reminder, $a = q^2/P$ and $q$ the inversion parameter. We define the associated Radon transform on $\mathcal{V}$:

**Definition 6.1.1.** *Let $f$ be an unknown function, non-negative, continuous and compactly supported. The Radon transform on V-lines of the function $f$ $\mathcal{R}_{\mathcal{A}_1 \cup \mathcal{A}_2} f$ maps $f$ into the set of its integrals over the family of V-lines $\mathcal{V}$ as*

$$
\mathcal{R}_{\mathcal{V}} f(\omega, \theta_{D_k}, a) = \int_0^\infty dr f\left(\left(\frac{a}{\tan \theta_{D_k}}, a\right) + r(\cos(\theta_{D_k} - \omega), \sin(\theta_{D_k} - \omega))\right) +
$$
$$
\int_0^\infty dr f\left(\left(\frac{a}{\tan \theta_{D_k}}, a\right) + r(\cos(\theta_{D_k} + \omega), \sin(\theta_{D_k} + \omega))\right). \quad (6.2)
$$

In the next paragraph, we derive the analytical inversion of this Radon transform.

### 6.1.3   Analytical inversion of $\mathcal{R}_{\mathcal{V}}$

**Proposition 6.1.1.** *Denoting*

$$
\mathcal{G} f(\theta_{D_k}, a) = \int_0^\pi \mathcal{R}_{\mathcal{V}} f(\omega, \theta_{D_k}, a) d\omega, \quad (6.3)
$$

*the unknown function $f$ is related to its projections $\mathcal{G} f$ by*

$$
f(x, y) = \frac{1}{2\pi} \mathcal{F}_2^{-1}\left(\sqrt{k_x^2 + k_y^2} \cdot \mathcal{F}_2(\mathcal{G} f(\rho, \phi))(k_x, k_y)\right)(x, y). \quad (6.4)
$$

*where $\mathcal{F}_2$ stands for the two-dimensional Fourier transform and $(k_x, k_y)$ are the duals of $(x, y)$.*

*Proof.* From the definitions of the operators $\mathcal{G}$ in (6.3) and $\mathcal{R}_{\mathcal{V}}$ in (6.2), one gets

$$
\mathcal{G} f(\theta_{D_k}, a) = \int_0^\pi \left[\int_0^\infty f\left(\frac{a}{\tan \theta_{D_k}} + r\cos(\theta_{D_k} - \omega), a + \sin(\theta_{D_k} - \omega)\right) dr + \right.
$$
$$
\left. \int_0^\infty f\left(\frac{a}{\tan \theta_{D_k}} + r\cos(\theta_{D_k} + \omega), a + \sin(\theta_{D_k} + \omega)\right) dr\right] d\omega. \quad (6.5)
$$

With the respective change of variables $(\omega' = \theta_{D_k} - \omega)$ and $(\omega' = \theta_{D_k} + \omega)$ in the above first and second integral and exploiting $2\pi$-periodicity of trigonometric functions, it follows that

$$
\mathcal{G} f(\theta_{D_k}, a) = \int_0^{2\pi} \int_0^\infty f\left(\frac{a}{\tan \theta_{D_k}} - r\cos \theta, a - r\sin \theta\right) dr d\theta. \quad (6.6)
$$

As in paragraph 2.2.2 of Chapter 2, we recognize the two-dimensional convolution of the function $f$ with the function $\gamma : (x, y) \longrightarrow (x^2 + y^2)^{-1/2}$, hence

$$
\mathcal{G} f(\theta_{D_k}, a) = \frac{1}{2\pi} (f \star \gamma)\left(\frac{a}{\tan \theta_{D_k}}, a\right), \quad (6.7)
$$

or substituting $\left(\frac{a}{\tan\theta_{D_k}}, a\right)$ by $(x_D, y_D)$, one gets

$$\mathcal{G}f(x_D, y_D) = \frac{1}{2\pi}(f \star \gamma)(x_D, y_D).$$ (6.8)

This relation ensures us the invertibility of the Radon transform and a similar procedure as the one proposed for the rho-filtered layergram algorithm. Finally, one gets (6.4). $\square$

### 6.1.4 Discussions and simulation results

If we go back to CCST, this extra degree of freedom means that the ring of detectors is no longer fixed. In this quest for having an inverse formula, we have lost the main advantage of the CCST.

Furthermore, relation (6.4) is a *deconvolution* formula, that is, we only need information from detectors positioned in a confused manner with the object. Such a type of acquisition is strictly impossible for a modality of Compton Scattering Tomography, since the source and the detectors are, by definition, outside the object.

We performed nevertheless simulations for this Radon transform. These simulations are only meant to illustrate and validate the proposed inverse formula. Consequently, this simulation cannot be put in relation with any possible CST system.

The chosen object was the Shepp-Logan phantom of size $N \times N = 128 \times 128$ pixels (similarly to the simulations performed in the first part of this chapter, see Figure 5.1). The discretization of the image domain for data acquisition is $(1 \times 1)$ pixels. The domain for the angle $\omega$ is $[1, 179]$ degrees, with an angular step of 1 degree. We present first, in figure 6.2, some images of data acquisition for different angle $\omega$ and then the result of the combination of them (that is, $\mathcal{G}f$).

Then, applying the same reconstruction algorithm as for the rho-filtered layergram (see Algorithm 2.2), we obtained the reconstruction result presented in Figure 6.3. The obtained reconstruction is globally blurred, with a difference of contrast between the top, the centre and the bottom of the image. Nevertheless, the little nodules of the Shepp-Logan phantom are quite well visible on the reconstruction. Moreover, we find, as on the reconstruction obtained in Chapter 5, blurred areas on the top and the bottom of the object. This may suggest that the real areas where there is a lack of information for the CCST are in these locations.
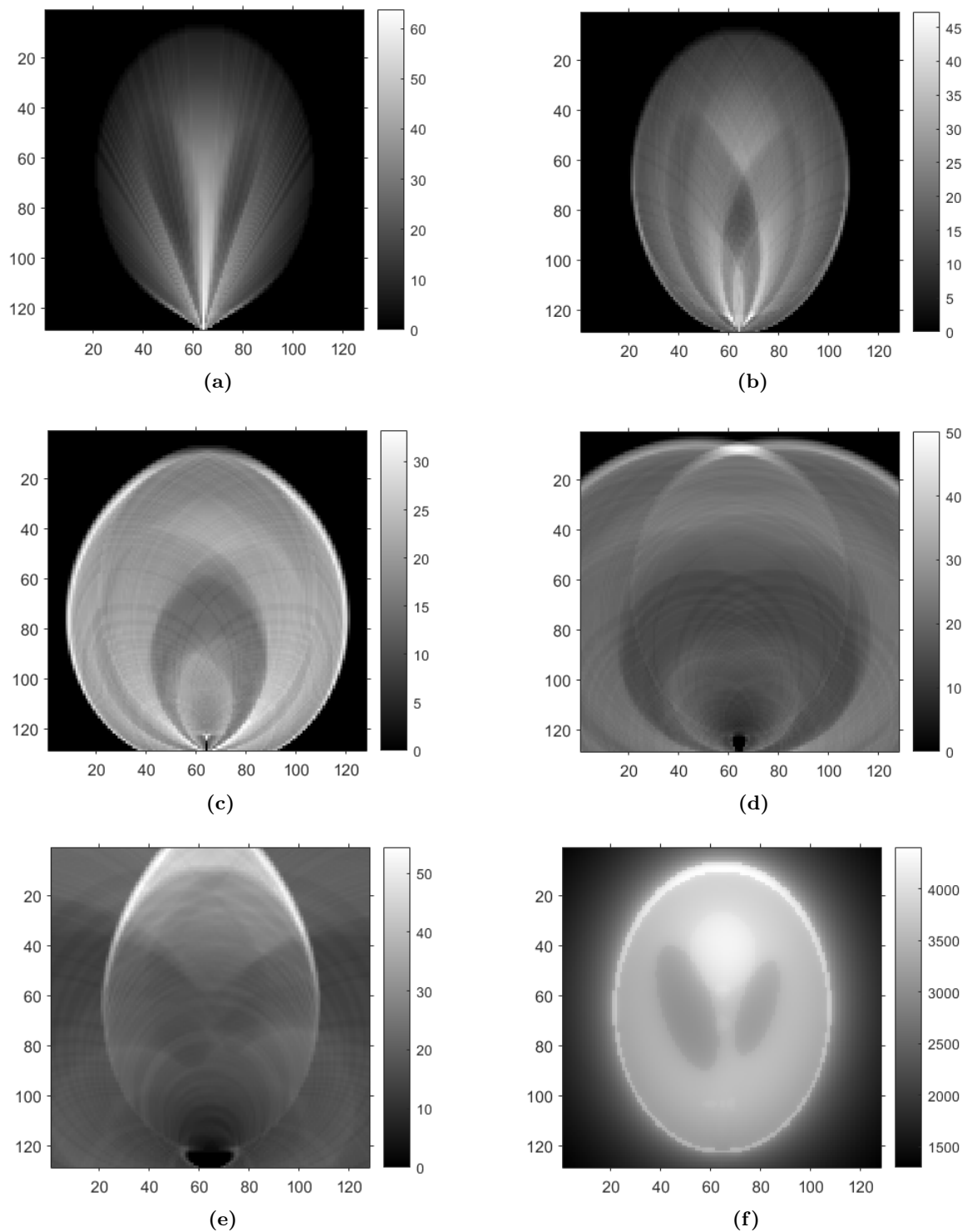
**Figure 6.2** – Examples of acquired data on V-lines $\mathcal{R}_\mathcal{V} f(x_D, y_D, \omega)$ when $\omega =$ (a) 0, (b) $\pi/5$, (c) $2\pi/5$, (d) $3\pi/5$, (e) $4\pi/5$. The sum of all of these images on the whole domain of $\omega$ gives $\mathcal{G} f(x_D, y_D)$ (f).
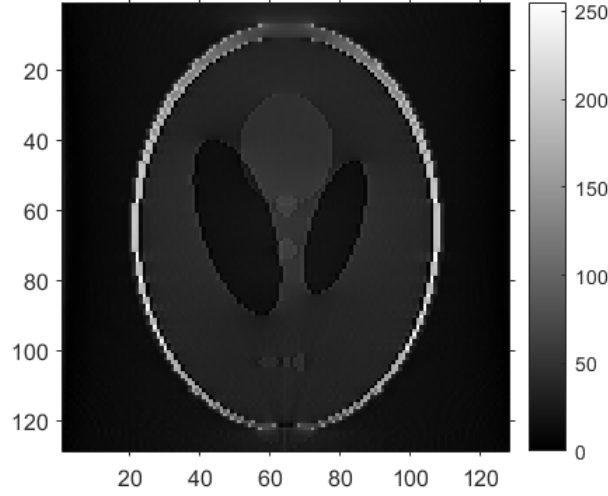
**Figure 6.3** – Reconstruction result from acquired data on the considered family of V-lines

## 6.2 Extension of the latter result in three dimensions: from V-lines to cones

The objective of this part is to establish an analytical inversion of the Radon transform on a special family of cones, obtained by extension of the previous family of V-lines in three dimensions. The family of cones under study is a family of pivoting cones whose axis is passing through the origin of the coordinate system and of opening angle the scattering angle $\omega$. We propose a parametrization for them in the next paragraph.

### 6.2.1 Parametrization of the family of pivoting cones under study

The vertex position of the cones[1] is noted in spherical coordinates $(b, \varphi, \theta) \in \mathbb{R} \times ]-\pi/2, \pi/2[ \times [0, 2\pi[$. We obtain then equation

$$\mathcal{C}(b, \varphi, \theta, \omega) = -b \left( \tan(\varphi)\, \boldsymbol{u}(\theta) \quad 1 \right)^t + r \left\{ \boldsymbol{\beta} \in \mathbb{S}_2 | \boldsymbol{v}(\varphi, \theta) \star \boldsymbol{\beta} = \cos \omega \right\}, \qquad (6.9)$$

the parametric equation of the surface of the cone of vertex position $(b, \varphi, \theta)$ and half-opening angle $\omega$ where $\boldsymbol{u}(\theta) = \left( \sin \theta \quad \cos \theta \right)^t$ and $\boldsymbol{v}(\varphi, \theta) = - \left( \boldsymbol{u}(\theta) \sin \varphi \quad \cos \varphi \right)^t$. $\star$ refers to the inner product. We can now define explicitly the associated Radon transform $\mathcal{R}_{\mathcal{C}}$.

**Definition 6.2.1** (The Radon transform on the family of cones $\mathcal{C}$). *Let $f$ be an unknown function, non negative, continuous and compactly supported in $\mathbb{R}^3$. The Radon transform*

---

[1]The vertex position is exactly the position of the considered *apparent* detectors. For the sake of readability, we note the position of detectors $(b, \varphi, \theta)$ instead of $(b_{D_k}, \varphi_{D_k}, \theta_{D_k})$ during this demonstration.

*denoted $\mathcal{R}_\mathcal{C}$ which maps $f$ into the set of its integrals over the family of pivoting cones $\mathcal{C}$ is*

$$\mathcal{R}_\mathcal{C} f(b, \varphi, \theta, \omega) = \sin \omega \int_{\mathcal{S}_2} dS(\boldsymbol{\beta}) \int_0^\infty dr\, r\, f(-b(\tan \varphi\, \boldsymbol{u}(\theta), 1) + r\boldsymbol{\beta})\, \delta(\boldsymbol{v}(\varphi, \theta) \star \boldsymbol{\beta} - \cos \omega). \tag{6.10}$$

### 6.2.2 Derivation of the analytic inversion formula

The proposed procedure for inversion is presented in the two next propositions. We follow first the scheme previously proposed in [79] where a relation is made between the conical Radon transform under study and the well known three-dimensional Radon transform, denoted $\mathcal{R}$, where

$$\mathcal{R}f(\boldsymbol{\beta}, s) = \int_{\boldsymbol{\beta}^\perp} f(s\boldsymbol{\beta} + \boldsymbol{y}) dS(\boldsymbol{y}), \tag{6.11}$$

with $(\boldsymbol{\beta}, s) \in (\mathbb{S}^2, \mathbb{R})$ (see Proposition 6.2.1). With $\boldsymbol{\beta} = \left( \sin \varphi \sin \theta \quad \sin \varphi \cos \theta \quad \cos \varphi \right)^t$, the inversion formula of the three-dimensional Radon transform is

$$f(\boldsymbol{x}) = \frac{1}{4\pi^2} \int_0^{2\pi} d\theta \int_0^\pi d\varphi \left. \frac{\partial^2 \mathcal{R}f(\boldsymbol{\beta}, s)}{\partial s^2} \right|_{s = \boldsymbol{x} \cdot \boldsymbol{\beta}} \sin \varphi. \tag{6.12}$$

During this procedure, we need also the Hilbert transform denoted $\mathcal{H}$, defined as

$$\mathcal{H}g(s) = \frac{1}{\pi} \text{p.v.} \int_{\mathbb{R}} \frac{g(t)}{s - t} dt, \tag{6.13}$$

with $(\omega, s) \in (\mathbb{S}^2, \mathbb{R})$ and p.v. stands for the Cauchy principal value. This relation ensures us the invertibility of $\mathcal{R}_\mathcal{C}$. We then establish an explicit inversion formula for $\mathcal{R}_\mathcal{C}$ the Proposition 6.2.2 following a trick suggested previously in [71].

**Proposition 6.2.1** (Relation between $\mathcal{R}_\mathcal{C}$ and $\mathcal{R}$)**.** *Let $f$ be compactly supported in $\mathbb{R}^3$. For $(b, \varphi, \theta) \in \mathbb{R} \times \, ]-\pi/2, \pi/2[ \, \times [0, 2\pi[$, one gets*

$$\mathcal{H}\mathcal{R}f\left( \boldsymbol{v}(\varphi, \theta), \frac{b}{\cos \varphi} \right) = \frac{1}{\pi} p.v. \int_0^\pi d\omega \, \frac{\mathcal{R}_\mathcal{C} f(b, \varphi, \theta, \omega)}{\cos \omega}. \tag{6.14}$$

*Here $\mathcal{H}$ acts on the second variable.*

*Proof.* From

$$\text{p.v.} \int_0^\pi d\omega \, \frac{\mathcal{R}_\mathcal{C} f(b, \varphi, \theta, \omega)}{\cos \omega}$$

$$= -\text{p.v.} \int_0^\pi \frac{d(\cos \omega)}{\cos \omega} \int_{\mathcal{S}_2} dS(\boldsymbol{\beta}) \cdot \tag{6.15}$$

$$\int_0^\infty dr \, r \, f(-b(\tan \varphi \, \boldsymbol{u}(\theta), 1) + r\boldsymbol{\beta}) \, \delta(\boldsymbol{v}(\varphi, \theta) \star \boldsymbol{\beta} - \cos \omega) \tag{6.16}$$

$$= -\text{p.v.} \int_{\mathcal{S}_2} dS(\boldsymbol{\beta}) \int_0^\infty dr \, r \, f(-(b\tan \varphi \, \boldsymbol{u}(\theta), b) + r\boldsymbol{\beta}) \, (u(\varphi, \theta) \star \boldsymbol{\beta})^{-1}, \tag{6.17}$$

the desired expression is obtained after multiple change of variables carried out in the following order, first $\boldsymbol{x} \longleftarrow r\boldsymbol{\beta}$,

$$\text{p.v.} \int_0^\pi d\omega \, \frac{\mathcal{R}_\mathcal{C} f(b, \varphi, \theta, \omega)}{\cos \omega} = -\text{p.v.} \int_{\mathbb{R}^3} d\boldsymbol{x} \, f(-(b\tan \varphi \, \boldsymbol{u}(\theta), b) + \boldsymbol{x}) \, (\boldsymbol{v}(\varphi, \theta) \star \boldsymbol{x})^{-1} \tag{6.18}$$

in a second step $\boldsymbol{x} \longleftarrow \boldsymbol{x} - (b\tan \varphi \, \boldsymbol{u}(\theta), b)$

$$\text{p.v.} \int_0^\pi d\omega \, \frac{\mathcal{R}_\mathcal{C} f(b, \varphi, \theta, \omega)}{\cos \omega} = -\text{p.v.} \int_{\mathbb{R}^3} d\boldsymbol{x} \, f(\boldsymbol{x}) \, (\boldsymbol{v}(\varphi, \theta) \star (\boldsymbol{x} + (b\tan \varphi \, \boldsymbol{u}(\theta), b)))^{-1} \tag{6.19}$$

and finally $\boldsymbol{x} \longleftarrow s \cdot \boldsymbol{v}(\varphi, \theta) + \boldsymbol{y}$

$$\text{p.v.} \int_0^\pi d\omega \, \frac{\mathcal{R}_\mathcal{C} f(b, \varphi, \theta, \omega)}{\cos \omega} = -\text{p.v.} \int_\mathbb{R} ds \, \left( s - \frac{b}{\cos \beta} \right)^{-1} \int_{\boldsymbol{v}(\varphi, \theta)^\perp} dy \, f(s \cdot \boldsymbol{v}(\varphi, \theta) + \boldsymbol{y}). \tag{6.20}$$

The $\boldsymbol{y}$-integral is the three-dimensionnal Radon transform of $f$ of parameters $(\boldsymbol{v}(\varphi, \theta), s)$

$$\text{p.v.} \int_0^\pi d\omega \, \frac{\mathcal{R}_\mathcal{C} f(b, \varphi, \theta, \omega)}{\cos \omega} = -\text{p.v.} \int_\mathbb{R} ds \, \mathcal{R} f(\boldsymbol{v}(\varphi, \theta), s) \left( s - \frac{b}{\cos \varphi} \right)^{-1}. \tag{6.21}$$

Using the fact that $f$ is compactly supported in the lower half space of $\mathbb{R}^3$ and from the definition of the Hilbert transform (6.13), ones gets (6.14). $\square$

**Remark 6.2.1.** *The obtained expression (6.14) makes appear a quite simple reconstruction algorithm. In fact, from the data obtained on cones, one can ① go back to the Hilbert transform of the three-dimensional Radon transform via the proposed relation (6.14), ② apply the inverse Hilbert filter and then ③ use the inversion formula of the three-dimensional Radon transform (6.12). This was our first attempt to perform numerical simulations. However, this formula actually hides zeros in denominator, which may make diverge the solution without regularization beforehand. This is also why it is more interesting to have an explicit inversion formula, where it is easier to evaluate potential difficulties.*

Now, we have the following explicit reconstruction formula

**Proposition 6.2.2** (Analytic inversion formula of $\mathcal{R}_\mathcal{C}$). *$f$ is uniquely recovered from its Radon projections $\mathcal{R}_\mathcal{C} f$ with the following expression*

$$f(\boldsymbol{x}) = \frac{1}{4\pi^4} \cdot \int_0^{2\pi} d\theta \int_0^\pi d\varphi \cos^2 \varphi \sin \varphi \cdot$$
$$p.v. \left\{ \int_\mathbb{R} db \frac{1}{(s\cos\varphi - b)} \int_0^\pi d\omega \frac{1}{\cos\omega} \frac{\partial^2 \mathcal{R}_\mathcal{C}(b, \varphi, \theta, \omega)}{\partial b^2} \right\} \Bigg|_{s=\boldsymbol{x}\cdot\boldsymbol{u}(\varphi,\theta)}. \quad (6.22)$$

*Proof.* The inverse Hilbert transform being the opposite of the Hilbert transform, we have

$$\mathcal{R}f(\boldsymbol{u}(\varphi,\theta), s) = -\mathcal{H}\mathcal{H}\mathcal{R}f(\boldsymbol{u}(\varphi,\theta), s) = \frac{-1}{\pi} p.v. \left\{ \int_\mathbb{R} dt \frac{\mathcal{H}\mathcal{R}f(\boldsymbol{u}(\varphi,\theta), t)}{s - t} \right\}. \quad (6.23)$$

With the substitution $t \longleftarrow b/\cos\varphi$ and using expression (6.14), it follows that

$$\mathcal{R}f(\boldsymbol{u}(\varphi,\theta), s) = \frac{1}{\pi^2} p.v. \left\{ \int_\mathbb{R} \frac{db}{s\cos\varphi - b} \int_0^\pi d\omega \frac{\mathcal{R}_\mathcal{C}(b, \varphi, \theta, \omega)}{\cos(\omega)} \right\}. \quad (6.24)$$

Furthermore, taking the second-order derivative relative to the variable $s$ of the above equation (6.24), we have

$$\frac{\partial^2 \mathcal{R}f(\boldsymbol{u}(\varphi,\theta), s)}{\partial s^2} = \frac{1}{\pi^2} p.v. \left\{ \int_\mathbb{R} db \int_0^\pi d\omega \frac{\mathcal{R}_\mathcal{C}(b, \varphi, \theta, \omega) \cos^2\varphi}{\cos\omega} \frac{\partial^2}{\partial b^2} \left( \frac{1}{s\cos\varphi - b} \right) \right\}. \quad (6.25)$$

Then, with an integration by parts on the right side of (6.25),

$$\frac{\partial^2 \mathcal{R}f(\boldsymbol{u}(\varphi,\theta), s)}{\partial s^2} = \frac{1}{\pi^2} p.v. \left\{ \int_\mathbb{R} \frac{db}{s\cos\varphi - b} \int_0^\pi d\omega \frac{\cos^2\varphi}{\cos\omega} \frac{\partial^2 \mathcal{R}_\mathcal{C}(b, \varphi, \theta, \omega)}{\partial b^2} \right\}. \quad (6.26)$$

Finally, using the analytical inversion formula of $\mathcal{R}$ (6.12), we get the desired expression (6.22). $\qquad \square$

**Remark 6.2.2.** *The explicit inversion formula (6.22) makes appear some details that have to be handled carefully. In fact, factors $1/\cos(\omega)$ and $1/(s\cos(\beta) - b)$ have zeros in denominators and the reconstruction formula need to be regularized two times.*

### 6.2.3   Discussions and simulation results

When we analyze the obtained reconstruction formula, we can see also that we need also information when the plane containing the vertices of the scanning cones intersects the object. This makes this formula impossible to use in a practical case, as in two dimensions.

We performed nevertheless simulations, in order to validate the proposed reconstruction formula. Again, as in two dimensions, this simulation cannot be put in relation with any

possible CST system.

As mentioned earlier, the formula (6.22) need to be regularized two times. When we discretized this formula, we introduced consequently two regularization parameters $\xi_1$ and $\xi_2$ in order to replace factors $1/\cos\omega$ and $1/(s\cos\beta - b)$ respectively by

$$\frac{\cos\psi}{\xi_1^2 + \cos^2\psi} \text{ and } \frac{(s\cos\beta - b)}{\xi_2^2 + (s\cos\beta - b)^2}.$$

For numerical simulations, we used a sphere of radius 7 (see Figure 6.4a). The regularization parameters were chosen arbitrarily, performing a random search to find a pair which gives us interesting results. Figure 6.4b shows the obtained result. The contour of the sphere is not defined enough, and the reconstruction suffers from a lack of contrast. There is also a problem with the reconstruction of the details, since the single pixel present on the first and the last cross-sections of the sphere are no longer visible in the reconstruction. Furthermore, from our experiments, we saw that the choice of $\xi_{1,2}$ has an important consequence on reconstruction quality, in particular on the blurred effect which can be observed in the proposed reconstruction. Extra work is needed to optimize the choice of these hyperparameters.

## 6.3 Concluding remarks

This work underlines that there is probably a trade-off between proposing advantageous CST systems (in terms of acquisition time, compactness, etc.) and the possibility of having an analytical inverse formula. Introducing an extra degree of liberty was tempting, however, dealing with an over-determined problem seems to not bring a solution if the objective is to propose a tomographic imaging concept. We hope nevertheless that this inversion formula may have applications elsewhere. Radon transforms on families of cones arise in other type of imaging, like in optical imaging [80] and in Compton camera imaging systems [73, 81, 82, 83, 84].
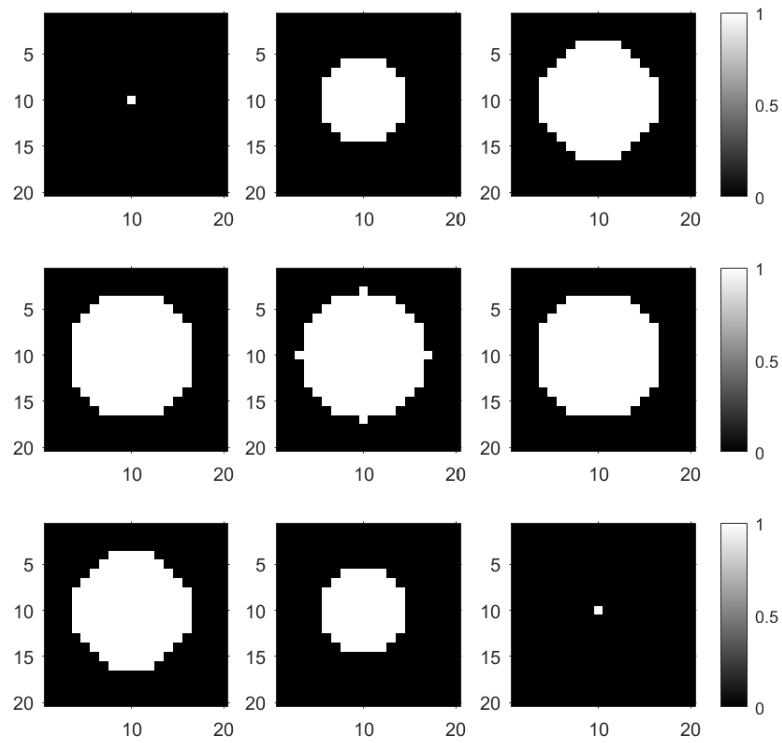
(a)
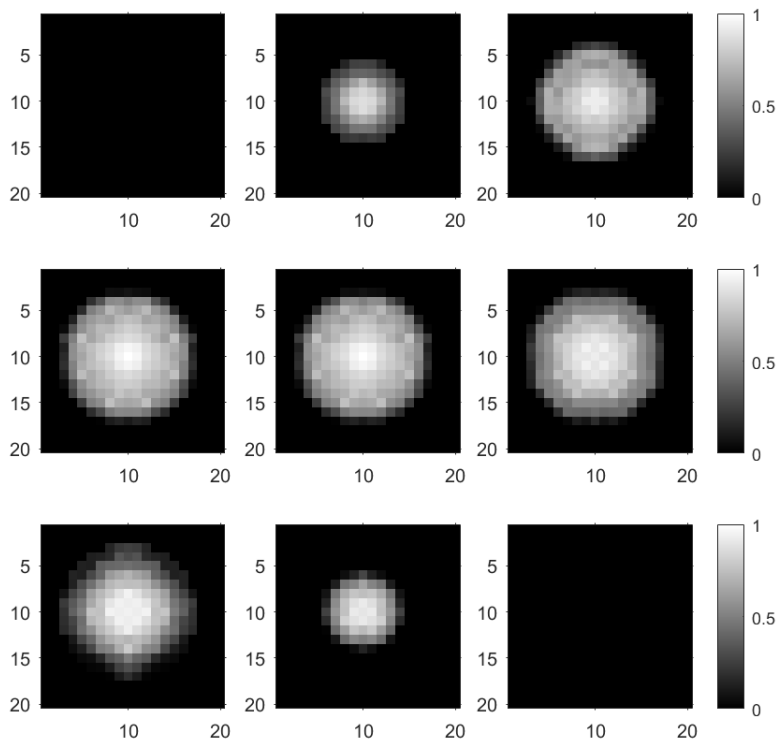


(b)

Figure 6.4 − (a) Original object. (b) Obtained reconstruction from data on the considered family of pivoting cones

# Concluding remarks on Part 2

We presented in this second part of the thesis the main contribution of the thesis, about the proposition of a modality of CST system, called Circular Compton Scattering Tomography. With this fixed setup, we propose a modality which meets two important requirements of biomedical imaging that were previously antagonistic, that is to be able to scan small objects (without missing data) with a fixed system. This feature will involve a reduction of acquisition time and consequently, a decrease of the amount of radiation necessary to perform acquisition.

Furthermore, this configuration, made of a fixed ring of detectors containing the source, extends the scanning possibilities for a CST system. In fact, we show its ability to acquire data from both small and large objects with two possible scanning configurations. Even if, some previous modalities offers also this ability, it is the first time that a modality completely fixed is convenient for both internal and external acquisition processes.

We studied CCST with and without collimation at detectors.

In case of using collimators, the detectors are able to split up photons incoming from the two circle arcs subtending the same scattering angle. In that case, the Radon transform modelling image formation is a Radon transform on circle arcs having a common extremity, the point source. The other end point is located on a circle passing through this fixed point. This circle models the ring of detectors. We proposed two procedures for inversion. The first one uses an inversion formula proposed by Cormack. From this inversion formula, we used the Hilbert transform to obtain a reformulation suitable for a numerical implementation. In fact, we obtained a reconstruction algorithm, which consists in, as for the well-known filtered back projection in conventional tomography, filtering data and then back-projecting them on the appropriated circles. The second proposed procedure for inversion employs geometric inversion, which converts the considered family of circle arcs in a family of half-lines, whose inversion of the corresponding Radon transform is established in this work. We ended up with a reconstruction algorithm, which is also a filtered back-projection algorithm, with two additional steps corresponding to the changes of variables of geometric inversion. The obtained reconstruction results were quite similar in terms of reconstruction quality, even if a slight loss of contrast have to be noticed for the result obtained with the second proposed procedure. Moreover, we noticed that reconstruction results exhibit streak artefacts in the

same location, with deformation of some outer contours. These artefacts are explained by the necessary rearrangement of data, since the reconstruction formula puts in relation polar coordinates of the object with the diameter and the angle relative to the $x$-axis of the scanning circles. In fact, with this rearrangement, circles having an *infinite* diameter has also a part of the information. We have here the first compromise to make for the use of an analytical formula. Moreover, we also considered the possibility of an external scanning providing also simulation results in that case.

We studied then CCST without collimation. This results in the consideration of a Radon transform on double circle arcs, since the detectors are not able from now to split up information coming from a circle arc to the other. We mentioned the difficulty of having an inversion formula for this configuration. In fact, the inversion formula often rests on some symmetrical properties of the considered manifolds, as well as a rotational or translational invariance. Since this considered family of circle arcs has not such properties, we cannot derive an inversion formula using this technique. In absence of inversion formula, we performed simulations via the Tikhonov regularization technique. We obtained completely a different type of artefacts on reconstruction comparatively to those obtained with the filtered back-projection type algorithms. In fact, the streak artefacts have given way to two blurred areas at the top and bottom of the image.

We proposed also to go a step further, considering a more general family of double circle arcs, which includes the one of interest. With this family, the circle containing the second end-point of the scanning circle arcs is no longer fixed. We proved the invertibility of the Radon transform on this extended family of circle arcs. To achieve this result, we proceeded also by geometric inversion and study the Radon transform on the family of V-lines equivalent to the extended family of circle arcs. However, the proposed inversion formula cannot be employed in a practical tomographic imaging scenario, since it only requires information exactly from the location of the objects. In other terms, detectors and objects should be at the same place. This work has been extended in three dimensions and revealed the same issue.

This study highlights the compromises that need to be made when working on CST systems, and in particular on CCST. Having an analytical inversion formula leading to a filtered-back projection type algorithm ensures us a fast, exact and efficient reconstruction result. However, this requires the use of collimators, which is a practical disadvantage for the modality. In fact, such equipment may introduce errors in the processing of incoming photons. Such a reconstruction algorithm introduces also an issue about missing data resulting in artefacts on reconstruction, a problem that does not exist originally. Otherwise, you can consider regularization or other iterative techniques for reconstruction. This type of reconstruction method allows considering the imaging system in a more practical scenario, however, we lose by the way the speed of the reconstruction and introduce hyperparameters that have to be chosen carefully.

The last idea of the work around the CCST modality consisted in introducing an additional degree of liberty in the system. In the process, we lost the major advantage of the CCST of being a fixed system and even if we established inversion formulas, these are not suitable for an imaging scenario.

Finally, the geometry of the CCST system offers undoubtedly more advantages than those previously proposed in the literature. Even if, this advantage is counterbalanced by the fact that it requires either constraining arrangements to be able to have a fast reconstruction algorithm, we showed that the CCST is capable of collecting sufficient set of data, to be able then to perform reconstructions with a good quality, either with reconstructions algorithms issued from an inversion formula or with regularization techniques. Next steps in the study of CCST will concern more practical scenarios, with the consideration of realistic physical effects as well as attenuation.

In the next part of this thesis, we consider two others CST configurations. The idea in the next part is to consider simpler configurations with non-collimated detectors. We will show, that these systems can provide sufficient data for image reconstruction. We will propose, then, fast and efficient reconstruction algorithms.

# Part III

# Other CST modalities studied

In this part, we present two CST configurations only made of a source and an un-collimated detector.

The first modality, of rotational geometry, is presented in Chapter 7. This configuration has been introduced during this thesis.

The second modality, previously introduced by Webber and presented in Chapter 8, has a translational geometry.

In both cases, we established an inversion formula, from which a fast and efficient reconstrution algorithm can be derived.

# 7

# A CST modality with fixed source and rotating detector

**Synopsis** We introduce in this chapter a CST system made of a single detector rotating around a fixed source. Since no collimator is used at detector, the manifold of the associated Radon transform is a family of double circular arcs. The analytic inversion for this Radon transform is achieved through the formulation of the transform in terms of circular harmonic expansion satisfying the consistency conditions in Cormack's sense. We propose also a fast and efficient numerical implementation via an alternative formulation based on Hilbert transform. Simulation results illustrate the theoretical feasibility of the new system.

## 7.1 Presentation of the system

The proposed modality is made of a fixed source $S$, assumed to be monochromatic and a detector $D$ moving on a circle of radius $R$ around the source (see Fig. 7.1), and localized by its angular position $\varphi$. Hence, $D$ can be defined by its Cartesian coordinates as $D(\varphi) = R(\cos\varphi, \sin\varphi)$. The object to scan is placed outside of this circle. In this two-dimensional setup, a plate collimator in the source restricts emitted photons to the plane $(x, y)$. Thus, cross-sections of the object are scanned. In contrast with other two-dimensional CST designs [9, 85, 52, 13], no collimator is required at the detector. This notable feature enables an increase of the amount of acquired data for a given position of the detector and thus a possible reduction in the acquisition time. In this setting, for an angular position $\varphi$ of the detector a scattering angle $\omega$ corresponds to two circular arcs. So, modelling of data acquisition with this collimation-free detector leads to a Radon transform on double circular arcs (DCART). Besides the uncollimated detector, this modality has other material advantages such as not requiring relative movement between the system and the object. In addition, the usage of a circular detector path enables reduction of the system size: with a linear detector, information corresponding to large scanning circles is recorded far from the source while with the proposed geometry photons are always collected at a fixed distance of it.
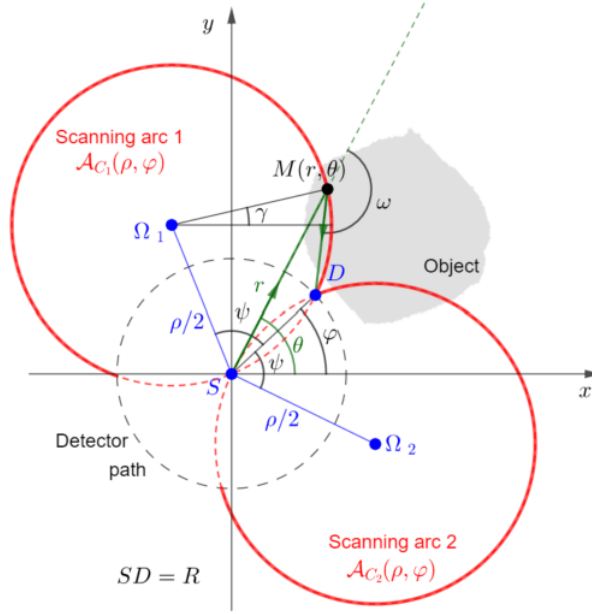
**Figure 7.1** – Setup and parameterization of the new CST modality. Black dotted circle: detector path, Red continuous curves: scanning double arcs, Red dotted curves: portion of circles not used for acquisition

## 7.2   Measurement model of the proposed CST system

Acquisitions using this system are made on a family of double circular arcs $\mathcal{A}_{C_1}$ and $\mathcal{A}_{C_2}$ of centre $\Omega_1$ and $\Omega_2$ whose union is denoted $\mathcal{D}$ in the rest of the paper: $\mathcal{D}(\rho, \varphi) = \mathcal{A}_{C_1}(\rho, \varphi) \cup \mathcal{A}_{C_2}(\rho, \varphi)$. This family of double circular arcs is then defined relatively to $\rho$ the diameter of scanning circles and $\varphi$ the angular position of the detector (see Fig. 7.1). In fact, using $\rho$ or $\omega$ in order to define the family of double circular arcs is equivalent, since they are related by $\rho = R/\sin\omega$, where $\omega \in [\pi/2, \pi[$. Given $\varphi$ the angular position of $D$ and $\omega$ the considered scattering angle, polar equations of $\mathcal{A}_{C_1}$ and $\mathcal{A}_{C_2}$ are defined as

$$\mathcal{A}_{C_m}(\rho, \varphi) : r = \rho \cos\left(\theta - (\varphi - (-1)^m \psi)\right), \ m \in \{1, 2\}, \tag{7.1}$$

where $\theta \in [\varphi, \varphi + 2\omega - \pi]$ for $\mathcal{A}_{\mathcal{C}_1}$, $\theta \in [\varphi - 2\omega + \pi, \varphi]$ for $\mathcal{A}_{\mathcal{C}_2}$ and $\psi = \cos^{-1}(R/\rho)$.

Data measurement using this CST system is modelized by the generalized Radon transform $\mathcal{R}_{\mathcal{D}_1}$ on the family of double circular arcs $\mathcal{D}$ whose definition is: Let $f$ be an unknown function, non negative, continuous and compactly supported outside the disc of radius $R$ centered at the origin. The Radon transform on double circular arcs $\mathcal{R}_{\mathcal{D}_1}$ maps $f$ into the set of its integrals over the family of double circular arcs $\mathcal{D}$ as

$$\mathcal{R}_{\mathcal{D}_1} f(\rho, \varphi) = \int_{\mathcal{D}(\rho, \varphi)} f(r, \theta)\, ds, \tag{7.2}$$

where $ds$ is the elementary arc length measure on the considered double circular arc ($s$ denotes the curvilinear abscissa).

## 7.3 An analytic inversion formula for the DCART

In this section, we derive the main equations of the procedure for inverting the DCART. First, we use a circular harmonic expansion to establish a relation between the components of a function $f$ and $\mathcal{R}_{\mathcal{D}_1} f$. Then, with a similar approach as Cormack's one, we obtain (7.7), which is the inversion formula in circular harmonic expansion. Finally, a closed formulation (7.16), which will be used in numerical simulations, is obtained.

### 7.3.1 Circular harmonic expansion

Functions $f(r, \theta)$ and $\mathcal{R}_{\mathcal{D}_1} f(\rho, \varphi)$ are expanded in terms of Fourier series, where $f_n(r)$ and $(\mathcal{R}_{\mathcal{D}_1} f)_n(\rho)$ are respectively their circular harmonic expansion components

$$f(r, \theta) = \sum_{n=-\infty}^{\infty} f_n(r)\, e^{in\theta}, \tag{7.3}$$

$$(\mathcal{R}_{\mathcal{D}_1} f)(\rho, \varphi) = \sum_{n=-\infty}^{\infty} (\mathcal{R}_{\mathcal{D}_1} f)_n(\rho)\, e^{in\varphi}, \tag{7.4}$$

where

$$f_n(r) = \frac{1}{2\pi} \int_0^{2\pi} f(r, \theta)\, e^{-in\theta}\, d\theta, \tag{7.5}$$

$$(\mathcal{R}_{\mathcal{D}_1} f)_n(\rho) = \frac{1}{2\pi} \int_0^{2\pi} \mathcal{R}_{\mathcal{D}_1} f(\rho, \varphi)\, e^{-in\varphi}\, d\varphi. \tag{7.6}$$

### 7.3.2 Inversion formula in circular harmonics expansion

**Proposition 7.3.1.** *Function $f$ is completely recovered via its circular harmonic expansion $f_n$ from circular expansion of data measurement $(\mathcal{R}_{\mathcal{D}_1} f)_n$ with*

$$f_n(r) = \frac{1}{\pi} \frac{d}{dr} \int_R^r \frac{\cosh\left(n \cosh^{-1}\left(\frac{r}{\rho}\right)\right)}{\rho \sqrt{\left(\frac{r}{\rho}\right)^2 - 1}} \frac{(\mathcal{R}_{\mathcal{D}_1} f)_n(\rho)}{2 \cos\left(n \cos^{-1} \frac{R}{\rho}\right)} d\rho. \tag{7.7}$$

*Proof.* Data projection on double circular arcs $\mathcal{R}_{\mathcal{D}_1} f(\rho, \varphi)$ can be decomposed on two Radon transforms on the families of circular arcs $\mathcal{A}_{\mathcal{C}_1}(\rho, \varphi)$ and $\mathcal{A}_{\mathcal{C}_2}(\rho, \varphi)$. Consequently, we denote $\mathcal{R}_{\mathcal{A}_{\mathcal{C}_1}} f(\rho, \varphi)$ and $\mathcal{R}_{\mathcal{A}_{\mathcal{C}_2}} f(\rho, \varphi)$ the Radon transforms on respectively $\mathcal{A}_{\mathcal{C}_1}(\rho, \varphi)$ and $\mathcal{A}_{\mathcal{C}_2}(\rho, \varphi)$, whose sum gives $\mathcal{R}_{\mathcal{D}_1} f$. On a similar way, $\mathcal{R}_{\mathcal{A}_{\mathcal{C}_1}} f(\rho, \varphi)$ and $\mathcal{R}_{\mathcal{A}_{\mathcal{C}_2}} f(\rho, \varphi)$ can be decomposed in Fourier series to obtain respectively $(\mathcal{R}_{\mathcal{A}_{\mathcal{C}_1}} f)_n$ and $(\mathcal{R}_{\mathcal{A}_{\mathcal{C}_2}} f)_n$. By linearity, we have $(\mathcal{R}_{\mathcal{D}_1} f)_n(\rho) = (\mathcal{R}_{\mathcal{A}_{\mathcal{C}_1}} f)_n(\rho) + (\mathcal{R}_{\mathcal{A}_{\mathcal{C}_2}} f)_n(\rho)$. First step of this demonstration is to make

explicit the circular expansions of $\mathcal{R}_{\mathcal{A}_{\mathcal{C}_m}} f$, $m \in \{1, 2\}$. An interesting property of $\mathcal{A}_{\mathcal{C}_1}$ and $\mathcal{A}_{\mathcal{C}_2}$ is their symmetry about $(\varphi + \psi)$ and $(\varphi - \psi)$ respectively (see Fig. 7.1). This feature allows us to see each $\mathcal{A}_{\mathcal{C}_m}$ as a combination of two equal and symmetric elements of arcs. One of these elements of arc can be rewritten as an angular shift of the other one, hence the following relation for $\mathcal{R}_{\mathcal{A}_{\mathcal{C}_m}} f$

$$\mathcal{R}_{\mathcal{A}_{\mathcal{C}_m}} f(\rho, \varphi) = \sum_{n=-\infty}^{\infty} \int_{\mathcal{A}_{\mathcal{C}_m}^{+}(\rho, \varphi)} f_n(r) \left( e^{in\theta} + e^{in[2(\varphi - (-1)^m \psi) - \theta]} \right) ds_m, \tag{7.8}$$

where $\mathcal{A}_{\mathcal{C}_m}^{+}$ denotes the half part of circular arc $\mathcal{A}_{\mathcal{C}_m}$,
$\theta \geq \varphi - (-1)^m \psi$ and $ds_m$ is the elementary arc length measure on $\mathcal{A}_{\mathcal{C}_m}$.

Observing that

$$e^{in\theta} + e^{in[2 + (\varphi - (-1)^m \psi) - \theta]} = 2 \, e^{in\varphi} \, e^{in\psi} \cos\left[n \left(\theta - (\varphi - (-1)^m \psi)\right)\right], \tag{7.9}$$

and plugging (7.9) into (7.8), one obtains the circular harmonic expansions of $\mathcal{R}_{\mathcal{A}_{\mathcal{C}_1}} f$ and $\mathcal{R}_{\mathcal{A}_{\mathcal{C}_2}} f$

$$\frac{(\mathcal{R}_{\mathcal{A}_{\mathcal{C}_m}} f)_n(\rho)}{2 \, e^{-(-1)^m in\psi}} = \int_{\mathcal{A}_{\mathcal{C}_m}^{+}(\rho, \varphi)} f_n(r) \cos\left[n \left(\theta - (\varphi - (-1)^m \psi)\right)\right] ds_m. \tag{7.10}$$

Straightforward computations show that

$$\theta - \varphi - (-1)^m \psi = \cos^{-1}(r/\rho) \text{ and } ds_m = \left(1 - (r/\rho)^2\right)^{-1/2} dr.$$

Equation (7.10) becomes

$$\frac{(\mathcal{R}_{\mathcal{A}_{\mathcal{C}_m}} f)_n(\rho)}{2 \, e^{-(-1)^m in\psi}} = \int_R^{\rho} f_n(r) \frac{\cos\left(n \cos^{-1}(r/\rho)\right)}{\sqrt{1 - (r/\rho)^2}} dr. \tag{7.11}$$

Hence, from the addition of the expressions in $(\mathcal{R}_{\mathcal{A}_{\mathcal{C}_1}} f)_n$ and $(\mathcal{R}_{\mathcal{A}_{\mathcal{C}_2}} f)_n$ in (7.11), the connection between circular components of $f$ and $\mathcal{R}_{\mathcal{D}_1} f$ can be written

$$\frac{(\mathcal{R}_{\mathcal{D}_1} f)_n(\rho)}{4 \cos(n\psi)} = \int_R^{\rho} f_n(r) \frac{\cos\left(n \cos^{-1}(r/\rho)\right)}{\sqrt{1 - (r/\rho)^2}} dr. \tag{7.12}$$

Then, denoting

$$G_n(\rho) = \frac{(\mathcal{R}_{\mathcal{D}_1} f)_n(\rho)}{2 \cos(n\psi)}, \tag{7.13}$$

and multipliying both sides of (7.12) by

$$\int_R^t \frac{\cosh\left(n\cosh^{-1}\left(t/\rho\right)\right)}{\rho\sqrt{\left(t/\rho\right)^2 - 1}} d\rho,$$

with $t \in \mathbb{R}, t > R$, one gets

$$\frac{1}{2}\int_R^t \frac{\cosh\left(n\cosh^{-1}\left(t/\rho\right)\right)}{\rho\sqrt{\left(t/\rho\right)^2 - 1}} G_n(\rho)d\rho =$$

$$\int_R^t f_n(r) \int_r^t \frac{\cosh\left(n\cosh^{-1}\left(t/\rho\right)\right)}{\rho\sqrt{\left(t/\rho\right)^2 - 1}} \frac{\cos\left(n\cos^{-1}\left(r/\rho\right)\right)}{\sqrt{1 - \left(r/\rho\right)^2}} d\rho dr, \quad (7.14)$$

where the right $\rho$-integral is $\pi/2$ [26]. Then, differentiating with respect to the variable $t$, one gets

$$f_n(t) = \frac{1}{\pi}\frac{d}{dt}\int_R^t \frac{\cosh\left(n\cosh^{-1}\left(t/\rho\right)\right)}{\rho\sqrt{\left(t/\rho\right)^2 - 1}} G_n(\rho)d\rho. \quad (7.15)$$

Going back to coefficients $(\mathcal{R}_{\mathcal{D}_1}f)_n$ and substituting $t$ by $r$, one finds (7.7). □

**Remark 7.3.1.** *Equation* (7.7) *demonstrates explicitly the Cormack's hole theorem: in order to determine $f(r,\theta)$ by its circular harmonic expansion $f_n(r)$, the knowledge of the coefficients $(\mathcal{R}_{\mathcal{D}_1}f)_n(\rho)$ in the annular domain $R < \rho < r$ is sufficient.*

### 7.3.3    A closed formulation of (7.7)

It is also possible to derive a closed formulation for (7.7).

**Proposition 7.3.2.** *Denoting $G(\rho,\varphi)$ the function corresponding to the Fourier series expansion $\sum_{n=-\infty}^{\infty} G_n(\rho)\,e^{in\varphi}$ with $G_n$ as defined in* (7.13), *$f$ can be completely recovered from $G$ as follows*

$$f(r,\theta) = \frac{1}{2\pi^2 r}\int_0^{2\pi} p.v.\left\{\int_R^\infty \frac{\partial G(\rho,\varphi)}{\partial\rho}\frac{\rho}{r - \rho\cos\left(\theta - \varphi\right)}d\rho\right\}d\varphi, \quad (7.16)$$

*where p.v. denotes the Cauchy principal value.*

*Proof.* This result is achieved introducing consistency conditions [27, 10] in terms of Cormack sense. The complete demonstration is proposed in the Appendice C. □

**Remark 7.3.2.** *Equation* (7.16) *can be rewritten using the Hilbert transform and implemented in a more efficient way using standard tools of discrete Fourier analysis, as we are going to show in the next section.*

## 7.4    Numerical inversion

### 7.4.1    Numerical formulation of the forward DCART

A parametrisation in Cartesian coordinates (instead of equations in polar coordinates) is preferable to perform numerical simulations in order to have the same distance between adjacent running points on the considered scanning circle. Hence, a scanning arc $\mathcal{A}_{C_m}$, $m \in \{1, 2\}$ can be seen as the shift of a circle centred at the origin of identical radius, to its center $\Omega_m(x_{\Omega_m}, y_{\Omega_m})$ with a restriction of the domain of the variable $\gamma$ (see Fig. 7.1) :

$$\mathcal{A}_{C_m}(\rho, \varphi) : (x_m(\gamma), y_m(\gamma)) = (x_{\Omega_m}(\rho, \varphi), y_{\Omega_m}(\rho, \varphi)) + \frac{\rho}{2}(\cos\gamma, \sin\gamma), \gamma \in [\gamma_{m_{min}}, \gamma_{m_{max}}]. \tag{7.17}$$

Cartesian parametrization of $\mathcal{A}_{C_m}$ is

$$\mathcal{A}_{C_m}(\rho, \varphi) : (x_m(\gamma), y_m(\gamma)) = \frac{\rho}{2}\left(\cos\left(\varphi - (-1)^m\psi\right) + \cos\gamma, \sin\left(\varphi - (-1)^m\psi\right) + \sin\gamma\right), \tag{7.18}$$

where $\gamma \in [\varphi - \psi, \varphi + 3\psi]$ for $\mathcal{A}_{C_1}$ and $\gamma \in [\varphi - 3\psi, \varphi + \psi]$ for $\mathcal{A}_{C_2}$. Then, the numerical computation of the forward DCART requires a discrete version of it. This process is achieved with a linear interpolation to make coincident the position of the object with the Cartesian parametrization of the double family of circular arcs and an approximation of the integral with a sum according to the equation

$$\mathcal{R}_{\mathcal{D}_1} f(\rho_i, \varphi_j) = \frac{\rho_i}{2}\Delta_\gamma \sum_{\substack{\gamma_k \in [\gamma_{1_{min}}, \gamma_{1_{max}}] \\ \cup [\gamma_{2_{min}}, \gamma_{2_{max}}]}} f\left(x(\gamma_k), y(\gamma_k)\right), \tag{7.19}$$

where $\Delta_\gamma$ is the sampling angular distance of $\gamma$, $\rho_i$ and $\varphi_j$ are the discrete versions of $\rho$ and $\varphi$ respectively : $\rho_i = i(\rho_{max} - R)/N_\rho$, $i = 1, ..., N_\rho$ and $\varphi_j = j \cdot (2\pi/N_\varphi)$, $j = 1, ..., N_\varphi$. Hence, $\mathcal{R}_{\mathcal{D}_1} f(\rho_i, \varphi_j)$ is a $N_\rho \times N_\varphi$ matrix. $\rho_{max}$ refers to the largest diameter of the scanning double circular arcs. Fig. 7.2 shows an example of data measurement for the Shepp-Logan phantom.

### 7.4.2    Reconstruction strategy

For image reconstruction, we use the Hilbert transform, related to the Cauchy principal value as

$$\mathcal{H}\{u\}(t) = \frac{1}{\pi} \text{ p.v.} \left\{\int_{-\infty}^{\infty} \frac{u(\tau)}{t - \tau} d\tau\right\}. \tag{7.20}$$

The Hilbert transform is also computed in the Fourier domain according to (2.9).

(a)    (b)
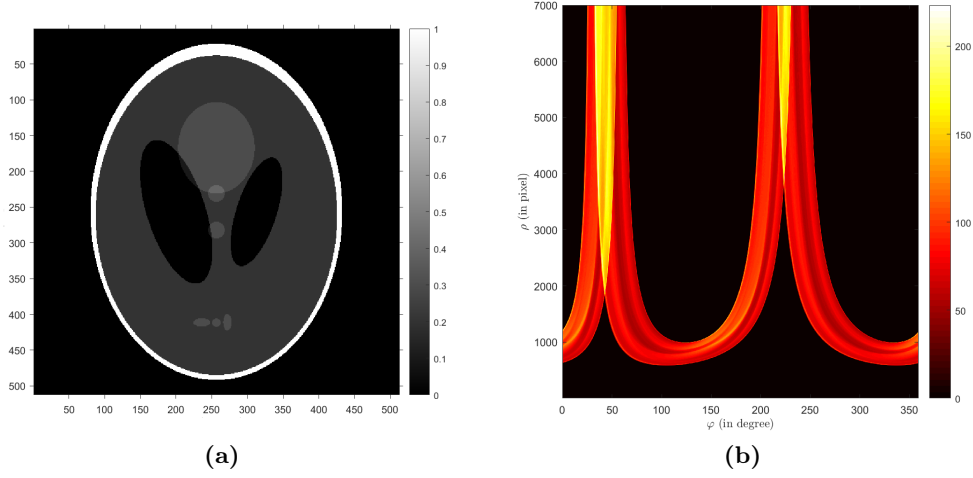
**Figure 7.2** – Left: Object. Right: corresponding DCART for $R = 256$, $\rho_{max} = 7000$, $N_\rho = 6744$ and $N_\varphi = 1609$.

Equation (7.16) of image reconstruction becomes consequently

$$f(r,\theta) = \frac{1}{2\pi r} \cdot \int_0^{2\pi} \frac{1}{\cos(\theta - \varphi)} \mathcal{H} \left\{ \frac{\partial G(\rho, \varphi)}{\partial \rho} \cdot \rho \right\} \left( \frac{r}{\cos(\theta - \varphi)} \right) d\varphi. \qquad (7.21)$$

Finally, using the correspondence between polar coordinates $(r, \theta)$ and Cartesian coordinates $(x, y)$ and $r\cos(\theta - \varphi) = x\cos\varphi + y\sin\varphi$, image reconstruction equation used for simulation is

$$f(x, y) =$$
$$\frac{1}{2\pi} \int_0^{2\pi} \frac{1}{x\cos\varphi + y\sin\varphi} \cdot \mathcal{F}^{-1} \left( -i \cdot \text{sign}(\nu) \mathcal{F} \left( \frac{\partial G(\rho, \varphi)}{\partial \rho} \rho \right) (\nu) \right) \left( \frac{x^2 + y^2}{x\cos\varphi + y\sin\varphi} \right) d\varphi. \qquad (7.22)$$

The projections $G(\rho, \varphi)$ are computed via the circular harmonic components of $\mathcal{R}_{\mathcal{D}_1} f(\rho, \varphi)$ with (7.13). However, zeros in the denominator may be source of instability and regularization may be required. According to [71], we add a regularization parameter $\epsilon$ in (7.13) (equal to 1 in the proposed simulation) in order to compute the circular harmonic components of $G$:

$$G_n(\rho) = \frac{\cos(n\psi)}{\epsilon^2 + \cos(n\psi)^2} \frac{(\mathcal{R}_{\mathcal{D}_1} f)_n(\rho)}{2}. \qquad (7.23)$$

Algorithm 7.1 summarizes the different steps for reconstructing the object from (7.22).

**Algorithm 7.1:** Reconstruction algorithm of the object $f$ from projections on double circle arcs $\mathcal{R}_{\mathcal{D}_1}$

---

**Data:** $\mathcal{R}_{\mathcal{D}_1} f(\rho, \varphi)$, projections on double circular arcs of function $f$

**Result:** $f(x, y)$

1    Compute circular harmonic expansion of $\mathcal{R}_{\mathcal{D}_1} f(\rho, \varphi)$ to compute $G_n(\rho)$ with (7.23) and recompose $G(\rho, \varphi)$.

2    Compute discrete derivation of $G(\rho, \varphi)$ relative to variable $\rho$ and multiply the result by $\rho$.

3    Write the Hilbert transform as a filtering operation in Fourier domain using (2.9).

4    For each $\varphi$, interpolate the data on the considered scanning circles $(x^2 + y^2)/(x \cos \varphi + y \sin \varphi)$ of (7.22).

5    Weight the result using the factor $1/(x \cos \varphi + y \sin \varphi)$.

6    Sum the weighted interpolations on all directions $\varphi$.

7    Weight the result by $\frac{1}{2\pi}$.

---

## 7.5 Experiments and study of the performance of the reconstruction algorithm

### 7.5.1 General parameter choices

We performed simulations on three different phantoms, the Shepp-Logan, the Derenzo (also called Jaszczak) and bars phantoms. These phantoms allow us to evaluate different criteria such as spatial resolution, contrast and the ability of the proposed algorithm to reconstruct singularities tangent to lines with arbitrary slopes. In all proposed simulations, the size of the object was $512 \times 512$ pixels. The detector was moving on a ring of radius $R = 256$ pixels with a constant step of arc length between two adjacent positions. This represents an amount of $N_\varphi = 2\pi R = 1609$ different positions for the detector to collect data. We know the parameter choices should satisfy the condition $N_\rho \times N_\varphi \geq N \times N$ according to [86], where $N_\rho$ is the number of double circular arcs per detector position. To quantitatively asses the quality of reconstructions, we used NMSE $= ||f - f_0||_2^2/N^2$ and NMAE $= ||f - f_0||_1/N^2$ metrics, where $f_0$ and $f$ are the respective original and reconstructed objects and $||.||_1$ and $||.||_2$ refer respectively to the 1 and 2-norm. These results are summed up in Table 7.1.

### 7.5.2 Study of the influence of some general parameters on reconstructions

**Choice of $\rho_{max}$**   First step consists in choosing the maximum diameter for scanning circular arcs $\rho_{max}$. This is equivalent to choosing the maximal scattering angle $\omega_{max}$ since $\omega_{max} = \pi - \arcsin(R/\rho_{max})$. We propose in Fig. 7.4 reconstructions of Derenzo and the

bar phantoms for $\rho_{max} = 3000, 5000$ and $7000$ with a discretization step $\Delta\rho = 1$ length unit. These choices correspond respectively to a maximal scattering angle $\omega_{max} = 175, 177$ and $178$ degrees. A higher $\rho_{max}$ allows to reconstruct the upper right and lower left slopes of straight lines tangent to the ellipses of Shepp-Logan and to the circles of Derenzo and small structures of Shepp-Logan. However, one can observe a visual loss of contrast when $\rho_{max}$ increases, maybe due to numerical approximation. This may explain higher NMSE and NMAE values (see Table 1).



**(a)** Bar phantom          **(b)** Derenzo phantom          **(c)** Shepp-Logan phantom
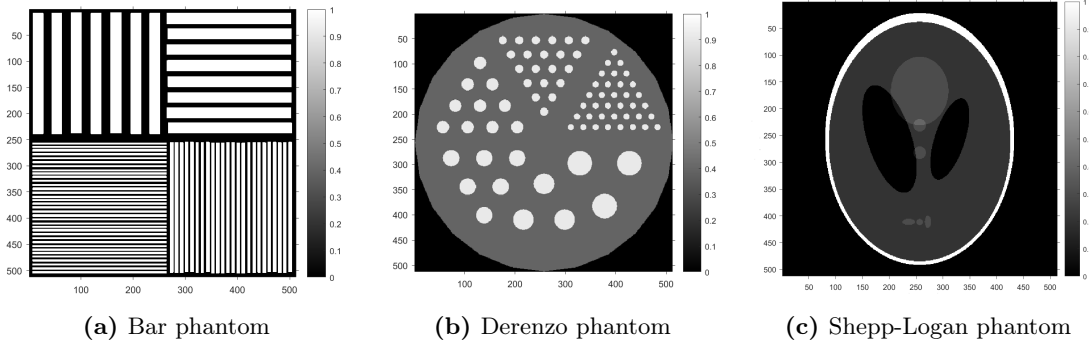
**Figure 7.3** – Original objects used in the following simulations - Objects of size $512 \times 512$ pixels.

**Table 7.1** – NMSE / NMAE of reconstruction results from the fixed source rotating detector CST modality

| phantoms | $\rho_{max}$ (Fig. 7.4) | | | $Q$ (Fig. 7.5) | | | SNR (Fig. 7.6) | | |
|---|---|---|---|---|---|---|---|---|---|
| | 3000 | 5000 | 7000 | 1 | 5 | 10 | 10dB | 15dB | 20dB |
| Bar | 0.1073 | 0.1736 | 0.2769 | 0.2300 | 0.1637 | 0.1320 | 0.3418 | 0.2601 | 0.1942 |
| | / | / | / | / | / | / | / | / | / |
| | 0.2866 | 0.3602 | 0.4362 | 0.4504 | 0.3598 | 0.3190 | 0.4861 | 0.4294 | 0.3783 |
| Derenzo | 0.0163 | 0.0223 | 0.0319 | 0.0257 | 0.0161 | 0.0159 | 0.0761 | 0.0490 | 0.0287 |
| | / | / | / | / | / | / | / | / | / |
| | 0.1019 | 0.1179 | 0.1399 | 0.1258 | 0.0973 | 0.0987 | 0.2235 | 0.1760 | 0.1323 |
| Shepp-Logan | 0.0098 | 0.0098 | 0.0110 | 0.0240 | 0.0121 | 0.0095 | 0.0198 | 0.0140 | 0.0109 |
| | / | / | / | / | / | / | / | / | / |
| | 0.0573 | 0.0618 | 0.0652 | 0.0728 | 0.0575 | 0.0550 | 0.0957 | 0.0763 | 0.0621 |

**Choice of $N_\rho$**   For the rest of the simulations, $\rho_{max}$ is fixed and equal to 5000, which seems to be, a good trade off between contrast and good reconstruction of small structures. The objective is now to evaluate the ratio of required data $N_\rho \times N_\varphi$ relative to the number of pixels to reconstruct $N^2$. We denote $Q$ this ratio : $Q = (N_\rho \times N_\varphi)/N^2$. $Q = 1$ represents the minimal case where $N_\rho = N_{\rho,min} = N^2/N_\varphi = 163$. This means that, for $Q = 1$, 163 values

**(a)** Recons. for $\rho_{max} = 3000$   **(b)** Recons. for $\rho_{max} = 5000$   **(c)** Recons. for $\rho_{max} = 7000$

**(d)** Recons. for $\rho_{max} = 3000$   **(e)** Recons.for $\rho_{max} = 5000$   **(f)** Recons. for $\rho_{max} = 7000$

**(g)** Recons. for $\rho_{max} = 3000$   **(h)** Recons. for $\rho_{max} = 5000$   **(i)** Recons. for $\rho_{max} = 7000$
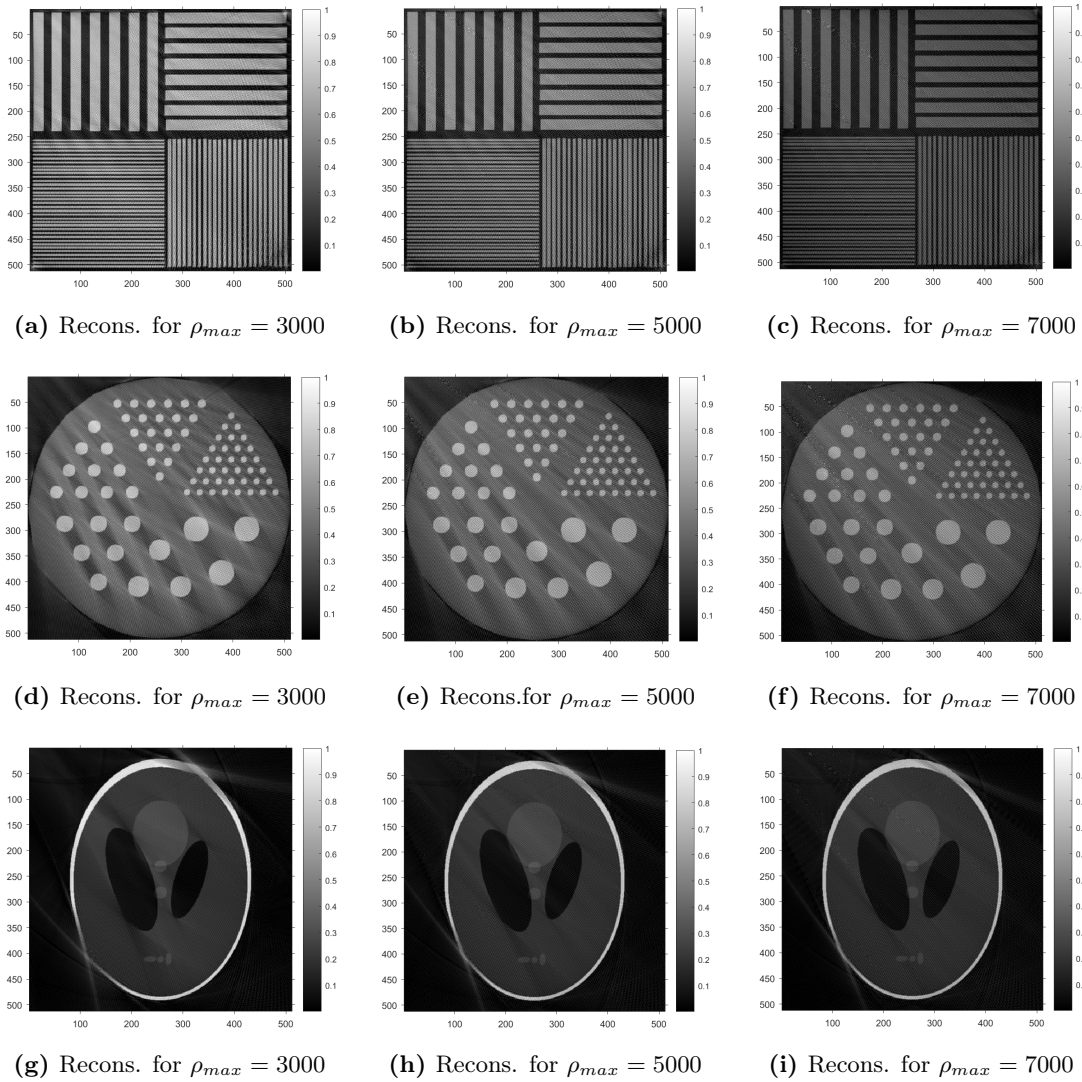
**Figure 7.4** – Reconstruction results of the bar (a), Derenzo (e) and Shepp-Logan (i) phantoms for $\rho_{max} = 3000$ (b,f,j), $\rho_{max} = 5000$ (c,g,k) and $\rho_{max} = 7000$ (d,h,l)

for $\rho$ are chosen uniformely between $R$ and $\rho_{max}$. Then, the other $N_\rho$ are the product of the chosen ratio $Q$ and $N_{\rho,min}$. Figure 7.5 shows the obtained reconstructions for $Q = 1, 5$ and 10. Although the reconstructions appears to be blurred for $Q = 1$, the algorithm already gives a first estimation of the objects to be reconstructed. The *optimal* choice of $Q$ seems to be specific to each object and not directly linked to the proposed algorithm (see Table 1).

**Robustness against noise**   $Q$ is now fixed and equal to 10. We carry out simulations adding to projections a Gaussian noise of signal-to-noise ratios SNR= 10, 15 and 20 dB. Figure 7.6 shows the obtained results for the three phantoms that exhibit grain artifacts for

**(a)** $Q = 1$

**(b)** $Q = 5$

**(c)** $Q = 10$

**(d)** $Q = 1$

**(e)** $Q = 5$

**(f)** $Q = 10$

**(g)** $Q = 1$

**(h)** $Q = 5$

**(i)** $Q = 10$
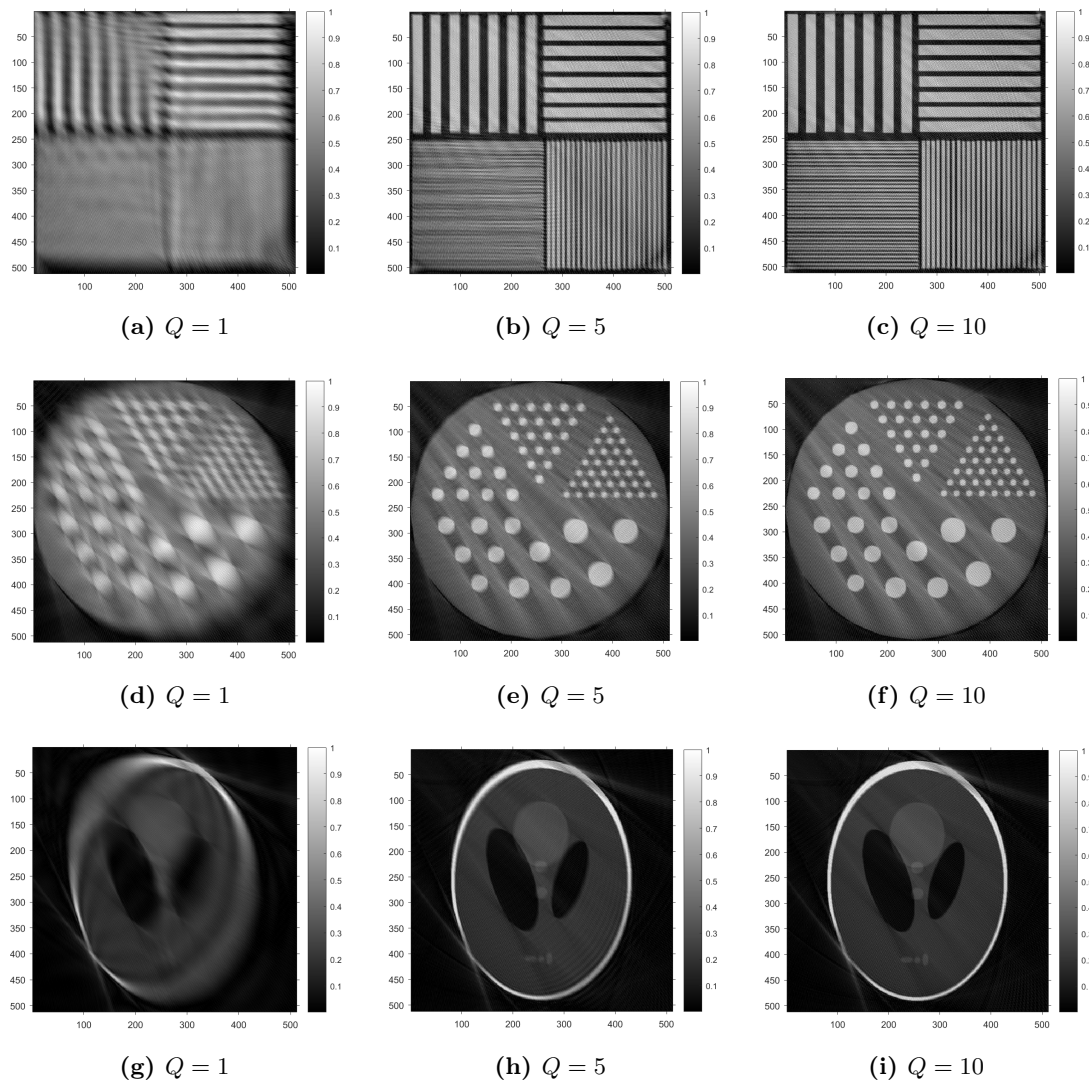
**Figure 7.5** – Reconstruction results of the bar (Fig. 7.3a), Derenzo (Fig. 7.3b) and Shepp-Logan phantoms (Fig. 7.3c) for $Q = 1$ (a, d, g), $Q = 5$ (b, e, h), $Q = 10$ (c, f, i)

the higher levels of noise.

**(a)** SNR = 10 dB    **(b)** SNR = 15 dB    **(c)** SNR = 20 dB

**(d)** SNR = 10 dB    **(e)** SNR = 15 dB    **(f)** SNR = 20 dB

**(g)** SNR = 10 dB    **(h)** SNR = 15 dB    **(i)** SNR = 20 dB
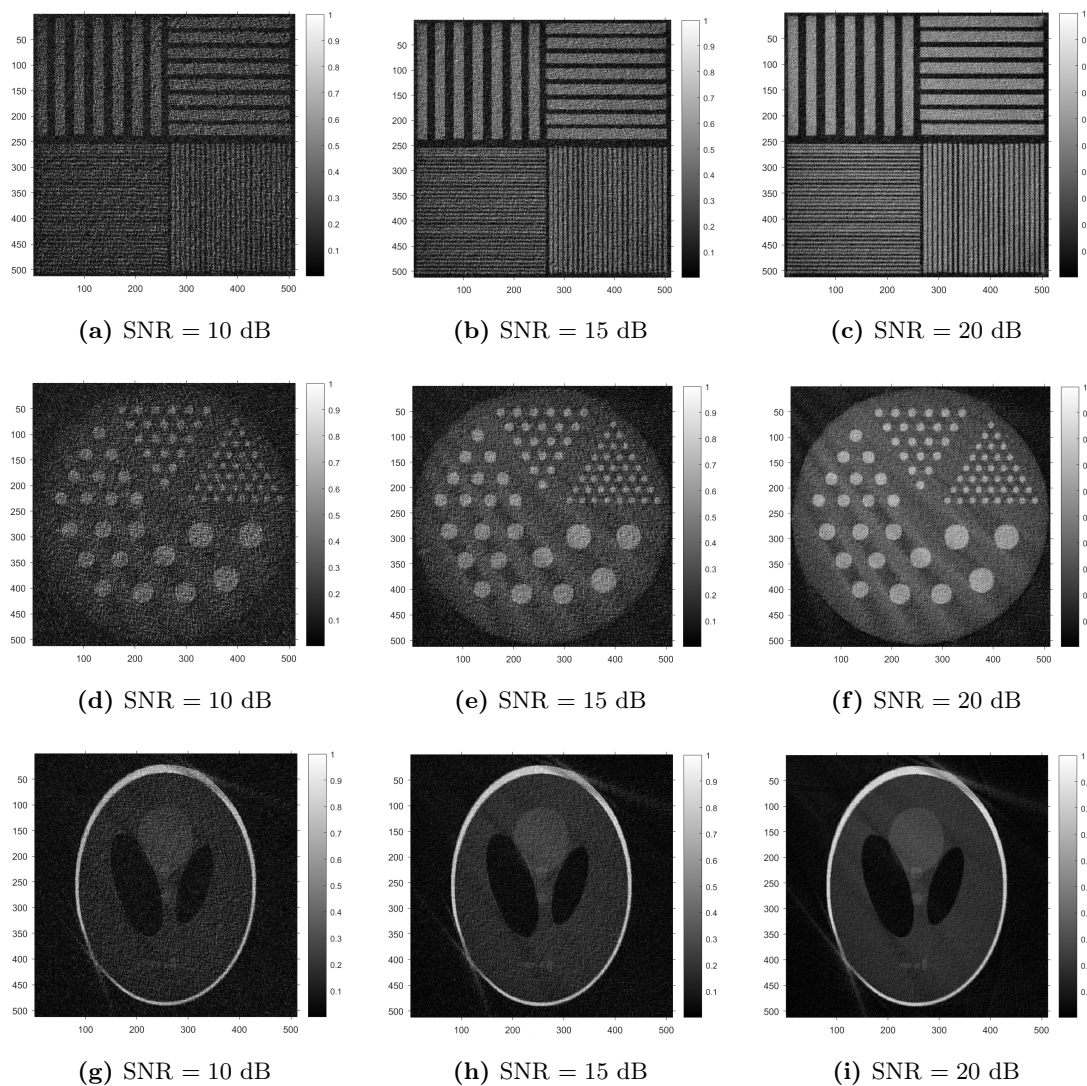
**Figure 7.6** – Reconstruction results of the bar (Fig. 7.3a) Derenzo (Fig. 7.3b) and Shepp-Logan phantoms (Fig. 7.3c) with the addition of a Gaussian noise (SNR = 10 dB (a, d, g), SNR = 15 dB (b, e, h), SNR = 20 dB (c, f, i))

## 7.6   Extension of this modality in three dimensions

We also studied the extensions of this modality in three dimensions. The source is now uncollimated and the detector can move on a sphere (see Figure 7.7).

In this work, we introduced the corresponding Radon transform on toric surfaces and proved its invertibility. The demonstration of this result has led to long mathematical derivations, which will not be discussed in detail in this manuscript. The interested reader can refer to the associated publication, [68]. Instead, after a brief explanation of the setup, we sum up
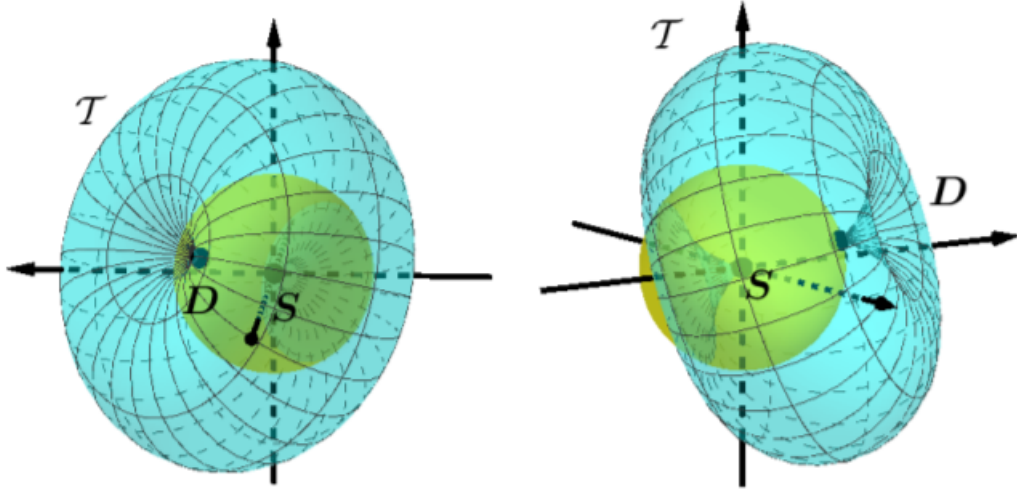
**Figure 7.7** – Two views of the three-dimensional fixed source rotating detector CST modality. The detector $D$ moves on a sphere in yellow. A particular scattering toric surface $\mathcal{T}$ is showed in blue.

the important steps of the proof.

### 7.6.1   Setup

As in two dimensions, the source $S$ is located at the origin of the coordinates. The single detector $D$ moves at a constant distance R of the origin, its path describing thus a sphere. The object under study $f(x, y, z)$ is placed outside this spherical path. When the detector $D$ is at a position labeled by angles $(\alpha, \beta)$ and registers a photon of energy $E(\omega)$, the interaction site is located somewhere on the surface of an apple torus through points $S$ and $D$, which is characterized by $\alpha$, $\beta$ and $\omega$. Thus, the flux of photons of energy $E(\omega)$ registered by $D$ at sites $(\alpha, \beta)$ is proportional to the integral of the function $f$ on a toric surface $\mathcal{T}^{\omega,\alpha,\beta}$, with $\alpha \in [0, 2\pi[$, $\beta \in [0, \pi]$ and $\omega \in ]\pi/2, \pi[$.

Before giving the definition of the Radon transform modeling the forward problem, let us introduce some notation. The coordinates of the detector $D$ are given by

$$D(\alpha, \beta) = R \begin{pmatrix} \cos\alpha\sin\beta & \sin\alpha\sin\beta & \cos\beta \end{pmatrix}^t, \quad \alpha \in [0, 2\pi[, \ \beta \in [0, \pi].$$

We define a parametrization of any torus $\mathcal{T}^{\omega,\alpha,\beta}$ as:

$$\Phi^{\omega,\alpha,\beta}(\gamma, \psi) = r^\omega(\gamma)\Theta^{\alpha,\beta}(\gamma, \psi), \tag{7.24}$$

with $\gamma \in ]0, 2\omega - \pi[$, $\psi \in ]0, 2\pi[$. Here, the radial part is given by

$$r^\omega(\gamma) = R\frac{\sin(\omega - \gamma)}{\sin \omega},$$

while the angular part is expressed as $\Theta^{\alpha,\beta}(\gamma, \psi) = u(\alpha)a(\beta)\Theta(\gamma, \psi)$, where

$$\Theta(\gamma, \psi) = \left(\cos \psi \sin \gamma, \sin \psi \sin \gamma, \cos \gamma\right)^t$$

is a point on $S^2$, the unit sphere in $\mathbb{R}^3$, and

$$u(\alpha) = \begin{pmatrix} \cos \alpha & -\sin \alpha & 0 \\ \sin \alpha & \cos \alpha & 0 \\ 0 & 0 & 1 \end{pmatrix} \text{ and } a(\beta) = \begin{pmatrix} \cos \beta & 0 & \sin \beta \\ 0 & 1 & 0 \\ -\sin \beta & 0 & \cos \beta \end{pmatrix} \tag{7.25}$$

are a rotation of angle $\alpha$ about the $z$-axis and a rotation of angle $\beta$ about the $y$-axis, respectively. Finally, given positive numbers $r_M$, $r_m$ such that $r_M > r_m > R > 0$, we define the spherical shell $S_h(r_m, r_M)$ as

$$S_h(r_m, r_M) = \{(x, y, z) \in \mathbb{R}^3 : r_m \leq \sqrt{x^2 + y^2 + z^2} \leq r_M\}.$$

We are now ready to introduce the toric Radon transform associated to this modality.

**Definition 7.6.1.** *Let $f(x, y, z)$ be a compactly supported function with support contained in $S_h(r_m, r_M)$. We define the toric Radon transform $\mathcal{R}_\mathcal{T} f$ of function $f$ as $\mathcal{R}_\mathcal{T} f(\alpha, \beta, \omega) = \int_{\mathcal{T}^{\omega,\alpha,\beta}} dS_\mathcal{T}\ f(x, y, z)$. Explicitly*

$$\mathcal{R}_\mathcal{T} f(\alpha, \beta, \omega) = \int_0^{2\omega - \pi} d\gamma \int_0^{2\pi} d\psi\ f\left(\Phi^{\omega,\alpha,\beta}(\gamma, \psi)\right) r^\omega(\gamma)\frac{\sin \gamma}{\sin \omega}, \tag{7.26}$$

*where $\omega \in ]\frac{\pi}{2}, \pi[$, $\alpha \in [0, 2\pi[$, $\beta \in [0, \pi]$.*

Equation (7.26) is the forward operator that models the data recorded, this integral transform is rotational invariant. Its manifold is the part of an apple torus through the origin outside the sphere of radius $R$.

### 7.6.2  Invertibility of $\mathcal{R}_{\mathcal{T}}$

**Spherical harmonics expansion**

The first step consists in making explicit the connection between the components of the spherical harmonics expansion of a function $f$ and those of its toric Radon transform $\mathcal{R}_{\mathcal{T}} f$. Spherical harmonics of degree $l$ and order $m$ are defined as:

$$Y_l^m(\gamma, \psi) = (-1)^m \sqrt{\frac{(2l+1)(l-m)!}{4\pi(l+m)!}} P_l^m(\cos \gamma) e^{im\psi}, \tag{7.27}$$

where $\gamma \in [0, \pi]$, $\psi \in [0, 2\pi[$ and $P_l^m(x)$ is the Legendre polynomial of degree $l$ and order $m$, see [87, 88] for details. The set $\{Y_l^m\}$, for $l \in \mathbb{N}$ and $|m| \leq l$ is a complete orthonormal system in $\mathbb{S}^2$. Any function $f \in C^\infty(\mathbb{R}^3)$ can be expanded in terms of $Y_l^m(\gamma, \psi)$ according to

$$f(r\Theta(\gamma, \psi)) = \sum_{l=0}^{\infty} \sum_{|m| \leq l} f_{lm}(r) Y_l^m(\gamma, \psi), \tag{7.28}$$

where

$$f_{lm}(r) = \langle f, Y_l^m \rangle = \int_0^{2\pi} \int_0^{\pi} f(r\Theta(\gamma, \psi)) \overline{Y_l^m(\gamma, \psi)} \sin \gamma \, d\gamma d\psi,$$

and $\langle, \rangle$ is the scalar product in $L^2(S^2)$, the overline denotes complex conjugation, and $r \in \mathbb{R}_0^+$ is fixed.

Following the ideas in [12], the spherical harmonics expansion of $\mathcal{R}_{\mathcal{T}} f$ can be written as

$$\mathcal{R}_{\mathcal{T}} f(\alpha, \beta, \omega) = \sum_{l \in \mathbb{N}} \sum_{|m| \leq l} (\mathcal{R}_{\mathcal{T}} f)_{lm}(\omega) Y_l^m(\alpha, \beta), \tag{7.29}$$

where coefficients $(\mathcal{R}_{\mathcal{T}} f)_{lm}(\omega)$ in the expansion are given by the following lemma.

**Lemma 7.6.1.** *The Fourier coefficients of data $(\mathcal{R}_{\mathcal{T}} f)_{lm}$ in (7.29) and those of the object $f_{lm}$ are related by*

$$(\mathcal{R}_{\mathcal{T}} f)_{lm}(\omega) = 2\pi \int_0^{2\omega - \pi} d\gamma \, r^\omega(\gamma) \frac{\sin \gamma}{\sin \omega} f_{lm}\left(r^\omega(\gamma)\right) P_l^0(\cos \gamma), \tag{7.30}$$

*where $P_l^0(.)$ is the zero order associated Legendre polynomial of degree $l$.*

**An alternative expression for the equation (7.26) in terms of a general Abel type integral equation**

In this second step, we show that (7.30) is a generalized Abel type integral equation with a kernel with zeros on its diagonal. We split up (7.30) in two parts having integration range

$(0, \omega - \frac{\pi}{2})$ and $(\omega - \frac{\pi}{2}, 2\omega - \pi)$, respectively and perform the substitution $\gamma = \omega - \sin^{-1}\left(\frac{r\sin\omega}{R}\right)$ in the first integral and $\gamma = \omega + \sin^{-1}\left(\frac{r\sin\omega}{R}\right) - \pi$ in the second one. After some calculations, making use of the identities $\cos(\sin^{-1} x) = \sqrt{1 - x^2}$ and $P_l^0(-x) = (-1)^l P_l^0(x)$ (see, for example, [89]), we arrive to

$$(\mathcal{R}_{\mathcal{T}}f)_{lm}(\omega) = \int_R^{\frac{R}{\sin\omega}} dr\, f_{lm}(r)\, \frac{1}{\sqrt{\left(\frac{R}{\sin\omega}\right) - r}} \times$$

$$\frac{2\pi}{\sin\omega} \sum_{\sigma = \pm 1} \frac{r\sin\left(\sin^{-1}\left(\frac{r\sin\omega}{R}\right) - \sigma\omega\right)}{\sqrt{\left(\frac{R}{\sin\omega}\right) + r}} (\sigma)^l P_l^0\left(\cos\left(\omega - \sigma\sin^{-1}\left(\frac{r\sin\omega}{R}\right)\right)\right). \quad (7.31)$$

The support of function $f_{lm}(r)$ enables to replace the lower integration limit $R$ by $r_m$. Making the substitution $p = R/\sin\omega$[1] and keeping the notation for readability[2], the integral equation reads:

$$(\mathcal{R}_{\mathcal{T}}f)_{lm}(p) = \int_{r_m}^p dr\, f_{lm}(r)\, \frac{1}{\sqrt{p - r}} K_l(p, r), \quad (7.32)$$

where the kernel is

$$K_l(p, r) =$$

$$\frac{2\pi}{R} \sum_{\sigma = \pm 1} \sigma^l \frac{p\, r\sin\left(\sin^{-1}\left(\frac{r}{p}\right) - \sigma\sin^{-1}\left(\frac{R}{p}\right)\right)}{\sqrt{p + r}} P_l^0\left(\cos\left(\sin^{-1}\left(\frac{R}{p}\right) - \sigma\sin^{-1}\left(\frac{r}{p}\right)\right)\right). \quad (7.33)$$

Equation (7.32) is a generalized Abel type equation. Notice that kernel (7.33) has zeros on the diagonal $p = r$, since the Legendre polynomials have zeros in the interval $[0, 1]$.

**On the invertibility of $\mathcal{R}_{\mathcal{T}}f$**

In [69], Schiefeneder and Haltmeier stated conditions for the uniqueness of the solution of this kind of equations with kernels with zeros on its diagonal. For the sake of completeness, we present their results in the following lemma.

**Lemma 7.6.2** ([69], Theorem 3.4). *Consider the generalized Abel type integral equation*

---

[1]Physically $p$ is the diameter of the circles that generate the torus as a surface of revolution.

[2]Strictly speaking, we should have changed the function after this substitution, for instance $(\mathcal{R}_{\mathcal{T}}f)_{lm}(\sin^{-1} R/p) = \widetilde{(\mathcal{R}_{\mathcal{T}}f)}_{lm}(p)$.

$$\forall t \in [a, b] : g(t) = \int_a^t ds\, f(s) \frac{1}{\sqrt{t - s}} K(t, s) \tag{7.34}$$

*where $g \in C([a, b])$ and $K \in C(\triangle(a, b))$, with $\triangle(a, b) := \{a \le s \le t \le b\}$, is a continuous kernel having zeros on the diagonal. Suppose $K : \triangle(a, b) \to \mathbb{R}$, where $a < b$, satisfies the following assumptions:*

1. *$K \in C^3(\triangle(a, b))$.*

2. *$N_K := \{s \in [a, b) | K(s, s) = 0\}$ is finite and consists of simple roots.*

3. *For every $s \in N_K$, the gradient $(\kappa_1, \kappa_2) = \nabla K(s, s)$ satisfies*

$$1 + \frac{1}{2} \frac{\kappa_1}{\kappa_1 + \kappa_2} > 0.$$

*Then, for any $g \in C([a, b])$, equation (7.34) has at most one solution $f \in C([a, b])$.*

We are now ready to introduce our claim.

**Theorem 7.6.1** (Invertibility of equation (7.32)). *For any $(\mathcal{R}_\mathcal{T} f)_{lm} \in C([r_m, r_M])$, equation (7.32) has at most one solution $f_{lm} \in C([r_m, r_M])$.*

*Proof.* We used lemma 7.6.2, in order to show the uniqueness of the solution of (7.32). The proof consists in checking all assumptions, 1, 2 and 3. Please refer to [68] for details.    □

Finally, the following corollary summarizes our result on uniqueness.

**Corollary 7.6.1** (Invertibility of the $\mathcal{R}_\mathcal{T} f$). *If $f_1$ and $f_2$ are compact supported functions in $C^\infty(S_h(r_m, r_M))$ and $\mathcal{R}_\mathcal{T} f_1 = \mathcal{R}_\mathcal{T} f_2$, then $f_1 = f_2$.*

*Proof.* Let $f$ satisfy $(\mathcal{R}_\mathcal{T} f)_{lm} = 0$ for all $l, m$ in the spherical harmonics expansion. According to Theorem 7.6.1, there is a unique solution $f_{lm} = 0$, which implies $f = 0$. The linearity of $\mathcal{R}_\mathcal{T} f$ yields the claim.    □

### 7.6.3   Numerical simulations

After the derivation of an alternative formula for the forward Radon transform suitable for numerical simulations, we use a discrete spherical harmonics expansion of the functions representing the data and the object. We employ then a product integration approach to model the discrete problem in the spherical harmonic domain. Finally, Tikhonov regularization is used to solve a set of normal equations. The next paragraphs give some details about these different steps.

**An alternative forward model**

An alternative definition of our toric Radon transform useful in numerical simulation is

$$\mathcal{R}_\mathcal{T} f(p, \alpha, \beta) = p^2 \int_0^\pi d\gamma \int_0^{2\pi} d\psi \cos\left(\gamma - \cos^{-1}\frac{R}{p}\right) \sin\gamma f\left(\Phi^{p,\alpha,\beta}(\gamma, \psi)\right), \qquad (7.35)$$

where $p \in (R, +\infty)$ is the diameter of the circles making the torus and

$$\Phi^{p,\alpha,\beta}(\gamma, \psi) = r\Theta^{\alpha,\beta}(\gamma, \psi)|_{r = p\cos(\gamma - \cos^{-1}\frac{R}{p})} \qquad (7.36)$$

is the parametrization of the toric surface labeled by variables $(p, \alpha, \beta)$. The unit vector $\Theta^{\alpha,\beta}(\gamma, \psi)$ was introduced in the definition (7.24). The scattering angle $\omega$ and the diameter $p$ are related through $p = R/\sin\omega$.

**The algebraic problem**

We use a discrete spherical harmonics expansion of order $N$ to write the problem as an algebraic product suitable for Tikhonov regularization. This is achieved using numerical algorithms for the Discrete-Inverse Spherical Harmonics transform (DSHT-IDSHT), see an outline in Appendix B of [68], with data as well as with the sought function according to equations (7.37) and (7.38). The code is also available on GitHub [90].

The pair DSHT-IDSHT allows us to write the problem in the domain of the spherical harmonics according to

$$\mathbf{g}_{nk}^j \underset{\text{IDSHT}}{\overset{\text{DSHT}}{\rightleftarrows}} \mathbf{g}_{lm}^j, \qquad (7.37)$$

$$\mathbf{f}_{nk}^i \underset{\text{IDSHT}}{\overset{\text{DSHT}}{\rightleftarrows}} \mathbf{f}_{lm}^i, \qquad (7.38)$$

where the discrete functions are $\mathbf{g}_{nk}^j = \mathcal{R}_\mathcal{T} f(p_j, \alpha_n, \beta_k)$, $\mathbf{g}_{lm}^j = (\mathcal{R}_\mathcal{T} f)_{lm}(p_j)$ with $j = 0, ..., N_p - 1$, $\mathbf{f}_{nk}^i = f(r_i \cos\psi_n \sin\gamma_k, r_i \sin\psi_n \sin\gamma_k, r_i \cos\gamma_k)$ and $\mathbf{f}_{lm}^i = f_{lm}(r_i)$ with $i = 0, ..., N_r - 1$. Variables $p$ and $r$ are in the range $]R, r_M^*]$ where $r_M^*$ is such that $r_M^* \geq r_M$ to cover the radial support of the function $f$. In this domain, the components of the vector representing the unknown function $\mathbf{f}_{lm}$ are related to components of the vector for the known data $\mathbf{g}_{lm}$ through the equation $\mathbf{g}_{lm} = A_l \mathbf{f}_{lm}$ that is an algebraic relative of equation (7.32). We are aimed to solve the equation for each combination $l, m$.

**Matrix generation**

The matrix $A_l \in \mathbb{R}^{N_p \times N_r}$ is the key for solving the numerical inverse problem. Given that we use an expansion of order $N$ and the kernel in (7.32) is $l$-dependent and $m$-independent,

there are only $N + 1$ different matrices. Adopting the convention $Np = Nr = M$ and splitting up the integration range in equation (7.32), we rewrite

$$(\mathcal{R}_\mathcal{T} f)_{lm}(p_j) = \sum_{q=1}^{j} \int_{r_{q-1}}^{r_q} dr\, f_{lm}(r) \frac{r}{\sqrt{p_j^2 - r^2}} \tilde{K}_l(p_j, r), \tag{7.39}$$

where $r_q = R + q(r_M^* - R)/M$ and $\tilde{K}_l(p_j, r) = \sqrt{p_j + r} K_l(p_j, r)/r$. We use product integration [91] but instead of using the mid-point rule we approximate $\tilde{K}_l(p_j, r)$ by its average $\tilde{K}_{lq}(p_j)$ in ten equidistant points in the interval $[r_{q-1}, r_q]$. Thus, the discrete form for the equation is

$$\mathbf{g}_{lm}^j = (\mathcal{R}_\mathcal{T} f)_{lm}(p_j) \simeq \sum_{q=1}^{j} w_{j,q} \tilde{K}_{lq}(p_j) f_{lm}(r_q), \tag{7.40}$$

where the weighting factor has been calculated analytically according to

$$w_{j,q} := \int_{r_{q-1}}^{r_q} dr \frac{r}{\sqrt{p_j^2 - r^2}}, \tag{7.41}$$

with $j, q = 1, ..., M$ and $w_{j,q} = 0$ if $j < q$. Finally, the entries of the lower-triangular matrix in the equation $\mathbf{g}_{lm} = A_l \mathbf{f}_{lm}$ are

$$A_l = \left( w_{j,q} \tilde{K}_{lq}(p_j) \right)_{j,q=1,....M} \in \mathbb{R}^{M \times M}. \tag{7.42}$$

**Overview of the reconstruction algorithm**

The aim is now recovering the vector $\mathbf{f}_{lm}$ from $\mathbf{g}_{lm}$ using the equation $\mathbf{g}_{lm} = A_l \mathbf{f}_{lm}$. When $A_l$ is non-singular and well-conditioned, the problem can be easily solved by forward substitution. Because the kernel has zeros on its diagonal, the matrix $A_l$ may have diagonal entries being zero or close to zero. Thus, solving the system may be ill-conditioned, and regularization methods must be applied. The algorithm is summarized in Table 7.2 and is aimed to solve the matrix problem $\mathbf{g}_{lm} = A_l \mathbf{f}_{lm}$ for $l = 0, ..., N$ and $|m| \leq l$. Tikhonov regularization requires to solve the normal equations

$$(A_l^T A_l + \lambda I)\mathbf{f}_{lm} = A_l^T \mathbf{g}_{lm}, \tag{7.43}$$

where $I$ is the identity matrix and $\lambda$ is a regularization parameter.

---

**Algorithm 7.2:** Used algorithm to carry out reconstructions from the matrix $A_l$.

---

**Data:** Matrix $A_l$ is precalculated according to (7.42).

**Result:** Reconstructed object $\mathbf{f}$

1    Chose a suitable value for $\lambda$ according to signal conditions.

2    Perform DSHT (7.37) to data $\mathbf{g}^j_{nk}$ to obtain $\mathbf{g}^j_{lm}$.

3    For each pair $l, m$ : solve the normal equations in (7.43) and obtain an
     approximation of $\mathbf{f}^i_{lm}$.

4    Perform IDSHT (7.38) to obtain the reconstruction $\mathbf{f}^i_{nk}$.

5    Interpolate to obtain the function $\mathbf{f}$ in discrete Cartesian coordinates.

---

For non-vanishing kernel diagonals, the product integration method is convergent [92]. To the best of our knowledge, there are no reported results on the convergence of product integration with vanishing kernel-diagonals. As suggested in [91], numerical evidence indicate that, for a suitable selection of the regularization parameter, a convergence analysis may be possible.

**Results**

Data was simulated using equation (7.35). A system where the detector moves on a sphere of radius $R = 1/8$ was considered. The object was a $64 \times 64 \times 64$ volume with two balls with different intensities, and different contrasts, gray on black, white on gray, etc. One object has also a defect (crack) in some planes, see figure 7.8. The function was supported in a cube of side $L = 1$ in the first octant with the coordinates $(x_{\min}, y_{\min}, z_{\min}) = (L/64, L/64, R)$. Discretization parameters of data are: $N_\alpha = 513$, $N_\beta = 256$ and $N_p = 512$. The maximal diameter of the circles generating the torus is $r^*_M = 2r_M$ where $[R, r^*_M]$ is the radial support of the cube containing the phantom. Numerical integration is performed in variables $\gamma$ and $\psi$ with $\Delta\psi = 2\pi/N_\psi$ and the variable step $\Delta\gamma = \cos^{-1}(p/R)/N_\gamma$, with $N_\gamma = 256$ and $N_\psi = 256$. Figure 7.9 shows simulated data for different values of angle $\alpha$. The trapezoidal rule was used to perform numerical integration. According to the discretization chosen for data, the order of the spherical harmonics expansion was $N = 256$ ($N_\alpha = 2N + 1$). In order to get more realistic simulations, data $\mathbf{g} = \mathbf{g}^j_{nk}$ were also corrupted with additive Gaussian noise with zero mean. Noise variance was manually adjusted to get several signal-to-noise ratios: SNR= 10, 20 and 30 dB. These SNR correspond to $\epsilon = 29$, 10 and 3% noise levels where $\epsilon = 100||\tilde{\mathbf{g}} - \mathbf{g}||_2/||\mathbf{g}||_2$, and $\tilde{\mathbf{g}}$ is the corrupted data. In order to assess the quality of reconstruction, we used the following measures of error, the Normalized Mean Square Error (%)

$$\text{NMSE} = \frac{100}{N^3} \frac{||\mathbf{f} - \tilde{\mathbf{f}}||_2^2}{\max_i \{\mathbf{f}_i^2\}}, \tag{7.44}$$

and the Normalized Mean Absolute Error (%)
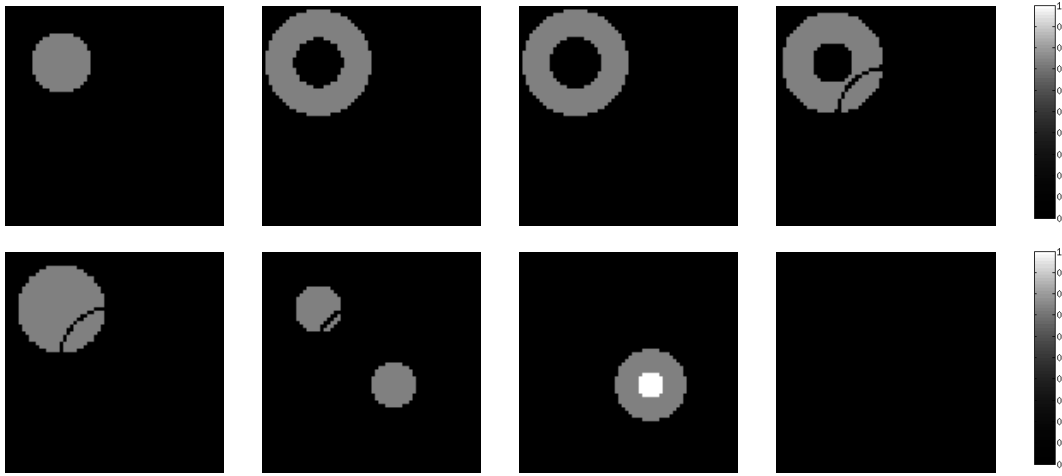
**Figure 7.8** – Original 3D phantom used for simulations. Notice the crack in some planes.

$$\mathrm{NMAE} = \frac{100}{N^3} \frac{||\mathbf{f} - \tilde{\mathbf{f}}||_1}{\max_i \{\mathbf{f}_i\}}, \tag{7.45}$$

where $\mathbf{f}$ is the original image and $\tilde{\mathbf{f}}$ is the reconstruction. We used the algorithm in Table 7.2 to carry out reconstructions for two values of the regularization parameter, $\lambda = 0.01$ (noiseless data) and $\lambda = 0.05$ (noisy). These values were chosen heuristically and are the same for all equations in a set (7.43), i.e. they do not depend on $l, m$. Figure 7.10 shows reconstructions for noiseless data and figures 7.11 to 7.13 show reconstructions from corrupted data. No post-processing was applied to images. The original function as well as reconstructions are shown at planes $z = 4, 14, 15, 22, 26, 31, 38$ and $58$ from top to bottom and from left to right and error metrics are displayed in figure captions. Reconstructions exhibit acceptable quality: structures inside the object are distinguished, shapes are kept and error metrics seem to be reasonable. Moreover, the crack is visible in all the images where its is expected. There are, however, background artifacts and blurring, particularly in upper planes. As expected, stronger regularization is required for noisy data and error metrics get worse with the level of noise. Although Tikhonov regularization performs well, reconstructions can be improved using more advanced regularization techniques. There are algorithms enforcing total variation minimization in the Cartesian domain [93, 94] that can be applied after step 5 in the algorithm 7.2.

From an algorithmic point of view, the reconstruction approach allows to split up the problem in several equations reducing the size of the matrices involved with respect to a standard algebraic treatment. In this framework, computation time may be saved through parallelization since the resulting algebraic equations are independent.

Numerical simulations confirm an additional advantage of this modality: the scanning is
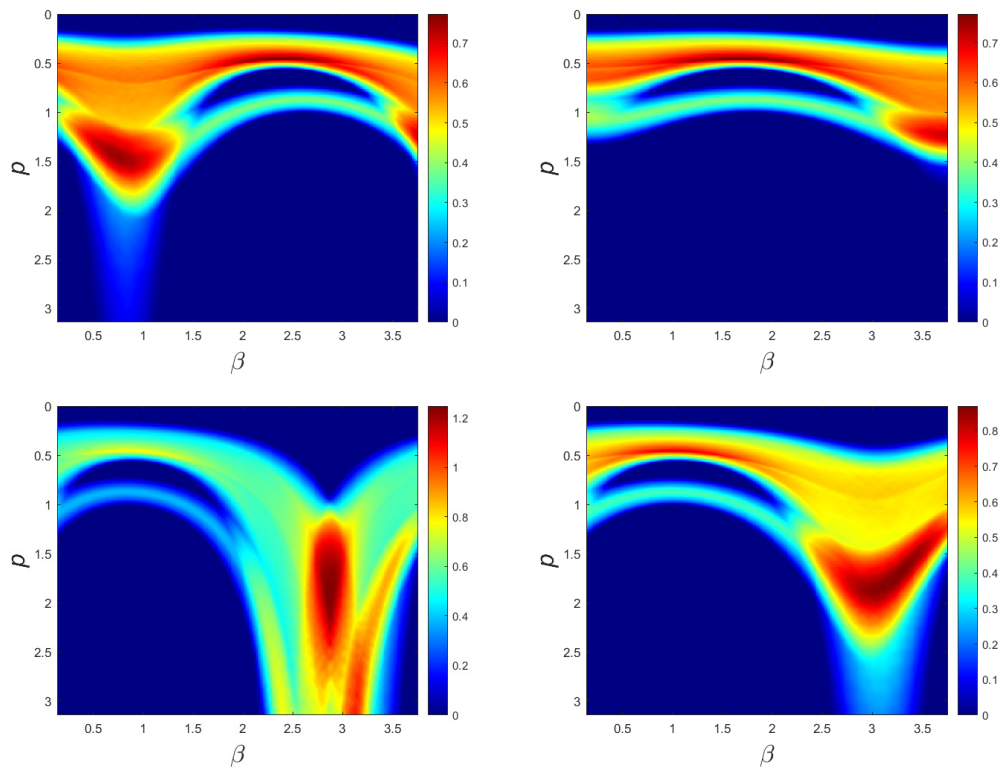
**Figure 7.9** – Data simulated using (7.35). Function $\mathcal{R}_{\mathcal{T}}(p, \alpha, \beta)$ is shown for the sets $\alpha = 0, 3\pi/4, 5\pi/4, 3\pi/2$.
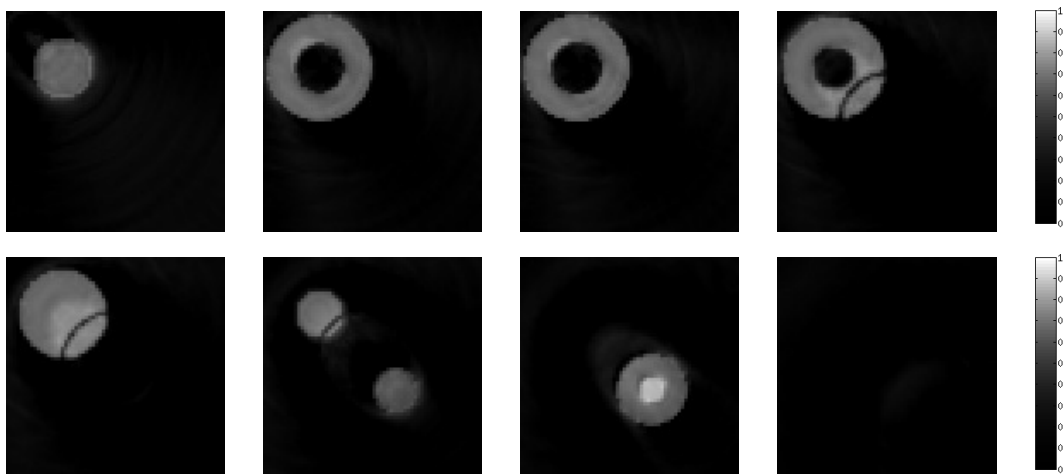


**Figure 7.10** – Reconstructions from noiseless data. Errors are NMSE=0.32 %, NMAE=3.81 %. Regularization parameter $\lambda = 0.01$.
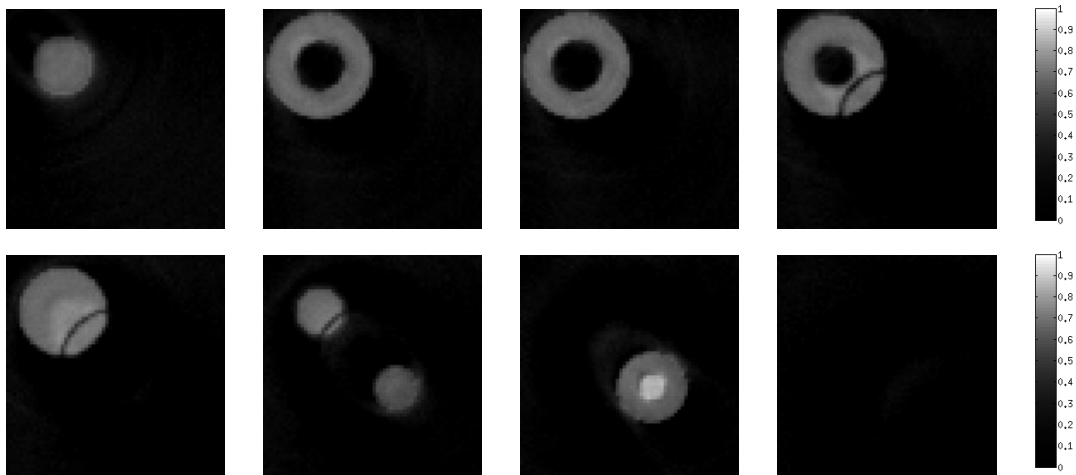
**Figure 7.11** − Reconstructions from noisy data with SNR=30 dB (relative level of noise 3 %). Errors are NMSE=0.34 %, NMAE=3.77 %. Regularization parameter $\lambda = 0.05$.
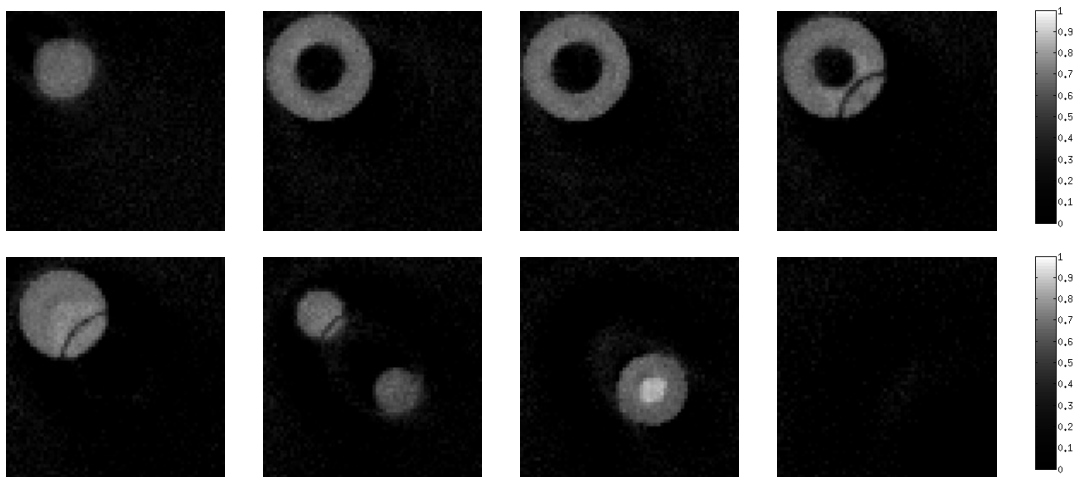


**Figure 7.12** − Reconstructions from noisy data with SNR=20 dB (relative level of noise 10 %). Errors are NMSE=0.40 %, NMAE=4.35 %. Regularization parameter $\lambda = 0.05$.
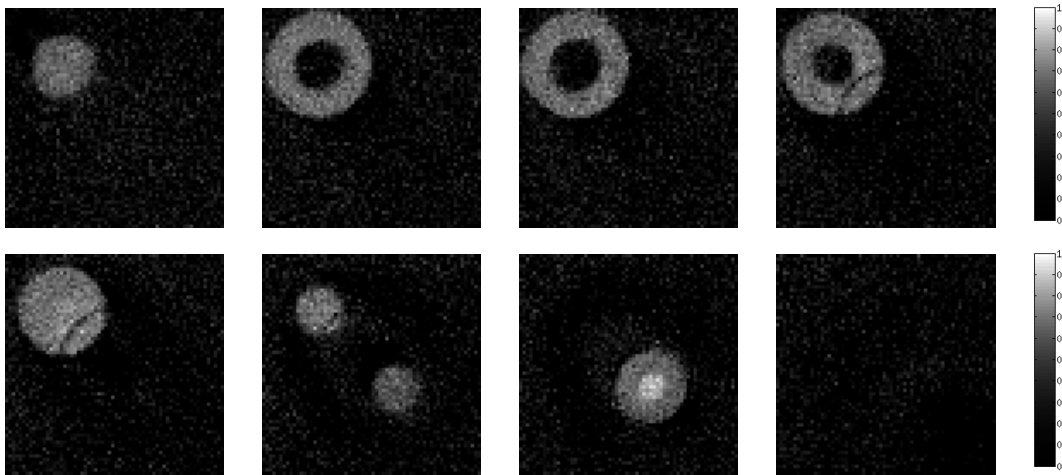
**Figure 7.13** – Reconstructions from noisy data with SNR=10 dB (relative level of noise 29 %). Errors are NMSE=0.92 %, NMAE=7.38 %. Regularization parameter $\lambda = 0.05$.

feasible when the system is smaller than the object under study. In the proposed simulation, we use an object whose side was eight times larger than the radius of the detection sphere.

## 7.7    Concluding remarks

In this chapter, we introduced a CST modality made of a fixed source and single detector rotating around the source. The object to scan is placed strictly outside the detection path. With such a system, the object does not need to be enclosed as Norton's, Truong and Nguyen's and Webber and Miller's modalities. However, this modality combines some interesting features of the ones previously proposed, namely its compactness and its fixed source. In two dimensions, we solved the reconstruction problem through an analytic inversion formula. As for the first proposed method of reconstruction for CCST without collimation, we used the Hilbert transform to obtain a suitable formulation for simulations. We obtained also a filtered back-projection type formula. Reconstructions exhibit similar streak artefacts also due to the necessary rearrangement of data to be able to apply the reconstruction algorithm. We also went a step further in the analysis of such filtered back-projection type algorithms by the analysis of the amount of data necessary for having a good reconstruction quality. We saw that from a choice for the maximal diameter for the scanning circle arcs, it is not necessary to have a fine discretization. Nevertheless, the amount of data needs to be larger than the number of pixels to reconstruct.

We also studied the Radon transform on toric surfaces, which models data acquisition of this modality in three dimensions. We showed the invertibility of this toric Radon transform. We carried out numerical reconstructions based on discrete spherical harmonics and Tikhonov regularization. The proposed algorithm reduced the three-dimensional problem

to a set of independent one-dimensional problems. Then, parallelization allows saving time of computation, in comparison with the standard matrix implementation. The obtained reconstruction results exhibit acceptable quality, however, suffer from the common limitations of Tikhonov regularization in terms of smoothing [40]. We are also faced the difficulty for such an algorithm to reconstruct well the contours of the object. We chose Tikhonov regularization since we wanted to work directly on the spherical harmonic domain. The TV regularization could help to better reconstruct the contours. However, in this case, it would be necessary to work in the Cartesian domain, and therefore with the full forward operator, which would slow down its calculation.

# A CST modality with translational geometry

**8**

**Synopsis** In this chapter, we address an alternative formulation for the exact inverse formula of the Radon transform on circle arcs arising in a modality of Compton Scatter Tomography in translational geometry proposed by Webber and Miller ([13], Inverse Problems (36)2, 025007, 2020). The original study proposes a first reconstruction method, using the theory of Volterra integral equations. This type of inverse formula may difficult to implement numerically, especially because of stability issues. Our motivation is to provide a formulation useful for simulations, which uses only common tools such as the fast Fourier transform algorithm. Simulations are carried out to illustrate the efficiency of the proposed reconstruction algorithm.

## 8.1 Context and purpose of this study

We are interested in the two-dimensional modality proposed by Webber and Miller in [13]. This modality is made of a source and a detector which translate along a line.

The original study proposes a first method of reconstruction, using the theory of Volterra integral equations. See Chapter 1 paragraph 1.3.4 for the details of demonstration. The numerical realization of such a type of inverse formula may exhibit some difficulties, mainly due to stability issues.

The objective of this chapter consists in providing a suitable formulation for exact inversion that can be straightforwardly implemented in the Fourier domain. Simulations are carried out to illustrate the efficiency of the proposed reconstruction algorithm.

## 8.2 Setup and measurement model of the CST system under study

### 8.2.1 Setup

The system under study is made of a source, assumed to be monochromatic, and a detector separated by a fixed distance from each other. The source and the detector move respectively on a horizontal line of equation $z = 3$ and $z = 1$. The horizontal position of the pair

source-detector is labelled by $x_0$ (see Figure 8.1). Alternatively, this system may be sketched with fixed lines of sources and detectors that will be used in pair. The object, placed below the detector path, is scanned transversely. As the modality in rotation proposed in the previous chapter, no collimation is used at the detector. Thus, the acquisition is performed on a family of double circle arcs (called toric sections in the original publication [13])[1].

We parameterize these circle arcs and define the corresponding Radon transform in the next paragraph.

### 8.2.2 Modelling of data acquisition using the CST system

Given a scattering angle $\omega$, data acquisition is made on a family of double circle arc of radius $r$ where $r = 1/\sin(\pi - \omega)$ (or equivalently, $\omega = \pi - \arcsin(1/r)$). For parameterization, these double circle arcs are obtained with the union of four half arcs denoted $S_j(x_0, r)$, $j \in \{1, 2, 3, 4\}$ of respective equation

$$x_1 = \sqrt{r^2 - 1} + \sqrt{r^2 - (z-2)^2}, \quad x_2 = \sqrt{r^2 - 1} - \sqrt{r^2 - (z-2)^2},$$
$$x_3 = -\sqrt{r^2 - 1} + \sqrt{r^2 - (z-2)^2}, \quad x_4 = -\sqrt{r^2 - 1} - \sqrt{r^2 - (z-2)^2}$$

and $z \in ]2 - r, 1[$. See Figure 8.1.

The Radon transform which mathematically models data measurement with this CST system is then defined as follows :

**Definition 8.2.1.** *Let $f$ be an unknown function, non-negative, continuous and compactly supported in the half plane $z < 1$. The Radon transform on double circle arcs $\mathcal{R}_{\mathcal{D}_2}$ maps $f$ into the set of its integrals over the family of double circle arcs as*

$$\mathcal{R}_{\mathcal{D}_2} f(x_0, r) = \int_{\bigcup_{j=1}^{4} S_j(x_0, r)} f(x, y) ds. \tag{8.1}$$

*where ds refers to the elementary arc length measure on the considered double circle arc. Then, after computation of the arc length measure, we have the explicit reformulation for $\mathcal{R}_{\mathcal{D}_2}$ [13, Proposition 3.1]*

$$\mathcal{R}_{\mathcal{D}_2} f(x_0, r) = \int_1^r \frac{1}{\sqrt{1 - \left(\frac{z}{r}\right)^2}} \left( \sum_{j=1}^{2} f_1\left( \sqrt{r^2 - 1} + (-1)^j r \sqrt{1 - \left(\frac{z}{r}\right)^2} + x_0, z \right) + \right.$$
$$\left. f_1\left( -\sqrt{r^2 - 1} + (-1)^j r \sqrt{1 - \left(\frac{z}{r}\right)^2} + x_0, z \right) \right) dz, \tag{8.2}$$

---

[1]We position ourselves in the same frame of study as the original article, with the same working assumptions. Thus, first order Compton scattering is the only source of attenuation for radiation and data acquisition is performed with a pair source detector, assumed to be point-like. These conditions are common in the literature [9, 12, 95, 11, 54, 85, 70] and have been already discussed in [8, 10, 12, 70].

**Figure 8.1** − Setup and parameterization of the CST modality proposed in [13]. The source $S$ and the detector $D$ are respectively represented by a red and a blue point. The black lines passing respectively through the source and the detector models their respective path. $M$ is a running point, in black, and an example of scattering site. An example of trajectory for a photon whose scattering site is $M$ is shown in purple. The red and purple continuous curves $S_1, S_3$ and $S_2, S_4$ are the examples of scanning circles arcs corresponding to the scattering angle $\omega$. $\Omega_{1,2,3,4}$ denote the centres of the circles supporting the half-arcs $S_{1,2,3,4}$. The object to scan is represented in gray.

*where $f_1(x,z) = f(x, 2 - z)$.*

In the original study of this modality, the invertibility of the corresponding Radon transform as well as its analytical inversion formula has been established. The invertibility was proven using the theory of integral equations and resulted in a Volterra integral equation with a weakly singular kernel in the Fourier domain. This study also leads to a formulation for inversion formula as an integral transformation with a kernel computed iteratively. The numerical calculation of this kind of kernel may require high computational time and/or memory. Furthermore, as mentioned in the Remark 3.4 of the original paper, the proposed approach by Webber is severely ill-posed, particularly in terms of stability. Implementing such a method can lead to large instabilities, even when these are due to small changes in the data.

## 8.3 An alternative formulation for the inversion formula of the Radon transform on double circle arcs

In this section, we state the main result of the paper, a different formulation for the associated inversion formula, that will be easier to implement numerically. Let us introduce before some notations that will be used in proofs.

### 8.3.1 Notations

It is useful to define the following transform pairs.

**Definition 8.3.1** (Fourier transform)**.** *Let $f$ be a compactly supported function in $\mathbb{R}^n$. The n-dimensional Fourier transform of $f$, denoted $\widehat{f}$, is given by*

$$\widehat{f}(\boldsymbol{\xi}) = \int_{\mathbb{R}^n} f(x) e^{-i\boldsymbol{x}\cdot\boldsymbol{\xi}} d\boldsymbol{x} \tag{8.3}$$

*with $\boldsymbol{\xi} \in \mathbb{R}^n$. The inverse Fourier transform is*

$$f(\boldsymbol{x}) = \frac{1}{(2\pi)^n} \int_{\mathbb{R}^n} \widehat{f}(\boldsymbol{\xi}) e^{i\boldsymbol{x}\cdot\boldsymbol{\xi}} d\boldsymbol{\xi}. \tag{8.4}$$

**Definition 8.3.2** (Fourier cosine transform [96])**.** *Let $f$ be a compactly supported function in $\mathbb{R}^+$. The Fourier cosine transform of $f$, denoted $\widehat{f}^c$, is given by*

$$\widehat{f}^c(\xi) = \sqrt{\frac{2}{\pi}} \int_0^\infty f(x) \cos(x\xi) dx \tag{8.5}$$

*with $\xi \in \mathbb{R}$. The inverse Fourier cosine transform is*

$$f(\xi) = \sqrt{\frac{2}{\pi}} \int_0^\infty \widehat{f}^c(\xi) \cos(x\xi) d\xi. \tag{8.6}$$

We define also the Hankel transform.

**Definition 8.3.3** (Hankel transform [86])**.** *Let $f$ be a compactly supported function in $\mathbb{R}^+$. The zero-order Hankel transform of $f$ is defined as*

$$\mathcal{H}_0 f(\eta) = \int_0^\infty f(r) J_0(\eta r) r dr \tag{8.7}$$

*where $J_0$ stands for the Bessel function of the first kind of order $0$.*

Finally, we recall the integral representation of the Bessel function $J_0$:

$$J_0(x) = \frac{1}{2\pi} \int_{-\pi}^{\pi} e^{ix\sin\theta} d\theta. \tag{8.8}$$

### 8.3.2   Inversion formula

**Proposition 8.3.1.** *Denoting $\mathcal{G}f(x_0, r)$ the operator whose Fourier transform according to the first variable is*

$$\widehat{\mathcal{G}}f(\xi, r) = \frac{\widehat{\mathcal{R}}_{\mathcal{D}_2}f(\xi, r)}{2r\cos(\xi\sqrt{r^2 - 1})}, \tag{8.9}$$

*if $r > 1$ and $0$ when $r \in [0, 1]$, the unknown function $f$ is completely recovered from $\widehat{\mathcal{G}}f$ as follows*

$$f(x, z) = \frac{1}{4\pi}\int_{-\infty}^{\infty}e^{ix\xi}\int_0^{\infty}\mathcal{H}_0\widehat{\mathcal{G}}f(\xi, \sqrt{\xi^2 + \sigma^2})\cos(\sigma(2 - z))\sigma\,d\sigma\,d\xi. \tag{8.10}$$

*Proof.* With the change of variables $s = z/r$ in (8.2) and taking the Fourier transform of $\mathcal{R}_{\mathcal{D}_2}$ respectively to variable $x_0$, one gets

$$\widehat{\mathcal{R}}_{\mathcal{D}_2}f(\xi, r) = \int_{-\infty}^{\infty}dx_0\int_{1/r}^1 ds\frac{re^{-ix_0\xi}}{\sqrt{1 - s^2}}\cdot\left(\sum_{j=1}^2 f_1\left(\sqrt{r^2 - 1} + (-1)^j r\sqrt{1 - s^2} + x_0, rs\right) + \right.$$
$$\left. f_1\left(-\sqrt{r^2 - 1} + (-1)^j r\sqrt{1 - s^2} + x_0, rs\right)\right). \tag{8.11}$$

With the second change of variables $x = x_0 \pm \sqrt{r^2 - 1} + (-1)^j r\sqrt{1 - s^2}$, one gets

$$\widehat{\mathcal{R}}_{\mathcal{D}_2}f(\xi, r) = 4\int_{1/r}^1 ds\frac{r}{\sqrt{1 - s^2}}\widehat{f_1}(\xi, rs)\cos(\xi\sqrt{r^2 - 1})\cos(\xi r\sqrt{1 - s^2}), \tag{8.12}$$

where $\widehat{f_1}$ stands for the one-dimensional Fourier transform relatively to variable $x$.

Using relation (8.9), multiplying both sides of (8.12) by $r \cdot J_0(\eta r)$ with $\eta \geq 1$ and integrating with respect to variable $r$, for $r > 1$, one recognizes the Hankel transform of $\widehat{\mathcal{G}}$, denoted $\mathcal{H}_0\widehat{\mathcal{G}}$

$$\mathcal{H}_0\widehat{\mathcal{G}}f(\xi, \eta) = 2\int_1^{\infty}dr\int_{1/r}^1 ds\frac{r}{\sqrt{1 - s^2}}\widehat{f_1}(\xi, rs)\cos(\xi r\sqrt{1 - s^2})J_0(\eta r). \tag{8.13}$$

Then, with the double substitution $(r = \sqrt{z^2 + b^2}, s = z/\sqrt{z^2 + b^2})$, one gets

$$\mathcal{H}_0\widehat{\mathcal{G}}f(\xi, \eta) = 2\int_1^{\infty}dz\widehat{f_1}(\xi, z)\int_0^{\infty}db\cos(\xi b)J_0(\eta\sqrt{z^2 + b^2}). \tag{8.14}$$

The result of the $b$-integral is given in the table [97] (page 55, equation (35)). Finally, one gets for $0 < \xi < \eta$

$$\mathcal{H}_0\widehat{\mathcal{G}}f(\xi, \eta) = 2\int_1^{\infty}dz\widehat{f_1}(\xi, z)\frac{1}{\sqrt{\eta^2 - \xi^2}}\cos(z\sqrt{\eta^2 - \xi^2}) \tag{8.15}$$

and $\mathcal{H}_0\widehat{\mathcal{G}}_1 f(\xi, \eta) = 0$ if $\eta \leq \xi$.

Let $0 < \xi < \eta$. Then with the fact $f_1(x, z) = 0$ for $z = [0, 1]$,

$$\int_0^\infty dz \widehat{f_1}(\xi, z) \cos\left(z\sqrt{\eta^2 - \xi^2}\right) = \frac{\sqrt{\eta^2 - \xi^2}}{2} \mathcal{H}_0 \widehat{\mathcal{G}} f(\xi, \eta). \tag{8.16}$$

The left-hand side is the Fourier cosine transform of $\widehat{f_1}(\xi, z)$ according the variable $z$. We can then extract $\widehat{f_1}(\xi, z)$, applying the inverse cosine transform to (8.16)

$$\widehat{f_1}(\xi, z) = \frac{1}{2} \int_0^\infty d\sigma \mathcal{H}_0 \widehat{\mathcal{G}} f(\xi, \sqrt{\xi^2 + \sigma^2}) \cos(z\sigma)\sigma, \tag{8.17}$$

where $\sigma = \sqrt{\eta^2 - \xi^2}$. The final equation is obtained going back to variable $f$ and applying the inverse Fourier transform. $\qquad\square$

**Remark 8.3.1.** *The projections $\mathcal{G}$ contain zeros in the denominator since the cosine function vanishes when $\xi\sqrt{r^2 - 1} = 2k\pi \pm \frac{\pi}{2}$, $k \in \mathbb{Z}$. From (8.13) to the end of the demonstration, it was supposed that $r$ is different from $\sqrt{1 + \left(\frac{\pi}{2\xi}(2k+1)\right)}$. Furthermore, this may be a source of instability in the simulations. The addition of a regularization parameter for simulations is discussed in Section 8.4.2 to prevent this.*

**Remark 8.3.2.** *Another reconstruction algorithm is also possible from the projections of $\mathcal{G}f$. This process is achieved performing geometric inversion. Geometric inversion is a mapping converting a point $X$ into a point $\tilde{X}$ such that $\tilde{X}X^T = q^2$, where $q \in \mathbb{R}_+^*$ is a constant value. The mapped point $\tilde{X}$ has the same direction as the original point $X$ but a distance of $q^2/||X||$ to the origin of the considered coordinate system. As an example, geometric inversion converts circles passing through the origin into straight lines. In the present case, the Radon transform on double circle arcs is converted into a Radon transform on an apparent family of circle arcs of similar geometry as the one studied in [10, 74]. Although the inverse problem can be alternatively solved using geometric inversion, the approach we employ here is more straightforward.*

## 8.4 Numerical formulations for the forward and inverse transform

### 8.4.1 Image formation

Let $N_{SD}$ be the number of position for the pair source - detector and $N_r$ the number of double scanning circle arcs per sensor position. We denote $x_{0,k}$, $k \in \{1, ..., N_{SD}\}$ and $r_l$, $l \in \{1, ..., N_r\}$ the discrete variables corresponding respectively to $x_0$ and $r$. The matrix of projection data $\mathcal{R}_{\mathcal{D}_2} f(x_{0,k}, r_l)$ is then computed, writing (8.2) under a discrete form, with

the change of variables $z = r \cos \theta$

$$\mathcal{R}_{\mathcal{D}_2} f(x_{0,k}, r_l) = r_l \, \Delta_\theta \sum_{\theta \in \left[\arcsin\left(\frac{1}{r_l}\right), \frac{\pi}{2}\right]} \left( \sum_{j=1}^{2} f_1(x_{0,k} + \sqrt{r_l^2 - 1} + (-1)^j r_l \cos \theta, r_l \sin \theta) + \right.$$

$$\left. f_1(x_{0,k} - \sqrt{r_l^2 - 1} - (-1)^j r_l \cos \theta, r_l \sin \theta) \right), \quad (8.18)$$

where $\Delta_\theta$ is the sampling angular distance of $\theta$. The above Cartesian parameterization allows having a constant distance between running points of the considered scanning circle arcs during simulations.

### 8.4.2 Image reconstruction

For image reconstruction, we need to compute the projections $\mathcal{G}f$ in the Fourier domain according to (8.9). This expression contains zeros in the denominator. This may induce instabilities on reconstruction. For simulations, we add a small regularization parameter, denoted $\epsilon$

$$\widehat{\mathcal{G}}f(\xi, r) = \frac{\widehat{\mathcal{R}}_{\mathcal{D}_2} f(\xi, r)}{2r} \frac{\cos\left(\xi\sqrt{r^2 - 1}\right)}{\epsilon^2 + \cos\left(\xi\sqrt{r^2 - 1}\right)^2}. \quad (8.19)$$

Then the most important step (in terms of computation time) in (8.10) is the calculation of $\mathcal{H}_0 \widehat{\mathcal{G}} f$. The idea is to lie the above operator with the Fourier transform of $\mathcal{G}^\ddagger f$, defined as follows

$$\mathcal{G}^\ddagger f(x, z) = \int_{-\infty}^{\infty} \mathcal{G}f(x_0, \sqrt{(x - x_0)^2 + z^2}) \, dx_0. \quad (8.20)$$

We have now the following proposition

**Proposition 8.4.1.** *Let $(\sigma, \xi) \in [0, \infty[ \times \mathbb{R}$. $\mathcal{H}_0 \widehat{\mathcal{G}} f(\xi, \sqrt{\xi^2 + \sigma^2})$ is related with the two-dimensional Fourier transform of the operator $\mathcal{G}^\ddagger$ as*

$$\mathcal{H}_0 \widehat{\mathcal{G}} f(\xi, \sqrt{\xi^2 + \sigma^2}) = 2\pi \widehat{\mathcal{G}^\ddagger} f(\xi, \sigma). \quad (8.21)$$

*Consequently, from the inversion formula (8.10), it follows in the Fourier domain*

$$\widehat{f_1}(\xi, \sigma) = 2\pi^2 |\sigma| \widehat{\mathcal{G}^\ddagger} f(\xi, \sigma). \quad (8.22)$$

*where $\widehat{f_1}$ is the two-dimensional Fourier transform of $f_1$.*

*Proof.* From the definitions of Fourier and Hankel transforms and with the integral representation of the Bessel function, one gets

$$\mathcal{H}_0 \widehat{\mathcal{G}} f(\xi, \sqrt{\xi^2 + \sigma^2}) = \frac{1}{2\pi} \int_{-\infty}^{\infty} dx_0 \int_0^{\infty} dr \, \mathcal{G}f(x_0, r) \left( \int_{-\pi}^{\pi} e^{ir\sqrt{\xi^2 + \sigma^2} \sin(\theta)} d\theta \right) e^{-i\xi x_0}. \quad (8.23)$$

There is an angle $\phi(\sigma, \xi) \in [0, 2\pi[$ which corresponds to the angular coordinates of the point $(\sigma, \xi)$, such that $\sigma = \sqrt{\xi^2 + \sigma^2} \cos(\phi(\sigma, \xi))$ et $\xi = \sqrt{\xi^2 + \sigma^2} \sin(\phi(\sigma, \xi))$. Using the property of periodicity of trigonometric functions, it follows that

$$\mathcal{H}_0 \widehat{\mathcal{G}} f(\xi, \sqrt{\xi^2 + \sigma^2}) = \frac{1}{2\pi} \int_{-\infty}^{\infty} dx_0 \int_0^{\infty} dr\, \mathcal{G}f(x_0, r) \left( \int_{-\pi}^{\pi} e^{ir\xi \sin\theta + \sigma \cos\theta} d\theta \right) e^{-i\xi x_0}. \quad (8.24)$$

Changing variables $x = r\cos\theta$ and $z = r\sin\theta$,

$$\mathcal{H}_0 \widehat{\mathcal{G}} f(\xi, \sqrt{\xi^2 + \sigma^2}) = \frac{1}{2\pi} \int_{\mathbb{R}^2} dxdz \left( \int_{-\infty}^{\infty} dx_0 \mathcal{G}f(x_0, \sqrt{(x - x_0)^2 + z^2}) \right) e^{-i(x\xi + z\sigma)} \quad (8.25)$$

The right-hand side of (8.25) is the two-dimensional Fourier transform of $\mathcal{G}^{\ddagger}$, weighted by $2\pi$ (8.21). We are now able to reformulate the inversion formula (8.17) as

$$\widehat{f}_1(\xi, z) = 2\pi \int_{-\infty}^{\infty} d\sigma \widehat{\mathcal{G}^{\ddagger}} f(\xi, \sigma) e^{iz\sigma} |\sigma|. \quad (8.26)$$

Taking the Fourier transform according to variable $z$ to the above equation (8.26) leads to (8.22). $\qquad \square$

This leads to the reconstruction algorithm summed up in Algorithm 8.1. The steps of this algorithm can be decomposed into three parts. The first part consists in obtaining rearranged data $\mathcal{G}f$ from $\mathcal{R}_{\mathcal{D}_2}$ using their relation in the Fourier domain (8.19). The second part is an operation of back-projection (8.20). The last part of this reconstruction consists in filtering the back-projected data in the Fourier domain (8.26).

---

**Algorithm 8.1:** Reconstruction algorithm of the object $f$ from projections on double circle arcs $\mathcal{R}_{\mathcal{D}_2}$.

---

**Data:** $\mathcal{R}_{\mathcal{D}_2} f(x_0, r)$, projections on double circular arcs of function $f$
**Result:** $f(x, y)$

1 Compute the one-dimensional Fourier transform of $\mathcal{R}_{\mathcal{D}_2} f(x_0, r)$ relative to the first variable.
2 Compute $\widehat{\mathcal{G}} f(\xi, r)$ according to (8.19)
3 Perform the inverse one-dimensional Fourier transform to recover $\mathcal{G}f(x_0, r)$.
4 Interpolate the obtained data to have the back-projected data $\mathcal{G}^{\ddagger} f(x, z)$.
5 Perform the two-dimensional Fourier transform of $\mathcal{G}^{\ddagger} f(x, z)$
6 Weight the result by $2\pi^2 |\sigma|$.
7 Compute the inverse two-dimensional Fourier transform of the result to recover $f$.

---

## 8.5    Simulations results

The original object used for simulations is Derenzo phantom, an object made of multiple circles of different sizes. The circles in the object also allow the study of the performance of the algorithm in front of different contrasts and spatial resolution, as well as its ability to reconstruct features locally tangent to lines of any slope. The unit length used here is the pixel. We suppose thus that the distance between the source and the detector paths of the modality is two pixels. The size of the object is $N \times N = 256 \times 256$ pixels in all simulations. Furthermore, given the linear geometry of this modality, there is no loss of generality to consider the object centred relatively to the $z$-axis.

### 8.5.1    Data acquisition

Data measurement is calculated according to (8.18). Figure 8.2 shows an example of data obtained for Derenzo phantom.



(a)  (b)
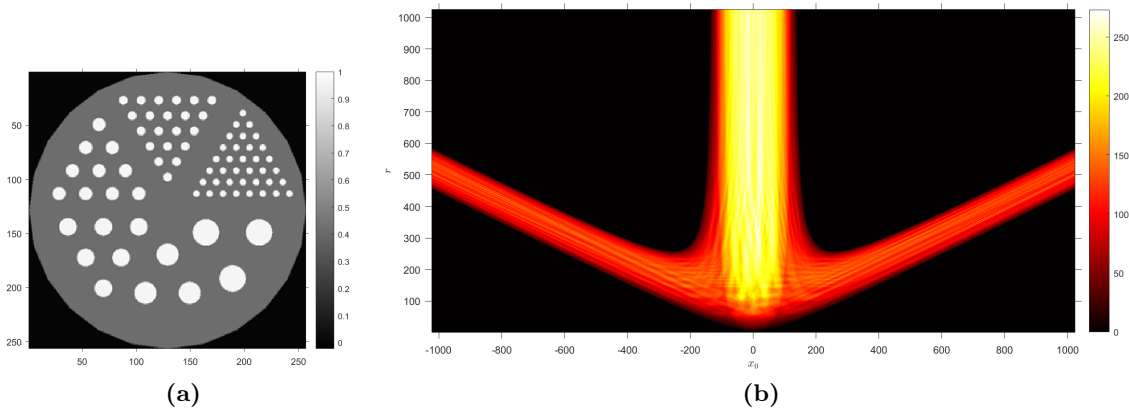
**Figure 8.2** – (a) Original object: Derenzo phantom. (b) Corresponding acquired data for $N_{SD} = 2048$ and $N_r = 1024$. A distance of one pixel is left between the upper part of the image and the detector path ($\delta = 1$, see 8.5.2).

### 8.5.2    Influence of some parameters on reconstruction quality

In the following paragraphs, we study the influence of the other general parameters of the system such as the position of the object, the number of required positions for sensors or the number of scanning circle arcs. In addition to a visual comparison of the reconstruction quality, we propose here to measure quantitatively the error rate between the original object $f_0$ and the reconstruction $f$ with the Normalized Mean Squared Error (NMSE) $= ||f - f_0||_2^2 / N^2$ where $||.||_2$ refers to the 2-norm.

The regularization parameter $\epsilon$, which has to be small, was arbitrarily set to 0.01.

**Position of the object relative to the detector path**

We analysed here the influence of the position of the object on reconstruction quality. Firstly, the number of positions $N_{SD}$ for the pair source - detector and the number of scanning circles per position $N_r$ was chosen to largely satisfy the well-known condition [86] $N_{SD} \times N_r \geq N^2$ and are set arbitrarily to $N_{SD} = 1024$ and $N_r = 1024$. A convenient choice for these parameters will be discussed later. We performed various acquisition, modifying the gap $\delta$ between the detector path and the upper part of the object (see Figure 8.1). Consequently, the object is in the square of Cartesian coordinates $\left(x \in \left[-\frac{N}{2} + 1, \frac{N}{2}\right]; z \in [-N - \delta, -\delta + 1]\right)$. Figure 8.3 shows the reconstruction results for $\delta = 1, 26$ and 51 pixels which correspond respectively a position for the object in the respective domains $[-N - 1, 0]$, $[-N - 26, -25]$ and $[-N - 51, -50]$ along the z-axis. The difference between the three reconstructions is on the top of the object. If the object is close to the line of movement of the detector, then this part is less well reconstructed. Indeed, this distance between the object and the detector path allows having arcs of circle tangent horizontally to this part of the object. An offset of $\delta = 51$ seems to be a good trade-off between quality of reconstruction and the applicability of such a measure in practical use. For the rest of the simulations, $\delta$ is set to 51.



**(a)** Reconstruction for $\delta = 1$ NMSE = 0.0112

**(b)** Reconstruction for $\delta = 26$ NMSE = 0.0074

**(c)** Reconstruction for $\delta = 51$ NMSE = 0.0061
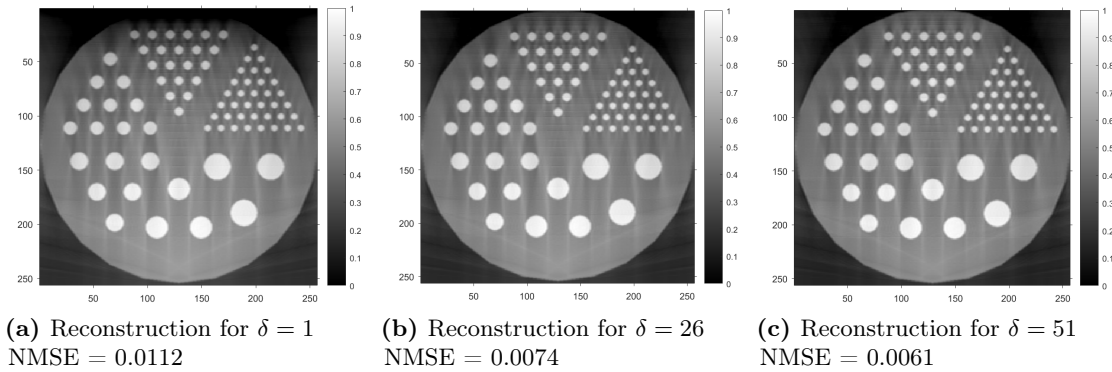
**Figure 8.3** – Reconstruction results of the Derenzo phantom 8.2a for $\delta = 1$ (a), $\delta = 26$ (b) and $\delta = 51$ (c) pixel(s).

**Number of necessary positions for the pair source-detector**

We studied then the number of different positions required for a good quality of reconstruction. The influence of two running parameters is analysed, first, the farthest position $x_{0,max}$ from the object for the source-detector pair (that is an array of length $[-x_{0,max}, x_{0,max}]$ for the source and detector paths) and the distance $\Delta_{x_0}$ between two adjacent positions of the pair.

Figures 8.4a, 8.4b and 8.4c show the reconstruction results when the farthest position from the object to the pair source detector is respectively $2N, 3N$ and $4N$ with a common $\Delta_{x_0}$ set to 1. Reconstruction from a domain $[-x_{0,max}, x_{0,max}] = [-2N, 2N]$ appears to be blurred with strong artefacts in the upper parts of the image. For $x_{0,max} = 3N$ and $4N$, reconstruction quality seems to be visually equivalent, even if the NMSE for $x_{0,max} = 4N$ is

higher. This may be due to numerical approximations. For the rest of the simulation, $x_{0,max}$ is set to $3N$.

The influence of the distance $\Delta_{x_0}$ between two adjacent positions of the pair is now evaluated. Figures 8.4d, 8.4e and 8.4f show the result for $\Delta_{x_0} = 2, 1$, and $0.5$ pixels. This represents a respective amount of $0.5, 1$ and $2$ detectors per unit length. In Figure 8.4d ($\Delta_{x_0} = 2$), we can see streaks suggesting a lack of data for reconstructing the object. On the contrary, the doubling of the number of detectors between Fig. 8.4e and Fig. 8.4f does not bring a better quality of reconstruction. Consequently, the use of one detector per unit length seems to be a good trade-off, and the value will remain constant in the rest of the paper.



(a) Reconstruction for $x_{0,max} = 2N$. NMSE $= 0.0084$



(b) Reconstruction for $x_{0,max} = 3N$. NMSE $= 0.0049$



(c) Reconstruction for $x_{0,max} = 4N$. NMSE $= 0.0061$



(d) Reconstruction for 0.5 detectors per unit length. NMSE $= 0.0046$



(e) Reconstruction for 1 detectors per unit length. NMSE $= 0.0049$



(f) Reconstruction for 2 detectors per unit length. NMSE $= 0.0049$
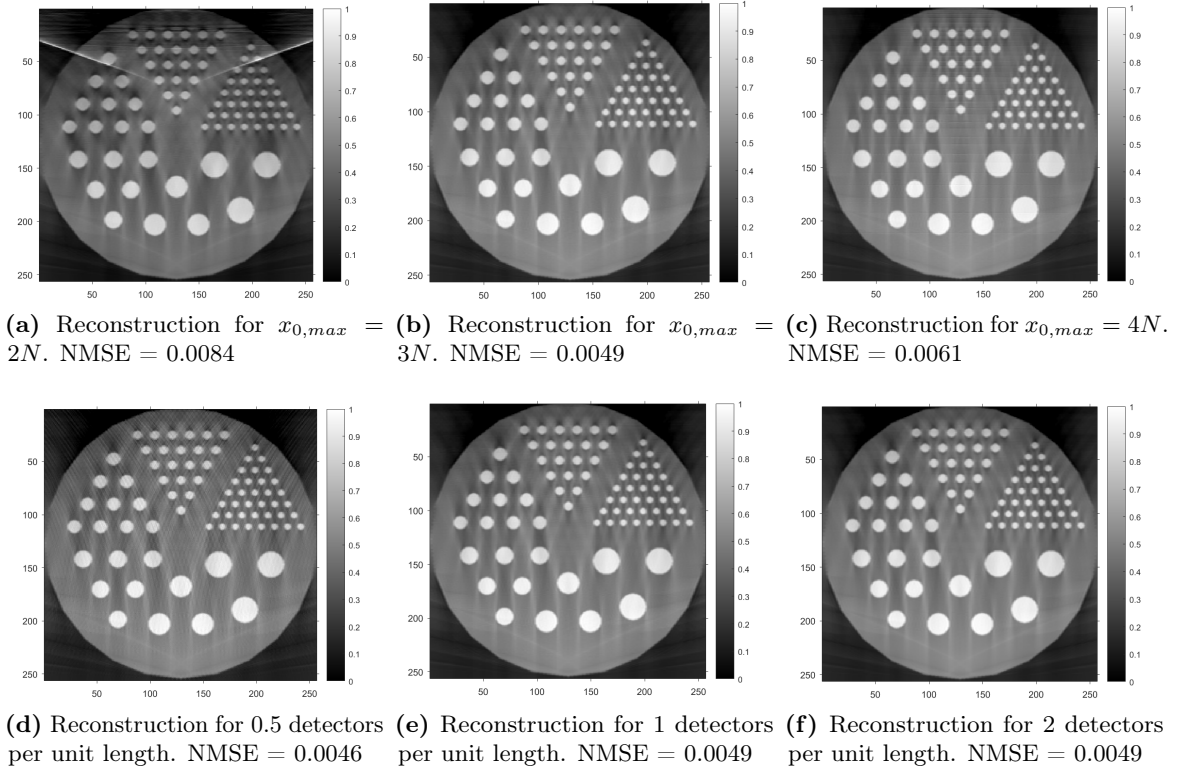
**Figure 8.4** – Evaluation of the number of source-detector positions on reconstruction quality. First row: Reconstruction results of the Derenzo phantom 8.2a for $x_{0,max} = 2N$ 8.4a, $3N$ 8.4b and $4N$ 8.4c where $\Delta_{x_0} = 1$. Second row: Reconstruction results for 0.5 8.4d, 1 8.4e and 0.5 8.4f detector per unit length and $x_{0,max} = 3N$ remains constant.

**Number of scanning circles per position of the pair source-detector**

The number of scanning circles necessary for reconstruction is now under study. In the same way, two parameters are of interest, that is, the maximum radius $r_{max}$ of the scanning double circle arcs to be taken and the discretization step $\Delta_r$ that have to be chosen. We first evaluate the consequences of the value of $r_{max}$ with three examples on Fig. 8.5a, 8.5b and 8.5c where $r_{max}$ is set respectively to $2N, 3N$ and $4N$ and $\Delta_r = 1$. For $r_{max} = 2N$, the reconstruction

suggests a lack of data in front of the obtained results for $r_{max} = 3N$ and $r_{max} = 4N$. Notice the higher NMSE for $r_{max} = 4N$, probably due to numerical approximations.

We were finally looking for the appropriate discretization step for $r$, setting $\Delta r$ to $1, 2$ and $4$. Reconstruction results are shown respectively in Fig. 8.5d, 8.5e and 8.5f. Reconstructions with a large discretization step exhibit blur.



**(a)** Reconstruction for $r_{max} = 2N$. NMSE = 0.0058

**(b)** Reconstruction for $r_{max} = 3N$. NMSE = 0.0040

**(c)** Reconstruction for $r_{max} = 4N$. NMSE = 0.0049

**(d)** Reconstruction for $\Delta_r = 1$. NMSE = 0.0040

**(e)** Reconstruction for $\Delta_r = 2$. NMSE = 0.0043
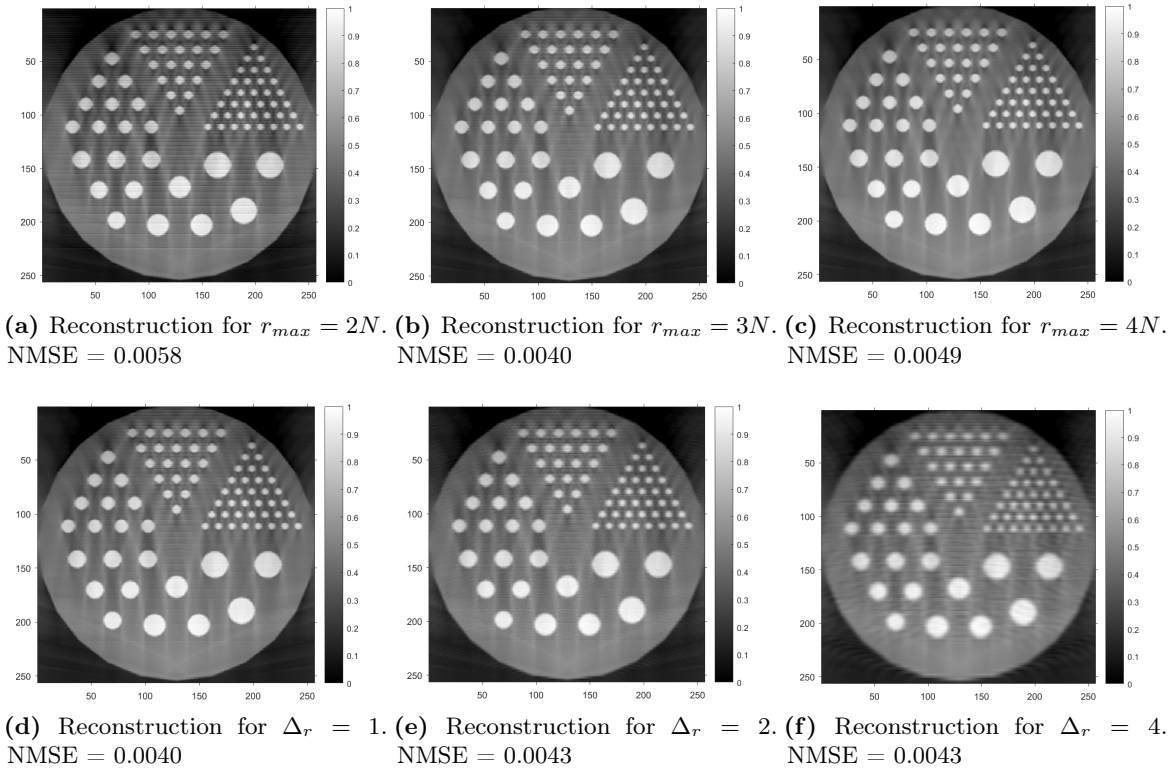
**(f)** Reconstruction for $\Delta_r = 4$. NMSE = 0.0043

**Figure 8.5** − Evaluation of the number of scanning circles on reconstruction quality. First row: Reconstruction results of the Derenzo phantom 8.2a for $r_{max} = 2N$ 8.5a, $3N$ 8.5b and $4N$ 8.5c where $\Delta_r = 1$. Second row: Reconstruction results for $\Delta_r = 1$ 8.5d, 2 8.5e and 4 8.5f detector per unit length and $r_{max} = 3N$ remains constant.

**Discussions**

The above simulations results show some interesting issues for the CST modality and the reconstruction quality that can be expected with such a system. First, this system is able to scan objects whose depth is largely oversized relative to the source-detector distance. However, this seems to be counterbalanced by the need for a consequent length for the source and detector linear paths, since sufficient reconstruction results appear for source and detector paths of length size six times greater than the object size. The necessary number of scanning circle arcs is also very important since, if we relate the values of $r_{max}$ with the scattering angles, the reconstruction quality is largely improved when $r_{max}$ is high whereas the angular distance between two values of $r_{max}$ is very small. Considering a larger distance

between the source and the detector paths for the system may reduce partially the required amount of projection data.

Moreover, the geometry offers a sufficient reconstruction quality for every tangent with arbitrary slopes. However, one can notice that vertical slopes are slightly less well reconstructed than the other ones. This can be seen if we pay carefully attention to the left and right sides of the reconstruction. This may be problematic if the object to scan is essentially made of vertical features. One way to avoid this is to perform additional scans by rotating the object, if possible. Some artefacts that look like shadows around the circles which compose the object remains also clearly visible.

# Concluding remarks on Part 3

In this part, we studied two other CST configurations, one with a rotational geometry, the other with a translational geometry. These geometries were of interest for us because, even if they employ a non-collimated detector, we established in both cases inversion formulas with associated fast and efficient reconstruction algorithms.

The first CST modality, made of a fixed source and a rotating detector, was introduced during this thesis. The second CST modality, previously introduced by Webber and Miller, consists of a pair source - detector which translates synchronously. For both modalities, the object is placed strictly outside the source-detector path, and the system employs back-scattered photons to scan the object. Since they use an uncollimated detector, the scanning manifolds are two families of double circle arcs.

The proposed procedure for inversion in each case rests on the exploitation of either the rotational or translational invariance and the symmetry of the considered scanning arcs. In the first case, we followed Cormack procedure, establishing first a relation between circular harmonic expansions of object and data. We also established the consistency condition in Cormack sense for our case, and finally derive a close formulation for the inverse formula. For Webber and Miller's modality, we established a relation between the two-dimensional Fourier transform of the object and the one of an intermediate function in relation with data. The latter differs from the first inverse formula proposed by Webber and Miller, since he established a formulation as an integral transformation with a kernel computed iteratively. Moreover, they mentioned their approach raises also problems of stabilities.

Both inversion formulas result in fast and efficient reconstruction algorithm.
For the first modality, we obtained a filtered back-projection type formula. The quality of reconstruction is similar to the one obtained with CCST with collimation. We observed streak artefacts, also due to the same kind of missing data. We showed also that such algorithms need an amount of data sufficiently large in front of the number of pixels to reconstruct. As a result, we observed reconstructions with sufficiently good quality when we have five pixels of data (which can have a zero or non-zero value) for each pixel to reconstruct.
The second algorithm is made of computations of Fourier transforms (which can be easily computed using the fast Fourier transform algorithm) and interpolations. In fact, we showed that the proposed algorithm is made of three phases: a first step of data rearrangement, a

second step of back-projection on the scanning circles and finally a third step of filtering. Even no simulations results were proposed by Webber in their original work (because of high computational time, memory requirements, and issues about stabilities), we can expect that ours is easier to implement numerically. We also performed several simulations to study the influence of several parameters on reconstructions. Our simulations revealed that to obtain a sufficient reconstruction quality, the length of the linear paths for source and detector need to be sufficiently large (about six times larger than the object). Hence, this algorithm, as the filtered back-projection type algorithms proposed before, need a sufficiently large amount of data. This fact counterbalances that the width of the system is very small compared to the size of the object. Extra work is needed in order to consider if a larger distance between the source and the detector can reduce partially the required amount of data. The compactness of the first discussed modality is thus an advantage over that of Webber and Miller.

We also investigated the extension of the rotational-invariant modality in three dimensions and established the invertibility of the corresponding Radon transform. In absence of inversion formula, we proposed reconstruction results obtained via Tikhonov regularization. We proposed also to compute the forward operator in its spherical harmonic expansion, which made it possible to parallelize its calculation. With these simulations, we showed that this modality is able to reconstruct objects larger than the system itself. Some work is on the way to find an inversion formula for such a modality.

Moreover, an interesting perspective concerns also the proposition of an alternative inversion formula suitable for simulations for the three-dimensional extension of Webber's modality. Some work is also on the way to find such an inversion formula.

# General concluding remarks and perspectives of this work

**Contributions of this thesis ·** On the beginning of the thesis, the main question was about the proposition of a modality of Compton scattering tomography, fixed and able to scan small objects. We achieved this challenge with the proposition of the circular Compton scattering tomography, a modality made of a ring of detectors containing the source. By combining these two features in a new tomographic concept, we met the requirements of biomedical imaging. In fact, the circular layout of detectors allows reducing the practical scanning time and thus the time of exposure to radiation.

From the CCST setup, we established a modelling for data acquisition with a Radon transform on double circle arcs. In particular, we studied two possible configurations for CCST, with or without collimation at detectors.

With collimation at detectors, we proposed two equivalent algorithms for image reconstruction. The first one is deduced from an analytical inversion formula previously proposed by Cormack. From this inversion formula, we proposed a filtered back-projection type algorithm, made of the same two main steps as the well-known algorithm in conventional tomography. Data is first filtered, before being back-projected on the appropriated circles. Such an algorithm offers a fast reconstruction result. The second proposed approach uses geometric inversion, to convert the considered family of circle arcs to a family of half-lines. We proved the invertibility of the Radon transform on this family of half-lines and established an inversion formula. From this inversion formula, we suggested a reconstruction algorithm, also of type filtered back-projection. To the best of our knowledge, it is the first time that these two filtered back-projection type algorithms convenient respectively for data issued from particular families of circles and half-lines are proposed.

In addition, we showed that CCST is able to scan large objects than the system itself, performing an external scanning. There is also the possibility of combining CCST with conventional fan-beam computed tomography, to design a double imaging system thanks to their similar configuration. Thus, this bi-imaging system provides both the attenuation map (by fan-beam CT) and the distribution of electrons (by CCST), which are two physical properties of the object under study.

Without collimation at detectors, we discussed the invertibility of the corresponding Radon

transform. In the absence of inverse formula in that case, we proposed to solve the inverse problem using Tikhonov regularization.

We also opened a more theoretical discussion around the invertibility of this Radon transform. This led to study an over-determined class of cones, whose Radon transform is invertible in two and three dimensions, but unfortunately, the proposed inversion formulas are not usable in the context of an imaging system. We then discussed the trade-off that can exist between the geometry of the system, which can be very advantageous, and the possibility of obtaining an analytical inverse formula for the corresponding Radon transform.

Moreover, we studied CCST under a practical setting and derived the integral transform modelling its data acquisition under realistic considerations. We then compared the resulting simulations with *ground truth* data obtained with Monte Carlo experiments.

Then, in the second part of the thesis about our contributions, we also modelled image formation and image reconstruction for two other CST systems.

The first one, introduced also in this thesis, is made of a fixed source and a collimator-free detector rotating around it. The proposition of this modality is motivated by the possibility of having a simpler system, made of a fixed source and a sing detector, also compact, but above all without collimation at detector. This modality performs only external scanning, and is able to scan objects larger than the system itself.

From this new setup, we proposed an analytical inversion formula in two dimensions. The proposed inversion formula leads also to a filtered back-projection type algorithm, the third algorithm of this type proposed in this thesis.

Moreover, we also studied the extension in three dimensions. With a three-dimensional CST system, we are able to reconstruct directly volumes of the object under study, removing the plate collimation which restricts the photon paths in a two-dimensional space. This led us to consider a Radon transform on toric surfaces, of which we established the invertibility. We proposed also reconstruction results using Tikhonov regularization. However, instead of computing a large forward operator to model data acquisition, we proposed to reduce its computation time, splitting up the three-dimensional problem into a set of independent one-dimensional problems.

In the last part of the thesis, we considered a modality previously proposed by Webber. This modality consists of a source and a detector which translate along a line synchronously. The objective of the work is therefore different from those presented previously, since it was not a question of introducing a new modality. Here, the objective was to propose a reconstruction algorithm from an analytical inverse formula of the Radon transform associated with this modality. In fact, in the original work about the modality, the resulting inversion formula was difficult to implement, firstly, because of stability issues. Secondly, the proposed solution contains also a kernel which has to be computed iteratively. Thus, the numerical simulation

of such a formula would also require a high computational time and memory space. In this thesis, we proposed an alternative reconstruction formula suitable for the development of a faster and efficient reconstruction algorithm. The associated reconstruction algorithm uses only well-known mathematical tools, easy and fast to implement.

**Comparison of the modalities introduced in this thesis with those previously proposed ·** During this thesis, we introduced two new configurations : CCST, with a fixed ring of detectors containing the source and the fixed source rotating detector CST modality. In this paragraph, we propose a comparison with the models proposed earlier.

Among the modalities able to perform an internal scanning, we have Nguyen and Truong modalities proposed in 2010 and 2011 and now CCST. The three configurations are compact, and suppose the placement of the object inside a circle, which is either the detector ring in the case of CCST or the circular path of the source and detector. While Nguyen and Truong's modalities require a mechanical rotation of the system, CCST is the only fixed system able to perform small objects scanning. This is achieved by using a set of detectors, while the two previously proposed modalities used only one. A reduction of acquisition time and, consequently, a reduction in the exposure of radiation are expected. However, it is technically easier to design Nguyen and Truong's modalities with collimation than CCST.

Among the modalities able to perform an external scanning, we find again Nguyen and Truong's modalities (2010, 2011), CCST, but also Norton's modality (1994), Webber and Miller's modality (2020) and the fixed source rotating detector configuration proposed here. Only three modalities may be completely fixed, that is Norton and Webber and Miller ones, and CCST. These configurations will have an advantage in front of others, since these systems may be completely fixed and in that respect provide an acquisition duration reduced. Note that this advantage is only possible in the case of implementation of Webber and Miller's modality, with linear array of sources and detectors. In this case, the synchronization of each detector source pair is mandatory. A small offset is also required to avoid having the emitted photons blocked by the detector array. Among these three fixed modalities, only CCST is compact, and thus a reduced system size. In fact, with a linear detector, information corresponding to large scanning circles is collected far from the source while with CCST, photons are always collected at a maximal distance equal to the diameter of this ring of detectors. Since Nguyen and Truong's and the fixed source rotating detector configurations are also compact, they have also the previous mentioned advantage. Furthermore, note that, all modalities except CCST and Norton's modality, exploit only back-scattered photons (i.e. photons scattered by an angle $\omega > \pi/2$) to perform an external scanning. Since these photons are less probable in proportion than forward-scattered photons (i.e. photons scattered by an angle $\omega < \pi/2$), this may result in a longer exposure time.

Moreover, three modalities have been studied with collimation-free detectors: CCST, Webber and Miller's and the fixed source rotating detector CST modality. Consequently, this feature

may enable an increase of the amount of acquired data for a given position of the considered detector.

These comments are summed up with a table in appendix D.

**About the proposed reconstruction algorithms ·** During this thesis we have focused on proposing exact inverse analytical formulas leading to reconstruction algorithms that can be easily and fast implemented.

The study of CCST with collimation and the fixed source rotating detector CST modality led to the proposition of three new filtered back-projection type reconstruction algorithms, which ensures us a fast and efficient numerical implementation. Note that, the first reconstruction algorithm discussed for CCST can be also used for Norton's system. Furthermore, it is also possible to have such type of reconstruction algorithm for the second modality proposed by Nguyen and Truong, from the established closed inversion formula. This type of algorithms have a huge advantage in front of the Chapman and Cary approach, which used the inversion formula linking circular harmonic decomposition of object and data. In fact, it requires computations of primitive integrals that are evaluated recursively. Nevertheless, some disadvantages for these filtered back projection type algorithms are also to be mentioned. First, this kind of algorithms requires a treatment of the data by parameterizing the circles in a more theoretical way and by moving away the variables of the initial imaging problem. We observed that this change of variables is responsible for a problem of missing data. This is reflected in the presence of streak artefacts and deformation of some contours on reconstructions. Second, the amount of required data should be overdetermined in front of the number of pixels of the object to reconstruct.

It is also with this in mind that we wanted to study Webber's modality. In fact, by exploiting the translation invariance of the family of scanning arcs of circle, we proposed a relation between the two-dimensional Fourier transforms of object and data. This formula led to a reconstruction algorithm made of the three following steps: rearrangement of data, back-projection on circles and filtering. Again, the proposed algorithm is more efficient than the one from the Webber and Miller's inverse formula since, in addition to having stability problems, it implies recursive calculations of integrals. As before, we showed also that the amount of data must be bigger than the number of pixels to reconstruct.

In absence of analytic inversion formula for CCST without collimation and the three-dimensional extension of the fixed source rotating detector modality, we used Tikhonov regularization method to perform reconstruction. We chose this regularization technique, since this method provides good reconstructions results in the case of having a complete amount of data. Tikhonov regularization offered us also extra advantages for the computation of the forward operator in the case of the three-dimensional fixed source rotating detector, as mentioned before. We found in our different simulations, its usual limitations, in terms of edge preservation.

However, the purpose of these simulations, whether derived from analytical formulas or regularization methods, was to illustrate the theoretical result, and the ability of the proposed modality to generate a complete data set needed for the final reconstruction. Thus, in all the works carried out within the framework of this thesis, this objective has been achieved. This type of reconstruction method is by no means a final reconstruction method that could be used with a prototype. This point brings us directly to the perspectives of this work.

**Perspectives of this work ·** On the theoretical level, a general question concerns the admissible configurations for the source and the detector(s) leading to an invertible Radon transform, but above all, to a modality able to provide a complete set of measurements. This question is even more important in three dimensions, where we are looking for the direct reconstruction of surfaces. In particular, this would also allow concluding about the viability of CCST extensions in three dimensions. In the logical continuation of this work, more particularly, it remains also to conclude about the invertibility of the Radon transform associated with the CCST without collimators. Moreover, the proposition of an inversion formulas leading to practicable reconstruction algorithms for the extensions of the fixed source rotating detector modality and Webber's modality in three dimensions are two open problems.

The next question consists in going back over the general hypotheses formulated at the beginning of this work – and common on the literature, for the mathematical tractability of the Radon transform which models data. In fact, the next steps for such imaging systems to emerge are necessary more oriented towards a modelling taking into account all realistic effects.

The first practical consideration concerns the Compton effect. We know that Compton effect is dominant in a wide range of middle-low energy. More precisions are nevertheless needed to quantify the effects of the other physical effects during the radiation exposure.

Similarly, we considered only first-order Compton scattering. First-order scattered photons certainly predominates, however, as shown in our Monte Carlo simulations, multiple scattering can also occur. The consequences that multiple scattering (second order or higher) may have on image quality are still unclear, and how to deal with is an open question. Even if the lower probability and the random nature of such events suggests that noise reduction strategies may be a good strategy, one can also model higher orders, and exploit them for image reconstruction. Rigaud [98] adopted this point of view in a recent work and proposed a first modelling for photons scattered twice inside matter.

Furthermore, attenuation and scattering should be considered in the forward model. Thus, it will be of interest to study the corresponding *attenuated Radon transforms* on circle arcs (or on toric surfaces in three dimensions). The problem becomes consequently more complicated since, this implies the consideration of an integral transform on a circular manifold including two integrals on two different linear paths. It involves also two different properties of the object, that is, attenuation and electronic density. The mathematical tractability of such

integral transforms still remains an open problem, and no exact solution is known at present. A solution to this problem could come from the use of more *physical*-based models. This would allow having models that more easily take into account the distribution of scattered photons as a function of the scattering angle, attenuation in matter, with better noise profiles.

Finally, some practical aspects also deserve special attention. In fact, in a practical scenario, real source and detector may have also huge consequences on the quality of reconstruction. Since they have a finite dimension, blur can be expected at reconstruction. The energy resolution is also non-ideal, and this feature may lead to uncertainties in the localization of scattering sites. Even sensors are in permanent progress, a careful knowledge of them and their performance will allow obtaining a more accurate modelling of the modality under study.

# A

# Data acquisition model of CCST with realistic parameters

**Synopsis** In this appendix, we give a complete derivation for the modelling of data acquisition with realistic parameters, following [99], from the emitted beam of photons to the Radon transform modelling data acquisition. We perform also simulations of the proposed Radon transform and compare them with Monte Carlo simulations.

## A.1 General formulation of the number of photons collected by a detector.

We consider a beam of photons emitted by a source at energy $E_0$ that undergo scattering with angle $\omega$ when they reach an electron. Then, scattered photons continue through its path and some reach a detector $D_k$. Neglecting attenuation coefficients due to emission and scattering phases of the photon trajectory, the number of photons $dN$ collected by a detector is given by the relation

$$dN = F\, d\sigma_c\, n_e dV, \tag{A.1}$$

where $F$ is the incident photon flux, $n_e dV$ is the number of electrons in the small volume $dV$ and $d\sigma_c$ is the differential Compton cross section. The distribution of photons with respect to the scattering angle $\omega$ into a solid angle $d\Omega$ (see Fig. A.1) is given by the Klein-Nishina differential cross section

$$\frac{d\sigma_c}{d\Omega}(E_0, \omega) = \frac{r_0^2}{2}\left(\frac{E_\omega}{E_0}\right)^2\left(\frac{E_\omega}{E_0} + \frac{E_0}{E_\omega} - \sin\omega^2\right), \tag{A.2}$$

where $r_0 = hc\alpha/2\pi m_e c^2$ is the classical electron radius with $h$ the Plank constant, $c$ the speed of light, $\alpha$ the fine structure constant, $m_e$ the electron mass and $E_\omega$ the energy of the photon after collision.

We now introduce in (A.1) the differential Compton cross-section per solid angle $d\sigma_c/d\Omega$

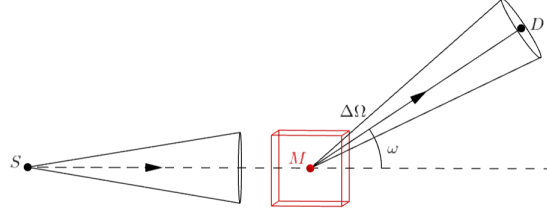$$dN = F\,\frac{d\sigma_c}{d\Omega}\,n_e\, d\Omega dV. \tag{A.3}$$

**Figure A.1** − Solid angle in Compton effect.

## A.2 Derivation of corresponding the Radon transform.

We scan planar cross-sectional maps of thickness $\Delta z$, hence we can assume that the photon flux and electronic density of the object are invariant along the $z$-direction. The incident photon flux $F$ can be expressed as

$$F(r, \theta, z) = \frac{s(\theta)}{r \Delta z}, \tag{A.4}$$

where $s(\theta)$ stands for the angular density of emitted photons by the source. Substituting $dV$ by $r dr d\theta \Delta z$ and according to (A.4), the number of photons incoming from a scattering site $M$ of polar coordinates $(r, \theta)$ collected by $D(r_{D_k}, \theta_{D_k})$ is rewritten as

$$dN(r, \theta, \theta_{D_k}) = s(\theta) \frac{d\sigma_c}{d\Omega}(E_0, \omega(r, \theta, \theta_{D_k})) \, n_e(r, \theta) \, d\Omega dr d\theta. \tag{A.5}$$

Given a scattering angle $\omega$, two scanning arcs $\mathcal{A}_1$ or $\mathcal{A}_2$ may correspond. For this demonstration, we group these two family into one, denoted $\mathcal{A}$, introducing the variable $\beta \in \, ] -\pi, \pi [ \backslash \{0\}$.

$$\mathcal{A}(\rho(\beta, \theta_{D_k}), \phi(\beta, \theta_{D_k})) : r = \rho(\beta, \theta_{D_k}) \cos(\theta - \phi(\beta, \theta_{D_k})), \quad \theta \in [\theta_{D_k}, \theta_{D_k} + \beta]. \tag{A.6}$$

When $\beta$ is positive, it describes the family $\mathcal{A}_1$, otherwise, it refers to $\mathcal{A}_2$.

Then, with the successive changes of variables from $(r, \theta, \theta_{D_k})$ to $(\beta, \theta, \theta_{D_k})$ and then $(E_\beta, \theta, \theta_{D_k})$, we arrive to the following expression of the count rate

$$dN(E_\beta, \theta, \theta_{D_k}) =$$
$$S(\theta) \frac{d\sigma_c}{d\Omega}(E_0, \beta) \, n_e(r(E_\beta, \theta, \theta_{D_k}), \theta) \, \frac{E_0}{E_\beta^2 \, k \sin \beta} \, \frac{P|\sin \theta_{D_k} \sin(\theta - \theta_{D_k})|}{\sin \beta^2} d\Omega dE d\theta \tag{A.7}$$

Integrating $dN(E_\beta, \theta, \theta_{D_k})$ over $\theta$, one can obtain $I(E_\beta, \theta_{D_k})$, the intensity of photons at

energy $E_\beta$ with a step $\Delta E$ collected by a detector $D$ into the solid angle $\Delta\Omega$:

$$
\begin{aligned}
I(E_\beta, \theta_{D_k}) &= \int_{\theta_{D_k}-\beta}^{\theta_{D_k}+\beta} dN(E_\beta, \theta, \theta_{D_k}) \\
&= \int_{\theta_{D_k}-\beta}^{\theta_{D_k}+\beta} S(\theta) \frac{d\sigma_c}{d\Omega}(E_0, \beta)\, n_e(r(E_\beta, \theta, \theta_{D_k}), \theta) \frac{E_0}{E_\beta^2\, k\sin\beta} \frac{P|\sin\theta_{D_k}\sin(\theta-\theta_{D_k})|}{\sin\beta^2} \\
&\quad \Delta\Omega\Delta E d\theta.
\end{aligned}
\tag{A.8}
$$

Introducing the delta distribution, one has

$$
\begin{aligned}
I(E_\beta, \theta_{D_k}) &= \int_{\theta_{D_k}-\beta}^{\theta_{D_k}+\beta} S(\theta) \int_0^\infty \frac{d\sigma_c}{d\Omega}(E_0, \beta)\, n_e(r, \theta) \frac{E_0}{E_\beta^2\, k\sin\beta} \\
&\quad \frac{P|\sin\theta_{D_k}\sin(\theta-\theta_{D_k})|}{\sin\beta^2}\delta(r - \rho(\beta, \theta_{D_k})\cos(\theta-\phi(\beta, \theta_{D_k})))\Delta\Omega\Delta E dr d\theta.
\end{aligned}
\tag{A.9}
$$

Going back to scattering angle $\omega$ and introducing a weighting function $q(r, \theta; \omega, \theta_{D_k})$ as

$$
q(r, \theta; \omega, \theta_{D_k}) = s(\theta)\frac{d\sigma_c}{d\Omega}(E_0, \omega)\frac{E_0}{E_\omega^2\, k\sin\omega}\frac{P|\sin\theta_{D_k}\sin(\theta-\theta_{D_k})|}{\sin\omega^2}\Delta\Omega\Delta E
\tag{A.10}
$$

one gets

$$
\begin{aligned}
I(\omega, \theta_{D_k}) &= \int_{\theta_{D_k}-\omega}^{\theta_{D_k}} \int_0^\infty n_e(r, \theta)q(r, \theta; -\omega, \theta_{D_k})\delta(r-\rho(-\omega, \theta_{D_k})\cos(\theta-\phi(-\omega, \theta_{D_k})))dr d\theta + \\
&\quad \int_{\theta_{D_k}}^{\theta_{D_k}+\omega} \int_0^\infty n_e(r, \theta)q(r, \theta; \omega, \theta_{D_k})\delta(r - \rho(\omega, \theta_{D_k})\cos(\theta - \phi(\omega, \theta_{D_k})))dr d\theta
\end{aligned}
\tag{A.11}
$$

Equation A.12 is the response obtained from detectors using CCST.

Finally, we use Dirac distribution to restrict the integration to the corresponding manifold and $I_1$ is written as a function of $(\theta_{D_k}, \omega)$ according

$$
\begin{aligned}
I_1(\theta_{D_k}, \omega) &= \sum_{i=1,2} (-1)^i \int_{\theta_{D_k}}^{\theta_{D_k}+(-1)^i\omega} \int_0^\infty a_1(E_0; r, \theta)\, n_e(r, \theta)\, q(\theta_{D_k}, \omega; r, \theta) \\
&\qquad\qquad\qquad\qquad a_2(\theta_{D_k}, E_\omega; r, \theta)\, \delta(r - \rho_i\cos(\theta - \phi_i))\, dr d\theta.
\end{aligned}
\tag{A.12}
$$

Finally, one can obtain the expression of solid angle $\Delta\Omega$

$$
\Delta\Omega(r, \theta; \omega, \theta_{D_k}) = \frac{a}{4\pi}\frac{\overrightarrow{MD_k}\cdot\overrightarrow{n}}{||\overrightarrow{MD_k}||^3} = \frac{a}{4\pi}\frac{\sin(\theta - \phi(\omega, \theta_{D_k}))}{\rho(\omega, \theta_{D_k})^2\cos(\theta - \theta_{D_k})^2},
\tag{A.13}
$$

where $a$ is the detector area and $\overrightarrow{n}$ the unitary normal vector to the considered detector.

## A.3    Numerical simulations

We perform in this section the numerical simulations of 3.9.

### A.3.1    General framework

**Object**

As an example, we consider a simple object of size $10 \times 10$ cm made of circles of carbon and aluminum. Its thickness is negligible. For simulations, the attenuation coefficients for aluminum and carbon of photoelectric absorption and incoherent scattering are computed by linear interpolation of ground truth data of NIST database [23]. See Figure A.2 and Table A.1.

**Setup of the CCST system**

The object is placed inside a ring of diameter $P = 20$ cm containing $K = 185$ detectors of arc length $L = L_{\max}$. This represents three detectors per unit length. We assume that we use an isotropic and mono-energetic point-like source emitting photons of energy $E_0 = 300$ keV. The energy resolution for detectors is set to $\Delta E = 1$keV. See Figure A.2.

| No. of circle | Coordinates of the center | | Radius | Component |
|:---:|:---:|:---:|:---:|:---:|
| | $x$ | $y$ | (cm) | |
| 1 | 0 | -10 | 5 | Al |
| 2 | 0 | -10 | 4 | C |
| 3 | 1.5 | -10 | 1 | Al |

**Table A.1** – Parameters of the phantom used for the computation of the realistic simulations.

### A.3.2    Simulation results and validation of the proposed measurement model with Monte Carlo simulations

We performed then data acquisition discretizing the proposed model in equation (3.9) and compared the results with Monte Carlo simulations. See Figure A.3. It was quite difficult to find a colour map for suitable for these measurements, since scattered photons with an energy close to $E_0$ and $E(\pi)$ are preponderant than others. This can be explained on one hand by the probability of having photon with a small angle is higher and one the second hand, even if back-scattered photons with a large $\omega$ is less probable, they will be recovered by a small set of detectors (which are close to the source). We choose to make appear the contours of the obtained data in order to see its shape. Even if the proposed modelling
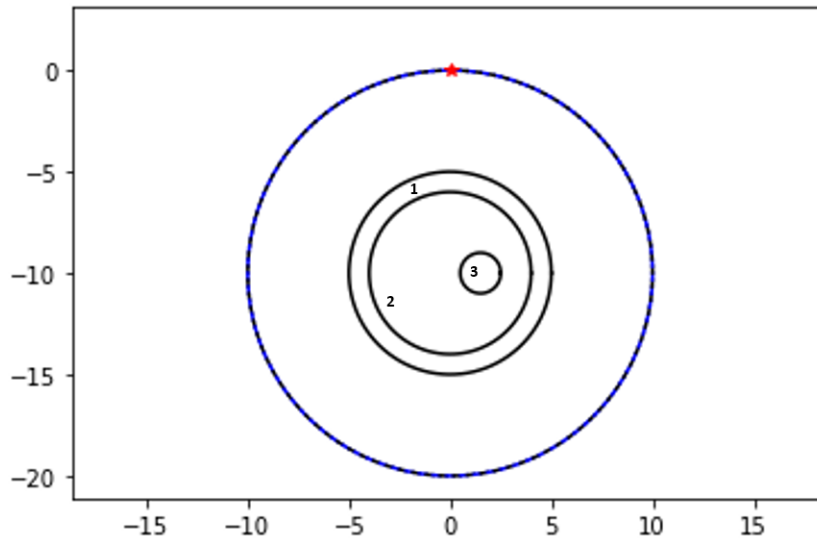
**Figure A.2** – Setup of the system and the phantom. The source is represented by a red star, and detectors are depicted alternatively in black and blue. The numbers $1, 2$ and $3$ refers to the number of the considered circle according to Table A.1

tends to overestimate the number of low scattering angle photons, we can observe the same behaviour on both figures.



(a)



(b)
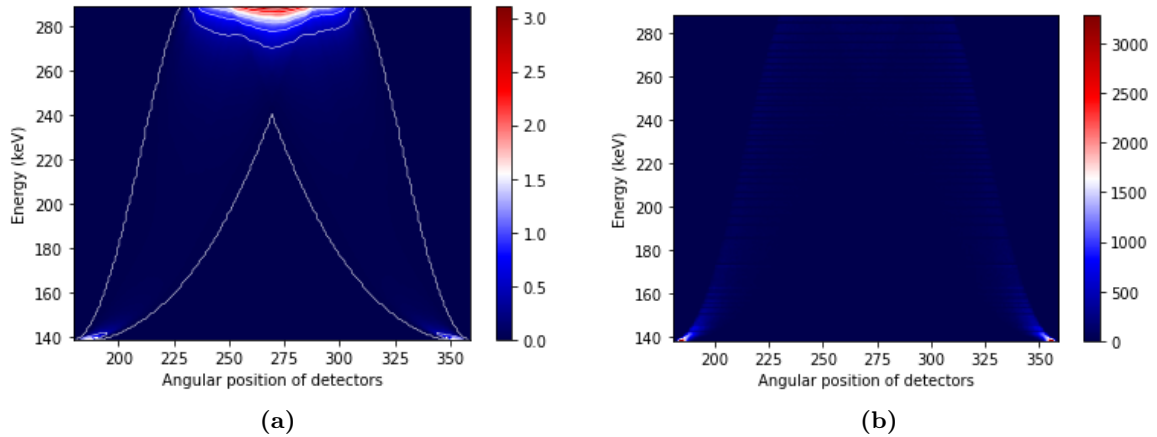
**Figure A.3** – (a) Acquisition data obtained from the expression of the generalized Radon transform (3.9). Comparison with (b) acquisition data by Monte Carlo simulations.

With Monte Carlo simulations, we confirm also that first order scattering is predominant in front of higher orders. Figure A.4a shows the result of data acquisition for all scattering orders combined. Figure A.4b illustrates that second scattered photons is already less predominant.

Then, suppose that we are in measure to separate *perfectly* photons incoming from one arc to the other. From figure A.3a, this leads us to acquired data on two separated figures, see
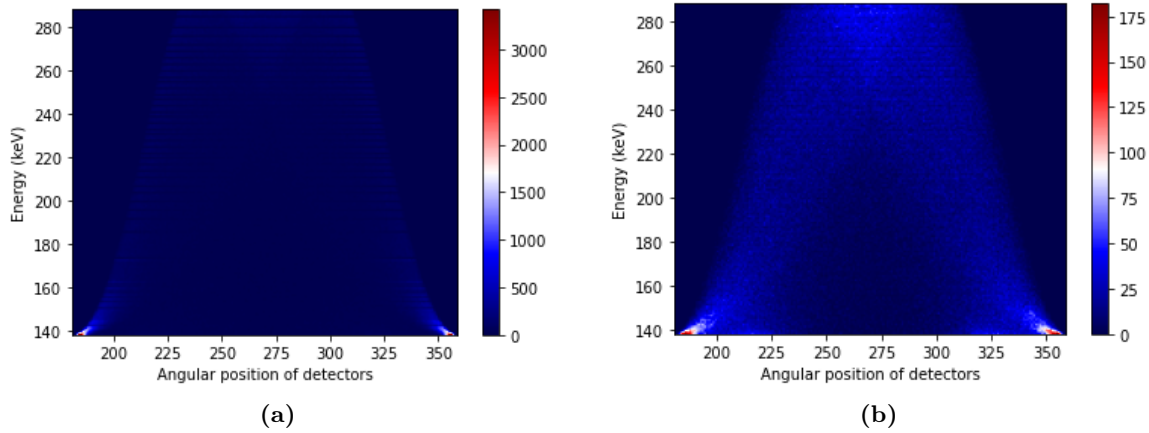
**Figure A.4** − Validation of the proposed model with Monte Carlo simulation results for (a) all combined scattering orders and (b) second scattering order only.
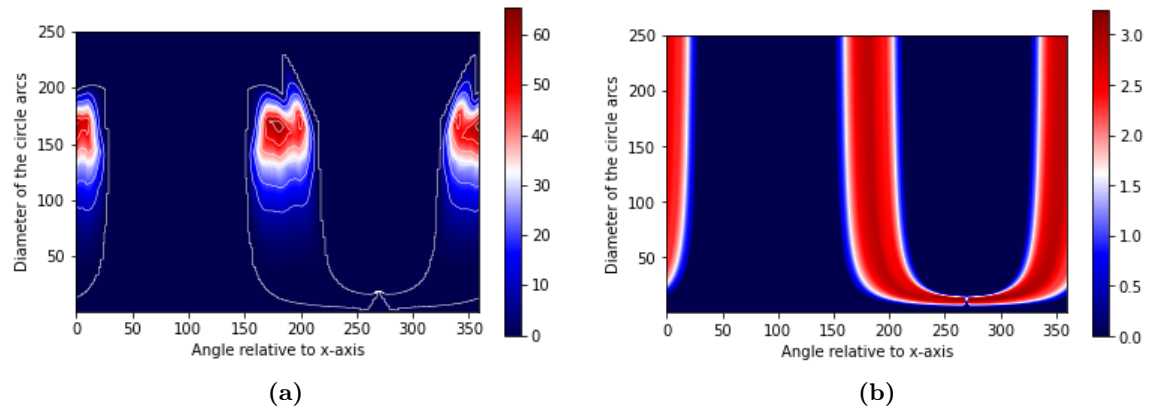
Figure A.5.
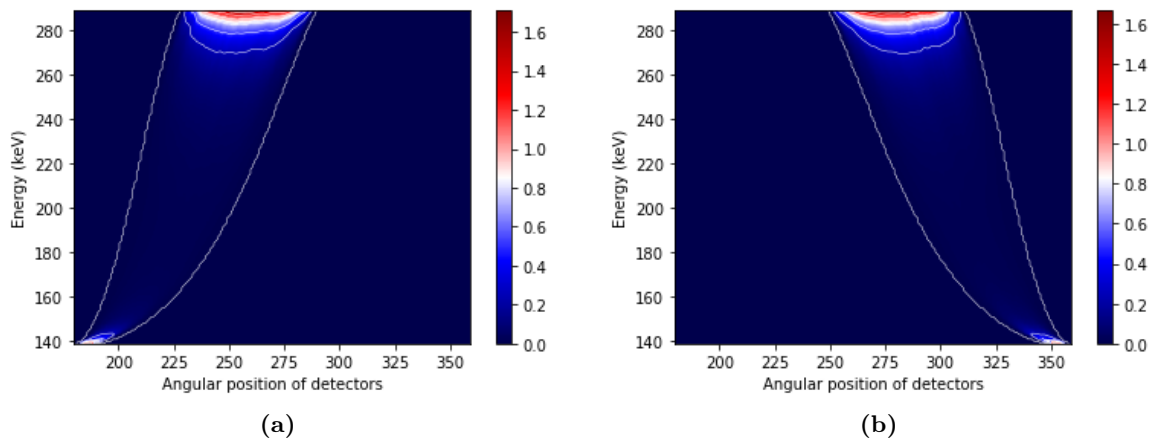


**Figure A.5** − Rearrangement of acquired data if a perfect collimation at detector is considered. (a) Acquisition data on $\mathcal{A}_1$. (b) Acquisition data on $\mathcal{A}_2$.

Furthermore, in the case where collimation is used, data can be rearranged according to the variables $(\rho, \phi)$, see the result in Figure A.6a. We recognize the U-shape previously observed. Compare the latter with acquire data acquisition assuming *ideal* theoretical conditions. The consequences of realistic energy resolution are two-fold. First, there is an abrupt cut-off, when $\rho$ increases (equivalently, when energy values are close to $E_0$) whereas we saw that theoretical circle arcs having a infinite diameter give also information on the object and prevent the presence of strong artifacts. In addition to few missing data caused by the distance between detectors adjacent to the source in figure A.6b.

Finally, we observe also in these figures the consequences of attenuation in matter, i.e. the

Radon transform is no longer linear.



(a)                                                      (b)

**Figure A.6** – Comparison of (a) rearranged data according to variables $(\rho, \phi)$ and (b) data acquisition results assuming the *ideal* theoretic conditions discussed in Section 3.5

# B

# Demonstration of the analytical inversion formula for the Radon transform of half-lines introduced in Chapter 4

**Synopsis**   In this appendix, we derive the analytic inversion of $\mathcal{R}_{\mathcal{A}}^{a^+} f$, the Radon transform on half-lines located above the horizontal line admitting for equation $y = a$. The demonstration of inversion for $\mathcal{R}_{\mathcal{A}}^{a^-} f$ is completely analogue.

First, we reformulate equation (4.19) as follows

$$\frac{\mathcal{R}_{\mathcal{A}}^{a^+} f(\xi, \tau)}{\sqrt{1 + \tau^2}} = \int_a^\infty dy\, f(\xi - y\tau, y). \tag{B.1}$$

Substituting $f(x, y)$ by its representation in the Fourier domain $\tilde{f}(x, y)$ as

$$f(x, y) = \int_{\mathbf{R}^2} dp\, dq\, e^{2i\pi(px + qy)} \tilde{f}(p, q), \tag{B.2}$$

one gets

$$\frac{\mathcal{R}_{\mathcal{A}}^{a^+} f(\xi, \tau)}{\sqrt{1 + \tau^2}} = \int_{\mathbf{R}^2} dp\, dq\, \tilde{f}(p, q) e^{2i\pi\, p\xi} \int_a^\infty dy e^{-2i\pi\, y(p\tau - q)}. \tag{B.3}$$

Moreover,

$$\int_a^\infty dy e^{-2i\pi\, y(p\tau - q)} = \int_{-\infty}^\infty dy H_a^+(y) e^{-2i\pi\, y(p\tau - q)},$$

with $H_a^+(y) = H(y - a)$ with $H$ is the Heaviside step function : $H_a^+(y) = 0,5 + 0,5 \cdot \mathrm{sign}(y - a)$.

Then,

$$\int_a^\infty dy\, e^{-2i\pi\, y(p\tau - q)} = \frac{1}{2} \int_{-\infty}^\infty e^{-2i\pi\, y(p\tau - q)}\, dy \tag{B.4}$$

$$+ \frac{1}{2} \int_{-\infty}^\infty \mathrm{sgn}(y - a)\, e^{-2i\pi\, y(p\tau - q)}\, dy$$

$$= \frac{1}{2}\left[ \delta(p\tau - q) + \frac{e^{-2i\pi a(\tau p - q)}}{i\pi\,(p\tau - q)} \right].$$

Eq. (B.3) becomes

$$\frac{\mathcal{R}^{a^+} f(\xi, \tau)}{\sqrt{1+\tau^2}}$$

$$= \int_{\mathbf{R}^2} dp\, dq\, \tilde{f}(p,q) e^{2i\pi\, p\xi} \cdot \frac{1}{2}\left[ \delta(p\tau - q) + \frac{e^{-2i\pi a(\tau p - q)}}{i\pi\,(p\tau - q)} \right],$$

$$= \frac{1}{2}\left[ \int_{\mathbf{R}} dp\, \tilde{f}(p, \tau p) e^{2i\pi p\xi} + \int_{\mathbf{R}} dp\, dq\, \frac{1}{i\pi} \frac{\tilde{f}(p,q)}{p\tau - q} e^{2i\pi p\xi} \cdot e^{-2i\pi a(p\tau - q)} \right].$$

Applying the Fourier transform on $\xi$ on both sides of the equation, one gets

$$\int_{\mathbf{R}} d\xi\, e^{-2i\pi\xi p} \frac{\mathcal{R}^{a^+} f(\xi, \tau)}{\sqrt{1+\tau^2}} = \frac{1}{2}\left[ \tilde{f}(p, \tau p) + \frac{1}{i\pi} \int_{\mathbf{R}} dq\, \frac{1}{i\pi} \frac{\tilde{f}(p,q)}{p\tau - q} \cdot e^{-2i\pi a(p\tau - q)} \right] \tag{B.5}$$

Denoting

$$\tilde{f}(p,q) = \int_{\mathbf{R}} d\xi\, e^{-2i\pi\xi q} g(p,\xi), \tag{B.6}$$

and considering the change of variables $u = p\tau - q$, the second part of Eq. (B.5) can be rewritten as

$$\int_{\mathbf{R}} dq\, \frac{\tilde{f}(p,q)}{p\tau - q} e^{-2i\pi a(p\tau - q)} = \int_{\mathbf{R}} d\xi\, e^{2i\pi\xi p\tau} g(p, \tau) \int_{\mathbf{R}} du\, \frac{e^{2i\pi(\xi - a)u}}{u}$$

$$= \int_{\mathbf{R}} d\xi\, e^{2i\pi\xi p\tau} g(p, \tau) \cdot i\pi\, \mathrm{sgn}(\xi - a).$$

Thereby,

$$\int_{\mathbf{R}} d\xi\, e^{-2i\pi\xi p} \frac{\mathcal{R}^{a^+} f(\xi, \tau)}{\sqrt{1+\tau^2}} = \frac{1}{2} \int_{\mathbf{R}} d\xi\, e^{-2i\pi\xi p\tau} g(p,\xi)(1 + \mathrm{sgn}(\xi - a)),$$

$$= \int_{\mathbf{R}} d\xi\, e^{-2i\pi\xi p\tau} H_a^+(\xi)\, g(p,\xi) \tag{B.7}$$

$$= \int_a^\infty d\xi\, e^{-2i\pi\xi p\tau} g(p,\xi). \tag{B.8}$$

For $p \in \mathbf{R}$, multiplying Eq. (B.7), by $: \int_{\mathbf{R}} d(\tau p) e^{2i\pi\tau pz}$, one gets

$$\int_{\mathbf{R}} d(\tau p) e^{2i\pi\tau pz} \int_{\mathbf{R}} d\xi \, e^{-2i\pi\xi p} \frac{\mathcal{R}^{a^+} f(\xi, \tau)}{\sqrt{1+\tau^2}} = \int_{\mathbf{R}} d(\tau p) e^{2i\pi\tau pz} \int_{\mathbf{R}} d\xi \, e^{-2i\pi\xi p\tau} H_a(\xi) \, g(p, \xi)$$

$$= \int_{\mathbf{R}} d\xi \, H_a^+(\xi) \, g(p, \xi) \int_{\mathbf{R}} d(\tau p) \, e^{2i\pi\tau p(z-\xi)}$$

$$= \int_{\mathbf{R}} d\xi \, H_a^+(\xi) \, g(p, \xi) \, \delta(z-\xi) \quad \text{(B.9)}$$

$$= H_a^+(z) \, g(p, z). \quad \text{(B.10)}$$

Then, $\forall z > a$,

$$g(p, z) = |p| \int_{\mathbf{R^2}} \frac{d\tau \, d\xi}{\sqrt{1+\tau^2}} e^{-2i\pi(\xi-\tau z)p} \mathcal{R}^{a^+} f(\xi, \tau), \quad \text{(B.11)}$$

and :

$$\tilde{f}(p, q) = \int_{\mathbf{R}} dz e^{-2i\pi zq} |p| \int_{\mathbf{R^2}} \frac{d\tau \, d\xi}{\sqrt{1+\tau^2}} e^{-2i\pi(\xi-\tau z)p} \mathcal{R}^{a^+} f(\xi, \tau). \quad \text{(B.12)}$$

From Eq. (B.2), we can reconstruct $f(x, y)$

$$f(x, y) = \int_{\mathbf{R^2}} dp \, dq \, e^{2i\pi(px+qy)} \int_{\mathbf{R}} dz e^{-2i\pi zq} |p| \int_{\mathbf{R^2}} \frac{d\tau \, d\xi}{\sqrt{1+\tau^2}} e^{-2i\pi(\xi-\tau z)p} \mathcal{R}^{a^+} f(\xi, \tau). \quad \text{(B.13)}$$

Integrating first on $dq$ and then on $dz$ with $z > a$, one can find that the result is non-zero if and only if $y > a$. Then, one can obtain

$$f(x, y) = H_a^+(y) \int_{\mathbf{R^2}} \frac{d\tau \, d\xi}{\sqrt{1+\tau^2}} \mathcal{R}^{a^+} f(\xi, \tau) \int_{\mathbf{R}} |p| \, dp \, e^{-2i\pi(\xi-\tau y-x)p}. \quad \text{(B.14)}$$

With the Fourier table, we have

$$\int_{\mathbf{R}} |p| \, dp \, e^{-2i\pi(\xi-\tau y-x)p} = \frac{-1}{2\pi^2} \frac{1}{(\xi-\tau y-x)^2}, \quad \text{(B.15)}$$

hence:

$$f(x, y) = \frac{-1}{2\pi^2} H_a^+(y) \, \text{p.v.} \left[ \int_{\mathbf{R^2}} \frac{d\tau \, d\xi}{\sqrt{1+\tau^2}} \frac{1}{(\xi-\tau y-x)^2} \mathcal{R}^{a^+} f(\xi, \tau) \right]. \quad \text{(B.16)}$$

Finally, using partial integration on $\xi$, the reconstruction equation for an function $f$ with the Radon transform on half-lines $\mathcal{R}^{a^+} f$ is

$$f(x, y) = \frac{1}{2\pi^2} H_a^+(y) \, \text{p.v.} \left\{ \int_{\mathbf{R^2}} \frac{d\tau \, d\xi}{\sqrt{1+\tau^2}} \frac{1}{(\xi-\tau y-x)} \frac{\partial}{\partial\xi} \mathcal{R}^{a^+} f(\xi, \tau) \right\}. \quad \text{(B.17)}$$

# C

# Technical details in demonstration of (7.16) of Chapter 7

**Synopsis**  In this appendix, we provide some details of the demonstration of (7.16) of Chapter 7. This result is achieved introducing consistency conditions, in terms of Cormack sense.

## C.1  Consistency conditions

We introduce consistency conditions [27, 10] in terms of Cormack sense in order to deduce a closed formulation of (7.7), more suitable for numerical computation. Equation (7.7) can be rewritten using the n-th order Tchebychev polynomial of the first kind $T_n$ as

$$f_n(r) = \frac{1}{\pi} \frac{d}{dr} \int_R^r \frac{T_{|n|}(r/\rho)}{\rho\sqrt{(r/\rho)^2 - 1}} \frac{(\mathcal{R}_{\mathcal{D}}f)_n(\rho)}{2\cos\left(n\cos^{-1}(R/\rho)\right)} d\rho, \tag{C.1}$$

Using the following relationship between Tchebychev polynomials of the first kind $T_n$ and the second kind $U_n$ [27]

$$\frac{T_{|n|}(r/\rho)}{\sqrt{(r/\rho)^2 - 1}} = \frac{\left((r/\rho) - \sqrt{(r/\rho)^2 - 1}\right)^{|n|}}{\sqrt{(r/\rho)^2 - 1}} + U_{|n|-1}(r/\rho), \tag{C.2}$$

and according to (7.13), (C.1) becomes

$$f_n(r) = \frac{1}{\pi} \frac{d}{dr} \left[ \int_R^r \frac{\left((r/\rho) - \sqrt{(r/\rho)^2 - 1}\right)^{|n|}}{\sqrt{(r/\rho)^2 - 1}} G_n(\rho)\frac{d\rho}{\rho} + \int_R^r U_{|n|-1}(r/\rho) G_n(\rho)\frac{d\rho}{\rho} \right]. \tag{C.3}$$

Furthermore, from (7.12), and changing the order of integration, one can obtain for $n \in \mathbb{N}^\star$

and $k = n, n - 2, n - 4, \dots > 0$

$$\int_R^\infty G_n(\rho) \frac{d\rho}{\rho^k} = 2 \int_R^\infty f_n(r) \int_r^\infty \frac{\cos\left(n \cos^{-1}\left(r/\rho\right)\right)}{\sqrt{1 - (r/\rho)^2}} \frac{d\rho}{\rho^k} dr. \tag{C.4}$$

With the change of variables $\rho = r/\cos\nu$, the previous $\rho$-integral becomes

$$\int_r^\infty \frac{\cos\left(n \cos^{-1}\left(r/\rho\right)\right)}{\sqrt{1 - (r/\rho)^2}} \frac{d\rho}{\rho^k} = r^{-k+1} \int_0^{\frac{\pi}{2}} \frac{\cos\left(n\nu\right)}{\cos\left(\nu\right)^{2-k}} d\nu. \tag{C.5}$$

We arrive to an $\nu$-integral whose result is given in [100]

$$\int_0^{\frac{\pi}{2}} \frac{\cos\left(n\nu\right)}{\cos\left(\nu\right)^{2-k}} d\nu = \frac{\pi}{(k-1)2^{k-1}} \frac{\Gamma(k)}{\Gamma\left(\frac{k+n}{2}\right)\Gamma\left(\frac{k-n}{2}\right)}, \tag{C.6}$$

where $\Gamma$ refers to the gamma function. For $n > 0$ and denoting $h(n) = \Gamma\left(\frac{k+n}{2}\right)\Gamma\left(\frac{k-n}{2}\right)$, one can remark that $k = n, n - 2, n - 4 > 0$ are poles of $h$. Since $h$ is even, then $k = -n, -n - 2, -n - 4 < 0$ for $n < 0$ are also poles of $h$. Consequently, one can conclude that this integral vanishes [10], i.e., for $n \in \mathbb{N}^\star$ and $k = n, n - 2, n - 4, \dots > 0$,

$$\int_R^\infty \frac{(\mathcal{R}_\mathcal{D} f)_n(\rho)}{2\cos\left(n\psi\right)} \frac{d\rho}{\rho^k} = 0. \tag{C.7}$$

Furthermore, since Tchebychev polynomials of second kind $U_{|n|-1}(r/\rho)$ are a linear sum of polynomials $1/\rho^k$ (see [100]), (C.7) leads to

$$\int_R^\infty U_{|n|-1}\left(\frac{r}{\rho}\right) \frac{(\mathcal{R}_\mathcal{D} f)_n(\rho)}{2\cos\left(n\psi\right)} d\rho = 0, n \in \mathbb{N}^\star. \tag{C.8}$$

## C.2    Derivation of formula (7.16)

This section uses consistency conditions established in (C.8) to obtain the final closed-form inversion formula (7.16). From (C.8), we deduce $\forall r \in [R, +\infty[$,

$$\int_R^r U_{|n|-1}\left(\frac{r}{\rho}\right) \frac{(\mathcal{R}_\mathcal{D} f)_n(\rho)}{2\cos\left(n\psi\right)} d\rho = - \int_r^\infty U_{|n|-1}\left(\frac{r}{\rho}\right) \frac{(\mathcal{R}_\mathcal{D} f)_n(\rho)}{2\cos\left(n\psi\right)} d\rho. \tag{C.9}$$

Consequently, using (C.9) and the relation between Tchebychev polynomials of the first and

the second kind (C.2), we obtain

$$
f_n(r) = \frac{1}{\pi} \frac{d}{dr} \left[ \int_R^r \frac{\left( (r/\rho) - \sqrt{(r/\rho)^2 - 1} \right)^{|n|}}{\sqrt{(r/\rho)^2 - 1}} \frac{(\mathcal{R}_\mathcal{D} f)_n(\rho)}{2\cos(n\psi)} \frac{d\rho}{\rho} - \int_r^\infty U_{|n|-1}(r/\rho) \frac{(\mathcal{R}_\mathcal{D} f)_n(\rho)}{2\cos(n\psi)} \frac{d\rho}{\rho} \right].
$$
(C.10)

Then, with $f$ and $G$ the projections of circular harmonic components of $G_n$ and $f_n$ in (C.10), we obtain

$$
f(r,\theta) = \frac{1}{\pi} \frac{d}{dr} \left[ \int_R^r \int_0^{2\pi} \frac{1}{2\pi\rho} \frac{G(\rho,\varphi)}{\sqrt{(r/\rho)^2 - 1}} \sum_{-\infty}^\infty \left( (r/\rho) - \sqrt{(r/\rho)^2 - 1} \right)^{|n|} e^{in(\theta-\varphi)} d\varphi d\rho - \right.
$$
$$
\left. \int_r^\infty \frac{1}{2\pi\rho} \int_0^{2\pi} G(\rho,\varphi) \sum_{-\infty}^\infty U_{|n|-1}(r/\rho)\ e^{in(\theta-\varphi)} d\varphi d\rho \right]. \quad \text{(C.11)}
$$

We need the two following lemmas to simplify (C.11).

**Lemma C.2.1** ([10], Lemma 3.8). *For $1 < \rho < r$, we have*

$$
1 + 2 \sum_{n=1}^\infty \left( r/\rho - \sqrt{(r/\rho)^2 - 1} \right)^n \cos(n(\theta - \varphi)) = \frac{-\sqrt{(r/\rho)^2 - 1}}{\cos(\theta - \varphi) - (r/\rho)}
$$
(C.12)

**Lemma C.2.2** ([10], Lemma 3.9). *For $0 < r < \rho$, we have*

$$
\sum_{n \in \mathbb{Z}} U_{|n|-1}(r/\rho)\, e^{in(\theta-\varphi)} = \frac{1}{\cos(\theta - \varphi) - (r/\rho)}
$$
(C.13)

Hence, we obtain :

$$
f(r,\theta) = \frac{1}{2\pi^2} \int_0^{2\pi} \frac{d}{dr} \text{p.v.} \left[ \int_R^\infty \frac{G(\rho,\varphi)}{r - \rho\cos(\theta - \varphi)} d\rho \right] d\varphi.
$$
(C.14)

Then, (7.16) is obtained first inverting the order of the $r-$derivative and the $\rho$-integral and then with the substitution $u = \rho/r$ and the fact that $G(\rho,\varphi) = 0$ for $\rho \in [0, R[$.

**Remark C.2.1.** *The intermediate result* (C.10) *is also an inversion formula based on circular harmonic expansion. However, the proposed formulation* (7.16) *is more practical for numerical reconstruction than* (C.10)*. In fact,* (C.10) *can be numerically implemented using a method similar to Chapman and Cary numerical approach [29], see for instance [101]. Nevertheless, the technique requires the evaluation of Tchebychev functions in* (C.10) *in terms of primitive integrals that are evaluated recursively. This implies either longer computational time or more memory.*

# D

## Summary table of the advantages and disadvantages of the CST modalities proposed in the literature and during this thesis

In this appendix, we sum up the advantages and drawbacks of the CST modalities. The modalities are presented in chronological order.
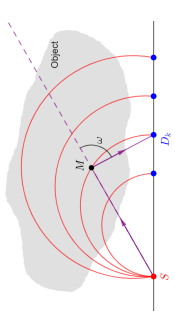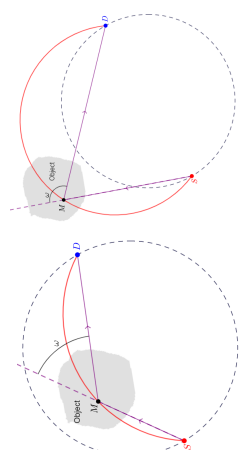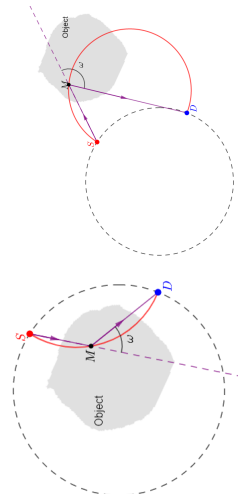
| Modalities | Setup | Advantages | Drawbacks |
|---|---|---|---|
| Norton's modality (1994)  | Fixed line containing a source and several detectors. Convenient for external scanning. | • Completely fixed<br>• Acquisition based on both forward and back-scattered photons | • Linear configuration<br>• Requires a set of detectors |
| Nguyen and Truong's modality (2010)  | Pair source - detector diametrically opposed in rotation around the object. Convenient for both internal and external scanning. | • Compact system<br>• Simple: only made of one source and one detector | • Requires a mechanical rotation of the source and the detector in a synchronized way |
| Truong and Nguyen's modality (2011)  | Pair source - detector in rotation around the object. Convenient for both internal and external scanning. | • Compact system<br>• Simple: only made of one source and one detector<br>• Convenient for both internal and external scanning | • Requires a mechanical rotation of the source and the detector in a synchronized way<br>• The position of the source-detector pair conditions the photon energy to be taken into account. |

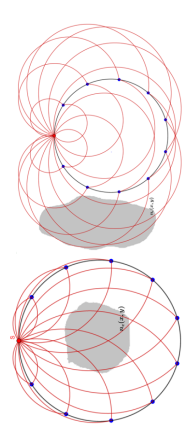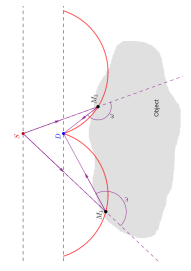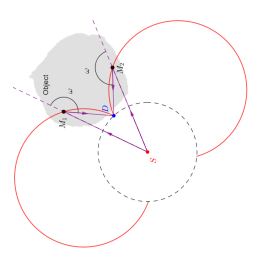**Table D.1** – Advantages and drawbacks of proposed systems - Part 1

| Modalities | Setup | Advantages | Drawbacks |
|---|---|---|---|
| CCST modality (2018)  | Fixed ring containing a set of detector and a source. Convenient for both internal and external scanning. | • Compact system<br>• Completely fixed<br>• Can be combined with Fan-beam CT to have a bi-imaging system | • In case of collimated detectors, the design may be more complicated.<br>• Requires a set of detectors. |
| Webber and Miller's modality (2020)  | Pair source - uncollimated detector in translation. Convenient for external scanning. | • Simple: only made of one source and one uncollimated detector<br>• Use an uncollimated detector | • Linear configuration<br>• Exploits only back-scattered photons<br>• Requires a mechanical translation of the source and the detector in a synchronized way |
| Fixed source rotating detector modality (2020)  | Fixed source - uncollimated detector in rotation around the source. Convenient for external scanning. | • Compact system<br>• Simple: only made of one fixed source and one uncollimated detector<br>• No synchronization needed between the source and the detector | • Exploits only back-scattered photons<br>• Requires a mechanical rotation of the detector |

**Table D.2** – Advantages and drawbacks of proposed systems - Part 2

# Bibliography

[1] J. Radon, "Über die Bestimmung von Funktionen durch ihre Integralwerte längs gewisser Mannigfaltigkeiten," *Akad. Wiss.*, vol. 69, pp. 262–277, 1917.

[2] A. M. Cormack, "Representation of a function by its line integrals, with some radiological applications," *Journal of Applied Physics*, vol. 34, no. 9, pp. 2722–2727, 1963.

[3] B. Çalişkan and A. C. Çalişkan, "Interaction with matter of ionizing radiation and radiation damages (Radicals)," in *Ionizing Radiation Effects and Applications*, IntechOpen, 2018.

[4] F. M. Khan and J. P. Gibbons, *Khan's the physics of radiation therapy.* Lippincott Williams & Wilkins, 2014.

[5] P. Lale, "The examination of internal tissues, using gamma-ray scatter with a possible extension to megavoltage radiography," *Physics in Medicine & Biology*, vol. 4, no. 2, p. 159, 1959.

[6] R. Clarke and G. Van Dyk, "Compton-scattered gamma rays in diagnostic radiography," in *Medical Radioisotope Scintigraphy. VI Proceedings of a Symposium on Medical Radioisotope Scintigraphy*, 1969.

[7] F. Farmer and M. P. Collins, "A new approach to the determination of anatomical cross-sections of the body by Compton scattering of gamma-rays," *Physics in Medicine & Biology*, vol. 16, no. 4, p. 577, 1971.

[8] S. J. Norton, "Compton scattering tomography," *Journal of applied physics*, vol. 76, no. 4, pp. 2007–2015, 1994.

[9] M. K. Nguyen and T. T. Truong, "Inversion of a new circular-arc Radon transform for Compton scattering tomography," *Inverse Problems*, vol. 26, no. 6, p. 065005, 2010.

[10] T. T. Truong and M. K. Nguyen, "Radon transforms on generalized Cormack's curves and a new Compton scatter tomography modality," *Inverse Problems*, vol. 27, no. 12, p. 125001, 2011.

[11] J. Cebeiro, M. K. Nguyen, M. Morvidone, and A. Noumowé, "New "improved" Compton scatter tomography modality for investigative imaging of one-sided large objects," *Inverse Problems in Science and Engineering*, vol. 25, no. 11, pp. 1676–1696, 2017.

[12] J. W. Webber and W. R. Lionheart, "Three dimensional Compton scattering tomography," *Inverse Problems*, vol. 34, no. 8, p. 084001, 2018.

[13] J. Webber and E. L. Miller, "Compton scattering tomography in translational geometries," *Inverse Problems*, vol. 36, no. 2, p. 025007, 2020.

[14] N. V. Arendtsz and E. M. Hussein, "Energy-spectral Compton scatter imaging. I. Theory and mathematics," *IEEE transactions on nuclear science*, vol. 42, no. 6, pp. 2155–2165, 1995.

[15] G. Redler, K. C. Jones, A. Templeton, D. Bernard, J. Turian, and J. C. Chu, "Compton scatter imaging: A promising modality for image guidance in lung stereotactic body radiation therapy," *Medical physics*, vol. 45, no. 3, pp. 1233–1240, 2018.

[16] K. C. Jones, G. Redler, A. Templeton, D. Bernard, J. V. Turian, and J. C. Chu, "Characterization of Compton-scatter imaging with an analytical simulation method," *Physics in Medicine & Biology*, vol. 63, no. 2, p. 025016, 2018.

[17] S. Gautam, F. Hopkins, R. Klinksiek, and I. Morgan, "Compton interaction tomography I. Feasibility studies for applications in earthquake engineering," *IEEE Transactions on Nuclear Science*, vol. 30, no. 2, pp. 1680–1684, 1983.

[18] G. Harding and E. Harding, "Compton scatter imaging: A tool for historical exploration," *Applied Radiation and Isotopes*, vol. 68, no. 6, pp. 993–1005, 2010.

[19] P. G. Prado, M. K. Nguyen, L. Dumas, and S. X. Cohen, "Three-dimensional imaging of flat natural and cultural heritage objects by a Compton scattering modality," *Journal of Electronic Imaging*, vol. 26, no. 1, p. 011026, 2017.

[20] E. M. Hussein, M. Desrosiers, and E. J. Waller, "On the use of radiation scattering for the detection of landmines," *Radiation Physics and Chemistry*, vol. 73, no. 1, pp. 7–19, 2005.

[21] P. E. Cruvinel and F. A. Balogun, "Compton scattering tomography for agricultural measurements," *Engenharia Agricola*, vol. 26, no. 1, pp. 151–160, 2006.

[22] O. Klein and Y. Nishina, *On the Scattering of Radiation by Free Electrons According to Dirac's New Relativistic Quantum Dynamics*, pp. 113–129. World Scientific Publishing Co. Pte. Ltd., 1994.

[23] J. H. Hubbell and S. M. Seltzer, "Attenuation Coefficients and Mass Energy-Absorption Coefficients (Version 1.4.)," 2004.

[24] T. T. Truong and M. K. Nguyen, "Recent developments on Compton scatter tomography: theory and numerical simulations," in *Numerical Simulation-From Theory to Industry*, IntechOpen, 2012.

[25] B. L. Evans, J. Martin, L. Burggraf, and M. Roggemann, "Nondestructive inspection using Compton scatter tomography," *IEEE Transactions on Nuclear Science*, vol. 45, no. 3, pp. 950–956, 1998.

[26] A. M. Cormack, "The Radon transform on a family of curves in the plane," *Proceedings of the American Mathematical Society*, vol. 83, no. 2, pp. 325–330, 1981.

[27] A. M. Cormack, "Radon's problem–old and new," in *SIAM-AMS Proceedings*, vol. 14, pp. 33–39, American Mathematical Society, 1984.

[28] G. Rigaud, M. K. Nguyen, and A. K. Louis, "Novel numerical inversions of two circular-arc Radon transforms in Compton scattering tomography," *Inverse Problems in Science and Engineering*, vol. 20, no. 6, pp. 809–839, 2012.

[29] C. Chapman and P. Cary, "The circular harmonic Radon transform," *Inverse Problems*, vol. 2, no. 1, p. 23, 1986.

[30] F. G. Tricomi, *Integral equations*, vol. 5. Courier corporation, 1985.

[31] G. Rigaud and B. N. Hahn, "3D Compton scattering imaging and contour reconstruction for a class of Radon transforms," *Inverse Problems*, vol. 34, no. 7, p. 075004, 2018.

[32] G. T. Herman, *Fundamentals of computerized tomography: image reconstruction from projections*. Springer Science & Business Media, 2009.

[33] J. Idier, *Approche bayésienne pour les problèmes inverses*. Hermès - Lavoisier, 2002.

[34] S. W. Rowland, "Computer implementation of image reconstruction formulas," in *Topics in Applied Physics*, pp. 9–79, Springer Berlin Heidelberg, 1979.

[35] M. Mamode, *Mathématiques pour la physique - Exercices et problèmes corrigés*. Ellipses, 2001.

[36] L. I. Rudin, S. Osher, and E. Fatemi, "Nonlinear total variation based noise removal algorithms," *Physica D: nonlinear phenomena*, vol. 60, no. 1-4, pp. 259–268, 1992.

[37] H. W. Engl, M. Hanke, and A. Neubauer, *Regularization of inverse problems*, vol. 375. Springer Science & Business Media, 1996.

[38] O. Scherzer, M. Grasmair, H. Grossauer, M. Haltmeier, and F. Lenzen, *Variational Methods in Imaging*. Springer Publishing Company, Incorporated, 1 ed., 2008.

[39] M. Haltmeier and D. Schiefeneder, "Variational regularization of the weighted conical Radon transform," *Inverse problems*, vol. 34, p. 124009, nov 2018.

[40] J. L. Mueller and S. Siltanen, *Linear and nonlinear inverse problems with practical applications.* SIAM, 2012.

[41] P. C. Hansen, *Rank-Deficient and Discrete Ill-Posed Problems: numerical aspects of linear inversion.* SIAM, 1998.

[42] G. H. Golub, M. Heath, and G. Wahba, "Generalized cross-validation as a method for choosing a good ridge parameter," *Technometrics*, vol. 21, no. 2, pp. 215–223, 1979.

[43] M. Hanke, "Limitations of the L-curve method in ill-posed problems," *BIT Numerical Mathematics*, vol. 36, no. 2, pp. 287–301, 1996.

[44] S. Osher and J. A. Sethian, "Fronts propagating with curvature-dependent speed: Algorithms based on Hamilton-Jacobi formulations," *Journal of computational physics*, vol. 79, no. 1, pp. 12–49, 1988.

[45] Y. Vardi, L. Shepp, and L. Kaufman, "A statistical model for positron emission tomography," *Journal of the American statistical Association*, vol. 80, no. 389, pp. 8–20, 1985.

[46] K. Lange, R. Carson, *et al.*, "EM reconstruction algorithms for emission and transmission tomography," *J Comput Assist Tomogr*, vol. 8, no. 2, pp. 306–16, 1984.

[47] S. Ganan and D. McClure, "Bayesian image analysis: An application to single photon emission tomography," *Amer. Statist. Assoc*, pp. 12–18, 1985.

[48] P. J. Green, "Bayesian reconstructions from emission tomography data using a modified EM algorithm," *IEEE transactions on medical imaging*, vol. 9, no. 1, pp. 84–93, 1990.

[49] J. Adler and O. Öktem, "Learned primal-dual reconstruction," *IEEE Transactions on Medical Imaging*, vol. 37, pp. 1322–1332, 2018.

[50] H. Chen, Y. Zhang, Y. Chen, J. Zhang, W. Zhang, H. Sun, Y. Lv, P. Liao, J. Zhou, and G. Wang, "LEARN: Learned experts' assessment-based reconstruction network for sparse-data CT," *IEEE transactions on medical imaging*, vol. 37, no. 6, pp. 1333–1347, 2018.

[51] J. He, Y. Yang, Y. Wang, D. Zeng, Z. Bian, H. Zhang, J. Sun, Z. Xu, and J. Ma, "Optimizing a parameterized plug-and-play admm for iterative low-dose CT reconstruction," *IEEE transactions on medical imaging*, vol. 38, no. 2, pp. 371–382, 2018.

[52] G. Rigaud, "Compton Scattering Tomography: Feature Reconstruction and Rotation-Free Modality," *SIAM Journal on Imaging Sciences*, vol. 10, no. 4, pp. 2217–2249, 2017.

[53] J. W. Webber and E. T. Quinto, "Microlocal analysis of a compton tomography problem," *SIAM Journal on Imaging Sciences*, vol. 13, no. 2, pp. 746–774, 2020.

[54] T. Truong and M. Nguyen, "Compton scatter tomography in annular domains," *Inverse Problems*, vol. 35, no. 5, p. 054005, 2019.

[55] G. Rigaud, R. Régnier, M. K. Nguyen, and H. Zaidi, "Combined modalities of Compton scattering tomography," *IEEE Transactions on Nuclear Science*, vol. 60, no. 3, pp. 1570–1577, 2013.

[56] C. Tarpau, J. Cebeiro, and M. K. Nguyen, "A new bi-imaging NDT system for simultaneous recovery of attenuation and electronic density maps," in *Eleventh Int. Conf. Non Destruct. Test. Aerosp*, 2019.

[57] L.-T. Chang, "A method for attenuation correction in radionuclide computed tomography," *IEEE Transactions on Nuclear Science*, vol. 25, no. 1, pp. 638–643, 1978.

[58] A. Maze, R. Collorec, P. Bourguet, and M. Pierpittte, "Iterative reconstruction methods for non uniform attenuation distribution in SPECT," in *1992 14th Annual International Conference of the IEEE Engineering in Medicine and Biology Society*, vol. 5, pp. 1821–1822, IEEE, 1992.

[59] H. Roitner, M. Haltmeier, R. Nuster, D. P. O'Leary, T. Berer, G. Paltauf, H. Grün, and P. Burgholzer, "Deblurring algorithms accounting for the finite detector size in photoacoustic tomography," *Journal of biomedical optics*, vol. 19, no. 5, p. 056011, 2014.

[60] C. Tarpau, J. Cebeiro, M. K. Nguyen, G. Rollet, and L. Dumas, "On the design of a CST system and its extension to a bi-imaging modality," 2020.

[61] M. K. Nguyen, J.-L. Delarbre, and T. Truong, "Study of the influence of energy resolution on image reconstruction quality in emission imaging based on Compton scattered radiation," in *IEEE Nuclear Science Symposium-Medical Imaging Conference*, (Dresden, Germany), 2008.

[62] T. T. Truong and M. K. Nguyen, "New properties of the V-line Radon transform and their imaging applications," *Journal of Physics A: Mathematical and Theoretical*, vol. 48, no. 40, p. 405204, 2015.

[63] R. N. Bracewell, "Numerical transforms," *Science*, vol. 248, no. II May, pp. 697–704, 1990. [doi:10.1126/science.248.4956.697].

[64] J.-C. Nosmas, "Analyse Microlocale et Tomographie Géométrique," in *ICAOS'96*, pp. 338–344, Springer, 1996.

[65] J. Frikel and E. T. Quinto, "Artifacts in incomplete data tomography with applications to photoacoustic tomography and sonar," *SIAM Journal on Applied Mathematics*, vol. 75, no. 2, pp. 703–725, 2015.

[66] E. T. Quinto, "Artifacts and visible singularities in limited data X-ray tomography," *Sensing and Imaging*, vol. 18, no. 1, p. 9, 2017.

[67] V. P. Krishnan and E. T. Quinto, "Microlocal analysis in tomography," *Handbook of mathematical methods in imaging*, pp. 1–50, 2014.

[68] J. Cebeiro, C. Tarpau, M. Morvidone, D. Rubio, and M. K. Nguyen, "On a three-dimensional Compton scattering tomography system with fixed source," *Inverse Problems*, 2021.

[69] D. Schiefeneder and M. Haltmeier, "The Radon transform over cones with vertices on the sphere and orthogonal axes," *SIAM Journal on Applied Mathematics*, vol. 77, no. 4, pp. 1335–1351, 2017.

[70] C. Tarpau, J. Cebeiro, M. K. Nguyen, G. Rollet, and M. A. Morvidone, "Analytic inversion of a radon transform on double circular arcs with applications in Compton scattering tomography," *IEEE Transactions on Computational Imaging*, vol. 6, pp. 958–967, 2020.

[71] S. Moon and M. Haltmeier, "Analytic inversion of a conical Radon transform arising in application of Compton cameras on the cylinder," *SIAM Journal on imaging sciences*, vol. 10, no. 2, pp. 535–557, 2017.

[72] E. T. Quinto, "The invertibility of rotation invariant Radon transforms," *Journal of Mathematical Analysis and Applications*, vol. 91, no. 2, pp. 510 – 522, 1983.

[73] M. Morvidone, M. K. Nguyen, T. T. T., and Z. H., "On the V-Line Radon Transform and Its Imaging Applications," *International Journal of Biomedical Imaging*, vol. 2010, p. 208179, 2010.

[74] T. T. Truong, "Function reconstruction from reflection symmetric radon data," *Symmetry*, vol. 12, no. 6, 2020.

[75] J. Cebeiro, M. Morvidone, and M. Nguyen, "Back-projection inversion of a conical Radon transform," *Inverse Problems in Science and Engineering*, vol. 24, no. 2, pp. 328–352, 2016.

[76] E. Y. Sidky, J. H. Jørgensen, and X. Pan, "Convex optimization problem prototyping for image reconstruction in computed tomography with the Chambolle–Pock algorithm," *Physics in Medicine & Biology*, vol. 57, no. 10, p. 3065, 2012.

[77] C. Tarpau, J. Cebeiro, M. K. Nguyen, G. Rollet, and L. Dumas, "On 3D imaging systems based on scattered ionizing radiation," in *Unconventional Optical Imaging II* (C. Fournier, M. P. Georges, and G. Popescu, eds.), vol. 11351, pp. 18 – 34, International Society for Optics and Photonics, SPIE, 2020.

[78] G. Rigaud and B. N. Hahn, "Reconstruction algorithm for 3D Compton scattering imaging with incomplete data," *Inverse Problems in Science and Engineering*, vol. 0, no. 0, pp. 1–23, 2020.

[79] B. Smith, "Reconstruction methods and completeness conditions for two Compton data models," *J. Opt. Soc. Am. A*, vol. 22, pp. 445–459, Mar 2005.

[80] L. Florescu, V. A. Markel, and J. C. Schotland, "Inversion formulas for the broken-ray Radon transform," *Inverse Problems*, vol. 27, p. 025002, jan 2011.

[81] F. Terzioglu, "Some inversion formulas for the cone transform," *Inverse Problems*, vol. 31, p. 115010, oct 2015.

[82] F. Terzioglu, "Exact inversion of an integral transform arising in Compton camera imaging," *Journal of Medical Imaging*, vol. 7, no. 3, pp. 1 – 10, 2020.

[83] V. Maxim, "Enhancement of Compton camera images reconstructed by inversion of a conical radon transform," *Inverse Problems*, vol. 35, p. 014001, nov 2018.

[84] M. K. Nguyen, T. T. Truong, and P. Grangeat, "Radon transforms on a class of cones with fixed axis direction," *Journal of Physics A: Mathematical and General*, vol. 38, pp. 8003–8015, aug 2005.

[85] C. Tarpau, J. Cebeiro, M. Morvidone, and M. K. Nguyen, "A new concept of Compton Scattering tomography and the development of the corresponding circular Radon transform," *IEEE Transactions on Radiation and Plasma Medical Sciences*, vol. (accepted for publication), 2019. [10.1109/TRPMS.2019.2943555].

[86] R. N. Bracewell, "Numerical transforms," *Science*, vol. 248, no. II May, pp. 697–704, 1990.

[87] L. C. Biedenharn and J. D. Louck, *Angular Momentum in Quantum Physics*. Reading, MA, USA: Addison Wesley Publishing Company, 1981.

[88] J. Driscoll and D. Healy, "Computing Fourier transforms and convolutions on the 2-sphere," *Advances in Applied Mathematics*, vol. 15, no. 2, pp. 202–250, 1994.

[89] H. N. Laden, *An historical and critical development of the theory of Legendre polynomials before 1900*. PhD thesis, University of Maryland, 1938.

[90] J. Cebeiro, C. Tarpau, M. A. Morvidone, D. Rubio, and M. K. Nguyen, "Algorithm for Discrete Spherical Harmonic Expansion of 3D functions," 6 2020.

[91] M. Haltmeier, S. Moon, and D. Schiefeneder, "Inversion of the Attenuated V-Line Transform with Vertices on the Circle," *IEEE Transactions on Computational Imaging*, vol. 3, no. 4, pp. 853–863, 2017.

[92] R. Weiss and R. A. Anderssen, "A product integration method for a class of singular first kind Volterra equations," *Numer. Math.*, vol. 18, pp. 442–456, 1971.

[93] L. Condat, "A direct algorithm for 1-D total variation denoising," *IEEE Signal Processing Letters*, vol. 20, no. 11, pp. 1054–1057, 2013.

[94] L. Condat, "A generic proximal algorithm for convex optimization. application to total variation minimization," *IEEE Signal Processing Letters*, vol. 21, no. 8, pp. 985–989, 2014.

[95] J. W. Webber and S. Holman, "Microlocal analysis of a spindle transform," *AIMS Inverse Problems and Imaging*, vol. 13, no. 2, pp. 231–261, 2019.

[96] I. S. Gradshteyn, I. M. Ryzhik, D. Zwillinger, and V. Moll, *Table of integrals, series, and products; 8th ed.* Amsterdam: Academic Press, Sep 2014.

[97] H. Bateman, *Tables of Integral Transforms*, vol. 1. New York: McGraw-Hill Book Compagny, 1954.

[98] G. Rigaud, "3D Compton scattering imaging: study of the spectrum and contour reconstruction," *arXiv preprint arXiv:1908.03066*, 2019.

[99] J. Wang, Z. Chi, and Y. Wang, "Analytic reconstruction of Compton scattering tomography," *J. Appl. Phys.*, vol. 86, no. 3, 1999.

[100] W. Magnus, F. Oberhettinger, and R. P. Soni, *Formulas and theorems for the special functions of mathematical physics*, vol. 52. Springer Science & Business Media, 2013.

[101] G. Rigaud, M. K. Nguyen, and A. K. Louis, "Novel numerical inversions of two circular-arc Radon transforms in Compton scattering tomography," *Inverse Problems in Science and Engineering*, vol. 20, no. 6, pp. 809–839, 2012.